

# Mechanics and Rheological Characterization of Construction Materials

BY

DAVID DANIEL PELOT  
B.S., Western Michigan University, 2006

THESIS

Submitted as a partial fulfillment of the requirements  
for the degree of Doctor of Philosophy in Mechanical Engineering  
in the Graduate College of the  
University of Illinois at Chicago, 2014

Chicago, Illinois

## Defense Committee

Alexander L. Yarin,	Chair and Advisor
W. J. Minkowycz,	Mechanical and Industrial Engineering
Farhad Ansari,	Civil and Materials Engineering
Kumar Natesaiyer,	United States Gypsum Co.
Suman Sinha-Ray,	United States Gypsum Co.

UMI Number: 3639759

All rights reserved

INFORMATION TO ALL USERS

The quality of this reproduction is dependent upon the quality of the copy submitted.

In the unlikely event that the author did not send a complete manuscript and there are missing pages, these will be noted. Also, if material had to be removed, a note will indicate the deletion.



UMI 3639759

Published by ProQuest LLC (2014). Copyright in the Dissertation held by the Author.

Microform Edition © ProQuest LLC.

All rights reserved. This work is protected against unauthorized copying under Title 17, United States Code



ProQuest LLC.  
789 East Eisenhower Parkway  
P.O. Box 1346  
Ann Arbor, MI 48106 - 1346

I dedicated this thesis to my wife, Sally M. Blechschmidt, and family, without whom it would never have been accomplished.

## ACKNOWLEDGEMENTS

I would like to thank my advisor, Professor Yarin, for the guidance and support in my education of becoming a scientist in the field of fluid engineering. With his constant support, he made sure I always moved forward and achieved success through dedication and hard work. He has made me independent of the education system; now I can learn.

I would like to thank my thesis committee members (Prof. Alex Yarin, Prof. W. J. Minkowycz, Prof. Farhad Ansari, Dr. Kumar Natesaiyer, and Dr. Suman Sinha-Ray) for the different experiences they have provided during my program. Each one of you has impacted me in a way that is unique and beneficial.

I would like to thank my lab mates for their generosity and support as well as providing a worldly experience while at home.

I would like to thank the ASME UIC student section and the Chicago section for introducing me to the world of engineering through a number of opportunities.

I would like to thank my family and friends for their never ending support, especially when I attempt to explain my research. To my friends who convince me to leave the lab and relax once in awhile. Without them I probably would have published more.

I would like to thank my wife for her constant support and for ensuring a quality of life that is sometimes forgotten during stressful times.

D. D. P.

Portions of this thesis have been published in peer reviewed journals. Sections 2.1.2 and 3.1 as well as Chapter 4 were published in Journal of Materials Chemistry by the Royal Society of Chemistry. Sections 2.2 and 3.2 as well as Chapter 5 were published in Langmuir by the American Chemical Society. Sections 2.3 and 3.3 as well as Chapter 6 were published in Journal of Rheology by AIP Publishing. Permission letters given by the publisher are in the Appendix.

## CONTRIBUTION OF AUTHORS

The work on self healing materials in Section 2.1, Section 3.1, and Chapter 4 represents a published manuscript [Sinha-Ray et al. (2012)] for which I was the primary author and conducted all experiments regarding fibers. The other main contributor, Dr. Sinha-Ray authored sections regarding Raman scattering, energy dispersive X-ray spectroscopy, fluorescence imaging, and SEM. The other authors contributed by revealing the response of the fibers when embedded in the material and some writing. The work on foam consolidation and drainage in Section 2.2, Section 3.2, and Chapter 5 represents a published manuscript [Jun et al. (2012)] for which I am the primary author, designer of the apparatus, and conductor of experiments. The theoretical section was completed by Dr. Jun, who assisted in the experimental work and writing. The gravity settler is a new apparatus in the laboratory and will be used in other published articles. The work on squeeze flows in Section 2.3, Section 3.3, and Chapter 6 represents a published manuscript [Pelot et al. (2013)] for which I am the primary author, designer of apparatus, and conductor of experiments. Rakesh Sahu contributed in the design and in conducting experiments. Dr. Sinha-ray contributed to the writing of the manuscript. In all published works my advisor, Dr. Yarin, contributed to the writing of the manuscript.

## TABLE OF CONTENTS

<u>CHAPTER</u>		<u>PAGE</u>
<b>1.</b>	<b>INTRODUCTION .....</b>	<b>1</b>
<b>2.</b>	<b>BACKGROUND AND LITERATURE REVIEW .....</b>	<b>3</b>
	2.1 Self-Healing Materials .....	3
	2.1.1 Self-Healing in Construction Materials .....	3
	2.1.2 Self-Healing in Epoxy Resin Materials .....	5
	2.2 Creation and Measurement of Foam Drainage .....	8
	2.3 Squeeze Flows of Soft Solids .....	11
	2.4 Bentonite: An Aging Material .....	17
	2.5 Spreading of Soft Solids .....	19
<b>3.</b>	<b>RESEARCH DESIGN AND OBJECTIVE .....</b>	<b>22</b>
	3.1 Encapsulation and Extrusion of Self-Healing Materials .....	22
	3.2 The Mechanical Properties of Foam Influence Drainage .....	23
	3.3 Design of a Squeezing Apparatus .....	24
	3.4 Transitions from Liquid-like to Solid-like Behavior of Bentonite ..	25
	3.5 Spreading of Carbopol Gels to Simulate Joint Compound Application .....	26
<b>4.</b>	<b>ENCAPSULATION OF SELF-HEALING MATERIALS BY COELECTROSPINNING, EMULSION ELECTROSPINNING AND SOLUTION BLOWING AND INTERCALATION .....</b>	<b>29</b>
	4.1 Introduction .....	29
	4.2 Experimental Materials and Methods .....	30
	4.2.1 Materials .....	30
	4.2.2 Preparation of Solutions .....	30
	4.2.3 Emulsion Electrospinning and Solution Blowing .....	31
	4.2.4 Coelectrospinning .....	32
	4.2.5 Self-Healing Composite Fabrication and Interlaminar Fracture Tests .....	32
	4.2.6 Observations .....	33
	4.3 Results and Discussion .....	34
	4.3.1 Creation of Core-Shell Fibers Using Self-Healing Materials .....	34
	4.3.2 Raman Scattering, EDX, and Fluorescent Imaging .....	44
	4.3.3 Self-Healing Core-Shell Fibers Embedded in Material .....	49
	4.4 Conclusion .....	51

## TABLE OF CONTENTS (continued)

<u>CHAPTER</u>		<u>PAGE</u>
<b>5.</b>	<b>FOAM CONSOLIDATION AND DRAINAGE .....</b>	<b>52</b>
5.1	Introduction .....	52
5.2	Theoretical Background .....	53
5.2.1	General Equations .....	53
5.2.2	Gravity Settler .....	57
5.3	Experimental Materials and Apparatus .....	63
5.3.1	Experimental Setup .....	63
5.4	Results and Discussion .....	65
5.5	Conclusion .....	83
<b>6.</b>	<b>STRONG SQUEEZE FLOWS OF YIELD-STRESS FLUIDS: THE EFFECT OF NORMAL DEVIATORIC STRESSES .....</b>	<b>84</b>
6.1	Introduction .....	84
6.2	Theoretical Background .....	85
6.3	Experimental Materials and Apparatus .....	92
6.3.1	Materials .....	92
6.3.2	Preparations of Solutions and Dispersions .....	92
6.3.3	Flow Curves in Simple Shear .....	93
6.3.4	Experimental Setup for Strong and Weak Squeeze Flow .....	94
6.4	Results and Discussion .....	96
6.4.1	Flow Curves of Carbopol Solution and Bentonite Clay Dispersion in Simple Shear .....	96
6.4.2	Squeeze Flow of Pure Newtonian Materials: Silicone Oils .....	99
6.4.3	Squeeze Flow of Carbopol Solution C3 and Bentonite Dispersion B10: No-Slip Conditions .....	102
6.4.4	Squeeze Flow of Carbopol Solution and Bentonite Dispersion .....	104
6.4.5	The Effects of Thixotropy .....	117
6.5	Conclusion .....	118
<b>7.</b>	<b>RHEOLOGY OF JOINT MATERIALS .....</b>	<b>120</b>
7.1	Introduction .....	120
7.2	Theoretical Background .....	120
7.3	Experimental Setup .....	121
7.3.1	Experimental Apparatuses .....	121
7.3.2	Experimental Methods .....	122
7.4	Results and Discussion .....	126
7.4.1	Qualitative Observations .....	126
7.4.2	Measuring Effective Viscosity .....	129
7.4.3	Yield Stress Measurements .....	133
7.4.4	Thixotropy .....	140
7.5	Conclusion .....	142



## TABLE OF CONTENTS (continued)

<u>CHAPTER</u>		<u>PAGE</u>
<b>8.</b>	<b>BENTONITE DISPERSIONS: TRANSITION FROM LIQUID-LIKE TO SOLID-LIKE BEHAVIOR AND CRACKING .....</b>	<b>143</b>
8.1	Introduction .....	143
8.2	Experimental Materials and Apparatus .....	144
8.2.1	Material .....	144
8.2.2	Squeezing Experiment .....	145
8.2.3	Bending Experiment .....	150
8.2.4	Buckling Experiment .....	151
8.3	Results .....	152
8.3.1	Squeezing Experiment .....	152
8.3.2	Bending Experiment .....	163
8.3.3	Buckling Experiment .....	169
8.4	Discussion .....	169
8.5	Conclusion .....	176
<b>9.</b>	<b>SPREADING OF CARBOPOL GELS: NEWTONIAN VS. NON-NEWTONIAN EFFECTS .....</b>	<b>178</b>
9.1	Introduction .....	178
9.2	Theoretical Background .....	179
9.2.1	Pressure and Flow Pattern for a Newtonian Fluid .....	179
9.2.2	Lubrication Approximation for a Newtonian Fluid .....	182
9.2.3	Pressure Distributions for a Newtonian Fluid .....	188
9.2.4	Velocity Field for a Newtonian Fluid .....	190
9.2.5	Pressure Distribution Under an Upper Surface Shaped as a Quadratic Profile for a Newtonian Fluid .....	191
9.2.6	Velocity Profile for a Bingham Fluid from Tichy (1991) .....	195
9.2.6.a	Floating Core .....	195
9.2.6.b	Core Attached to Upper Surface .....	198
9.3	Experimental Materials and Apparatus .....	203
9.3.1	Material Preparation .....	203
9.3.2	Experimental Procedure .....	204
9.4	Results .....	207
9.5	Discussion .....	219
9.5	Conclusion .....	225
<b>10.</b>	<b>CONCLUSION .....</b>	<b>227</b>
<b>11.</b>	<b>CITED LITERATURE .....</b>	<b>229</b>
<b>12.</b>	<b>APPENDIX .....</b>	<b>243</b>
<b>13.</b>	<b>CURRICULUM VITAE .....</b>	<b>248</b>

## LIST OF TABLES

<u>TABLE</u>		<u>PAGE</u>
4.1	Experimental parameters of emulsion electrospinning of two emulsions: PAN and DCPD in DMF, and PAN and isophorone diisocyanate in DMF .....	31
4.2	Experimental parameters of emulsion solution blowing of two emulsions, namely PAN and DCPD in DMF, and PAN and isophorone diisocyanate in DMF .....	32
5.1	Results for different concentrations of shampoo and PEO (in one case) .....	76
5.2	Results for different air flow rates, soap concentrations, and addition of PEO in one case. Values are averaged over two trials .....	77
5.3	Viscosity for different concentrations of shampoo and PEO in unfoamed solutions. Measurements were conducted using a Brookfield cone and plate viscometer .....	77
5.4	Viscosity for different concentrations of PEO in solutions of USG soap at concentrations of 0.25% stable and 0.25% unstable. Measurements were conducted using a Brookfield cone and plate viscometer. (*) The assumed value, as for water .....	78
5.5	Time, in minutes, needed for different concentrations of foam to drain fractions of the initial liquid volume .....	78
6.1	pH of several Carbopol solutions with NaOH added .....	96
6.2	Viscosity of the Silicone oils measured in the squeeze experiments vs. standard values. The viscosity values listed are the averages of two trials .....	101
6.3	Viscosity $\mu$ and the characteristic time $\tau_c$ for Carbopol solution C3 and Bentonite dispersion B10 established in strong squeeze experiments. The characteristic time $\tau_c$ , which is affected not only by the viscous forces but also by the yield stress, is introduced in Eqs. (19) and (20) .....	108
6.4	Experimental data for the yield stress of C3 .....	111
6.5	Experimental data for the yield stress of B10 .....	111
6.6	Elongational strain rate during strong squeezing, $\dot{\gamma}_{\text{elong fast}}$ , elongational strain rate at saturation, $\dot{\gamma}_{\text{elong sat}}$ calculated using Eq. (21) and shear strain rate, $\dot{\gamma}_{\text{shear}}$ established in squeezing experiments with C3 and B10 .....	115

## LIST OF TABLES (continued)

<u>TABLE</u>	<u>PAGE</u>
7.1 Calculation of the proportionality factor relating data from the Visco-Corder to the viscosity of the fluid .....	124
7.2 Average effective viscosities of various joint compounds with variances for all mass loads employed. Values with an (*) had a single outlier and removed from calculation .....	131
7.3 Experimental values of the yield stress of different joint compounds averaged over two experiments .....	135
7.4 Characteristic time, $\tau_c$ , for different joint compounds under different loads .....	138
7.5 Cessation of fast squeezing time moment $t_{cess}$ for different joint compounds under different loads .....	138
7.6 Elongational strain rate ( $s^{-1}$ ) for fast and slow stages for different joint compounds under different loads .....	139
7.7 Shear strain rate ( $s^{-1}$ ) for different joint compounds under different loads .....	140
7.8 Parameters for a best fit line for viscosity data in Fig. 14 .....	141
8.1 Rheological parameters of bentonite dispersions based on three trials in each case .....	166
8.2 Strain at cracking in the buckling experiment for 20 wt% bentonite .....	169
9.1 Experimental parameters and calculated viscosity using the Newtonian model (Eq. 9.31) and the Bingham model (Eq. 9.54) .....	208

## LIST OF FIGURES

<u>FIGURE</u>	<u>PAGE</u>
4.1 An emulsion of DCPD/DMF in PAN/DMF. (a) Tiny droplets of DCPD/DMF while the emulsion is wet. (b) Droplets of dried DCPD/DMF embedded in the matrix. It is emphasized that the emulsions are polydisperse, which might explain the fact that droplets in two different samples shown in panels (a) and (b) have different sizes. In addition, it is worth mentioning that droplets flatten when they dry, which can also be responsible for a larger size of the dried droplets in panel (b) .....	35
4.2 Optical images of core-shell fibers electrospun from emulsion are shown. Panels (a) and (b) show core-shell fibers obtained from emulsion of DCPD in PAN and DMF, while panels (c) and (d) show core-shell fibers obtained from emulsion of PAN and isophorone diisocyanate in DMF. The scale bar in all images is 10 $\mu\text{m}$ .....	36
4.3 Optical images of the core-shell fibers obtained by emulsion solution blowing. Panels (a) and (b) show core-shell fibers obtained from emulsion of DCPD in PAN and DMF, while panels (c) and (d) show core-shell fibers obtained from emulsion of PAN and isophorone diisocyanate in DMF. The scale bar in all images is 10 $\mu\text{m}$ .....	38
4.4 Optical images of the coelectrospun core-shell PAN/DCPD nanofibers. Panels (a) and (b) illustrate different fiber morphologies. The scale bar in both images is 5 $\mu\text{m}$ ....	39
4.5 SEM images of undamaged core-shell fibers. Panels (a) and (b) show isophorone diisocyanate/PAN core-shell fibers before squeezing, and panels (c) and (d) show DCPD/PAN core-shell fibers before squeezing. It is seen that the core-shell fibers have no protrusions on their walls .....	41
4.6 SEM images of squeezed isophorone diisocyanate/PAN core-shell fibers. Panels (a)-(d) illustrate different morphological aspects. The arrows indicate solid protrusions found on the fiber walls. Under squeezing, isophorone diisocyanate is released from the fiber core, makes contact with the catalyst (water) and solidifies creating the visible protrusions .....	42
4.7 SEM images of squeezed DCPD/PAN core-shell fibers. In panel (a) the arrow shows the rough cross-section of a fiber. In (b) the arrow indicates a solid blob protruding from the core and in panel (c) the arrow shows the solid protrusion formed at the end of a fiber. As a result of squeezing, DCPD is released from the fiber core, comes in contact with the catalyst [Tungsten (VI) Chloride] and solidifies .....	43

## LIST OF FIGURES (continued)

<u>FIGURE</u>	<u>PAGE</u>
4.8 EDX spectrum of (a) nanofiber shell (PAN), (b) cross-section of PAN/DCPD nanofiber. It can be seen that the presence of N is practically masked by the neighboring carbon peak in the spectrum owing to the energy resolution of the detector. Panel (c) corresponds to cross-section of PAN/isophorone diisocyanate nanofibers. Panel (c) shows a visible rise in the oxygen peak compared to panel (a). This rise is attributed to the presence of the oxygen-containing isophorone diisocyanate in the fiber core .....	46
4.9 (a) PAN and (b) PAN/DCPD cut nanofiber mats after the immersion in Rhodamine B solution at 40 °C with the subsequent rinsing in cold water. It can be seen that pure PAN nanofibers are white, whereas the PAN/DCPD nanofiber mat is slightly pink .....	48
4.10 (a) Optical image and (b) fluorescent image of the fiber mat shown in Figure 9b .....	49
4.11 SEM image of core-shell PAN nanofiber-toughened interface (a). SEM image of a failed core-shell PAN nanofiber at the interface with depleted healing agent (b). SEM image of a failed core-shell PAN nanofiber at the interface with released healing agent (c) .....	50
5.1 A filled cylinder of foam with surfactant solution (drained liquid) below. The top of the foam is at $z=0$ and the bottom of the cylinder is at $z=-h$ .....	57
5.2 Filling gravity settler using the funnel-hose system (a). Filling gravity settler using the foam generator with attached hose system (b). The system is raised with the foam height so that the foam exiting the hose is at the top of the foam column .....	64
5.3 Sketch of the experimental setup .....	65
5.4 Images taken during drainage of 2% shampoo foam. The images (a)-(h) correspond to 1.5 min, 5 min, 10 min, 15 min, 20 min, 25 min, 30 min, and 3 h (the end of draining), where the volume of liquid drained is $0.16 \text{ cm}^3$ , $3.37 \text{ cm}^3$ , $10.50 \text{ cm}^3$ , $18.88 \text{ cm}^3$ , $23.43 \text{ cm}^3$ , $25.85 \text{ cm}^3$ , $27.26 \text{ cm}^3$ , and $31.18 \text{ cm}^3$ , respectively. The dashed line indicates the height of the drained liquid in the previous frame .....	66
5.5 Height of liquid column drained for the first 1000 s (before the drainage process cessation is felt) in Trial 1 of 2% shampoo. The two lines show the crossover of a slow (initial) and fast (maximum) drainage processes. The ratio of maximum drainage rate to initial drainage rate in this case is 2.03 .....	67

## LIST OF FIGURES (continued)

<u>FIGURE</u>	<u>PAGE</u>
5.6 Volume drained from foams created with different air flow rates with soap concentration of 0.25% stable and 0.25% unstable. The dashed box highlights the domain with relatively similar drainage rates at the initial stages of drainage. The curve saturation corresponds to the full drainage .....	68
5.7 Drainage curves for different concentrations of shampoo (and addition of PEO). The volume of liquid in the foam, $V$ , is normalized by the total volume of liquid in the foam, $V_0$ . For each concentration the result of one trial is shown because the data are consistent between trials. Blue-2% shampoo, red-4% shampoo, green-8% shampoo, and purple-8% shampoo and 0.05% PEO .....	69
5.8 Normalized volume of liquid in the foam for different air flow rates during foam creation and the addition of 500 ppm PEO in one case .....	70
5.9 Normalized volume of liquid drained for different amounts of PEO added. The air flow rate during foam formation in all cases is 1.5 LPM and soap concentration of 0.25% stable and 0.25% unstable .....	71
5.10 Normalized volume of liquid in foams for different soap concentrations. The air flow rate during foam formation in all cases is 1.5 LPM .....	72
5.11 Drainage data fitted with Eq. (34). The diamonds represent the experimental data and the line is the fitted curve according to Eq. (34). (a) 2% shampoo, (b) 4% shampoo, (c) 8% shampoo, and (d) 8% shampoo with 0.05% PEO .....	82
6.1 Schematic of the velocity profiles in squeeze flows of (a) Newtonian material, and (b) Bingham plastic. The current sample thickness is denoted $h$ .....	87
6.2 Sketch of a sample with the coordinate axes .....	89
6.3 The experimental setup: (a) schematic, (b) image of the squeezing apparatus .....	95

## LIST OF FIGURES (continued)

<u>FIGURE</u>		<u>PAGE</u>
6.4	(a) Flow curves of Carbopol solution C1 at two different concentrations of NaOH. Parallel-plate viscometer: 2% NaOH (solid line) and 4% NaOH (dash-dotted line). Vane viscometer: 2% NaOH (dashed line) and 4% NaOH (dotted line). All lines are practically indistinguishable in this graph. (b) Flow curves of Carbopol solution C3 at two different concentrations of NaOH. Parallel-plate viscometer: 2% NaOH (solid line) and 4% NaOH (dash-dotted line). Vane viscometer: 2% NaOH (dashed line) and 4% NaOH (dotted line). In panel (b) the viscosity values measured in strong squeeze flow of C3 with 2% NaOH (symbols) are superimposed using the same strain rate axis for both shear rate in simple shear and the uniaxial elongation in the radial direction in squeezing. (c) Flow curves of Bentonite dispersion B10. Parallel-plate viscometer: (solid line), vane viscometer (dashed line). In panel (c) the viscosity values measured in strong squeeze flow of B10 (symbols) are superimposed using the same strain rate axis for the shear rate in simple shear and the uniaxial elongation in the radial direction in squeezing .....	97
6.5	Typical deformation curves: (a) Area A versus time t, and (b) the corresponding $A^4(t)$ dependences for S1. Curves 1 correspond to 165 g, 2-to 305 g, and 3-to 465 g ..	100
6.6	Typical deformation curves: (a) Area A versus time t, and (b) the corresponding $A^4(t)$ dependences for S2.5. Curves 1 correspond to 165 g, 2-to 305 g, and 3-to 465 g.	100
6.7	Viscosity obtained from the squeeze flows of S1 (squares) and S2.5 (circles). Horizontal dashed lines depict the viscosity values provided by the manufacturer of these oils .....	101
6.8	Upper row: Carbopol solution C3 being strong squeezed under a mass load of 230 g. Lower row: Bentonite dispersion B10 being strong squeezed under a mass load of 465 g. (a) $t=0$ , (b) 32.5 ms, (c) 39 ms, (d) 45.5 ms. 1- The aggregate of black dye that did not move during the squeezing process. 2- The aggregate of black dye that was smeared because it was deeply embedded into the sample. The dashed circles correspond to the initial circumference of the samples of C3 (in the upper row) and B10 (in the lower row). In the upper row for C3 the bigger dark ring is created by incoming light from the light source being partially refracted due to the sample geometry. Therefore, the inner circumference of the dark ring represents where the material ceases to make contact with the top and bottom disks and the outer circumference represents the leading edge of the sample. In the lower row for B10 the outer circumference of the dark area corresponds to the leading edge of the sample. There is no dark ring in this case because the material is opaque .....	103
6.9	Typical deformation curves for C3. (a) $A(t)$ , and (b) the corresponding $A^4(t)$ dependences. Curves 1 correspond to 230 g, 2-to 305 g, and 3-to 465 g. The inset in panel (a) resolves the initial stage of sample spreading. Weak squeezing: the load was applied softly .....	105

## LIST OF FIGURES (continued)

<u>FIGURE</u>	<u>PAGE</u>
6.10 Typical deformation curves for B10. (a) $A(t)$ , and (b) the corresponding $A^4(t)$ dependences. Curves 1 correspond to 230 g, 2-to 305 g, and 3-to 465 g. The inset in panel (a) resolves the initial stage of sample spreading. Weak squeezing: the load was applied softly .....	106
6.11 Comparison of deformation curve for Newtonian (S1, S2.5) and Bingham (C3 and B10) materials under a squeezing load of 465 g. (a) Short time evolution. (b) Longer time behavior. Curve 1-S2.5, 2-S1, 3-C3, and 4-B10. Weak squeezing: the load was applied softly .....	107
6.12 Typical deformation curves for (a) C3 and (b) B10 in strong squeezing. Curves 1-230 g, 2-305 g, 3-465 g, and 4-the tangent line corresponding to the instant when the maximum rate of spreading occurs for curves 3 .....	109
6.13 Shear layer thickness relative to the sample semi-thickness during the entire squeezing process for: (a) C3 solution, and (b) B10 dispersion. The mass load corresponding to curve 1 was 230 g, and to curve 2 - 465 g. The relative shear layer thicknesses corresponding to the maximum slopes of the dependences $A(t)$ are designated by open circles .....	113
6.14 The experimental deformation curves with the cross-over asymptotics of Eqs. (20) and (22). (a) C3 and (b) B10 under a mass load of 465 g. The solid line depicts the experimental data, the short-dash line-Eq. (20), and the long-dash line-Eq. (22). The long-dash lines are plotted according to Eq. (22) with $\tau_c=0.00253$ s for C3 and $\tau_c=0.00545$ s for B10 .....	114
7.1 Sketch of a sample with the coordinate axes .....	121
7.2 (a) Schematic of the squeezing device experimental setup. (b) Image of squeezing device. (c) Image of Visco-Corder. (d) Image of spindle used in Visco-Corder .....	122
7.3 Experimental data from the Visco-Corder using three silicone oils of viscosity 0.49 Pa·s (squares), 0.99 Pa·s (triangles), and 4.90 Pa·s (diamonds) .....	123
7.4 Dispensing a sample of compound C (left). The sample after it had been cut from the dispenser (right) .....	127
7.5 Dispensing a sample of compound F (left). The sample after it had been cut from the dispenser (right) .....	128
7.6 Dispensing a sample of compound E (left). The sample after it had been cut from the dispenser (right) .....	128



## LIST OF FIGURES (continued)

<u>FIGURE</u>	<u>PAGE</u>
7.7 Dispensing a sample of compound K (left). The sample after it had been cut from the dispenser (right) .....	129
7.8 Experimental data of joint compounds using the Visco-Corder. Data points were taken every 20 rpm, however, the utilization of lines helps discern different compound curves. Compound C (blue), compound F (red), compound E (green), and compound K (purple) .....	130
7.9 Calculated viscosity found using the Visco-Corder for each joint compound. Compound C (blue diamond), compound F (red square), compound E (green triangle), and compound K (purple circle) .....	130
7.10 Average effective viscosities for different joint compounds under mass loads of 165g, 315g, and 415g. The error bar represents the maximum and minimum values of viscosity measured. Compound C (blue diamond), compound F (red square), compound E (green triangle), and compound K (purple X). To clearly see the error bars, the values of the mass loads were shifted either positively or negatively around the mass loads used; compound E represents the correct mass load. Lines were added for guidance .....	132
7.11 Schematic of the velocity profiles in squeezing flows of (a) Newtonian and (b) Bingham fluids .....	134
7.12 Average yield stress for different joint compounds under various mass loads. The error bar represents the experimental values of yield stress measured and the symbol represents the average from Table 3. Compound C (blue diamond), compound F (red square), compound E (green triangle), and compound K (purple circle). Lines were added for guidance .....	136
7.13 The experimental deformation curves with Eq. (5) fitted for compound C under mass load of 415 g. The solid line depicts the experimental data and the dash line is Eq. (5) with $\tau_c=0.00667$ s .....	137
7.14 Viscosities of compounds under a mass load of 465 g after up to 80 minutes of resting time. Compound C (blue diamond), compound C uncapped (blue X), compound F (red square), compound E (green triangle), and compound K (purple circle) .....	141
8.1 (a) and (b)The leading edge of 11 wt% bentonite dispersion. (c) and (d) The leading edge of a $10^4$ Pa·s silicone oil. The samples were pushed from syringe by a plunger .....	147

## LIST OF FIGURES (continued)

<u>FIGURE</u>	<u>PAGE</u>
8.2 A sketch of a sample with: (a) Vertical and radial coordinates, $x$ and $y$ , respectively, the force, $F$ , and the cross-sectional area, $A$ . (b) The height of the sample, $h$ , the shear plane defined by the unit normal, $\mathbf{n}$ , its unit tangent, $\boldsymbol{\tau}$ , and the angle of inclination of the plane, $\alpha$ .....	149
8.3 Sketch of the apparatus used in squeezing experiments. By adding water to the reservoir, the magnitude of the magnitude of the applied force $F$ can be increased in time .....	150
8.4 (a) Sketch of the three-point bending setup for layers of bentonite dispersions. (b) Sketch of the buckling setup used to evaluate cracking stress of bentonite dispersion layers .....	152
8.5 Samples of several bentonite dispersions after a 48 h resting period which revealed cracking during compression under different loads. Cracks are highlighted by arrows. A sample of 11 wt% bentonite: (a) Initial sample image, (b) final spreading of the sample under 84 g load. A sample of 12 wt% bentonite: (c) Initial sample image, (d) final spreading of the sample under 153 g load. The vertical line at the center of the sample was caused by an irregularity in the syringe. A sample of 13 wt% bentonite (this trial is an example of a sample that spread very quickly once cracking initiated): (e) Initial sample image, (f) final spreading of the sample under 275 g load. The vertical line at the center of the sample was caused by an irregularity in the syringe .....	157
8.6 Cross-sectional area $A$ [cf. Figure 8.2(a)] of bentonite dispersion samples as they spread due to an increasing load in time. (a) Area versus time, (b) Area versus force. 11 wt% with a resting time of 48 h with corresponding images labeled as in Figures 5(a) and 5(b) (solid line). 12 wt% with a resting time of 48 h with corresponding images labeled as in Figures 5(c) and 5(d) (dashed line). 13 wt% with a resting time of 48 h with corresponding images labeled as in Figures 5(e) and 5(f) (dashed-dotted line) .....	158
8.7 Final images from the video of a 12 wt% bentonite sample being squeezed under load causing cracking after different resting times: (a) 0 h resting, cracking load 131 g, (b) 3 h resting, cracking load 142 g, (c) 6 h resting, cracking load 107 g, (d) 12 h resting, cracking load 120 g, (e) 24 h resting, cracking load 123 g, (f) 48 h resting, cracking load 153 g, and (g) 72 h resting, cracking load 172 g .....	159
8.8 The data corresponding to the appearance of the first crack. (a) The magnitude of the compressive stress $\sigma_{xx}$ , (b) the cross-sectional diameter $D$ , (c), the cracking plane angle $\alpha$ measured from the images, (d) the shear stress magnitude $\sigma_{nt}$ . The data for the 11 wt% bentonite samples (circles), 12 wt% bentonite (squares), and 13 wt% bentonite (diamonds). Error bars represent maximum and minimum values for each set of experiments .....	160

## LIST OF FIGURES (continued)

<u>FIGURE</u>	<u>PAGE</u>
8.9 Sample that reveals both liquid-like and solid-like behavior. The 11 wt% bentonite after a resting time of 24 h and under a mass load of 83 g (40 s after loading started; achieved at the rate 1-2 g/s). Bulging around the circumference (1) and cracking (2) .....	161
8.10 (a)-(c) Images of 11% bentonite after a resting time of 12 h being slowly compressed by the top plate. In particular, panel (a) corresponds to the initial time, (b)-to 7 s after loading has been started, and (c)-to 10 s. The initial sample configuration is traced by the dashed straight lines in panels (a)-(c). The corresponding creeping evolution of the circumference tip diameter of the sample in (a)-(c) is depicted in panel (d). The latter are reminiscent of those in Figure 8.9. (e) Strain versus time, and fitting according to the Kelvin-Voigt rheological constitutive equation with $t=0$ corresponding to 12 s of panel (d) when a pronounced bulging has started to develop under an approximately constant compression stress; $D_0 = 3.33$ cm and $D_\infty = 4.5$ cm; solid line-the experimental data, dashed line-the Kelvin-Voigt model .....	162
8.11 Sketch of the bending test and the sample cross-section .....	164
8.12 The images of the 18 wt% bentonite layer subjected to pure bending. (a) The initial intact sample. (b) The bent state at the moment when cracking starts at the bottom surface .....	165
8.13 Stress-strain dependences of bentonite dispersions of different contents. Solid line corresponds to 18 wt% bentonite, long dash - 20 wt% bentonite, and short dash - 22 wt% bentonite .....	167
8.14 The measured rheological parameters of bentonite dispersions corresponding to Table 1. (a) Young's modulus $E$ . (b) Yield stress $Y$ . (c) Strain at yield $\varepsilon_Y$ . (d) Stress at cracking $\sigma_{xx, crack}$ . (e) Strain at cracking $\varepsilon_{crack}$ .....	168
8.15 (a) Yield stress versus bentonite concentration found in the present study (squares) and in Pelot et al. (2013) (circle). It is emphasized that this linear dependence spans the yield stress $Y$ found for the liquid-like bentonite dispersions with $Y$ found for the solid-like bentonite dispersions. The yield stress $Y=F/A$ . (b) Average (over all resting times) stress magnitude at cracking versus bentonite concentration. Error bars represent the standard deviation. Some error bars are too small to be seen. Note that in panel (b) the magnitude of the normal stress at cracking of the 11-13 wt% bentonite dispersions in the squeezing experiments is found as $\sigma_{nn} = (F/A)\cos^2 \alpha$ , which is to be compared to $\sigma_{xx}$ in the bending and buckling experiments .....	174

## LIST OF FIGURES (continued)

<u>FIGURE</u>	<u>PAGE</u>
8.16 Storage (solid lines) and loss (dashed lines) moduli. (a) 11 wt% bentonite: 1-storage modulus at 10% strain, 2-storage modulus at 30% strain, 3-loss modulus at 10% strain, 4-loss modulus at 30% strain. (b) 22 wt% bentonite: 1-storage modulus at 2% strain, 2-storage modulus at 5% strain, 3-loss modulus at 2% strain, 4-storage modulus at 5% strain .....	175
8.17 Shear stress required to initiate cracking at different concentrations after 3 days resting time (squares) found in the present work, and in Gotoh and Shimizu (1965) for 7 days of resting time (compression – open triangles and in shear – solid triangles) .....	175
9.1 Spreading flow and the corresponding flow field .....	180
9.2 Sketch of pressure distribution corresponding to Figure 9.1 .....	181
9.3 The balance of forces .....	187
9.4 Pressure distribution along the wedge-like domain between the two plates. The values of $\bar{H}_0$ are labeled by the numerals near the curves .....	189
9.5 Dimensionless velocity field shown as a contour plot. Panel (a) $\bar{H}_0 = 1.1$ , (b) $\bar{H}_0 = 5$ , (c) $\bar{H}_0 = 20$ and (d) $\bar{H}_0 = 100$ .....	190
9.6 Dimensionless height and pressure distributions versus dimensionless longitudinal coordinate for $\bar{H}_0 = 2$ (a) and (b), as well as for $\bar{H}_0 = 5$ (c) and (d). Here $\bar{H}$ is given by Eq. (9.37) and the lines are labeled by the corresponding values of $\bar{a}$ , associated with the curvature .....	193
9.7 Bending the knife. Squares correspond to the linear shape and circles to the curved quadratic shape .....	194
9.8 Dimensionless height and pressure versus dimensionless longitudinal coordinate corresponding to the knife in Fig. 7 for $\bar{H}_0 = 8$ (a) and (b), as well as for $\bar{H}_0 = 15$ (c) and (d). The lines are labeled by the corresponding values of $\bar{a}$ related to the curvature ...	195
9.9 Typical velocity profile for attached upper core (solid line) with $\bar{\tau}_0 = 1.0$ , floating core (dashed line) with $\bar{\tau}_0 = 0.25$ , and no core (dotted line). For all profiles $d\bar{p}/d\bar{x} = 4$ .....	201

## LIST OF FIGURES (continued)

<u>FIGURE</u>	<u>PAGE</u>
9.10 Sketch Dimensionless pressure gradient $d\bar{p}/d\bar{x}$ for the two extreme experimental cases $\bar{H}_0 = 9.6$ (solid line) and $\bar{H}_0 = 86.5$ (dashed line) compared to the pressure gradient used in Figure 9.9 (dotted line) .....	202
9.11 (a) Viscosity of Carbopol 940 found using vane propeller (solid line), parallel plate with smooth plates (long dash) and rough plates (short dash), and the squeezing apparatus (circle). The fitting line for the vane data reveals the rheological parameter values as $n = 0.12$ and $K = 88 \text{ Pa}\cdot\text{s}^n$ , parallel plate with smooth plates-as: $n = 0.17$ and $K = 196 \text{ Pa}\cdot\text{s}^n$ and using rough plates-as: $n = 0.23$ and $K = 176 \text{ Pa}\cdot\text{s}^n$ . (b) Yield stress, $\tau_0$ , for different mass loads measured using the squeezing apparatus .....	204
9.12 Sketch (a) and image (b) of the experimental setup with the $20^\circ$ angle of inclination of the spreading plate .....	206
9.13 Two consecutive mages of seeding particles 0.5 s apart. The inclination angle is $20^\circ$ , the exit height is 0.65 mm, and the velocity of the moving surface is 0.24 m/s. Solid arrows in panel (a) point to two specific particles, and dashed arrows in panel (b) point to the same particles in 0.5 s .....	209
9.14 Shear rate fields $d\bar{u}/d\bar{y}$ for Newtonian fluid found using Eq. (9.7) for: (a) $\bar{H}_0 = 18.4$ , and (b) $\bar{H}_0 = 86.5$ .....	210
9.15 Stagnation zone close to the inclined spreading plate. The inclination angle of the plate is $5^\circ$ with the exit height of 1.5 mm; $\bar{H}_0 = 9.6$ . The two consecutive images are taken 3 s apart (the right-hand side image first). Arrows point to two seeding particles (encircled) that reveal no motion .....	210
9.16 Reverse flow zone. The angle of the spreading plate inclination is $20^\circ$ with the exit height of 0.650 mm; $\bar{H}_0 = 79.9$ . The two consecutive images are taken 4 s apart (the right-hand side image first). All three particles (encircled) move in the reverse direction, with particle 1 being slower than particles 2 and 3 .....	211
9.17 Experimental velocity fields measured for Carbopol gel (a) under a wedge at $\alpha = 5^\circ$ and $H_1 = 0.6$ mm versus the corresponding theoretical velocity fields for a (b) Bingham fluid with a floating core from $\bar{x} = 0$ to $\bar{x} = 0.92$ , and no core, or Newtonian profile, from $\bar{x} = 0.92$ to $\bar{x} = 1$ and (c) Newtonian fluid. Legend shows the dimensionless velocity values where the wall velocity is 0.167 m/s. Arrows in (a) point to representative velocities in the respective region of flow and in (b) and (c) the theoretical velocities are given at the same respective location as in (a) .....	212

## LIST OF FIGURES (continued)

FIGURE	PAGE
9.18 Experimental velocity fields measured for Carbopol gel (a) under a wedge at $\alpha = 5^\circ$ and $H_1 = 1.5$ mm versus the corresponding theoretical velocity fields for a (b) Bingham fluid with an attached upper core from $\bar{x} = 0$ to $\bar{x} = 0.80$ , and no core, or Newtonian profile, from $\bar{x} = 0.80$ to $\bar{x} = 1$ and (c) Newtonian fluid. Legend shows the dimensionless velocity values where the wall velocity is 0.167 m/s. Arrows in (a) point to representative velocities in the respective region of flow and in (b) and (c) the theoretical velocities are given at the same respective location as in (a) .....	213
9.19 Experimental velocity fields measured for Carbopol gel (a) under a wedge at $\alpha = 10^\circ$ and $H_1 = 0.8$ mm versus the corresponding theoretical velocity fields for a (b) Bingham fluid with a floating core from $\bar{x} = 0$ to $\bar{x} = 0.95$ , and no core, or Newtonian profile, from $\bar{x} = 0.95$ to $\bar{x} = 1$ and (c) Newtonian fluid. Legend shows the dimensionless velocity values where the wall velocity is 0.167 m/s. Arrows in (a) point to representative velocities in the respective region of flow and in (b) and (c) the theoretical velocities are given at the same respective location as in (a) .....	214
9.20 Experimental velocity fields measured for Carbopol gel (a) under a wedge at $\alpha = 10^\circ$ and $H_1 = 1.5$ mm versus the corresponding theoretical velocity fields for a (b) Bingham fluid with a floating core from $\bar{x} = 0$ to $\bar{x} = 0.90$ , and no core, or Newtonian profile, from $\bar{x} = 0.90$ to $\bar{x} = 1$ and (c) Newtonian fluid. Legend shows the dimensionless velocity values where the wall velocity is 0.167 m/s. Arrows in (a) point to representative velocities in the respective region of flow and in (b) and (c) the theoretical velocities are given at the same respective location as in (a) .....	215
9.21 Experimental velocity fields measured for Carbopol gel (a) under a wedge at $\alpha = 20^\circ$ and $H_1 = 0.6$ mm versus the corresponding theoretical velocity fields for a (b) Bingham fluid with a floating core from $\bar{x} = 0$ to $\bar{x} = 0.98$ , and no core, or Newtonian profile, from $\bar{x} = 0.98$ to $\bar{x} = 1$ and (c) Newtonian fluid. Legend shows the dimensionless velocity values where the wall velocity is 0.167 m/s. Arrows in (a) point to representative velocities in the respective region of flow and in (b) and (c) the theoretical velocities are given at the same respective location as in (a) .....	216
9.22 Experimental velocity fields measured for Carbopol gel (a) under a wedge at $\alpha = 20^\circ$ and $H_1 = 1.3$ mm versus the corresponding theoretical velocity fields for a (b) Bingham fluid with a floating core from $\bar{x} = 0$ to $\bar{x} = 0.96$ , and no core, or Newtonian profile, from $\bar{x} = 0.96$ to $\bar{x} = 1$ and (c) Newtonian fluid. Legend shows the dimensionless velocity values where the wall velocity is 0.167 m/s. Arrows in (a) point to representative velocities in the respective region of flow and in (b) and (c) the theoretical velocities are given at the same respective location as in (a) .....	217

## LIST OF FIGURES (continued)

<u>FIGURE</u>	<u>PAGE</u>
9.23 Experimental velocity fields measured for Carbopol gel (a) under a wedge at $\alpha = 20^\circ$ and $H_1 = 0.65$ mm versus the corresponding theoretical velocity fields for a (b) Bingham fluid with a floating core from $\bar{x} = 0$ to $\bar{x} = 0.98$ , and no core, or Newtonian profile, from $\bar{x} = 0.98$ to $\bar{x} = 1$ and (c) Newtonian fluid. Legend shows the dimensionless velocity values where the wall velocity is 0.240 m/s. Arrows in (a) point to representative velocities in the respective region of flow and in (b) and (c) the theoretical velocities are given at the same respective location as in (a) .....	218
9.24 Experimental velocity fields measured for Carbopol gel (a) under a wedge at $\alpha = 20^\circ$ and $H_1 = 1.5$ mm versus the corresponding theoretical velocity fields for a (b) Bingham fluid with a floating core from $\bar{x} = 0$ to $\bar{x} = 0.95$ , and no core, or Newtonian profile, from $\bar{x} = 0.95$ to $\bar{x} = 1$ and (c) Newtonian fluid. Legend shows the dimensionless velocity values where the wall velocity is 0.240 m/s. Arrows in (a) point to representative velocities in the respective region of flow and in (b) and (c) the theoretical velocities are given at the same respective location as in (a) .....	219

## SUMMARY

The main goal of this work is to investigate mechanical behavior and develop rheological characterization methods of complex construction materials. It aims to improve on already existing construction materials, such as gypsum board and joint compounds. Creating a more advanced gypsum board typically means either making it stronger, more flexible, or less dense; whereas enhancing joint compounds typically means it is easier to apply to the wall.

The creation of self-healing core-shell nanofibers was the first step in developing a material that is still usable after it fails. Furthermore, creating the fibers from a multitude of ways will give manufacturers flexibility in making these fibers. Therefore, self-healing core-shell fibers were created using three techniques, namely: emulsion electrospinning, coelectrospinning, and solution blowing. Each technique has its advantages and disadvantages which are discussed, but all are more economically viable and easier to incorporate into large scale manufacturing than techniques used by other researchers (also given the fact that the other groups did not develop nano-scale self-healing materials). The main mechanism that allows the fibers to heal the bulk material is that a slightly porous and weak (compared to the bulk material) fiber shell encapsulates a liquid healing agent. When the bulk material is stressed beyond a defined point, the fiber shell fails and the liquid core material is released due to the applied stress. The core material will polymerize in the fractured zone in contact with a preliminary dispersed/present catalyst, essentially healing the fractured area. The core material can be chosen to polymerize either when it makes contact with another material in the bulk, similar to Grubb's catalyst, or when it makes contact with the humidity in the air. Evidence was collected that reveals the core material exits the shell in multiple ways and polymerizes when being released.



The addition of air to construction materials to make them less dense is usually accomplished by pumping foam into the material while it is still in its slurry state. However, the mechanical properties of foam are unknown making it difficult to predict how the slurry will be affected by the addition of foam. By modeling foam as a consolidating medium, as in soil mechanics, the mechanical properties of foam, such as Young's modulus, Poisson's ratio, permeability, and consolidation coefficient, are elucidated. Furthermore, it is revealed that the drainage of foam in a gravity settler can be divided into three main stages. First, an initial slow drainage occurs. Then, at a characteristic time related to the consolidation coefficient, a faster drainage will occur that is twice as fast as the initial rate. Lastly, when the liquid in the foam starts to become exhausted, a decreasing rate of drainage will continue until the all liquid is drained (the third stage). This was confirmed on foams created with different surfactants, air contents, and the addition of a polymer.

What makes a brand of joint compound attractive, is mainly subjective criteria given by a practitioner about the compound's performance. Therefore, creating a better joint compound starts with understanding how individual components affect the compound's performance during application and relating the performance to mechanical properties, such as a viscosity and yield stress. Measuring the compounds mechanical properties using a traditional viscometer, however, is not possible due to the high stiffness, high yield stress, and roughness of the compound. Therefore, a model and homemade apparatus was developed for their rheological characterization, which revealed their Bingham-like behavior, and measuring viscosity and yield stress of such soft solids. Representative soft solids, Carbopol and Bentonite, were used to verify the model and apparatus. Then, joint compounds created with different proportions of components were tested in the apparatus. It was found that these Bingham-like fluids, when

stressed above the yield stress, reveal their viscosity. Also, each fluid has a characteristic time associated with the cessation of spreading caused by the presence of a yield stress. Moreover, it was identified that components of joint compound, such as cellulose, decrease the viscosity as its content increases, and that the yield stress increases as the clay content increases. With the development of this apparatus, the mechanical properties of joint compounds were measured and then can be correlated to the compounds performance.

Bentonite shows a transition of mechanical and rheological responses as a result of changing concentration or aging. That is, the response to normal stress reveals a transition from liquid-like behavior to solid-like behavior. When the concentration is low and aging time is small, bentonite will react to stress like a liquid, by flowing. However, when the concentration and aging time is past a critical value, it will react similarly to a solid, in that it will crack. Although it was previously shown that bentonite would flow or crack under very broad conditions, this study investigates for the first time the specific conditions for the transitional behavior from liquid to solid, which were found to happen in narrow ranges of concentration, aging time, and applied stress. It was found that under a small change in concentration, namely from 12 wt% to 13 wt% with no aging time under a critical stress, that bentonite changes its response from liquid-like to solid-like. Furthermore, a stress-strain profile created using a three point bending test elucidated independently the mechanical properties of bentonite (Young's modulus, yield stress, and cracking stress) as a semi-solid material.

The process of applying joint compounds is modeled using a variant of the one-dimensional lubrication approximation for a Newtonian fluid as well as a Bingham fluid. Using Carbopol gel (a Herschel-Bulkley fluid) to simulate joint compound, novel experiments are conducted using wedge geometry with several entrance-to-exit height ratios and two wall

velocities. From the experiments, the force on the wedge is measured and then the viscosity of the gel is calculated using the derived expression. Also, the velocity profile under the wedge is measured using seeding particles. The presence of the reverse flow and formation of a core in its domain, due to the yield stress, is visualized. The experimental velocity profile and the theoretical velocity profile for a Newtonian fluid and Bingham fluid are compared. It is seen that in zones of high shear, where the yield stress is overcome, the velocity profile is similar to that of a Newtonian fluid; however, in zones of low shear a core is formed and the velocity is lower for the yield stress fluid shown by the Bingham fluid model. Also, the viscosity of Carbopol gel measured using a vane viscometer and from the wedge experiment was in agreement, which substantiated our novel technique.

## 1. INTRODUCTION

Construction materials have been around from the pre-historic times. They are typically the evidence for a society's lifestyle, structure, available resources, and technology. Hence, there has always been an interest in more advanced materials to suit the growing society's needs. This includes material cost, structural capability, thermal management, and economic viability to name a few.

As with most new complex materials, they might be first expensive and time-consuming to produce. Then a process is created to make them more economically feasible. In the early 20th century, mass production of gypsum board created an efficient way to make indoor walls or partitions and installations. Installing segments of wall next to each other meant that another material had to fill the gap to make the finished wall look continuous, hence, the creation of joint compound. Since these materials are installed by practitioners, ease of installation will directly translate into cost effectiveness. Two of the main drawbacks of gypsum board, in its early development, are the high density and brittleness. Therefore, the addition of foam made the product less dense and provided some ductility. Similarly, joint compounds initially were also of high density and difficult to apply due to the consistency and the formation of craters. Therefore, modifying the formulation allowed joint compounds to become less dense, and viscosity modifiers allowed the compounds to be applied with ease.

In this thesis an additional structural components to potentially enhance construction and engineering materials are presented (Chapter 4). The creation of self-healing core-shell nanofibers using a variety of methods is introduced and the expulsion of the liquid in the case of damage is demonstrated (Chapter 4).

Foam is another component of construction materials which is used to lighten them and increase ductility. The mechanics of foams was widely explored in the past 50 years, albeit many aspects of foam drainage were poorly understood (Chapter 5). In this work an additional aspects of foam behavior were uncovered, which facilitate the process of integrating foam into construction materials in a more controlled way. We explored at different surfactant concentrations, air contents, and by adding a polymer and revealed foam as an example of consolidating material.

Further on, rheological investigations are conducted on soft solid materials that are similar to joint compounds to better understand the slight differences between formulations of the latter (Chapter 6). The peculiar mechanical properties caused by differences in formulation of joint compounds are explored in Chapter 7. It is also shown that complicated soft solid materials, like bentonite, show a dramatic change in behavior transient from a liquid-like material to a solid-like material in a very narrow range of parameter variation (Chapter 8).

The process of application of soft solid materials is important to practitioners because the efficiency in which these materials can be applied is directly correlated to cost. Therefore, the flow of soft solid materials inside a wedge is used to simulate spreading of materials on a wall in Chapter 9.

Overall conclusions are drawn in Chapter 10 followed by the cited literature in Chapter 11.

## 2. BACKGROUND AND LITERATURE REVIEW

### 2.1 Self-Healing Materials

#### 2.2.1 Self-Healing in Construction Materials

As the US left the 20th century, it was becoming clear that infrastructure inspection, maintenance, and repair are not cost effective. With this issue now in focus, long term solutions are now being researched that will improve the durability and lifetime of future construction materials [Gilford III et al. (2013)]. Specifically, Hager et al. (2010) state that the next decade of research on self-healing materials will not only lead to new commercial applications but that other properties than mechanical will be explored.

One infrastructure material that would have a large impact if self-healing capabilities can be accomplished is cementitious composites [Qian et al. (2009)]. Cracks in these materials occur due to freeze thaw cycles, shrinkage, compressive, and tensile forces [Gupta et al. (2013)]. This causes an increase in permeability and porosity creating pathways for aggressive liquids and gasses containing harmful chemicals [Gupta et al. (2013); Kan and Shi (2012)]. One method of detecting crack healing is the formation of hydrates at the crack site [Hager et al. (2010)].

Self-healing improves durability, permeability, and mechanical properties by closing cracks as they are being created [Kan et al. (2012)]. Robust autogenous self-healing, according to [Schmets and van der Zaken (2007)], requires the following: pervasiveness, stability, economics, reliability, quality, and repeatability. There have been different strategies to date, including expansive agent, bacteria, encapsulation, and mineral admixtures, and shape memory materials [Gupta et al. (2013); Kan and Shi (2012); Pelletier et al. (2011); Wu et al. (2012); Yang et al. (2009); Yang et al. (2011)].

Traditionally, cementitious materials are repaired using epoxy-based fillers or latex binding agents but their thermal expansion, health hazard, high cost, and weak bonding motivate the search for better options [Gupta et al. (2013)]. Recently biomineralization has been explored as a safer alternative. It is defined by Gupta et al. (2013) as, “a process in which organism(s) create a local microenvironment with conditions that allow optimal extracellular chemical precipitation of a mineral phase.” However, its novelty makes it unattractive because identifying bacteria that have a high pH resistance, high production amount, long-term viability, resistance to high calcium content and high pressures has proven difficult [Gupta et al. (2013)]. Another, more practiced self-healing technique is encapsulation, or plastic capsules filled with a self-healing agent [Pelletier et al. (2011)]. Pelletier et al. (2011) has shown that the capsules do not affect the compressive strength but are able to reduce corrosion and increase flexural strength after healing. Also, Gilford III et al. (2013) reported an increase in the modulus of elasticity of 11% and 30% when using sodium silicate and DCPD microcapsules, respectively.

The most promising technology is Engineered Cementitious Composites (ECC) according to Wu et al. (2012). ECC have shown full recovery if the crack width is less than 50  $\mu\text{m}$  and partial recovery is less than 150  $\mu\text{m}$  [Schmets and van der Zaken (2007)]. According to Kan and Shi (2012), experimental results reveal that the design of ECC, high tensile ductility and self-controlled crack width, is suited for self-healing behavior. However, the maximum crack length and width that can be mended is still an open question [Hager et al. (2010)]. A short review of self-healing technologies is found in Wu et al. (2012) and a more thorough review is given in Schmets and van der Zaken (2007). Typical self-healing technique of ECC uses PVA fibers integrated into the concrete which dissolve in water used during wet-dry cycles and precipitates in the crack [Kan and Shi (2012)]. The ultimate tensile strength and tensile strain has

shown to either become close to matching or exceed the virgin sample [Kan and Shi (2012); Yang et al. (2009); Yang et al. (2011)]. Also, deflection capacity can almost recover or exceed virgin samples and flexural stiffness was also retained [Qian et al. (2009); Qian et al. (2010)]. Moreover, self-healing in transport properties has also shown to be achievable by Yang et al. (2009).

ECC materials with embedded PVA appear to create a better material after self-healing; however, this only occurs when the environment promotes the proper mechanisms. For example, specimens cured in air do not recover nearly as well as those in water and early age specimens do not recover as efficiently compared to mature specimens [Qian et al. (2009); Yang et al. (2011)]. Also, repeatability has yet to be confirmed for tensile load cycles [Schmets and van der Zaken (2007)]. Pre-processing of the PVA fibers by coating them with an oiling agent is necessary to reduce interfacial bond strength between the fiber and material [Kan and Shi (2012); Yang et al. (2011)]. Overall, ECC materials show a promising future in self-healing after further research has been conducted.

### **2.1.2 Self-Healing in Epoxy Resin Materials**

Advanced composites made of a polymer matrix (typically thermosetting epoxy) reinforced “with high-performance fibers have found rapidly expanding applications in aerospace, aeronautical and ground vehicles, windmill blades, and sports utilities, among others. This is due to their high specific strength and stiffness, excellent manufacturability, superior corrosion resistance and their ability to be tailored for specific properties” [Sinha-Ray et al. (2012)]. Yet, the unique hierarchical fiber architecture embedded in a brittle polymer matrix results in unavoidable crack nucleation and growth in polymer composites when subjected to



external loads. From the physical point of view, all the damage and failure processes identified in conventional polymer composites are thermodynamically irreversible, i.e. the material properties always gradually degrade with time. Thus, damage monitoring, healing and maintenance costs become high priority once damage and failure occur in high-value composite structures; especially in military aircrafts and spacecrafts, as well as antennas on satellites or space stations. Therefore, producing polymer composites carrying self-healing functionality which mimic biological processes in nature is highly desirable in materials science and engineering.

In principle, healing micro-cracks in situ can significantly increase structural lifetime and suppress maintenance costs of polymer composites. Any crack formation can compromise the material strength, safety and reliability. Hence, it is especially important to avoid micro-cracking in applications where identification is difficult or impossible. To date, the market of composite materials has been continually growing and healable materials are necessary for the continuation of that growth. One of the first attempts to heal a thermoplastic polymeric material was associated with the conventional heating method [Murphy and Wudl (2010)]. In this method, the broken polymer parts are subjected to hot plate welding in which they are elevated to temperatures above their glass transition temperatures. However, it was found that the fractured part always remained the weakest portion [Bucknall et al. (1980)].

Historically, engineering has always found inspiration in nature. For example, the ability of mammals to heal themselves autonomously (such as bleeding, bruising, and healing of bone fracture) and return to a previous state is a process that scientists are trying to mimic. As in mammals, self-healing materials should have sub-systems in which automatic responses are triggered by minor damage [Youngblood and Sottos (2008); White et al. (2001); Wool (2001)]. According to Wu et al. (2008), “a suitable self-healing system should be (a) easily encapsulated

[and ruptured]; (b) remains stable and reactive over the service life of the polymeric components under various environmental conditions; (c) respond quickly to repair damage once triggered;” (d) low cost and low adverse impact on the original material properties. The very first trial to incorporate such smart healing capabilities in engineering was performed by encasing composites with glass capillaries/tubing filled with self-healing agents [Bleay et al (2001)]. However, handling such systems is troublesome. Therefore, the incorporation of healing agents inside the composites becomes imperative [White et al. (2001); Blaiszik et al. (2008)]. As described in van der Zwaag (2007), the works of several authors on poly(dicyclopentadiene) and Grubbs’ catalyst opened the way to using them as healing agents because of their excellent chemical stability. After this seminal discovery, however, substitutes were searched due to the high cost and limited availability of the catalysts. In this search, tungsten hexachloride was found to be a superior substitute due to its wide availability and enhanced melting point [van der Zwaag et al. (2007)]. However, some healing materials, such as isophorone diisocyanates, can use the humidity in the surrounding air as a catalyst, therefore, avoiding the need for a second chemical in the material matrix [van der Zwaag (2007); Toohey et al. (2007)].

All the above-mentioned encapsulation processes of self-healing materials involve chemically complex and expensive routes of manufacturing. Moreover, these routes commonly rely on microscopic hollow fibers or spherical capsules with diameters over 100  $\mu\text{m}$ . The direct incorporation of the healing agents via these carriers may adversely influence the superior specific properties of fiber-reinforced polymer composites. In fact, reliable interfacial toughening and self-healing strategies are desired for the ultrathin resin-rich interlayers of these polymer composites where localized damage and interlaminar fracture commonly occur under external loading [Jones (1999)]. In the past years, a novel interfacial toughening technique based on

entangling small fibers at interfaces (interlayers) has been proposed [Dzenis and Reneker (2001); Dzenis (2008)], which is specifically suitable for toughening fiber-reinforced polymer composites. These toughening small fibers can be compliant continuous polymer nanofibers or polymer-derived carbon nanofibers produced by means of the low-cost electrospinning technique [Doshi and Reneker (1995); Reneker and Chun (1996); Reneker et al. (2007); Reneker and Yarin (2008); Dzenis (2004); Sun et al. (2003); Zussman et al. (2006)]. Recently, accumulated experimental data from Wu (2009), Lin et al. (2008), Ozden et al. (2010), and Chen et al. (2011) and modeling results from Wu (2009) have validated this interfacial toughening strategy. Due to its intrinsic low cost in fabrication, low fiber concentration and ease to be merged into the conventional composites processing, this interfacial toughening technique would have promising future in composites engineering and industry. Yet, this interfacial toughening technique does not carry any self-healing function.

## **2.2 Creation and Measurement of Foam Drainage**

Jun et al. (2012) has stated:

The theoretical and experimental investigations of foams were in focus due to their multiple applications in material processing, pharmaceutical, construction and food industries [Kornev et al. (1999); Koehler et al. (2000); Colak (2000)]. Multiple investigations of foams differ by the method of foam creation and measurement technique. One way of creating foam is to pass a gas through an aqueous solution of surfactant. For example, Germick et al. (1994) and Ramani et al. (1993) generated foam by bubbling nitrogen through their solution. Since bubbling gas through a solution takes time to fill a column with foam, drainage

from the first bubble layer would begin as soon as it is created, making foam evolution less uniform. On the other hand, foams created through mechanical agitation can be expected to have a more uniform distribution of liquid compared to the foams generated by bubbling a gas through surfactant solutions [Bhakta and Ruckenstein (1995)]. Saint-Jalmes et al. (1999) used a high speed mixing chamber in which the surfactant solution and gas were mixed to create foam. One of the major advantages of this method is that large amounts of uniform foam can be created.

Different measurement techniques have been devised to measure the liquid content in foam during drainage [Germick et al. (1994); Ramani et al. (1993); Magrabi et al. (2001)]. In particular, to find the liquid fraction Magrabi et al. (2001) measured the transmission speed of sound waves from a speaker to a microphone. In the work of Weaire et al. (1995), the inside of a foam-containing column was vertically lined with wires allowing AC conductivity measurements to find the liquid fraction. Lastly, Stevenson et al. (2007) used nuclear magnetic resonance imaging (NMRI) to find the liquid fraction and then were able to calculate the liquid drained. Their technique was sensitive enough that they developed a method to find the amount of excess liquid drained due to bubble breakage.

When measuring foam drainage, it was found by different authors that only certain factors influence the drainage rate and amount drained, although there are disagreements. For example, Saint-Jalmes and Langevin (2002) found that different gases used in creating foams can change the drainage rate and

overall drainage time. From Germick et al. (1994), it was concluded that foam drainage was faster and the amount of liquid drained was larger for smaller bubbles and larger initial heights, whereas in the work of Ramani et al. (1993) it was stated that the drainage rate was slower for larger initial heights and the maximal rate was the same regardless of height. However, factors such as column diameter and column material have no effect on rate or drainage time according to Ramani et al. (1993). In addition, Magrabi et al. (2001) found that the time to full drainage was inversely related to the liquid fraction.

Several empirical equations were proposed to fit foam drainage data. One of the first empirical foam drainage equations was proposed by Ross (1943). This equation relates the fraction of liquid in the foam to an exponential function involving the current and characteristic time, with the latter being a fitting parameter. Its popularity is probably the result of its simplicity and sufficient accuracy. An equation that predicts the liquid drained as a function of time was also proposed by Ramani et al. (1993). However, in addition to the liquid volume fraction, this equation involves such parameters as bubble diameter, solution viscosity, radius of Plateau border [Kornev et al. (1999) and the lamellae thickness in the foam, which cannot be easily established in ordinary foams. (p. 5323-5324) Reprinted with permission from Jun, S., Pelot, D. D., & Yarin, A. L. (2012). Foam consolidation and drainage. *Langmuir*, 28(12), 5323-5330. Copyright (2012) American Chemical Society.

One factor in determining the effectiveness of creating a porous material is based on the mechanics of the foam. Specifically, foam impregnation into construction materials such as

gypsum wallboard has both advantages and disadvantages. Since air has a lower thermal conductivity than gypsum wallboard, the presence of pores increases the thermal resistivity of the overall material [Akthar and Evans (2010); Skujans et al. (2007)]. Furthermore, compared to other insulating materials, porous gypsum wallboards are economical, incombustible, and stiffer [Tonyan and Gibson (1992a); Tonyan and Gibson (1992b)]. On the other hand, as the density decreases from the increase in pores, the compressive strength diminishes [Colak (2000); Tonyan and Gibson (1992b); Skujans et al. (2007)]. Controlling the pore size and distribution is also a factor, since irregular structures lead to lower mechanical strength [Vimmrova et al. (2011)]. Moreover, it was found that the flexural strength decreases [Yu and Brouwers (2011)]. Therefore, Tonyan and Gibson (1992b) state that the application will dictate the mechanical properties and density required.

### **2.3 Squeeze Flows of Soft Solids**

Soft solids attract significant attention because of their non-trivial and not fully understood flow behavior as well as their important practical applications [Ovarlez et al. (2010); Butt (2011); Koos and Willenbacher (2011)]. Squeeze flows of such materials are common in the processing of construction compounds, ceramics, metals, polymers, cosmetics and personal care products, as well as in the food, biomedical, chemical and pharmaceutical industries [Cardoso et al. (2009); Rabideau et al. (2009); Meeten (2002); Luu and Forterre (2009); Nasserri et al. (2003)]. In many cases soft solid materials undergo deformations with both shear and elongational components, albeit traditional shear and elongational rheometers [Koos and Willenbacher (2011); Aksel and Heymann (2007); Barnes (2007); McKinley (2007); te Nijenhuis (2007)] can hardly be applied to them due to their high stiffness and yield stress.

Frequently vane viscometers are applied to evaluate rheological behavior of such materials, albeit the interpretation of the results in the framework of tensorial rheological constitutive equations requires studies of the other types of flow, e.g. squeeze flow [Meeten (2000, 2002, 2004a, 2004b)]. The values of the rheological parameters established using vane viscometer and squeeze flow can differ significantly [Meeten (2004a)]. Moreover, since it is not known a priori whether such materials follow the no-slip condition at the wall, their flow behavior becomes even more obscure. In the light of such uncertainties, squeezing disk-like samples with a constant force between two transparent disks, which causes the material to flow radially, can yield significant benefits as a research tool to characterize their behavior. Indeed, sufficiently large squeezing forces are readily available for initiating such flows practically irrespective of the material stiffness and yield stress. Squeeze flows possess both shear and elongational components, which are dominant in different flow domains and can be analyzed separately. The observations of slip (if any) through the transparent disks can be relatively easy. The above-mentioned potential benefits of squeeze flow between two disks determine such flow geometry as the main tool in the present work.

Three different variants of squeeze flow have been investigated so far. Namely, (i) A Constant Area flow, in which the sample material completely fills the gap between circular disks (in this case the sample radius is constant but the volume varies during squeezing because the material is released at the gap edges). It is emphasized that this type of squeeze flows was introduced into fluid mechanical repertoire in the seminal works of Stefan (1874) and Reynolds (1886) and is discussed in the classical text of Landau and Lifshitz (1987). Meeten (2010) recently showed that this type of flow cannot be used for accurate rheological measurements due to the effects associated with the extrudate flow outside the gap edges. (ii) An Imperfect Squeeze

flow: the case where a bath filled with the sample is compressed by a disk smaller than the bath size, which is a variant of flow (i); cf. Hoffner et al. (1997). (iii) A Constant Volume flow, in which the disk radius is much larger than the largest spreading radius of the sample (in this case the sample volume between the disks is constant throughout squeezing, but the sample radius varies). In the present work we employ the Constant Volume flow (iii). This means that in the present experiments the entire cylindrical sample is squeezed between two larger disks throughout the compression process.

A discussion of the theoretical description and some experimental results on macroscopic responses in squeeze flows of Newtonian and power-law fluids, Herschel-Bulkley yield-stress fluids, as well as elastic and viscoelastic materials, in different squeeze flows and subjected to different boundary conditions, such as perfect slip, partial slip or no slip can be found in [Covey and Stanmore (1981); Cardoso et al. (2009); Luu and Forterre (2009); Nasser et al. (2003); Reznik and Yarin (2002); Engmann et al. (2005); Campanella and Peleg (2002); Dienes and Klemm (1946); Meeten (2004a)]. In particular, [Dienes and Klemm (1946)] contains a detailed theory of Constant Volume flow (iii) for viscous Newtonian materials, which is of significant interest in the framework of the present work. The effect of surface tension at the free surface of constant volume samples in squeeze flow was shown to be negligible when compared to the internal stresses developed in the material during such flow [Luu and Forterre (2009)]. Covey and Stanmore (1981) assumed rheological behavior according to the Herschel-Bulkley rheological constitutive equation, or its particular case-the Bingham fluids, and the no-slip boundary conditions at the wall. The flow between the squeezing plates was subdivided into three different layers: the central plug-flow layer, and two shear layers adjacent to the squeezing walls. In the radial projection of the inertialess momentum balance equation, they accounted for



only shear stress  $\tau_{rz}$  and pressure  $p$ , and completely neglected the normal deviatoric stress  $\tau_{rr}$ , where  $r$  denotes the radial direction and  $z$ -the squeezing direction. As a result, they attributed the resistance to squeezing to only pressure generated due to the presence of shear stresses. Note that, the presence of the central plug in squeeze flows has been reported in Lipscomb and Denn (1984).

In distinction from some other materials (polymer solutions and melts), workable micro-mechanical rheological constitutive equations are unavailable for such complex materials as the yield-stress materials in general, and Carbopol solutions and Bentonite dispersions, in particular, as well as their rheological description is fully phenomenological. Phenomenological rheology implies that a rheological constitutive equation (RCE) for the internal stresses is assumed ad hoc. The equation should satisfy several formal requirements, such as the invariancy and objectivity [cf., for example, Astarita and Marrucci (1974)]. If an RCE has passed this test, it is tested in simplified situations (typically, tensorial equations are constructed to guarantee the behavior already observed in such simple tests). If it is capable of describing such simplified situations, the rheological parameters are fitted to this limited data, and the tensorial equation with these values of the parameters is believed to be valid in any other flow of the tested material. As a simple test, simple shear flow is typically chosen. Many complex non-Newtonian fluids show the shear-thinning behavior in such simple shear flows, which can be fitted with the so-called power-law fluid model, or if one believes (according to the observations) that a yield stress is also present, the latter is added to the former and the following ad hoc model appears for the shear stress  $\sigma_{xy}$

$$\sigma_{xy} = \tau_0 + K \dot{\gamma}^n, \tau_0 = \frac{Y}{\sqrt{3}} \quad (2.1)$$

Here  $x$  and  $y$  are the flow and shearing directions, respectively. The expression for the shear stress in Eq. (2.1) involves 3 rheological parameters, the yield stress in shear  $\tau_0$ , and the consistency and flow behavior indexes,  $K$  and  $n$ , respectively, with  $\dot{\gamma}$  being the shear rate. The yield stress in shear  $\tau_0$  is related to the yield stress in compression  $Y$  by the von Mises yield criterion.

Equation (2.1) is known as the Herschel-Bulkley law. It was fitted to the experimental data for Carbopol solutions in Divoux et al. (2012), with  $n$  typically in the range 0.5-1. It is emphasized that Bingham plastics correspond to a particular case of Eq. (2.1),  $n=1$  and  $K=\mu$ , when such fluid is capable of flow, e.g. for  $\sigma_{xy} > \tau_0$ . Bentonite, possesses  $n=0.96$ , which is practically identical with the Newtonian behavior when its dispersion flows well above the yield stress [Luu and Forterre (2009)]. Moreover, in many cases  $\sigma_{xy}$  is sufficiently large compared to  $\tau_0$ , and Eq. (2.1) reduces to  $\sigma_{xy} = \mu \dot{\gamma}$ .

The simplest tensorial equation for the Herschel-Bulkley fluid is

$$\boldsymbol{\tau} = 2 \left[ \frac{\tau_0}{|\mathbb{II}_{2\mathbf{D}}|^{1/2}} + K |\mathbb{II}_{2\mathbf{D}}|^{(n-1)/2} \right] \mathbf{D} \quad \text{for } \mathbb{II}_{\boldsymbol{\tau}} > \tau_0^2, \quad (2.2)$$

where  $\boldsymbol{\tau}$  is the deviatoric part of the stress tensor (i.e. the stress tensor  $\boldsymbol{\sigma} = -p\mathbf{I} + \boldsymbol{\tau}$ , with  $p$  being pressure and  $\mathbf{I}$ -tensor unit),  $\mathbf{D}$  is the rate-of-strain tensor,  $\tau_0$ ,  $K$ , and  $n$  are the basic invariant, i.e. flow-independent, rheological parameters, and  $\mathbb{II}_{\mathbf{X}}$  represents the second invariant of a tensor  $\mathbf{X}$ .

In steady-state simple shear flows, Eq. (2.2) reduces to Eq. (2.1). However, there are no works on the yield-stress fluids, e.g. Carbopol solutions and Bentonite dispersions, in which the Herschel-Bulkley model (2.2) was fully verified by data for more complicated flows (e.g. squeeze flows) without introducing additional fitting parameters (e.g. slip at the wall) with the

same values of  $\tau_0$ ,  $K$  and  $n$  as those established in steady-state simple shear flow for the same fluid. Note, that for example, in Divoux et al. (2012) Eq. (2.1) was not tested in the transient shear flow where a plug still (for hours) exists in the viscometer gap. There is no reason to believe that the momentum balance equation with Eq. (1) used for the shear stress and the values of  $\tau_0$ ,  $K$  and  $n$  established in steady-state simple shear flow will be able to reproduce the transient data in Figs. 3-11 in Divoux et al. (2012). The comparison of the values of the parameters  $\tau_0$  and  $K$  (at a fixed  $n$ ) in the Herschel-Bulkley model established in shear and squeeze flows of Carbopol in Rabideau et al. (2009) shows disagreement in the range 10-18%. In the work of Meeten et al. (2004a) the Herschel-Bulkley model was applied to several yield-stress soft solids in shear and squeeze flows, and the disagreement between the parameter values found in both flows was quite significant. Also, Shaukat et al. (2012) pointed out that "...most of the real fluids that possess the yield stress are thixotropic and show complicated rheological behavior for any simple mathematical model to work well", which also shows the limited nature of Eq. (2.2). A similar statement can be found in Meeten (2004b). Note also, that in works employing the Herschel-Bulkley model in squeeze flows, wall slip is frequently used as a fitting parameter in comparison with the experimental data, which might have a much larger effect than the values of the rheological parameters [Sherwood and Durban (1998); Yang (1998); Estelle and Lanos (2007)].

Ovarlez et al. (2010) reported an important finding for gels, emulsions and colloidal suspensions, namely, that when a sufficiently strong flow is imposed in one direction and creates a nearly uniform stress state close to the yield stress in that direction, there is no yield-stress in the orthogonal direction. Meeten (2001) reported that an in-plane rotation of a disk significantly facilitates the approach of two disks with samples of yield stress materials squeezed in between.

These findings mean that shear flow near the walls in a squeezing apparatus could practically eliminate the yield stress in the squeezing direction, and the Newtonian fluid model might be an appropriate approximation for describing strong squeeze flows of such yield-stress materials as Carbopol solutions and Bentonite dispersions.

Joint compounds have been characterized as soft fluids that exhibit two distinct types of behavior depending on the amount of stress applied. When the applied stress is below the value of the yield stress, the material does not deform. When the applied stress is higher than the yield stress, the material flows as approximately a Newtonian fluid so it may be approximated as a Bingham fluid. Bingham fluids have this type of behavior due to their microstructure and are common among clays, gels, dispersions, slurries and suspensions.

#### **2.4 Bentonite: An Aging Material**

Bentonite is mainly composed of montmorillonite, a plate or leaflet shaped mineral that gives bentonite its unique properties such as the ability to swell. Its structure was first uncovered in Hoffman et al. (1933). Marshall and Krinbill (1942) described montmorillonite as two silica sheets that sandwich an alumina sheet. Within the structure, rearrangement is also possible, that is, magnesium atoms can replace aluminum atoms and aluminum atoms can replace silicon atoms, as described by Mering (1946) and Siguin et al. (1993) who give a general chemical formula. According to Marshall (1937) the plates organize themselves with nearby particles in quasi-parallel groups. Then, Mering (1946) attempted to describe various levels of organization of the platelets from small groups of platelets to parallel platelets joint laterally, as well as combinations of the two to create an organized structure within the material.

The most renowned property of bentonite is its ability to swell when dispersed in water. This is caused by cations leaving the structure through dissociation and entering the water layer between sheets causing repulsion. This can result in swelling up to a factor of 30 of the original volume [Foster (1955); Siguin et al. (1993)]. Swelling up to 7 times the original volume has been confirmed by measuring the inter-planar spacing using X-ray diffraction by Norrish (1954) and a relationship was found between swelling and isomorphic substitutions in homoionic types [Siguin et al. (1993)]. Although it is possible for water to penetrate the silica sheet, the swelling is mainly caused by platelets being forced away from each other [Norrish (1954); Mering (1946)]. Using the swelling pressure, attractive forces, and repulsive forces, Komine and Ogata (1996) predict the swelling of sodium bentonite and compare to experimental data. An extensive review of sodium bentonite behavior is given by Luckham and Rossi (1999) and a review including other clays can be found in Murray (2000).

A rheological study of dispersed bentonite at a concentration of 10 wt% was conducted in the recent work of the present group in Pelot et al. (2013). Pelot et al. (2013) employed uniaxial compression with a constant force to samples of a given volume and demonstrated that such materials behave as Bingham liquids, i.e. approximately follow the phenomenological constitutive equation determined by a viscosity and yield stress. In their seminal but practically forgotten work, Gotoh and Shimizu (1965) studied cracking of bentonite dispersions after a resting time of seven days. They removed coarse particles from their samples by using suspension settling and created different concentrations through evaporation. However, the transition from flowing to cracking bentonite samples through an increase in concentration or resting time, i.e. the transition from the liquid-like to solid-like behavior has not been studied, as to our knowledge. Since bentonite has multiple applications which utilize different concentration

ranges, understanding how and when such a transition occurs has significant importance. This is one of the motivations of the present work.

According to Clem and Doehler (1961) bentonite has many industrial applications, in particular, as a binding agent, plasticizer, and suspending agent but can also be used as a filter or barrier. As a binding agent, bentonite is commonly used in foundry molding sand but can also be used in rock wool for insulation, pellets for animal feed, and pelleting of finely divided magnetite concentrates. It can be used as a plasticizer in ceramic, concrete products, other construction materials, paints, greases, lubricants, and cosmetics. As a suspending agent it is used as a viscosity modifier, drilling mud, fire retardant gel, and media for ingesting medicine. Due to the platelet shape of bentonite, it has a high surface to volume ratio, which makes it an ideal carrier for chemicals, such as insecticides, or as a filter for decolorizers of oil, clarifying agents in wine and beer, paper coatings, paint, pharmaceuticals, cosmetics, and metals from the environment [Hassanien et al. (2010); Karakaya et al. (2011); Clem and Doehler (1961)]. Lastly, it can also be used as a containment barrier as in cutoff walls, geosynthetic clay liners, landfill liners, overpack for radioactive canisters, and for borehole and shaft sealing [Kock (2002); Tay et al. (2001); Bohnhoff et al. (2013); Pusch (1992)]. It is not surprising then that in 2005 over 3.5 million metric tons of bentonite were used in the United States according to the U.S. Geological Survey (2005).

### **2.5 Spreading of Soft Solids**

The spreading of soft materials is a widely encountered phenomenon, such as spreading of creams, lotions, foods, and construction materials, to name a few. During the application of soft materials, sensory feedback is one of the major factors determined by the arising stresses.

The spreading process is similar to a journal bearing or screw extruder and therefore can be naturally considered as a lubrication-like process. Then, the lubrication approximation can be used as a powerful tool to describe spreading behavior [Schlichting (1987), Tichy (1991), and Weinstein and Ruschak (2004), Tadmor and Gogos (2006)].

Most of the soft materials possess a yield stress which might influence their flow profile and pressure when they are spread on a stationary plate by another moving inclined plate (effectively, flowing inside a wedge). It has been shown theoretically by Tichy (1991) and Batra (1996) that in the lubrication approximation for the Bingham yield-stress fluids, the load capacity, moment of friction, and coefficient of friction are to be increased compared to the corresponding Newtonian fluid. In addition, it was shown experimentally by Milne (1954) that stagnation zones arise in specific areas at a certain eccentricity inside a journal bearing containing grease which possesses a yield stress and typically is considered as a Bingham fluid. Furthermore, Wada et al. (1974) showed experimentally that the pressure within the journal bearing will be increased with the use of a Bingham fluid, and thus the eccentricity can be decreased compared to the corresponding Newtonian fluid to sustain the same load.

The existence of a yield stress creates what has been described as a core, or an unsheared plug. It was first qualitatively described by Milne (1954) who studied a journal bearing and witnessed fluid adhering to the immobile surface when the clearance was large. Core formation is related to the pressure gradient, film thickness, and the relative velocity [Wada et al. (1973)]. Core formation in hydrodynamic lubrication has been shown to occur when the pressure gradient is positive (adverse), or as the film thickness increases in the vertical direction, or as the velocity decreases, or at any combination of these. Wada et al. (1973) and Tichy (1991) described different types of cores; namely, an attached core or a floating core. An attached core is defined

as a plug with equal velocity to that of the plate it is attached to. On the other hand, a floating core is a plug that exists between two domains of flow. If the shear stress on the stationary plate is less than the yield stress, an attached core will form, but if the shear stress is greater than the yield stress than a floating core will occur [Wada et al. (1973)].

According to Tichy (1991) the flow with a floating core does not admit the existence of a closed-form Reynolds lubrication equation because the equation for the pressure gradient cannot be explicitly solved. However, using a modified equation for the pressure gradient for either a floating or attached core allowed for a modified Reynolds equation to be derived. Other authors have used other analyses or assumptions to determine the velocity field inside a flat wedge-like domain characteristic of spreading. For example, Dorier and Tichy (1992) expressed the viscosity profile of the fluid as a function dependent on a stress parameter loosely related to the yield stress and a strain-rate parameter. If the strain-rate parameter tends to infinity, a Newtonian viscosity is recovered. On the other hand, if the parameter tends to zero, the viscosity increases dramatically representative of a Bingham fluid. Batra (1966), who only considered attached cores, divided the journal bearing flow into three distinct domains following Milne's (1954) analysis of core formation as a result of the interplay between the pressure gradient, plug height, and the yield stress. Wada et al. (1973) were only able to establish an implicit Reynolds equation.



### 3. RESEARCH DESIGN AND OBJECTIVE

#### **3.1 Encapsulation and Extrusion of Self-Healing Materials**

The addition of self-healing components is the next generation of advanced materials. The incorporation of the self-healing technology will dramatically improve the material properties of several types of composites. Electrospinning, coelectrospinning, and solution blowing will be used in the present work as enabling technologies to develop self-healing materials.

In this study, our group produced novel ultrathin nanofibrous interlayers carrying both interfacial toughening and self-healing functions for use in fiber-reinforced polymer composites. These nanofibrous interlayers consist of electrospun core-shell polymer nanofibers encapsulating healing agents. In particular, we explore several novel techniques to encapsulate the healing agents inside ultrathin polymer fibers, which could also add to the structural capabilities of the material. By using coelectrospinning, emulsion electrospinning and emulsion solution blowing, two healing agents were incorporated into the core of micron size polymer fibers. These three methods offer the capability of encapsulation in a vascular network-like structure.

To validate the deliverability of healing agent of these core-shell nanofibers and nanotubes, novel fiber-crush tests were designed. Proof-of-concept carbon-fiber/epoxy composites reinforced with the novel nanofibrous self-healing interlayers were fabricated, interlaminar fracture tests were performed, and the toughening and self-healing mechanisms were explored by fractographical analysis of the failure interfaces. “Furthermore, once nanofiber scission happens due to crack-opening, fiber stretching and pull-out induced breakage, the liquid healant stored in the core-shell nanofiber network would automatically release at crack fronts

under the action of capillary force and then heal the cracks, resulting in interfacial self-healing effect and stiffness/strength recovery” [Wu et al. (2012)].

### **3.2 The Mechanical Properties of Foam Drainage**

Creating a large amount of uniform foam requires the use of a mechanical mixer as opposed to the shaking method or blowing bubbles method. The shaking method would have required more instrumentation since hundreds of milliliters of foam should be created at a time. The blowing bubbles method is problematic because the time between the first and last bubble created would have resulted in different properties of the two. Once a large amount of foam, approximately 1 liter, was created in the present work, a 1 meter tall column of foam was filled. This relatively tall cylinder is important for several reasons characteristic of our experiment. First, it enables hydrostatic pressure to be a relevant factor affecting foam consolidation. Second, the initial drainage is clearly visible. Third, the volume of liquid in the foam provided a non-invasive optical technique to be used to measure the amount of liquid drained.

By only measuring the amount of liquid drained, several mechanical properties of the foam were elucidated. This was elucidated by the idea that foam is a consolidating medium, which was motivated by the present experiments and guided them. Therefore, using a very simple optical measuring technique, mechanical properties such as Young’s modulus, permeability, consolidation coefficient, and Poisson’s ratio were found. Thus far, several surfactants, air contents, and the addition of polymer have all been tested and revealed additional important features of the drainage process.

### **3.4 Design of a Squeezing Apparatus**

In experiments with squeezing, the Constant Area squeeze flow (i) builds up the test material just outside the perimeter of the disks which creates an additional transient pressure which is difficult to characterize and control. Constant volume flow (ii), in which the squeezing piston has a smaller diameter than that of the bath containing the fluid again creating a transient pressure as the fluid rises in the outer bath. On the other hand, the constant volume flow (iii) does not have the drawbacks characteristic of flows (i) and (ii). That is the reason of choosing the constant volume flow in the experiments in the present work. In the present work a non-intrusive optical technique was applied in the experiments with squeeze flow. The rate of spreading of cylindrical soft solid samples placed between two parallel disks and subjected to a constant squeeze force is used to characterize the material response. Our goals are: (i) to evaluate the effect of the normal deviatoric stresses on strong squeeze flows of such yield-stress materials as Carbopol solutions and Bentonite dispersions; (ii) to elucidate the no-slip boundary condition at the wall in such flows; (iii) to measure viscosity and the yield stress using the squeeze data.

Joint compounds, provided by USG, contain several components. Of these components, it is unclear which one has an effect on the viscosity and the yield stress, and by how much do they affect these parameters? Since there are a large amount of components in such complex materials, it is natural to initially vary the components that are large in quantity or with known rheological behavior and measure the difference in the overall joint compound behavior. In the present case, these components are cellulose, starch, and clay. The exact names and types of these materials have been withheld for discretion.

It is of importance to know, in general, the rheological behavior of the compound's individual components so that the overall behavior of the compound after varying the component

concentration can be elucidated. At low shear rates cellulose acts as a Newtonian fluid and at higher shear rates it becomes pseudoplastic, likely due to the breaking of long chain molecules due to high shear [Dow Chemical Co. (2000), Missaghi et al. (2009)]. Clay is typically thixotropic, pseudoplastic, and increases viscosity and yield stress with concentration [Haden and Schwint (1967), Packter (1962), Wood et al. (1955)]. The starch is similar to other thickeners, an increase in concentration results in an increase in viscosity. Furthermore, it exhibits shear thinning and can show thixotropic behavior [Tate & Lyle Co. (1998)].

It is difficult to measure the viscosity and the yield stress of joint compounds, or any slurry, dispersion, or gelatinous material, using traditional rheometers due to their high stiffness, high yield stress and abrasiveness. These limitations constrict the measuring devices that can be used and these devices are sometimes not supported by theoretically-sound data processing. Therefore, the creation of a device that measures viscosity and yield stress backed by theory allows the mechanical properties of joint compounds to be measured.

### **3.4 Transitions from Liquid-Like to Solid-Like Behavior of Bentonite**

Although there are a wide variety of applications for bentonite, each application has a unique range of concentrations that is most appropriate for its purpose. For example, pelletizing iron ore concentrates use a concentration of less than 1 wt% bentonite, whereas drilling mud can be as low as 3 wt% bentonite, and molding sands in foundries can be in the range of 5 wt% to 12 wt% bentonite [Murray (2000); Mahto and Sharma (2004)]. In outside applications, such as liners or back fill, bentonite will be subjected to rain, humidity, or evaporation (desiccation) where the change in concentration could alter the yield strength, flow properties, and cracking stress, therefore changing the permeability of the material. Furthermore, the resting time of

bentonite dispersions can also have an effect on the yield stress as was shown in Cheng (1986). It is in this regard that this study was undertaken. We aimed at understanding how small changes in concentration or extended resting periods affect the mechanical behavior of bentonite. In particular, we were interested to establish and measure mechanical properties of bentonite dispersions in a range of concentrations that reveal both liquid and solid behavior and understand the cracking mechanism.

In order to find the stress required to crack the bentonite sample, an increasing load was applied to the sample and ample time was allowed for the sample time to respond to the applied load. This is different than the typical constant volume squeeze flow which squeezes the sample with a constant vertical velocity and measuring the responding force. The method used in this investigation used a free moving vertical plate which enabled noticing of a distinct change in vertical position of the plate when the sample cracked. This change in sample behavior made the stress required to cause cracking very clear. Furthermore, the sample was observed from the side using a CCD camera making the evolution of the crack to be viewed. Also, a three point bending test and buckling of higher concentration bentonite samples further support the validity of bentonite acting as a solid material.

### **3.5 Spreading of Carbopol Gels to Simulate Joint Compound Application**

The approach employing Newtonian fluid approximation in the lubrication flows has its advantages and disadvantages. As stated by Wienstein and Ruschak (2004), the major advantage of the Newtonian fluid approximation leading to the one-dimensional Reynolds lubrication equation allows for a straightforward calculation of the flow field for a given geometry. Even though in the spreading flows the pressure distribution is one-dimensional (depends only on the

longitudinal coordinate), the velocity profile is two-dimensional and can describe the velocity where the shear rate is high. The Bingham fluid model also has advantages and disadvantages. The Bingham fluid model can predict reverse flow velocities and core formation; however, its modified Reynold's Equation discussed earlier does not allow for a theoretical analysis of the force produced to be created. The analysis of spreading of soft materials using the Newtonian fluid model and the Bingham fluid model in combination allows one to shed light on the physical phenomena characteristic of spreading. Mainly, the Newtonian fluid model will describe the velocity in the high shear regions as well as the show trends in the force produced by different geometries and velocities. On the other hand where the shear is low, the Bingham fluid model will predict the type and location of a core and the velocity within. Furthermore, a viscosity value is found in every case for a Newtonian fluid and Bingham fluid. Milne (1954) implied that it might be insufficient to characterize a non-Newtonian fluid using an average viscosity based on a mean shear rate; therefore, the present results demonstrate that a range of viscosities exist within the wedge and can be elucidated using the appropriate model based on the shear rate. Furthermore, qualitative descriptions of cores, floating and attached, found from experimental data are shown and discussed.

The spreading of joint compound can then be modeled using flow through a wedge-shaped gap. The fluid flow beneath the wedge can be modeled in the lubrication approximation and mechanical properties, such as viscosity can be calculated then from the experimental data. The use of Carbopol gel with seeding particles enabled the velocity profile to be constructed experimentally and compared to theoretical results for a Newtonian fluid and a Bingham fluid. The reverse flow of the compound was also of interest since it is also observed under the trowel as it spreads joint compounds. Since the model material used, Carbopol, has a yield stress, the

formation of a core is also possible. Two types of cores, attached and floating, were in different experimental parameter range. It should be emphasized that the size of the wedge, its inclination, spreading speed, and the rheological parameters of Carbopol are representative of joint compounds. Furthermore, Carbopol is optically transparent permitting the use of tracking seeding particles.

## 4. ENCAPSULATION OF SELF-HEALING MATERIALS BY COELECTROSPINNING, EMULSION ELECTROSPINNING AND SOLUTION BLOWING

### 4.1 Introduction

Different techniques for encapsulating self-healing materials (liquid monomers) inside polymer fibers [polyacrylonitrile (PAN)] were explored. Two types of healing materials were used [dicyclopentadiene (DCPD) and isophorone diisocyanate]. To encapsulate the self-healing materials inside polymer nanofibers, coelectrospinning, emulsion electrospinning and emulsion solution blowing were used. The presence of self-healing materials inside polymer fibers was corroborated by using optical and scanning electron microscopy, energy dispersive X-ray spectroscopy, and preferential imprinting of fluorescent dye. Furthermore, fiber crush tests were used to validate the encapsulation of liquid self-healing agents. Proof-of-concept carbon-fiber/epoxy composites reinforced with ultrathin nanofibrous interlayers of the self-healing core-shell nanofibers were fabricated and the release of self-healing agent in polymeric matrix was characterized.

The materials used and experimental details, apparatus and parameters employed, are described in Section 4.2. In Section 4.3 the results and discussion contains sufficient evidence of core-shell fibers being created and fibers response to stress. Conclusions are drawn in section 4.4.



## **4.2 Experimental Materials and Methods**

### **4.2.1 Materials**

Polyacrylonitrile (PAN,  $M_w=150$  kDa) was obtained from Polysciences Inc. *N*-Dimethyl Formamide (DMF) anhydrous 99.8%, dicyclopentadiene (DCPD), isophorone diisocyanate, benzene and tungsten (VI) chloride were obtained from Sigma Aldrich. All the chemicals were used as received without any further purification or change. Copper plates obtained from McMaster-Carr were cut into 1 x 1 in.<sup>2</sup> pieces and used as collection plates in the emulsion electrospinning and emulsion solution blowing processes were further used for the crush tests. The substrates were cleaned with acetone prior to use.

### **4.2.2 Preparation of Solutions**

For emulsion electrospinning and emulsion solution blowing, emulsions of DCPD in a solution of PAN in DMF and an emulsion of isophorone diisocyanate in a solution of PAN in DMF were prepared using the following route. A 12 wt% PAN solution in DMF was prepared first. Then, DCPD and DMF were added to achieve the concentrations of 8 wt% PAN and 5 wt% DCPD in DMF. For preparing an emulsion containing 8 wt% PAN and 5 wt% isophorone diisocyanate in DMF, all three components were mixed simultaneously. Both solutions were prepared at a temperature of 75 °C with continuous stirring.

For coelectrospinning, a solution of 10 wt% PAN in DMF was prepared for the outer jet (shell) and a solution of 10 wt% DCPD in DMF was prepared for the inner jet (core).

### **4.2.3 Emulsion Electrospinning and Solution Blowing**

Core-shell fibers prepared by emulsion electrospinning used the standard electrospinning setup described elsewhere [Sun et al. (2003); Zussman et al. (2006); Yarin (2011); Yarin et al. (2001); Bazilevsky et al. (2007a); Sinha-Ray et al. (2011a); Sinha-Ray et al. (2010); Reneker et al. (2000)]. Randomly oriented fibers were collected onto a glass slide and copper plates for 1-3 min. The parameters for electrospinning of different emulsions are summarized in Table 4.1.

**Table 4.1.** Experimental parameters of emulsion electrospinning of two emulsions: PAN and DCPD in DMF, and PAN and isophorone diisocyanate in DMF.

<b>Emulsion</b>	<b>Needle to collector distance (cm)</b>	<b>Voltage (kV)</b>	<b>Flow rate (mL/hr)</b>
PAN/DCPD/DMF	7-12	16-18	0.3-0.4
PAN/isophorone diisocyanate/DMF	20	20	0.6-0.7

For emulsion solution blowing of core-shell nanofibers the experimental setup was employed [Sinha-Ray et al. (2011a); Sinha-Ray et al. (2010)]. In brief, a digital syringe pump supplied the emulsion to the needle exit where it was subjected to a co-axial high velocity (~150-200 m/s) air flow field. The air flow was issued from an annular nozzle concentric to the needle supplying the emulsion. The air flow pulled the emulsion jet causing vigorous bending instability similar to that in electrospinning [Reneker et al. (2007); Yarin et al. (2001); Reneker et al. (2000)]. The parameters for emulsion solution blowing of the different emulsions are listed in Table 4.2.

**Table 4.2:** Experimental parameters of emulsion solution blowing of two emulsions, namely PAN and DCPD in DMF, and PAN and isophorone diisocyanate in DMF.

Emulsion	Needle to collector distance (cm)	Air pressure (psi)	Flow rate (ml/h)
PAN/DCPD/DMF	30-35	30	6
PAN/isophorone diisocyanate/DMF	30-35	30	6

#### **4.2.4 Coelectrospinning**

In addition, standard coelectrospinning was employed to produce core-shell PAN fibers which encapsulated liquid DCPD. During this process, a lab-made coaxial needle setup was utilized for generating the core-shell jet [Reneker et al. (2007); Sun et al. (2003); Zussman et al. (2006); Yarin (2011)]. The inner diameter of the exterior needle was 0.97 mm, while the outer and inner diameters of the interior needle were 0.71 mm and 0.48 mm, respectively. The solution of 10 wt% PAN in DMF was issued as the outer jet (shell) and the solution of 10 wt% DCPD in DMF was issued as the inner jet (core). The flow rates of the outer jet (shell) and the inner jet (core) were controlled by two digital syringe pumps as 1.5 ml/h and 1.0 ml/h, respectively. A DC voltage of 18 kV was generated by a high DC voltage power supply (Gamma High Voltage Research, Inc., Ormond Beach, FL) and applied between the coaxial needle and an aluminum plate covered with an aluminum foil (used as fiber collector) at a distance of 25 mm.

#### **4.2.5 Self-Healing Composite Fabrication and Interlaminar Fracture Tests.**

In addition, a proof-of-concept self-healing polymer composite was fabricated and utilized to validate the deliverability of self-healing agent in a novel polymer composite system, which consisted of six layers of carbon-fiber fabrics (Fiber Glast, OH) in epoxy resin (volume fraction ~40%). The epoxy resin was prepared by mixing Epon 828 epoxide (Shell Chemicals,

Inc.) with diethylenetriamine curing agent (Shell Chemicals, Inc.) in the volume fraction 100:12. About 1% (by weight) Grubbs' catalyst was further added into the resin mixture before infusion. To form the composite panel, the wetted layup method was first applied, in which a thin layer of core-shell PAN nanofibers containing DCPD (produced by coelectrospinning) was inserted at the interface between the 3<sup>rd</sup> and 4<sup>th</sup> layers of carbon-fiber fabrics, and a Teflon film was also inserted to generate an artificial crack for interlaminar fracture. After the wetted layup, the vacuum-assisted resin transfer molding (VARTM) technique was further applied to the wetted composite panel to drive off the air bubbles and homogenize the resin inside the fiber fabrics. After curing at room temperature for 24 h, the composite laminate with an ultrathin nanofibrous self-healing layer at the middle interface was cut into small samples with the dimensions ~20 mm×5 mm×1.7 mm by using a water-cooled diamond rotary saw. Finally, a sharp wedge was used to open the self-healing samples along the artificial crack to mimic the mode I interlaminar fracture test. Failed sample surfaces were coated with a thin carbon layer for surface characterization of the core-shell nanofibers and exploring the self-healing mechanisms by using a high-resolution scanning electron microscope.

#### **4.2.6 Observations**

All scanning electron microscopy of core-shell fiber mats was done using a JEOL JSM-6320F microscope with a cold emission source. Prior to SEM observation, the fiber mats were sputter-coated with Pt/Pd to a thickness of 6-8 nm. The transmission electron microscopy was done using JEOL JEM 3010 TEM microscope. The optical images of emulsion electrospun and emulsion solution blown fibers were captured using Olympus BX51 microscope in refraction mode. The collected coelectrospun core-shell PAN/DCPD fibers were characterized using IX 71

Olympus optical microscope with the objective magnification of 40X and a fluorescent microscope.

### **4.3 Results and Discussion**

#### **4.3.1 Creation of Core-Shell Fibers Using Self-Healing Materials**

Prior to emulsion electrospinning or emulsion solution blowing, the emulsions were observed carefully both visually and under the optical microscope. It was found that there was no appreciable color difference between the emulsions containing healing agents and pure PAN solutions used as a matrix, in distinction from the PAN/ PMMA [Poly(Methyl Methacrylate)], emulsions described by Bazilevsky et al. (2007a). It should also be mentioned that even after leaving the unstirred emulsions on a shelf for a couple of days, there was no visible phase separation similar to that indicated by Bazilevsky et al. (2007a). For further characterization, the emulsions were spread on a glass slide and observed under an optical microscope (Figure 4.1). It was found that the DCPD emulsion in PAN/DMF possessed a few tiny droplets with the diameter of about 5-15  $\mu\text{m}$  (Figure 4.1). On the other hand, the emulsion of isophorone diisocyanate in PAN/DMF showed no droplets, which means that all the droplets were under submicron scale. In contrast, the emulsions of PMMA in PAN/DMF possessed large droplets of PMMA (with the diameter of about 100  $\mu\text{m}$ ) [Bazilevsky et al. (2007a)]. It is emphasized that the formation of core-shell fibers as described below is an indirect proof of the emulsion nature of isophorone diisocyanate in PAN/DMF solutions.

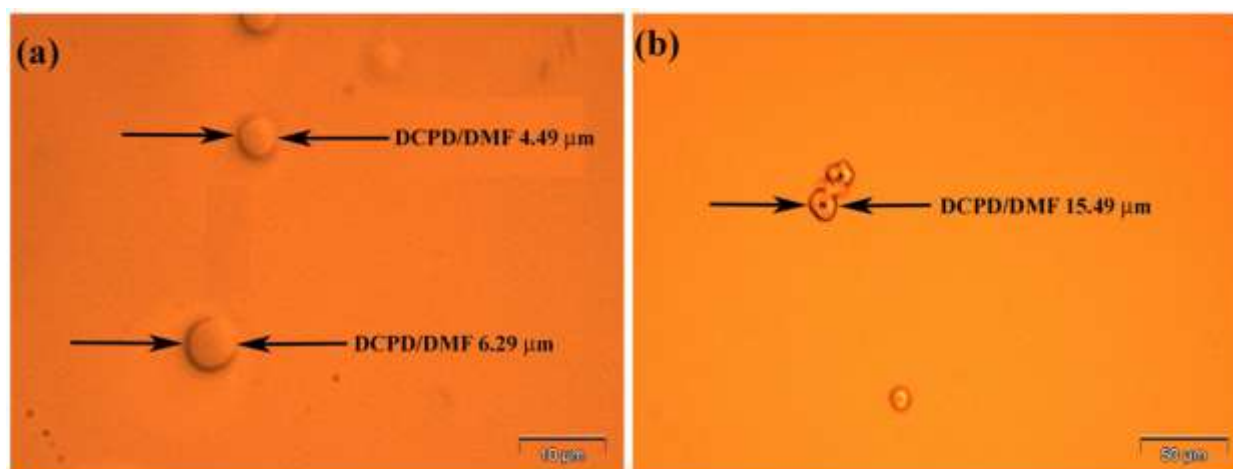


**Figure 4.1.** An emulsion of DCPD/DMF in PAN/DMF. (a) Tiny droplets of DCPD/DMF while the emulsion is wet. (b) Droplets of dried DCPD/DMF embedded in the matrix. It is emphasized that the emulsions are polydisperse, which might explain the fact that droplets in two different samples shown in panels (a) and (b) have different sizes. In addition, it is worth mentioning that droplets flatten when they dry, which can also be responsible for a larger size of the dried droplets in panel (b).

The fibers electrospun from emulsions are shown in Figure 4.2. The electrospun fibers from an emulsion of 8 wt% PAN and 5 wt% DCPD were collected on a glass slide and observed under an optical microscope in refraction mode (Figure 4.2a,b). In all images captured, it was found that the majority of fibers are core-shell fibers. There were very few monolithic fibers. It can be observed that sometimes the fibers are slightly beaded (Figure 4.2b), which can be explained by the onset of capillary instability. The diameter of the fiber shell is in an approximate range of 1.5  $\mu\text{m}$  to 3  $\mu\text{m}$ , whereas the core diameter approximate range is from 0.4  $\mu\text{m}$  to 1.5  $\mu\text{m}$ . The emulsion electrospinning of 8 wt% PAN and 5 wt% isophorone diisocyanate in DMF resulted in an abundance of uniform core-shell fibers (Figure 4.2 c,d). From the optical images it was found that there were no monolithic fibers. In every image inspected, all fibers

were core-shell fibers. It was found that the shell diameter in this case ranged from 1.75  $\mu\text{m}$  to 3.81  $\mu\text{m}$  and the core diameter from 0.51  $\mu\text{m}$  to 2.01  $\mu\text{m}$ .

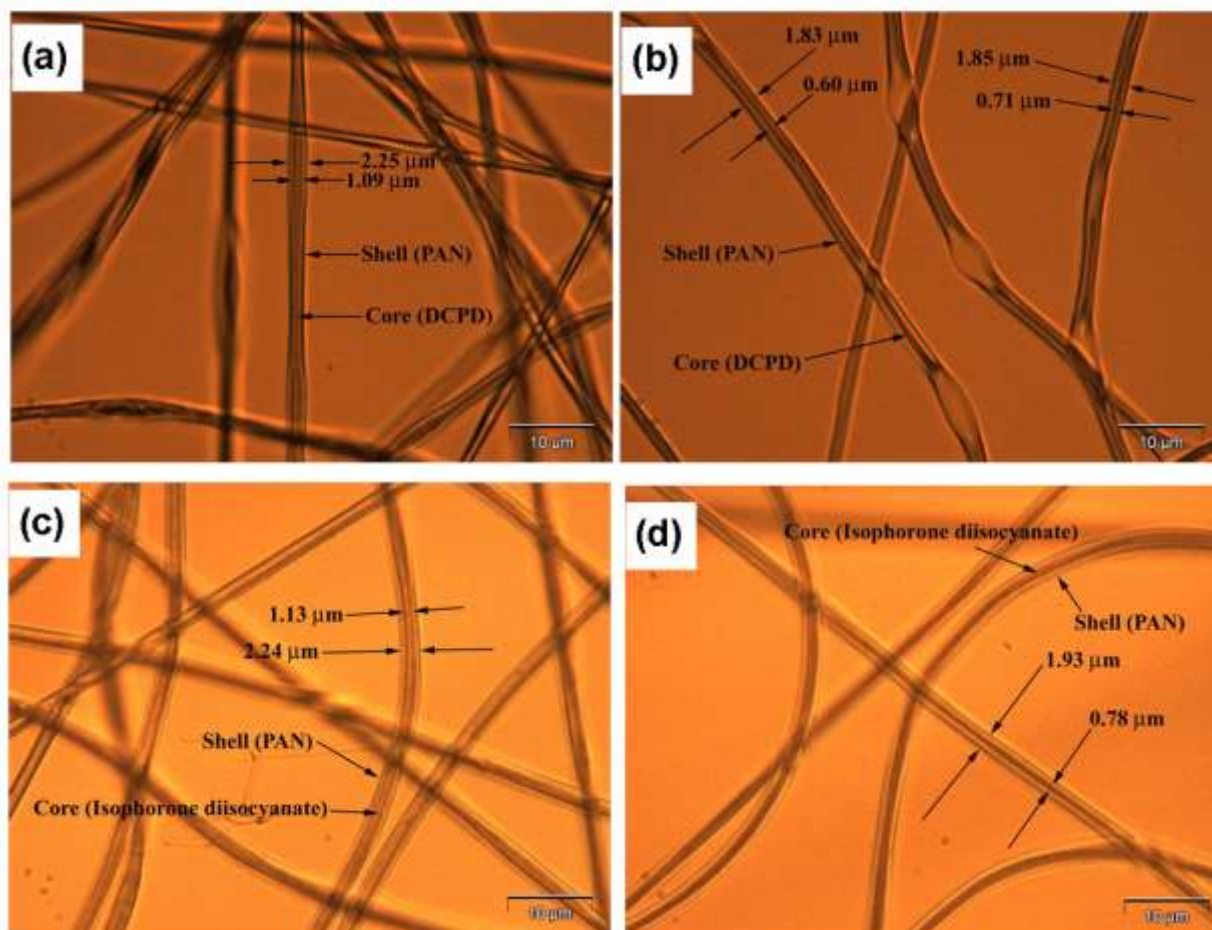


**Figure 4.2.** Optical images of core-shell fibers electrospun from emulsion are shown. Panels (a) and (b) show core-shell fibers obtained from emulsion of DCPD in PAN and DMF, while panels (c) and (d) show core-shell fibers obtained from emulsion of PAN and isophorone diisocyanate in DMF. The scale bar in all images is 10  $\mu\text{m}$ .

The same emulsions which were used in the emulsion electrospinning were also used in emulsion solution blowing. The solution-blown fibers were collected on glass slides for 1-3 mins

and inspected under the optical microscope. The optical images of the fibers obtained from the emulsions of PAN/DCPD in DMF and PAN/isophorone diisocyanate in DMF are shown in Figures 4.3 a-b and 4.3 c-d, respectively. It can be seen that the majority of the collected fibers reveal the core-shell structure. It is seen from Figures 4.3 a-b that for PAN/DCPD in DMF the shell diameter approximately ranges from 1.35  $\mu\text{m}$  to 3.00  $\mu\text{m}$ , while the core diameter is in the range of 0.44  $\mu\text{m}$  to 1.30  $\mu\text{m}$ . For PAN/isophorone diisocyanate in DMF (Figures 4.3 c-d), the shell diameter ranges from 1.80  $\mu\text{m}$  to 2.90  $\mu\text{m}$ , while the core diameter ranges from 0.40  $\mu\text{m}$  to 0.95  $\mu\text{m}$ .



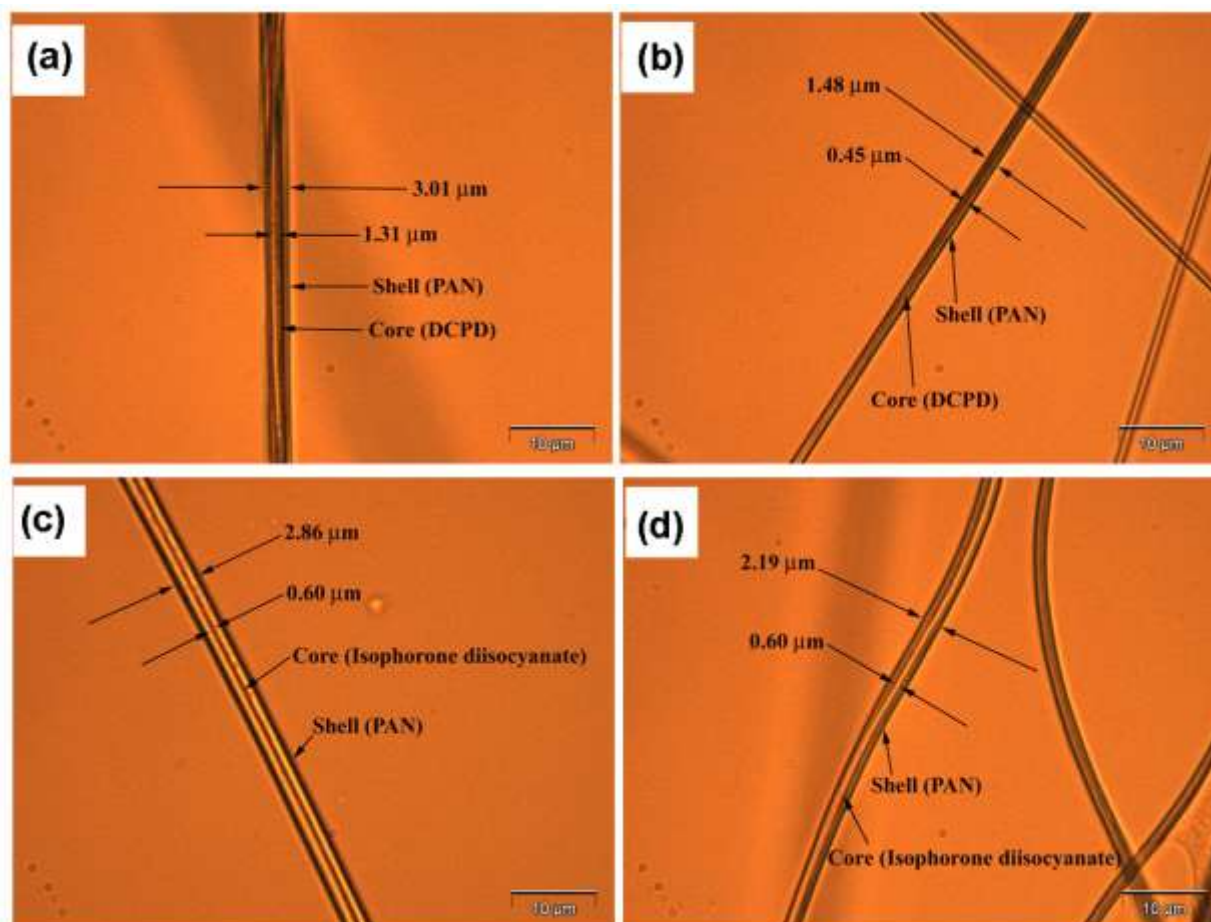


**Figure 4.3.** Optical images of the core-shell fibers obtained by emulsion solution blowing. Panels (a) and (b) show core-shell fibers obtained from emulsion of DCPD in PAN and DMF, while panels (c) and (d) show core-shell fibers obtained from emulsion of PAN and isophorone diisocyanate in DMF. The scale bar in all images is 10  $\mu\text{m}$ .

Figure 4.4 shows the coelectrospun core-shell PAN/DCPD nanofibers. It can be observed (Figure 4.4a) that the fibers contain about 10 wt% of liquid DCPD dissolved in DMF as the core encapsulated by the outer shell created from the 10 wt% PAN solution under the proper conditions found in this study. It is emphasized that here and hereinafter all the component concentrations in the fibers are fully determined by the initial solution concentrations and the

flow rates used in the fiber forming processes. They can also be evaluated from the core and shell sizes in the images. Correspondingly, the component concentrations in dry fibers after solvent evaporation are fully predetermined by the fiber forming process and known. Once the solvent evaporated off through the shell [Dror et al. (2007)], liquid DCPD was encapsulated inside the PAN shell to form the desired core-shell PAN/DCPD nanofibers which could also be exploited for self-healing purposes in ultra-thin geometries. In addition, surface and core instabilities were occasionally observed in the collected fiber network as shown in Figure 4.4b similar to Figure 4.2b, which resembles capillary instabilities of liquid jets [Yarin (2003)]. Mechanics of capillary instability of the electrified core-shell fibers has been sufficiently developed (for the review, see Yarin (2011) and references therein).

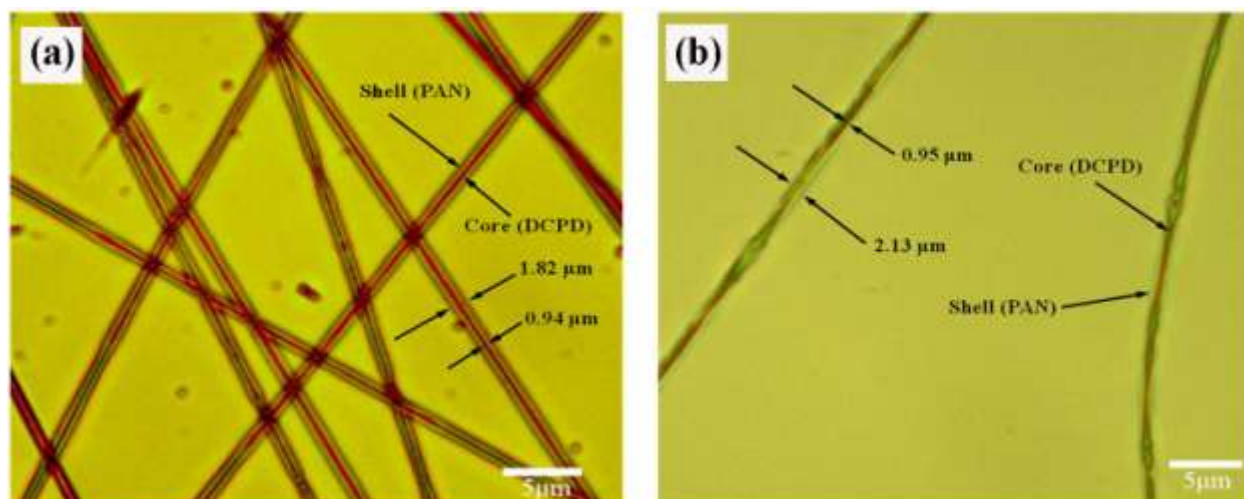


**Figure 4.4.** Optical images of the coelectrospun core-shell PAN/DCPD nanofibers. Panels (a) and (b) illustrate different fiber morphologies. The scale bar in both images is 5  $\mu\text{m}$ .

Figures 4.2-4.4 show that either emulsion electrospinning, emulsion solution blowing, or coelectrospinning are capable of producing core-shell fibers with healing agents encapsulated in

the core. There is no doubt that the healing agents are encapsulated in the core, while polymer is in the shell because only the viscoelasticity of the polymer can provide the shell with the spinnability and structural stability needed for fiber formation.

In addition, to demonstrate the presence of the healing material in the fiber core, a fiber crush test was employed. First, the fibers were collected on a copper plate roughened by sand paper (600 grade) and the catalyst for the corresponding self-healing process was distributed on a second roughened copper plate. Then, they were pressed against each other under a mass of 1 kg overnight. In the case of isophorone diisocyanate/PAN fibers, water was used as a catalyst and for DCPD/PAN fibers Tungsten (VI) Chloride was chosen as a catalyst. The fibers were observed before and after squeezing. The fibers before squeezing are shown in Figures 4.5 a-b (isophorone diisocyanate/PAN) and 4.5 c-d (DCPD/PAN). The same fibers after squeezing are shown in Figures 4.6 (isophorone diisocyanate/PAN) and 4.7 (DCPD/PAN). The fibers which were smooth before squeezing developed different protrusions at their surfaces as a result of squeezing. Namely, the fiber shell was broken at some locations and the encapsulated healing agents were released from the core. At the fiber surface, these agents came in contact with their catalysts, polymerized and solidified to form the protrusions. The release of the healing agent from the fiber core was also observed in the axial direction and the solidified blobs were formed at the fiber edges (Figure 4.7).

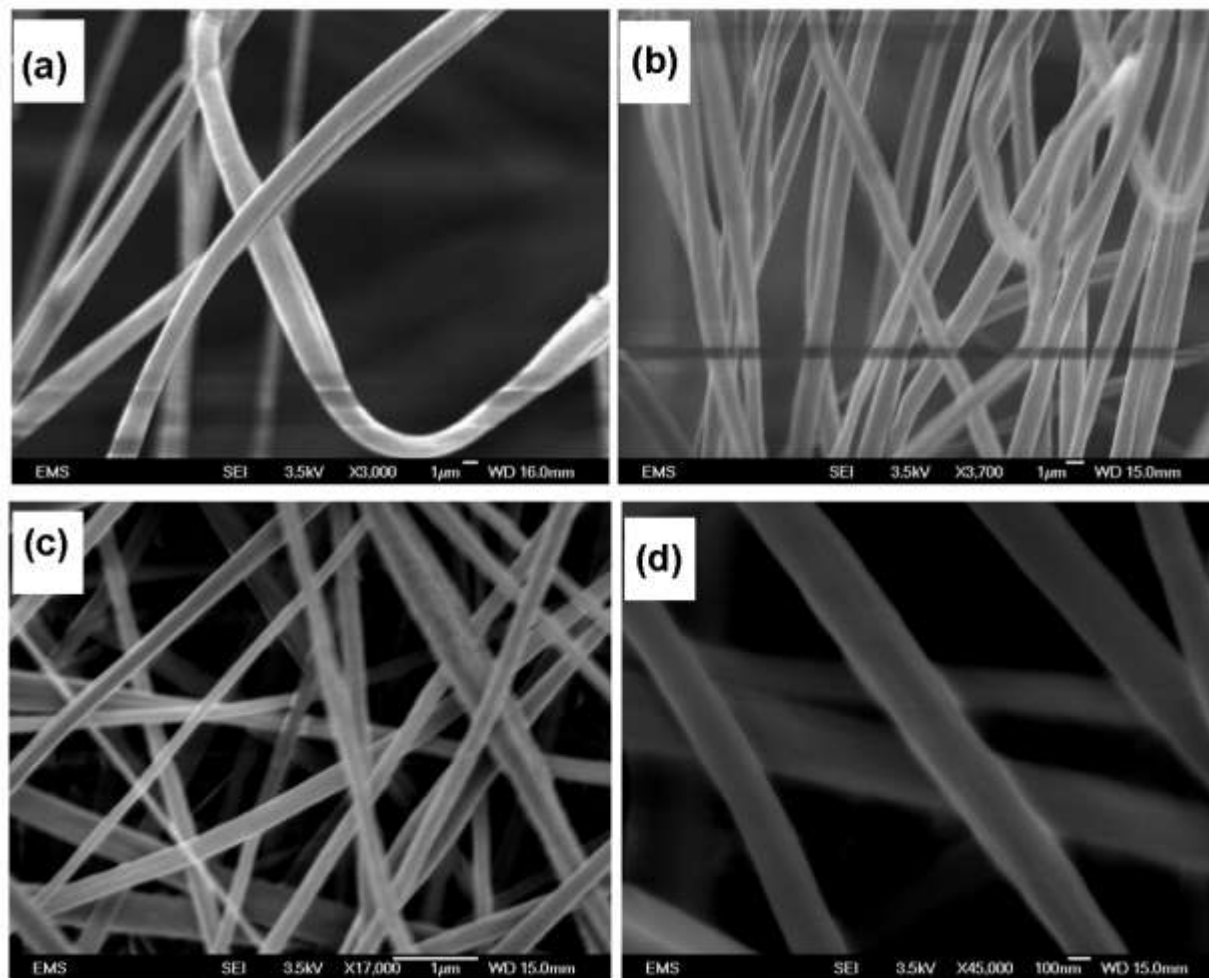


**Figure 4.5.** SEM images of undamaged core-shell fibers. Panels (a) and (b) show isophorone diisocyanate/PAN core-shell fibers before squeezing, and panels (c) and (d) show DCPD/PAN core-shell fibers before squeezing. It is seen that the core-shell fibers have no protrusions on their walls.

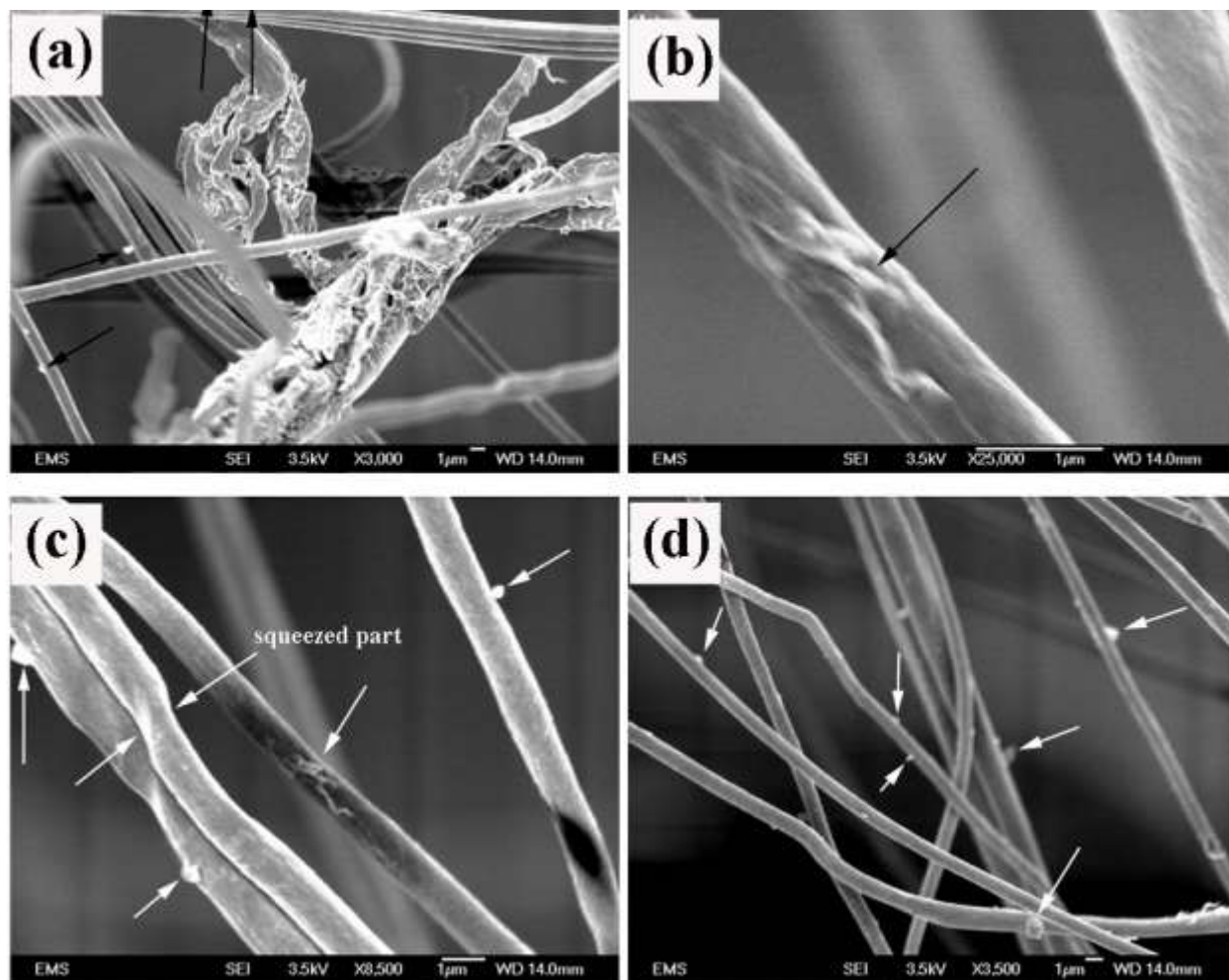


**Figure 4.6.** SEM images of squeezed isophorone diisocyanate/PAN core-shell fibers. Panels (a)-(d) illustrate different morphological aspects. The arrows indicate solid protrusions found on the fiber walls. Under squeezing, isophorone diisocyanate is released from the fiber core, makes contact with the catalyst (water) and solidifies creating the visible protrusions.



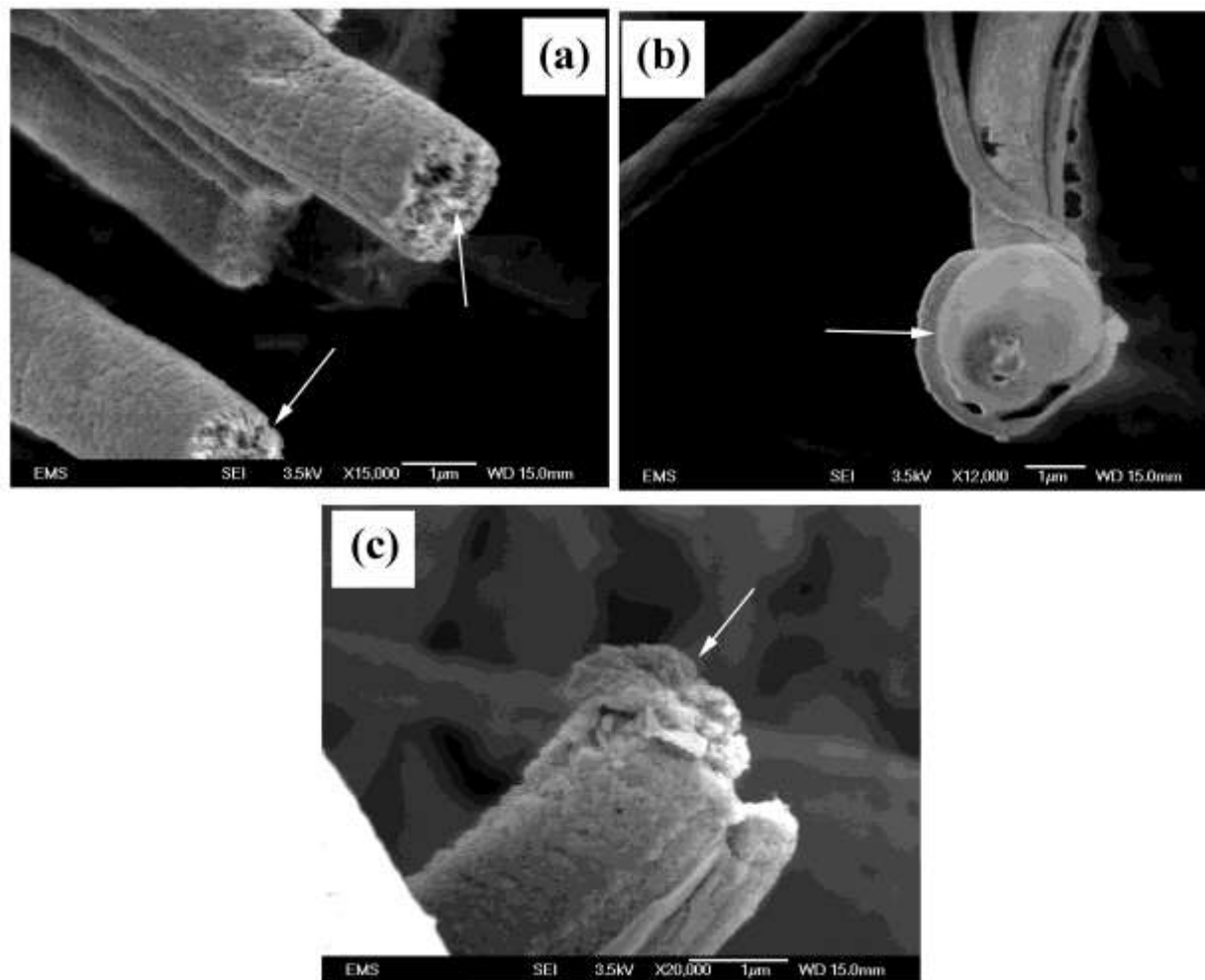


**Figure 4.7.** SEM images of squeezed DCPD/PAN core-shell fibers. In panel (a) the arrow shows the rough cross-section of a fiber. In (b) the arrow indicates a solid blob protruding from the core and in panel (c) the arrow shows the solid protrusion formed at the end of a fiber. As a result of squeezing, DCPD is released from the fiber core, comes in contact with the catalyst [Tungsten (VI) Chloride] and solidifies.

### 4.3.2 Raman Scattering, EDX, and Fluorescent Imaging

My labmate Suman Sinha-Ray helped me with the material characterization and his help is greatly appreciated.

It is also tempting to apply micro-Raman or micro-IR technique to characterize the internal structure of core-shell fibers. However, this is impossible due to the following reasons. In micro-Raman or micro-IR the spot size is of the order of 1-2  $\mu\text{m}$ . To get a reliable signal from a sample, its size needs to be at least somewhat larger than the spot size. The core-shell fibers (Figures 4.2-4.4), have the outer shell diameters of the order of 1-2  $\mu\text{m}$ , and the core diameter is about 450 nm-1  $\mu\text{m}$ . This clearly shows that the core diameter in most of the cases is much smaller than the spot size, which makes it impossible to receive any reliable signal from a single fiber. If it were possible to observe fiber cross-sections in a bundle of perfectly aligned core-shell fibers closely located to each other and perfectly facing the oncoming laser beam, micro-Raman or micro-IR could have shed light on the internal structure of the fibers. However, the distances between the fiber cores in the bundle would still be on the scale of 1-2  $\mu\text{m}$  according to Theron et al. (2001) and Reneker et al. (2007), which is comparable to the spot size, which makes it impossible to obtain a reliable signal.

A number of additional experiments were conducted to prove the presence of healing materials in the fiber cores. Note first, that in the present work two different self-healing core-shell structures were formed- PAN/DCPD and PAN/isophorone diisocyanate. The molecular weights of PAN, DCPD and isophorone diisocyanate are 150 kDa, 132 Da and 222 Da, respectively, and PAN is a polymer, whereas the other two compounds are monomers. Among these three compounds, only PAN possesses viscoelasticity which results in spinnability and fiber formation when PAN is in the shell, whereas DCPD or isophorone diisocyanate stay in the

core, and alone would not facilitate fiber formation. The energy dispersive X-ray spectroscopy (EDX) was employed to reveal the presence of DCPD or isophorone diisocyanate in the fiber core. It is emphasized that quantification of light elements by EDX is extremely difficult and may lead to incorrect results due to absorption of low energy X-rays in a specimen, in the detector window and Silicon dead layer. Also, there is an additional obstacle. To avoid any possible interference, a sample cannot be sputter-coated with metal. As a result of that, samples should be inspected in differential-pressure SEM, which employs gas ions to neutralize the electric charge. This causes the beam to widen resulting in difficulties with localization at any analysis conducted. This widening can begin from a submicron-sized spot in an ultra-high vacuum SEM to a spot of about 100  $\mu\text{m}$  in differential-pressure SEM (in addition, to a possible movement of nanofiber mat under electron beam).

When energy dispersive X-ray spectroscopy (EDX) is employed, materials are characterized based on their  $K\alpha$  energy shell. In the core-shell nanofibers in the present work the shell consists of PAN  $[(\text{C}_3\text{H}_3\text{N})_n]$  and the core is comprised of either isophorone diisocyanate ( $\text{C}_{12}\text{H}_{18}\text{N}_2\text{O}_2$ ) or DCPD ( $\text{C}_{10}\text{H}_{12}$ ). In PAN/DCPD core-shell system it seems that EDX spectrum of the core (DCPD) which will show no or minimal presence of nitrogen will be easily distinguishable from the shell spectrum containing nitrogen. A careful observation of EDX series reveals that carbon corresponds to  $K\alpha$  value of 0.277 Kev and nitrogen - to 0.392 Kev. The energy resolution of the detector is  $\sim 0.140$  Kev, which means that in EDX spectrum positions of nitrogen and carbon overlap, which makes it impossible to do a reliable characterization based on nitrogen presence or absence. Indeed, it can be seen from Figures 4.8a and 4.8b for PAN/DCPD core-shell fibers that the N peak is, in fact, completely absorbed by the neighboring C peak, which makes it impossible to prove the existence of DCPD in the core by EDX. On the



other hand, the spectrum of cross-section of PAN/isophorone diisocyanate (Figure 4.8c) is more informative. It can be seen in Figure 4.8c that the oxygen peak in the core in such fibers is much higher (~8%; Figure 4.8c) than that of the shell (~3%; Figure 4.8a). This points out at the presence of isophorone diisocyanate in the fiber core. However, the difference in the oxygen peak is not very pronounced, and the comparison of Figures 4.8a and 4.8c is rather qualitative than really quantitative.

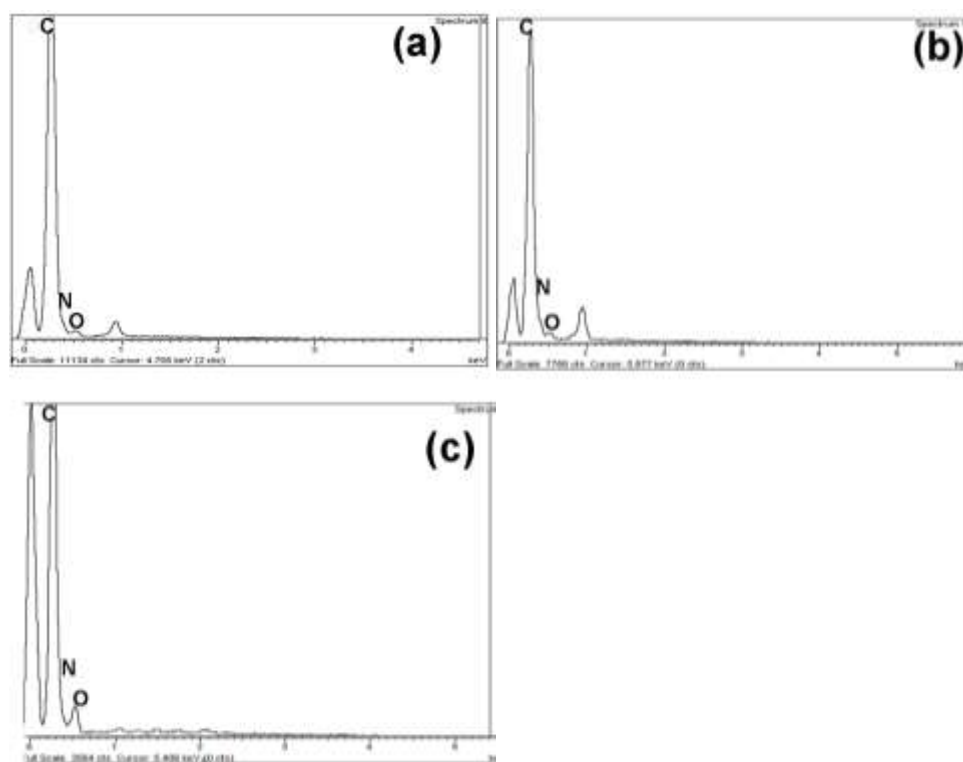


**Figure 4.8.** EDX spectrum of (a) nanofiber shell (PAN), (b) cross-section of PAN/DCPD nanofiber. It can be seen that the presence of N is practically masked by the neighboring carbon peak in the spectrum owing to the energy resolution of the detector. Panel (c) corresponds to cross-section of PAN/isophorone diisocyanate nanofibers. Panel (c) shows a visible rise in the oxygen peak compared to panel (a). This rise is attributed to the presence of the oxygen-containing isophorone diisocyanate in the fiber core.

Since EDX was incapable of a reliable confirmation of the presence of DCPD in the core-shell PAN/DCPD nanofibers, we employed an indirect routine based on preferential imprinting of fluorescent dye (Rhodamine B). PAN has a melting/degradation point of 300 °C, while DCPD has a melting point of 32 °C. For the imprinting test, mats of PAN/DCPD nanofibers and of pure PAN nanofibers were cut. Then, they were immersed in a dye solution of Rhodamine B at 40 °C for two hours. After that, they were rinsed with cold water the same number of times over 24 h. After the rinsing, photographs were taken of both mats for comparison (Figure 4.9). In particular, Figure 4.9a shows the rinsed PAN nanofiber mat, whereas Figure 4.9b shows the rinsed PAN/DCPD nanofiber mat. Comparing Figures 4.9a and 4.9b, one observes that the PAN/DCPD nanofiber mat in Figure 4.9b is slightly pink. This can be explained as follows. For co-electrospinning, both PAN and DCPD were dissolved in the same solvent DMF. As the solvent was evaporating through the shell, pores in the shell were formed, as explained and demonstrated by Dror et al. (2007) and Sinha-Ray et al. (2011c). At 40 °C DCPD melted in the core, and dye reached the molten core through the pores in the shell and the cut portion of the mat. The dye could adhere to molten DCPD being physically adsorbed. No strong physical adsorption is expected at 40 °C on a still solid PAN shell, or solid pure PAN fibers (Figure 4.9a). Therefore, after cooling and rinsing, DCPD should still retain Rhodamine B and be pink (Figure 4.9b), while rinsing of solid PAN removed all the dye and left it white. As a result, the observations in Figure 4.9 show that in the core-shell nanofibers, the core indeed contains DCPD.

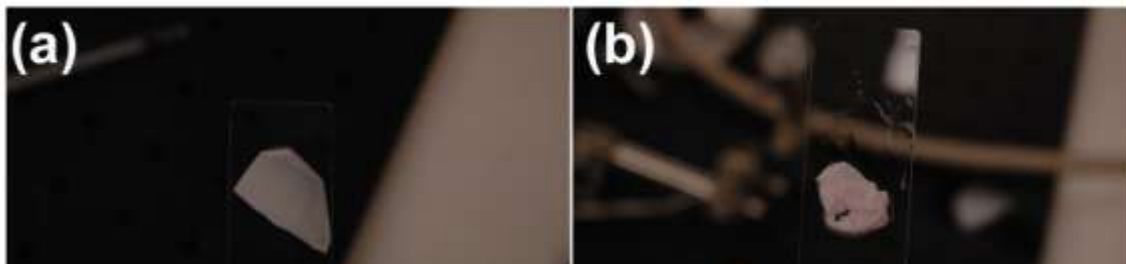


**Figure 4.9.** (a) PAN and (b) PAN/DCPD cut nanofiber mats after the immersion in Rhodamine B solution at 40 °C with the subsequent rinsing in cold water. It can be seen that pure PAN nanofibers are white, whereas the PAN/DCPD nanofiber mat is slightly pink.

In addition, to demonstrate the presence of dye adsorbed to DCPD core, fluorescence imaging of the PAN/DCPD nanofiber mat shown in Figure 4.9b was done using a Nikon microscope (Eclipse E800) equipped with a 60x objective. The optical image of the nanofiber mat is shown in Figure 4.10a, whereas fluorescent image is shown in Figure 4.10b (the same place is marked by arrows in Figures 4.10a and 4.10b). It can be seen that the fiber diameter is larger in Figure 4.10a than in Figure 4.10b. This remarkable observation stems from the fact that in Figure 4.10a the fiber shell is visible, whereas in Figure 4.10b-only the nanofiber core, which is DCPD stained by fluorescent dye. Note, that in the fluorescent image in Figure 4.10b some fibers are invisible, which means that either fluorescent dye did not reach the core through the pores in those sections, or that it was rinsed even from the core there during the subsequent rinsing. The observations in Figure 4.10 conclusively prove the presence of DCPD in the fiber core.

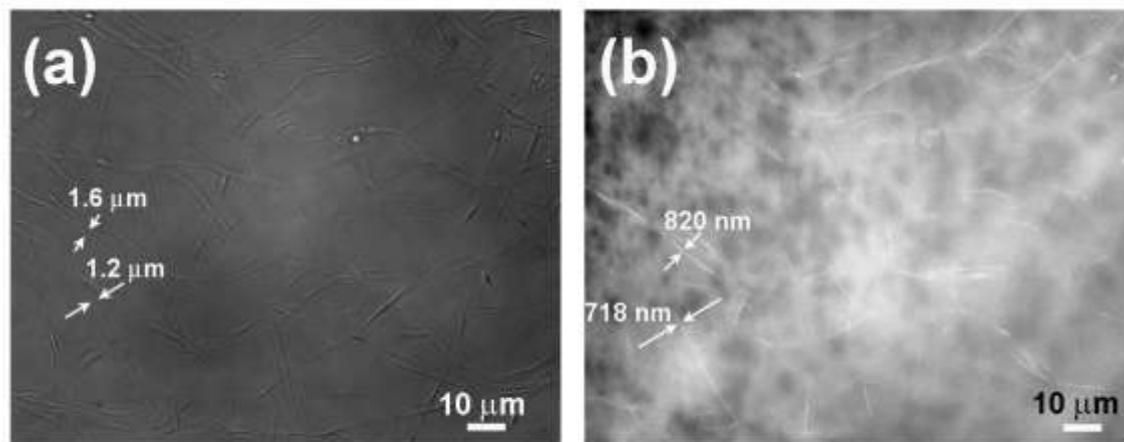


**Figure 4.10.** (a) Optical image and (b) fluorescent image of the fiber mat shown in Figure 4.9b.

### **4.3.3 Self-Healing Core-Shell Fibers Embedded in Material**

Figure 4.11a shows a typical failed surface of self-healing composite samples after interlaminar fracture. It can be observed that the core-shell PAN nanofibers were well entangled with the epoxy resin at the interface to form an ultrathin self-healing nanofiber-reinforced nanocomposite layer between neighboring carbon-fiber fabrics. The failure (toughening) modes include nanofiber pull-out, debonding, breakage, plastic necking, matrix cracking and related stress shielding and crack kinking in the matrix interlayers, similar to those induced by solid electrospun PAN nanofibers as studied previously [Wu (2009)]. These failure modes are expected to dissipate significant strain energy compared to pure resin failure (cracking) in virgin polymer composite without nanofiber reinforcement at the interface. Furthermore, once nanofibers broke, liquid DCPD were released under the action of the external stressing and capillary effect as shown in Figures 4.11a-c. In particular, Figure 4.11b shows a failed core-shell structure with an empty core region due to release of the healing agent, while Figure 4.11c shows the conic structure due to the release (pull-out) of liquid (soft) healing agent. If touched with catalyst particles dissolved in a composite matrix, ring-opening polymerization would be

triggered and heal the interfacial crack as expected. Thus, the present SEM-based fractographical analysis has explored the main toughening mechanisms at composite interfaces and also validated the deliverability of self-healing agent at composite interfaces.

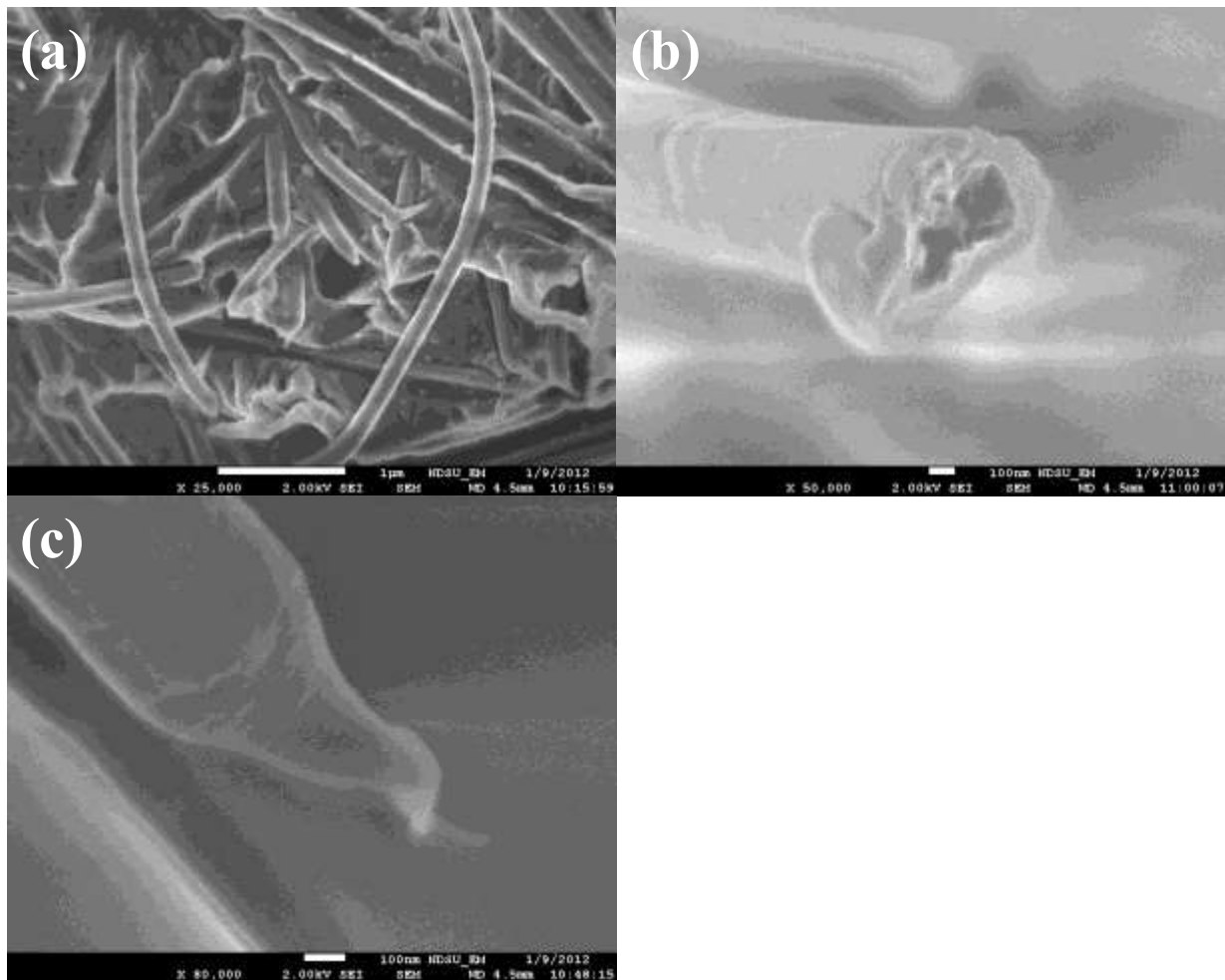


**Figure 4.11.** SEM image of core-shell PAN nanofiber-toughened interface (a). SEM image of a failed core-shell PAN nanofiber at the interface with depleted healing agent (b). SEM image of a failed core-shell PAN nanofiber at the interface with released healing agent (c).

#### **4.4 Conclusion**

Emulsion electrospinning, emulsion solution blowing, and coelectrospinning of core-shell fibers using PAN as the fiber-forming shell, has been successfully applied to encapsulate healing agents, such as DCPD or isophorone diisocyanate, in the fiber core. The core-shell structure of the fibers was observed visually by using optical microscope. In addition, the presence of the healing agents in the core was demonstrated in the fiber crush tests. Namely, when the fibers were squeezed between two copper plates in the presence of their corresponding catalysts the healing agents were released through the broken fiber shell or at the broken fiber cross-sections. After the release, the healing agents polymerized and solidified to form multiple protrusions which were observed through SEM. The presence of the healing materials in the fiber core was also revealed by energy dispersive X-ray spectroscopy, and preferential imprinting of fluorescent dye.

Finally, novel proof-of-concept hybrid polymer composites reinforced with self-healing core-shell nanofibers at the interfaces have been produced, and relevant toughening mechanisms and deliverability of healing agent examined and validated. All of the preceding techniques provide a plethora of ways to encapsulate healing materials to be used in production of smart composites with embedded self-healing agents on a mass scale.

## 5. FOAM CONSOLIDATION AND DRAINAGE

### 5.1 Introduction

As in Jun et al. (2012):

A theoretical model of foam as a consolidating continuum is proposed. The general model is applied to foam in a gravity settler. It is predicted that liquid drainage from foam in a gravity settler begins with a slow drainage stage. Next, a stage with faster drainage occurs where the drainage rate doubles compared to the initial stage. The experiments conducted within the framework of this work confirmed the theoretical predictions and allowed measurements of foam characteristics. Foams of three different concentrations of Pantene Pro-V Classic Care Solutions shampoo were studied, as well as the addition of polyethylene oxide (PEO) in one case. The shampoo's main foaming components are sodium lauryl sulfate and sodium laureth sulfate. (p. 5323)

Also, foams created by United States Gypsum Corporation (USG), stable and unstable soap, at three different air flow rates were studied, as well as the effect of the addition of polyethylene oxide (PEO). "It is shown to what extent foam drainage is slowed down by using higher shampoo concentrations" [Jun et al. (2012)], how different air flow rates have little effect on drainage but mainly affect the total volume of liquid drained, and how in every case the drainage rate is further decreased by adding polymer (PEO).

In the present work, foam is considered in the framework of consolidation theory (section 5.2) and the predictions made are compared to our experiments of foam drainage in a gravity

settler, described in section 5.3. The discussion is given in section 5.4. Conclusions are drawn in section 5.5.

## **5.2 Theoretical Background**

Theoretical Background accredited to Seongchul Jun

### **5.2.1 General Equations**

As stated in Jun et al. (2012):

According to Kornev et al. (1999), foam in which gas bubbles have already crowded, begun to collide, and press on each other significantly, possess elasticity. The bubbles and surfactant-stabilized liquid lamellae in foam form an elastic skeleton. In addition, solvent drains through the lamellae driven by a pressure gradient according to Darcy's law

$$\mathbf{v}^{LS} = \mathbf{v}^L - \mathbf{v}^S = -\frac{k}{\mu} \nabla p \quad (5.1)$$

where  $\mathbf{v}^L$ ,  $\mathbf{v}^S$  and  $\mathbf{v}^{LS}$  are the liquid and skeleton velocities and the liquid-relative-to-skeleton average velocity, respectively,  $k$  is the skeleton permeability on the order of  $k=\delta^2/12$  with  $\delta$  being the average lamella thickness,  $\mu$  is the solvent viscosity and  $p$  is the solvent pressure.

Foam, as a system, comprised of an elastic skeleton assumed to follow Hooke's law with viscous liquid drainage in the lamellae perfectly resembles the medium dealt with by consolidation theory of soil mechanics [Terzaghi (1947); Fowler (1997)] and is a medium kindred of liquid-saturated concentrated slurries [Yarin et al. 2006]. In such cases, a concerted volumetric deformation of the



elastic skeleton occurs in reaction to the viscous drainage of an incompressible viscous liquid, which is described by the balance equation

$$\frac{\partial \varepsilon_v}{\partial t} - \frac{k}{\mu} \nabla^2 p = 0 \quad (5.2)$$

following from Darcy's law Eq. (5.1) with  $t$  being time.

In Eq. (5.2) the volumetric strain is given by

$$\varepsilon_v = \text{div} \mathbf{u} \quad (5.3)$$

where  $\mathbf{u}$  is the displacement vector, such that

$$\mathbf{v}^s = \frac{\partial \mathbf{u}}{\partial t} \quad (5.4)$$

The consolidation theory, according to Terzaghi's principle [Fowler (1997), p. 107], implies that the total stress  $\boldsymbol{\sigma}$  in any cross-section of the system under consideration is comprised of the isotropic part solely associated with the liquid pressure  $p$  and the deviatoric elastic part  $\boldsymbol{\sigma}'$ , where  $\boldsymbol{\sigma}'$  is the effective stress tensor in the skeleton responsible for its deformation. In other words, the total stress tensor  $\boldsymbol{\sigma} = -p\mathbf{I} + \boldsymbol{\sigma}'$  where  $\mathbf{I}$  is tensor unit. Since deformations are assumed to be relatively slow, the momentum balance equation reduces to the following form [Fowler (1997), p. 108]

$$\nabla \cdot \boldsymbol{\sigma}' - \nabla p = 0 \quad (5.5)$$

The deviatoric stress tensor is given by Hooke's law [Landau and Lifshitz (1970)]

$$\boldsymbol{\sigma}' = \frac{E}{1+\nu} \boldsymbol{\varepsilon} + \mathbf{I} \frac{E\nu}{(1+\nu)(1-2\nu)} \text{div} \mathbf{u} \quad (5.6)$$

where  $\boldsymbol{\varepsilon} = (1/2) [\nabla\mathbf{u} + \nabla\mathbf{u}^T]$  is the strain tensor,  $E$  is the effective Young's modulus and  $\nu$  is the effective Poisson's ratio (both assumed to be constant) of the elastic skeleton.

We assume that the average bubble radius  $a$  in the foam is sufficiently large to neglect capillary pressure in the bubbles  $4\gamma/a$  (with  $\gamma$  being the surface tension, and the factor 4 corresponds to the two free surfaces surrounding a bubble) compared to the surrounding atmospheric pressure  $p_0$ , which is indeed true for bubbles with  $a \approx 300 \mu\text{m}$ , characteristic of our foams. Therefore, gas inside the bubbles has pressure  $p_0$ . Foam elasticity results from the compressibility of the gas inside the bubbles since the liquid is practically incompressible. Assuming gas inside the bubbles being non-condensable and ideal, one can easily see that the bulk modulus of foam  $K$  is equal to the gas pressure  $p_0$ , i.e.  $K = E/[3(1-2\nu)] = p_0$ . Therefore,

$$E = 3p_0\phi, \quad \nu = \frac{1-\phi}{2} \quad (5.7)$$

where  $\phi$  is the gas volume fraction in the initial foam. It is emphasized that Eq. (5.7) relates the foams effective Young's modulus and Poisson's ratio,  $E$  and  $\nu$ , to the known parameters  $p_0$  and  $\phi$ . The second Eq. (5.7) shows that as the gas volume fraction in the initial foam  $\phi \rightarrow 0$ , the foam becomes incompressible, since correspondingly  $\nu \rightarrow 1/2$ .

Equation (5.6) allows one to find, as in Landau and Lifshitz (1970), that

$$\nabla \cdot \boldsymbol{\sigma}' = \frac{1}{2} \frac{E}{(1+\nu)} \left[ \nabla^2 \mathbf{u} + \frac{1}{1-2\nu} \nabla(\text{div} \mathbf{u}) \right] \quad (5.8)$$

Equations (5.2) and (5.3) and combined Eqs. (5.5) and (5.8) form a system of two equations for the two unknowns  $p$  and  $\mathbf{u}$ , namely

$$\frac{\partial(\operatorname{div}\mathbf{u})}{\partial t} = \frac{k}{\mu} \nabla^2 p \quad (5.9)$$

$$\frac{1}{2} \frac{E}{(1+\nu)} \left[ \nabla^2 \mathbf{u} + \frac{1}{1-2\nu} \nabla(\operatorname{div}\mathbf{u}) \right] = \nabla p \quad (5.10)$$

Taking the divergence of Eq. (5.10) yields

$$\frac{E(1-\nu)}{(1+\nu)(1-2\nu)} \nabla^2(\operatorname{div}\mathbf{u}) = \nabla^2 p \quad (5.11)$$

Equation (5.9) allows us to exclude  $p$  from Eq. (5.11), which yields the following scalar equation containing solely  $\mathbf{u}$ , in particular,  $\varepsilon_v = \operatorname{div}\mathbf{u}$ ,

$$\frac{\partial \varepsilon_v}{\partial t} = c_v \nabla^2 \varepsilon_v \quad (5.12)$$

where

$$c_v = \frac{k}{\mu} \frac{E(1-\nu)}{(1+\nu)(1-2\nu)} \quad (5.13)$$

Equation (5.12) describes the evolution of the volumetric strain during skeleton consolidation accompanying liquid drainage. It coincides formally with the standard parabolic heat transfer equation, where the role of the transport coefficient, in the present case, is played by the consolidation coefficient  $c_v$  given by Eq. (5.13) [Fowler (1997)].

In addition, Eq. (5.11) can be integrated, which yields the following relation between  $p$  and  $\varepsilon_v$

$$p = \frac{E(1-\nu)}{(1+\nu)(1-2\nu)} \varepsilon_v + F(\mathbf{r}, t) \quad (5.14)$$

where  $F$  is any harmonic function of the position vector  $\mathbf{r}$ , which can also contain time as a parameter. (p. 5324-5325)

### 5.2.2 Gravity Settler

As described in Jun et al. (2012):

In an axisymmetric cylindrical gravity settler initially filled with uniform foam up to height  $h$  a new physical factor, namely gravity, plays role and liquid drainage to the bottom is anticipated (Figure 5.1).

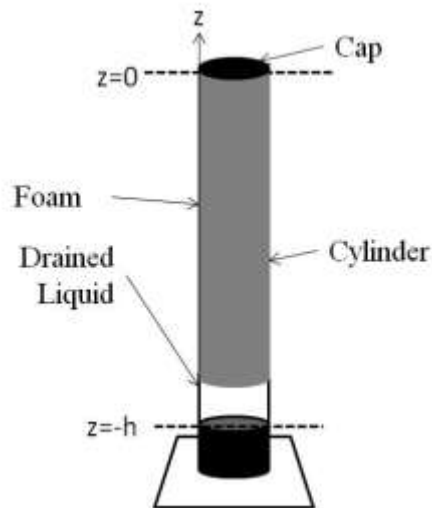


**Figure 5.1.** A filled cylinder of foam with surfactant solution (drained liquid) below. The top of the foam is at  $z=0$  and the bottom of the cylinder is at  $z=-h$ .

In presence of gravity, Darcy's law (5.1) is amended and takes the following form [Barenblatt et al. (1990)]

$$\mathbf{v}^{LS} = \mathbf{v}^L - \mathbf{v}^S = -\frac{k}{\mu} \nabla (p + \rho g z) \quad (5.15)$$

where  $\rho$  is the liquid density,  $g$  is the acceleration due to gravity, and  $z$  is the vertical coordinate with  $z=0$  corresponding to the free surface and  $z=-h$  to the bottom. Equation (5.15) expresses the fact that the hydrostatic pressure distribution in the lamellae at rest ( $p=p_0-\rho gz$  with  $z$  being negative and  $p_0$  being atmospheric pressure), should not result in any drainage against gravity, as is physically expected.

The presence of the gravity-related term in Eq. (5.15) does not preclude arriving at Eq. (5.2) by the previous derivation, since  $\nabla^2 z \equiv 0$ . Also, Eq. (5.5) which expresses the balance of the elastic stresses due to the surfactant lamellae and liquid pressure (whatever it is) acting on them does not change. Then Eqs. (5.8)-(5.14) also do not change. In particular, Eqs. (5.12) and (5.14) in the present case reduce to the following equations

$$\frac{\partial \varepsilon_v}{\partial t} = c_v \frac{\partial^2 \varepsilon_v}{\partial z^2} \quad (5.16)$$

$$p = \frac{E(1-\nu)}{(1+\nu)(1-2\nu)} \varepsilon_v + Az + B \quad (5.17)$$

where  $A$  and  $B$  are constants.

Substituting Eq. (5.17) into Eq. (5.16), we obtain the following equation for the liquid pressure

$$\frac{\partial p}{\partial t} = c_v \frac{\partial^2 p}{\partial z^2} \quad (5.18)$$

The drainage velocity  $v$  in the gravity direction according to Eq. (5.15) is given by

$$v = -\frac{k}{\mu} \frac{\partial (p + \rho gz)}{\partial z} \quad (5.19)$$

The drainage velocity  $u$  is equal to zero at the bottom (at  $z=-h$ ). It can also be assumed to equal zero at the free surface, so that the boundary conditions for Eq. (5.18) at  $t>0$  read

$$\left. \frac{\partial p}{\partial z} \right|_{z=0 \text{ or } z=-h} = -\rho g \quad (5.20)$$

The boundary condition (5.20) at  $z=0$  implies that foam is pinned at the column top where  $z=0$ , which is indeed the case as discussed below. It is also emphasized that in the experiments of section 3, the drained (un-foamed) liquid column accumulates near the settler bottom in the course of drainage and the lower boundary of foam moves from  $z=-h$  up. However, during the entire drainage process the height of this drained liquid column is less than 7 cm, whereas the foam column height is 104 cm. Therefore, in the first approximation, dealing with foams with the initial gas volume fraction  $\phi$  of about 0.95 (Tables 5.1 and 5.2), we neglect the effect of motion of the lower foam boundary and displace the boundary condition (5.20) to  $z=-h$  for any  $t$ .

The initial condition corresponds to uniform foam

$$p|_{t=0} = p_0 \quad (5.21)$$

Equations (5.18) and (5.20) show that the problem has an integral invariant

$$\int_{-h}^0 p dz = p_0 h = \text{const} \quad (5.22)$$

which can be recast with the help of Eq. (5.17) into

$$\int_{-h}^0 \varepsilon_v dz = \frac{(1+v)(1-2v)}{E(1-v)} \left( p_0 h + \frac{Ah^2}{2} - Bh \right) = \text{const} \quad (5.23)$$

It is easy to see that the left hand side of Eq. (5.23) corresponds to nothing but the liquid content in the foam layer  $-h \leq z \leq 0$ , which obviously should not change in time. Indeed, according to Eq. (5.4) it does not.

It is convenient to introduce  $P=p+\rho gz$ , and render  $t$  dimensionless by  $h^2/c_v$ ;  $p$ ,  $p_0$  and  $P$  by  $\rho gh$ ; and  $z$  by  $h$ . Then, the problem (5.18), (5.20) and (5.21) can be recast to the following dimensionless form

$$\frac{\partial P}{\partial t} = \frac{\partial^2 P}{\partial z^2} \quad (5.24)$$

$$\frac{\partial P}{\partial z} \Big|_{z=0 \text{ or } z=-1} = 0 \quad \text{at } t > 0 \quad (5.25)$$

$$P = P_0(z) = p_0 + z \quad \text{at } t=0 \quad (5.26)$$

where bars over the dimensionless parameters are omitted for brevity.

The integral invariant (5.22) takes the form

$$\int_{-1}^0 P dz = p_0 - \frac{1}{2} \quad (5.27)$$

corresponding to Eqs. (5.24)-(5.26).

Finding the solution of the problem (5.24)-(5.26) and returning from  $P$  to the dimensionless pressure  $p$ , one obtains

$$p = p_0 - \sum_{n_{\text{odd}}=1}^{\infty} \frac{4}{\pi^2 n^2} \left[ 1 - \exp(-\pi^2 n^2 t) \right] \cos(\pi n z) \quad (5.28)$$

It is easy to see that as  $t \rightarrow \infty$ , according to Eq. (5.28)  $p \rightarrow p_{\infty} = p_0 - z - 1/2$ . In the dimensional units it means that pressure distribution tends to

$$p = p_0 - \frac{\rho gh}{2} - \rho gz \quad (5.29)$$

As a result, one expects that at the pinned free surface  $z=0$  (i.e. the free surface of foam which cannot slip down the settler wall during foam drainage), pressure will become lower than the atmospheric pressure, namely,  $p_0 - \rho gh/2$ . The difference is small,  $\rho gh/2 \approx 0.01p_0$ , and represents itself the price of the assumption that the free surface is pinned. In reality, the free surface was pinned at the settler wall and cap.

Using the solution (5.28) and Eq. (5.19), we find the dimensional drainage velocity in the following form (albeit  $z$  is still dimensionless)

$$v = -\frac{k\rho g}{\mu} \left\{ \sum_{n_{\text{odd}}=1}^{\infty} \frac{4}{\pi n} [1 - \exp(-\pi^2 n^2 t)] \sin(\pi n z) + 1 \right\} \quad (5.30)$$

Equation (5.30) shows that at  $t=0$  at any  $z$  (in particular at the settler bottom) the drainage velocity  $v = -k\rho g/\mu$ . At time  $t > h^2/(\pi^2 c_v)$ , the drainage velocity at any  $z$  doubles,  $v = -2k\rho g/\mu$ .

Foam in the settler does not detach from the walls. Therefore, in the present case  $u_{xx} = u_{yy} = 0$ , while  $\varepsilon_v = u_{zz}$ . Then, according to Eq. (5.6), we find in the present case

$$\sigma_{zz} = \frac{E\varepsilon_v(1-\nu)}{(1+\nu)(1-2\nu)} - p \quad (5.31)$$

whereas the lateral stresses  $\sigma_{xx}$  and  $\sigma_{yy}$  are non-zero, as is expected in the laterally restricted situation.

Using Eq. (5.17), it is easy to see that



$$\varepsilon_v = \frac{(1+\nu)(1-2\nu)}{(E/\rho gh)(1-\nu)} \sum_{n_{\text{odd}}=1}^{\infty} \frac{4}{\pi^2 n^2} \exp(-\pi^2 n^2 t) \cos(\pi n z) \quad (5.32)$$

with  $t$  and  $z$  being dimensionless.

Then, from Eqs. (5.31), (5.32) and (5.28) we find that the stress, rendered dimensionless by  $\rho gh$ , is given by

$$\sigma_{zz} = -p_0 - \sum_{n_{\text{odd}}=1}^{\infty} \frac{4}{\pi^2 n^2} \left[ 2 - \exp(-\pi^2 n^2 t) \right] \cos(\pi n z) \quad (5.33)$$

This equation shows that the stress on the bubbles near the bottom is always compressive (negative) and its magnitude increases in time from the dimensionless value of  $(p_0+1/2)$  to  $(p_0+1)$ . The experiments show that the increasing pressure near the settler bottom leads to breakup of larger bubbles and formation of the smaller ones. This, however, cannot change the effective Young's modulus  $E$  and Poisson's ration  $\nu$  of the foam if no gas is lost, i.e.  $\varphi=\text{const}$  [cf. Eqs. (5.7)].

It is emphasized that the above theory assumes that the lamellae thicknesses in the foam are sufficiently large to neglect the effect of the long-range forces (e.g. the van der Waals forces) associated with the disjoining pressure [Kornev et al. (1999); Derjaguin (1934)]. This assumption is sufficiently accurate for the lamellae thicknesses above 1  $\mu\text{m}$ . However, at the later stage of liquid drainage from the foam the lamellae can thicken below this threshold and the disjoining pressure tends to stabilize them, which decelerates the latest stage of the drainage process [Kornev et al. (1999)]. This effect will also be visible in the experimental results described in section 4, and the present theory cannot be applied to the latest stage of drainage. (p. 5325-5326)

## **5.3 Experimental Materials and Apparatus**

### **5.3.1 Experimental setup**

Jun et al. (2012) describes the setup as follows:

In order to create a large amount of uniform foam, the mechanical mixing method was chosen over the blowing bubbles method. To create the surfactant solution, Pantene Pro-V Classic Care Solutions shampoo (store bought and mostly containing sodium lauryl sulfate and sodium laureth sulfate) and DI water were placed into a mixing bowl in various proportions to produce different concentrations by volume. Poly(ethylene oxide), PEO, of  $M_w = 8$  MDa was also added to the surfactant solution in one case. PEO was purchased from Sigma Aldrich. A standard household mixer, Hamilton Beach, stirred the solution on the highest setting for 2 min except when PEO was added. In the latter case, PEO was added to the DI water and mixed for 2 min, then the shampoo was added and stirred again for 2 min. It is emphasized that a wire impeller was used because of its ability to create a more uniform bubble size and better mixed foam (no excess water) than the standard propeller. The foam was then poured into a squeezable funnel with a flexible hose (inside diameter was 1.7 cm) attached to the end. The funnel was squeezed to force the foam through the hose. The cylinder of the gravity settler was filled from the bottom up as shown in Figure 5.2a. As the level of foam increased, the funnel-hose system was raised correspondingly so that the foam exiting the hose would be at the top. When the foam was filled to the top of the cylinder, the funnel-hose system was removed and the cylinder was capped, which effectively prevented loss of liquid vapor or gas from the settler during the

entire experiment. The time to fill the cylinder with foam averaged about 1 min, during which no drained liquid was visible. (p. 5326)

In the case using USG soap, USG provided two types of surfactant, namely, stable and unstable soap. The amount of air in the foam was controlled by a foam generator. The filling process and time are the same despite the surfactants used.

The inside dimensions of the cylinder were 2.58 cm in diameter and 104 cm tall. The drained liquid height was measured using a CCD camera and a backlight shown in Figure 5.3.

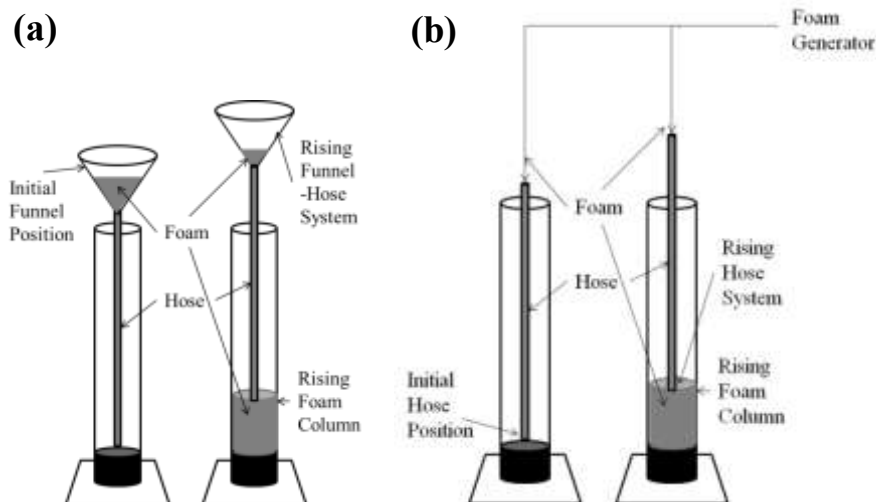


**Figure 5.2.** Filling gravity settler using the funnel-hose system (a). Filling gravity settler using the foam generator with attached hose system (b). The system is raised with the foam height so that the foam exiting the hose is at the top of the foam column. Reprinted with permission from Jun, S., Pelot, D. D., & Yarin, A. L. (2012). Foam consolidation and drainage. *Langmuir*, 28(12), 5323-5330. Copyright (2012) American Chemical Society.

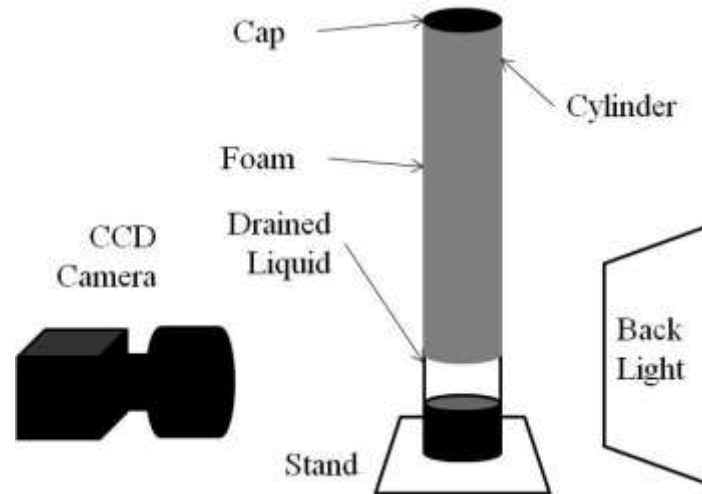


**Figure 5.3.** Sketch of the experimental setup. Reprinted with permission from Jun, S., Pelot, D. D., & Yarin, A. L. (2012). Foam consolidation and drainage. *Langmuir*, 28(12), 5323-5330. Copyright (2012) American Chemical Society.

#### **5.4 Results and discussion**

As discussed in Jun et al. (2012):

The present work aims at measuring the amount of liquid drained as well as the rate of drainage as functions of time. The height of the drained liquid/foam interface was measured by counting pixels in the images taken by the CCD camera and using the outside cylinder width as a reference scale. Each pixel corresponded to approximately 0.13 mm. Several images taken during drainage of liquid in an experiment with 2% shampoo foam are shown in Figure 5.4. The dashed line indicates the level of the drained liquid from the previous image. Figure 5.4a corresponds to the first instant when drained liquid appears 1.5 minutes after the column was capped. The progressive images show how the rate

of drainage initially increases from Figure 5.4a to Figure 5.4d and then decreases from Figure 5.4e to Figure 5.4h.

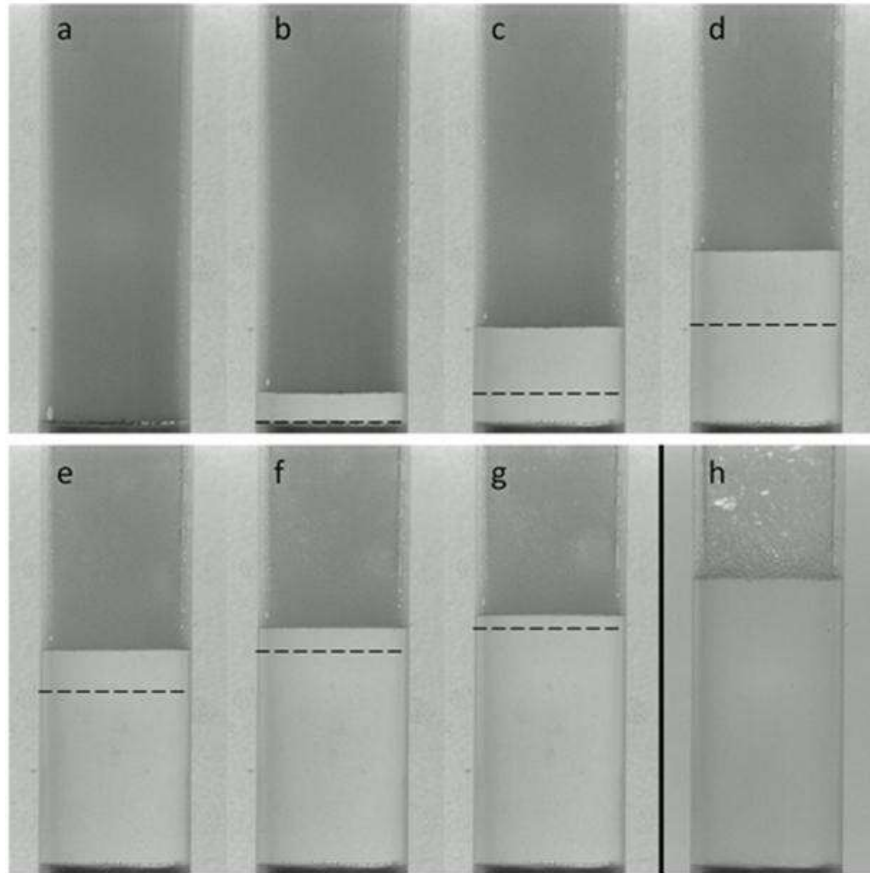


**Figure 5.4.** Images taken during drainage of 2% shampoo foam. The images (a)-(h) correspond to 1.5 min, 5 min, 10 min, 15 min, 20 min, 25 min, 30 min, and 3 h (the end of draining), where the volume of liquid drained is  $0.16 \text{ cm}^3$ ,  $3.37 \text{ cm}^3$ ,  $10.50 \text{ cm}^3$ ,  $18.88 \text{ cm}^3$ ,  $23.43 \text{ cm}^3$ ,  $25.85 \text{ cm}^3$ ,  $27.26 \text{ cm}^3$ , and  $31.18 \text{ cm}^3$ , respectively. The dashed line indicates the height of the drained liquid in the previous frame.

The evolution of the drainage rate was found to be in agreement with the theoretical predictions of section 2. When drainage begins, its initial rate is

relatively slow and is approximately constant (Figure 5.5). Next, the drainage rate increases in time until a maximum is reached, corresponding to twice the initial drainage rate, and proceeds at this constant higher rate (Figure 5.5). Figure 5.5 also shows that the drainage process begins to slow down compared to the maximum rate of drainage at  $t > 800$  s. This phenomenon is probably characteristic of older and/or dryer foam, in which the lamellae thickness is below  $1 \mu\text{m}$  and the disjoining pressure (not accounted for in the present theory) decelerates the drainage process.

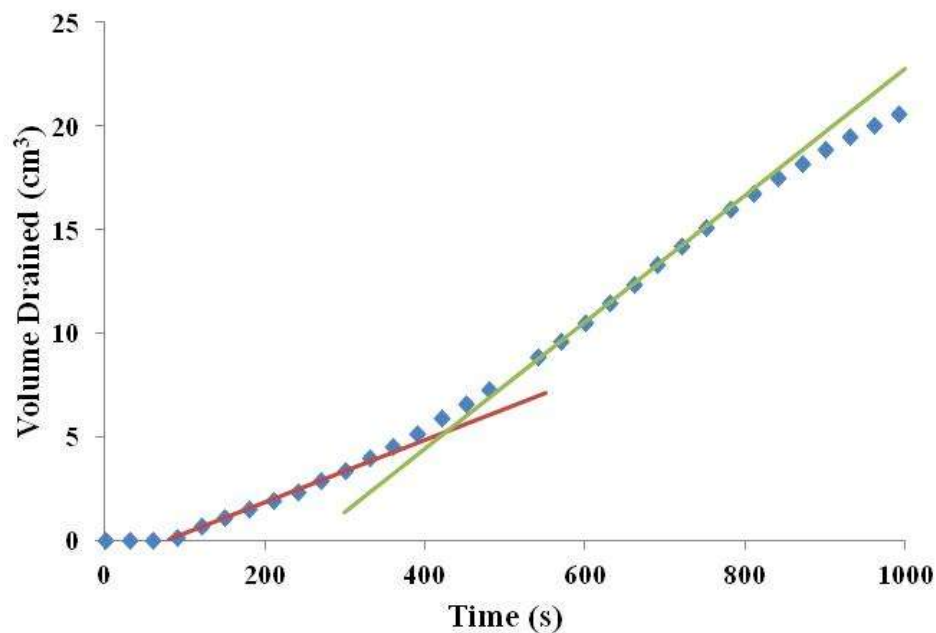


**Figure 5.5.** Height of liquid column drained for the first 1000 s (before the drainage process cessation is felt) in Trial 1 of 2% shampoo. The two lines show the crossover of a slow (initial) and fast (maximum) drainage processes. The ratio of maximum drainage rate to initial drainage rate in this case is 2.03. (p. 5327)

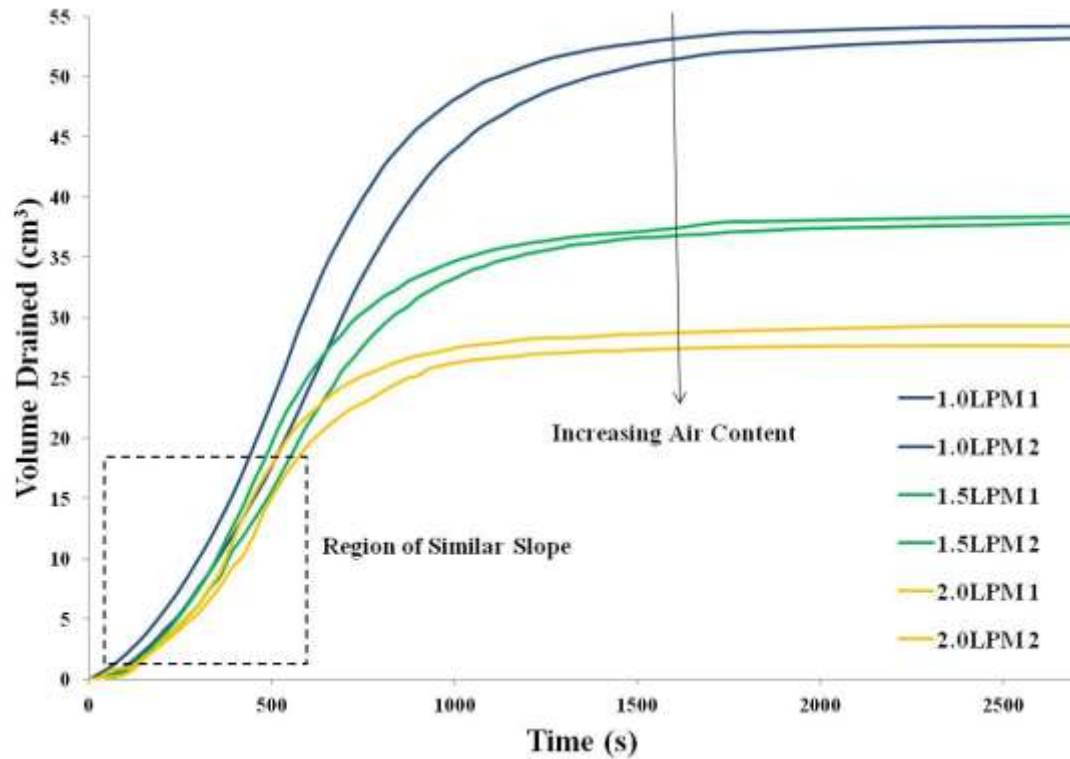


**Figure 5.6.** Volume drained from foams created with different air flow rates with soap concentration of 0.25% stable and 0.25% unstable. The dashed box highlights the domain with relatively similar drainage rates at the initial stages of drainage. The curve saturation corresponds to the full drainage.

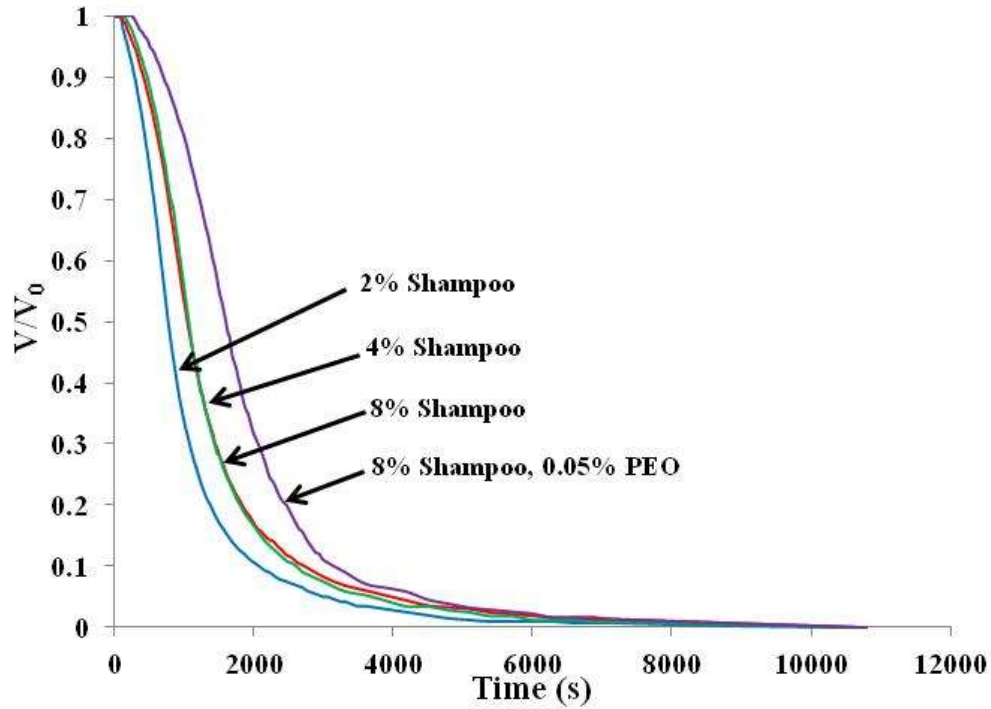


**Figure 5.7.** Drainage curves for different concentrations of shampoo (and addition of PEO). The volume of liquid in the foam,  $V$ , is normalized by the total volume of liquid in the foam,  $V_0$ . For each concentration the result of one trial is shown because the data are consistent between trials. Blue-2% shampoo, red-4% shampoo, green-8% shampoo, and purple-8% shampoo and 0.05% PEO. Reprinted with permission from Jun, S., Pelot, D. D., & Yarin, A. L. (2012). Foam consolidation and drainage. *Langmuir*, 28(12), 5323-5330. Copyright (2012) American Chemical Society.



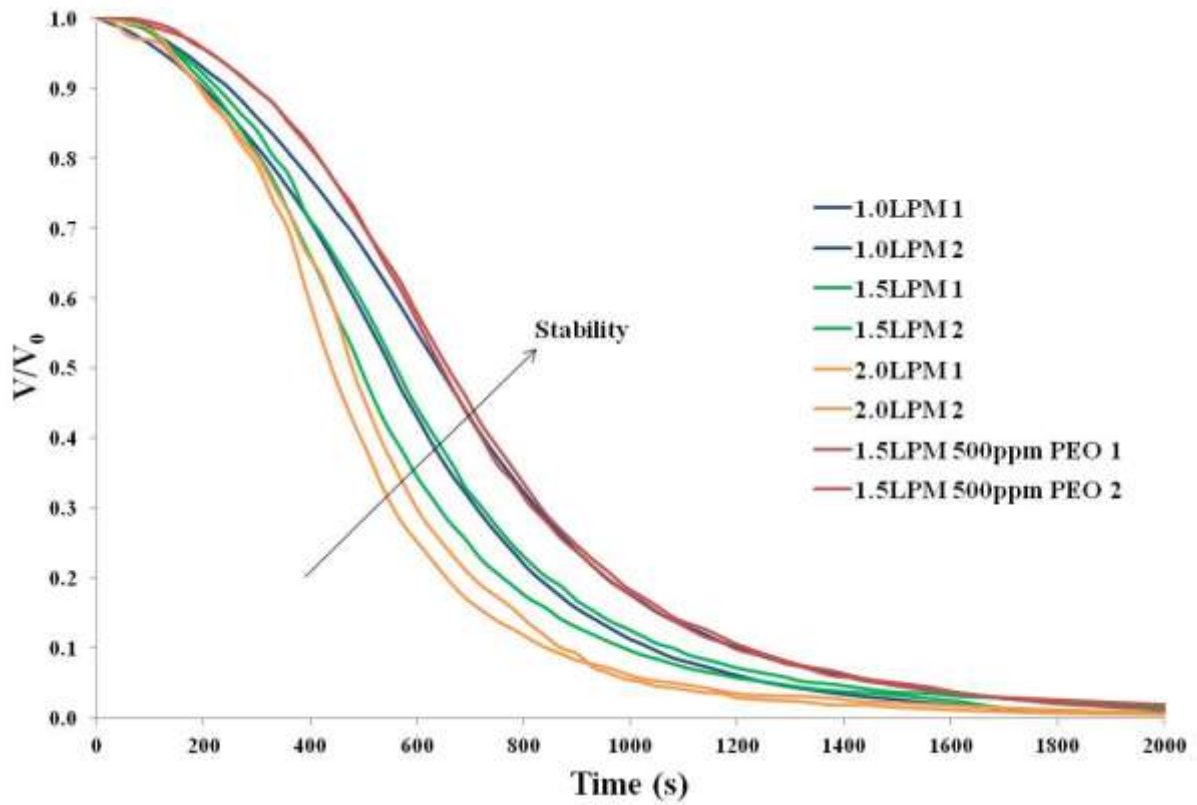


**Figure 5.8.** Normalized volume of liquid in the foam for different air flow rates during foam creation and the addition of 500 ppm PEO in one case.

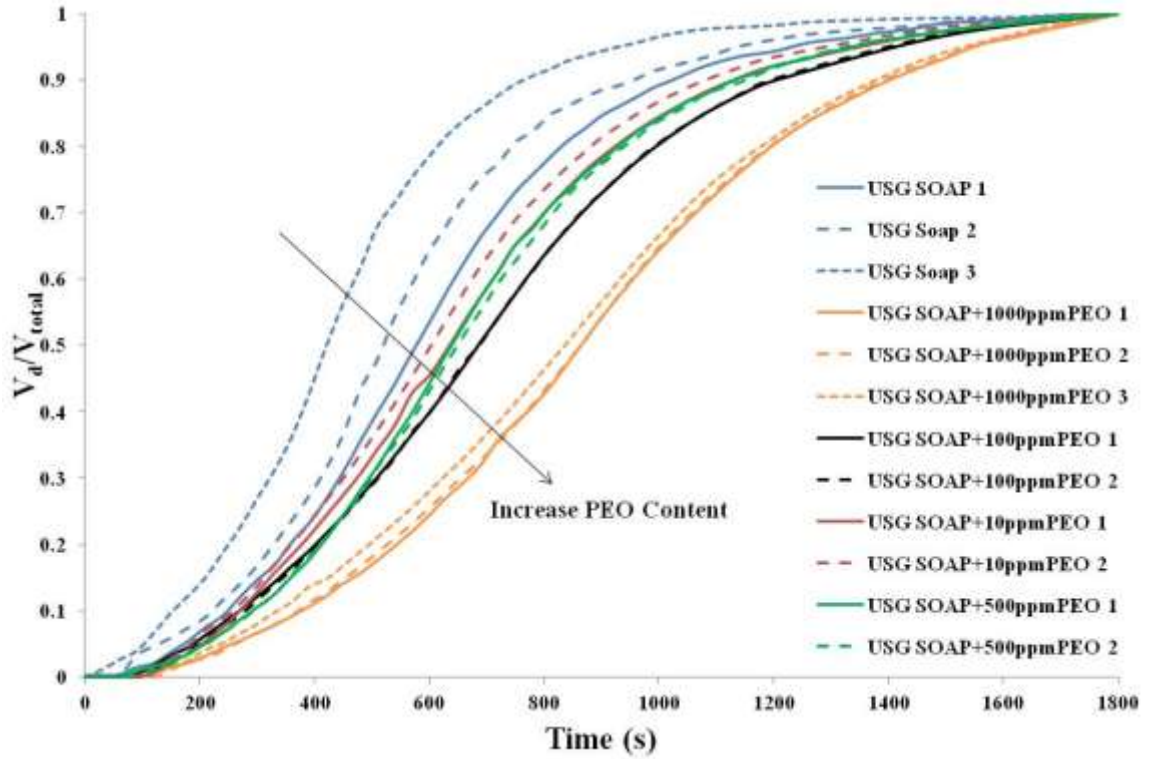


**Figure 5.9.** Normalized volume of liquid drained for different amounts of PEO added. The air flow rate during foam formation in all cases is 1.5 LPM and soap concentration of 0.25% stable and 0.25% unstable.

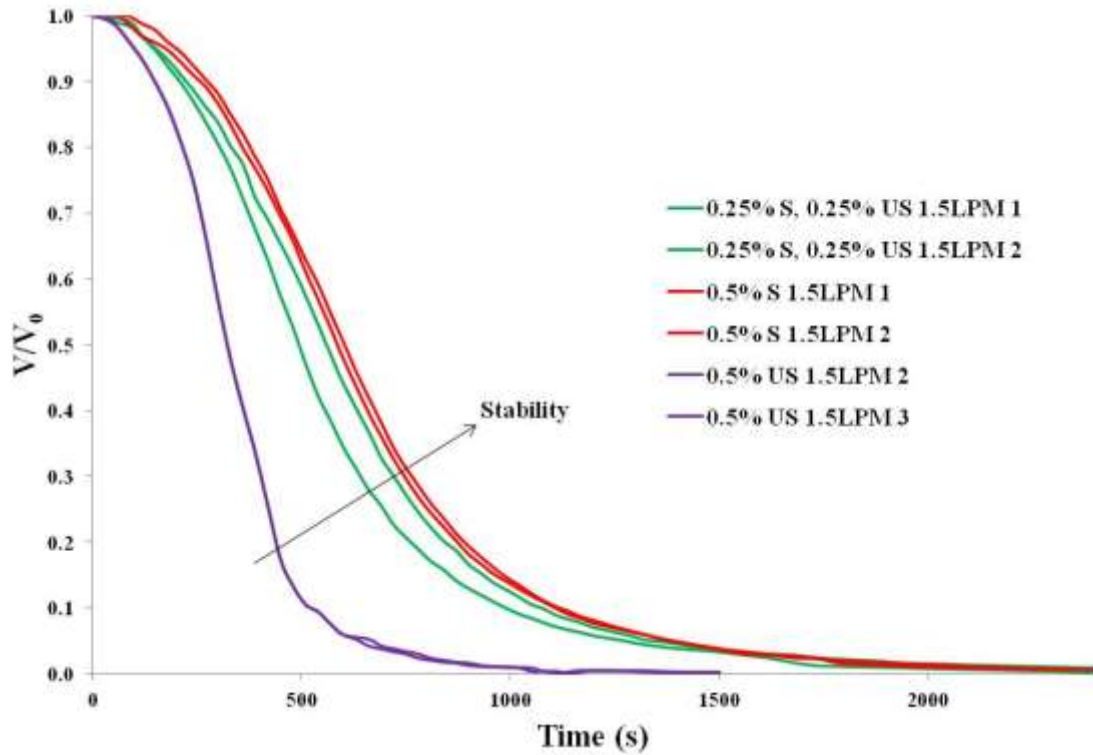


**Figure 5.10.** Normalized volume of liquid in foams for different soap concentrations. The air flow rate during foam formation in all cases is 1.5 LPM.

Figure 5.6 shows that an increase in air flow rate during foam formation decreases the amount of liquid in the foam. The densities of the foams for 1.0 LPM, 1.5 LPM, and 2.0 LPM are 0.100 g/cm<sup>3</sup>, 0.070 g/cm<sup>3</sup>, and 0.053 g/cm<sup>3</sup>, respectively. Interestingly, the initial stage of the drainage process is very similar for all foams and they all have approximately the same initial drainage rate  $\sim 0.030$  cm<sup>3</sup>/s. Furthermore, the maximum drainage rates are also within a small range, namely 0.064 cm<sup>3</sup>/s to 0.072 cm<sup>3</sup>/s. It can be concluded that the amount of air in the gravity settler has only minor effect on the drainage rates. However, it has a dominant effect on the duration of the drainage process, which terminates earlier when more air and less liquid is in foam.

Jun et al. (2012) states:

Figure 5.7 shows that an increase in shampoo concentration from 2% to 4% slows the drainage process. However, a further increase from 4% to 8% results in an insignificant change in the drainage duration or rates. This is due to the fact that the critical micelle concentration (cmc) of surfactant is being reached between 2% and 4%. Indeed, the main surfactant in the shampoo is sodium lauryl sulfate which has a cmc of 0.243% [Phillips and Mysels (1955); Wilson et al. (1957)]. The water content in 2% shampoo is close to 99.6%. That means that the remaining 0.4% is composed of surfactant and other additives. However, the contents of surfactant and additives are not known separately, but there is likely more surfactant. Therefore, the surfactant content in 2% shampoo is at least 0.2%, whereas in 4% shampoo it is at least 0.4%. Therefore, cmc is already reached in 4% shampoo, and a further increase in the surfactant content does not affect the surface properties of the foam. The latter manifests itself in the practically indistinguishable results for 4% and 8% shampoo in Figure 5.7. As a result, additional surfactant molecules in 8% shampoo have no effect on the drainage process, since all the free surfaces in foam are already fully occupied by shampoo molecules, and only an accumulation in the bulk (probably in the form of micelles) continues. However, it is seen in Figure 5.7 that even though adding more shampoo is unable to slow down the drainage process, an addition of a small amount of PEO can still dramatically reduce the drainage rate.

The quantitative parameters of the data shown in Figure 5.7 are listed in Table 5.1. In particular, it includes the minimum and maximum slopes, and the

ratio of the maximum to the minimum slopes. It is emphasized that these slopes are directly proportional to the drainage rates, i.e. to the drainage rate  $v$  predicted by Eq. (5.30). It is clear from Figure 5.7 and Table 5.1 that increasing shampoo concentration, as well as the addition of PEO, reduce both minimum and maximum rates of drainage. However, their ratios are approximately the same in all cases and are close to 2, which agrees with the theoretical prediction of section 2. This reveals that the theory presented in section 2 is capable of describing foams that contain such additives as PEO, and not only foams containing a surfactant. (p. 5327-5328)

When the surfactant concentration in foam is small, as in all cases presented here, the surface area to volume ratio can have a large effect on the stability of the foam column. Since the foam created with 2.0 LPM air flow rate has a lower density than that of 1.0, its surface area to volume ratio is larger. This means that it will need more surfactant at the air water interface to stabilize the foam structure, or if the amount of surfactant is kept constant, then the foam with the lower surface area to volume ratio will be the most stable. This is shown in Figure 5.8 where the foam with the highest air flow rate during formation has the lowest stability, while the foam with the lowest air flow rate has the highest stability. Furthermore, in Figure 5.8 it is seen that the stability can be increased further with an addition of 500 ppm of PEO.

The stabilizing effect of PEO on foam is detailed in Figure 5.9. The amount of PEO varied from 10 ppm to 1000 ppm under standard USG foam formation conditions (0.25% stable soap and 0.25% unstable soap at 1.5 LPM). It is clearly seen in Figure 5.9 that as the concentration of PEO increases, so does the foam stability. It was expected that the trials using 500 ppm PEO would give results between 100 ppm PEO and 1000 ppm PEO. However, the 500

ppm PEO case is between 10 ppm PEO and 100 ppm PEO. The trials with 10 ppm, 100 ppm, and 1000 ppm of PEO were conducted at one time and the trials with 500 ppm PEO were conducted three months later, therefore showing a certain inconsistency in the foam generating process.

In addition, the effect of the soap composition in foam was explored. Using either 0.5% stable soap or 0.5% unstable soap at 1.5 LPM was compared to the USG standard foam of 0.25% stable soap and 0.25% unstable soap at 1.5 LPM of air supply during foam formation. As shown in Figure 5.10, the foam containing only stable soap was slightly more stable than the USG standard foam. On the other hand, the foam containing only unstable soap was dramatically less stable.

The quantitative parameters corresponding to the data shown in Figures 5.6, 5.8 and 5.10 are listed in Table 5.2 and Figure 5.7 in Table 5.1. In particular, it includes the minimum and maximum slopes, and the ratio of the maximum to the minimum slopes. It is emphasized that these slopes are directly proportional to the drainage rates, i.e. to the drainage rate  $v$  predicted by Eq. (5.30). It is shown in Figure 5.6 and Table 5.2 that increasing air flow rate during foam formation has only a minor effect on the drainage rate. The addition of PEO reduces both minimum and maximum rates of drainage. The use of only stable soap, as in Figure 5.10, also shows a reduction in the minimum and maximum drainage rates compared to the USG standard foam. Lastly, foam containing only unstable soap shows an increase in both minimum and maximum drainage. Nevertheless, as in Jun et al. (2012), all “ratios are approximately the same in all cases and are close to 2, which agrees with the theoretical prediction of section 5.2. This reveals that the theory presented in section 5.2 is capable of describing foams that contain such additives as PEO [or were formed at different air contents], and not only foams containing a surfactant, [as in the preliminary work, but also soaps at different compositions]”.

**Table 5.1.** Results for different concentrations of shampoo and PEO (in one case). Reprinted with permission from Jun, S., Pelot, D. D., & Yarin, A. L. (2012). Foam consolidation and drainage. *Langmuir*, 28(12), 5323-5330. Copyright (2012) American Chemical Society.

Concentration	2% Shampoo		4% Shampoo		8% Shampoo		8% Shampoo with 0.05% PEO	
	1	2	1	2	1	2	1	2
Trial number	1	2	1	2	1	2	1	2
Minimum slope $\times 10^3$ (cm <sup>3</sup> /s)	15	15	9	11	9	10	5	6
Maximum slope $\times 10^3$ (cm/s)	31	29	21	23	21	21	14	14
Max. slope/Min. slope	2.03	2.01	2.22	2.04	2.33	2.17	2.78	2.29
Average permeability, k, $\times 10^7$ (cm <sup>2</sup> )	1.54	1.49	1.01	1.16	1.00	1.04	2.03	2.34
Consolidation coefficient, $c_v$ , (cm <sup>2</sup> /s)	2.57	2.57	1.90	1.96	1.64	1.89	1.16	1.24
Initial gas volume fraction, $\phi$	0.943	0.942	0.949	0.945	0.953	0.950	0.955	0.951
Young's modulus [Eq. (5.7)], E, $\times 10^{-5}$	0.29	0.29	0.29	0.29	0.29	0.29	0.29	0.29
Young's modulus [Eq. (5.13)], E, $\times 10^{-5}$	0.17	0.17	0.19	0.17	0.16	0.18	0.19	0.18

**Table 5.2.** Results for different air flow rates, soap concentrations, and addition of PEO in one case. Values are averaged over two trials.

Concentration	0.25% Stable and 0.25% Unstable Soap				0.5% Stable Soap	0.5% Unstable Soap
	1.0 LPM	1.5 LPM	2.0 LPM	0.05% PEO 1.5 LPM		
Air flow rate	1.0 LPM	1.5 LPM	2.0 LPM	0.05% PEO 1.5 LPM	1.5 LPM	1.5 LPM
Minimum slope $\times 10^3$ ( $\text{cm}^3/\text{s}$ )	33	30	28	23	23	45
Maximum slope $\times 10^3$ ( $\text{cm}^3/\text{s}$ )	72	61	64	50	53	118
Max. slope/Min. slope	2.2	2.0	2.3	2.2	2.3	2.6
Time Period of Max Slope (min)	8-11	7.5-9.5	7-8	8.5-12.5	7-11	3.5-6
Average permeability, $k$ ( $\text{cm}^2$ ) $\times 10^7$	3.5	3.1	3.1	4.8	2.5	5.3
Consolidation coefficient, $c_v$ ( $\text{cm}^2/\text{s}$ )	3.13	3.30	3.16	2.72	3.22	8.98
Initial gas volume fraction, $\phi$	0.90	0.93	0.95	0.93	0.93	0.93
Young's Modulus, [Eq. (5.7)], (Pa) $\times 10^{-5}$	2.74	2.83	2.88	2.83	2.83	2.82
Young's Modulus, [Eq. (5.13)], $E$ (Pa) $\times 10^{-5}$	0.90	1.07	1.05	5.69	1.28	1.64

**Table 5.3.** Viscosity for different concentrations of shampoo and PEO in unfoamed solutions. Measurements were conducted using a Brookfield cone and plate viscometer. Reprinted with permission from Jun, S., Pelot, D. D., & Yarin, A. L. (2012). Foam consolidation and drainage. *Langmuir*, 28(12), 5323-5330. Copyright (2012) American Chemical Society.

Concentration	2% Shampoo	4% Shampoo	8% Shampoo	8% & 0.05% PEO
Viscosity (cP)	1.0	1.0	1.1	3.4



**Table 5.4.** Viscosity for different concentrations of PEO in solutions of USG soap at concentrations of 0.25% stable and 0.25% unstable. Measurements were conducted using a Brookfield cone and plate viscometer. (\*) The assumed value, as for water.

Concentration	USG soap	USG soap & 10 ppm PEO	USG soap & 100 ppm PEO	USG soap & 500 ppm PEO	USG soap & 1000 ppm PEO
Viscosity (cP)	1.00*	0.94	1.50	1.95	3.70

**Table 5.5.** Time, in minutes, needed for different concentrations of foam to drain fractions of the initial liquid volume. Reprinted with permission from Jun, S., Pelot, D. D., & Yarin, A. L. (2012). Foam consolidation and drainage. *Langmuir*, 28(12), 5323-5330. Copyright (2012) American Chemical Society.

Concentration	2% Shampoo		4% Shampoo		8% Shampoo		8% Shampoo with 0.05% PEO	
	1	2	1	2	1	2	1	2
Trial number	1	2	1	2	1	2	1	2
Time (min) at which $V/V_0=0.9$ ; 10% drainage	4.8	4.5	7.0	6.3	7.8	6.8	11.5	11.3
Time (min) at which $V/V_0=0.5$ ; 50% drainage	12.8	13	17.5	16.5	17.5	17	26.5	25.5
Time (min) at which $V/V_0=0.1$ ; 90% drainage	34.5	35	45	45	44	44	52.5	51

As stated Jun et al. (2012):

[Table 5.1] also contains the values of the average permeability for each foam concentration studied. To measure the permeability value, the formulae for the minimum and maximum drainage velocities  $v=-k\rho g/\mu$  (at  $t=0$ ) and  $v=-2k\rho g/\mu$  [at

$\tau > h^2/(\pi^2 c_v)$ ], respectively, were used. The values of  $v$  were measured experimentally; the other parameters were taken as  $\rho=1 \text{ g/cm}^3$ ,  $g=981 \text{ cm/s}^2$  and the viscosities as measured and listed in Table 5.2. The values of  $k$  were then calculated for the slow and fast drainage processes. They were approximately equal to each other. The values of  $k$  listed in Table 5.1 represent their averages.  
(p. 5328)

For the experiments using shampoo, the permeability values ranged between  $1 \cdot 10^{-7} \text{ cm}^2$  to  $2.4 \cdot 10^{-7} \text{ cm}^2$  and in the experiments using USG soap the values ranged between  $3.1 \cdot 10^{-7} \text{ cm}^2$  to  $5.3 \cdot 10^{-7} \text{ cm}^2$ . This shows that foam permeability decreases when shampoo concentration increases or air flow rate during foam formation increases, which corresponds to slowing down of the drainage process. Also stated in Jun et al. (2012):

Another way to evaluate the permeability is to employ direct observations under a microscope of the liquid lamellae in the foam and consider them as planar channels supporting Poiseuille-like drainage flow. For planar Poiseuille flow the permeability is equal to  $k=\delta^2/12$  where  $\delta$  is the channel (lamella) width (thickness), which follows from the Poiseuille law written in the form of Darcy's law [Loitsyanskii (1966)]. For all concentrations of shampoo with no PEO added, the lamellae thickness  $\delta$  in fresh foam ranges from  $20 \text{ }\mu\text{m}$  to  $50 \text{ }\mu\text{m}$ , as measured using the foam images. Therefore, the permeability value estimates for the Poiseuille-like channel flow range from  $3.3 \cdot 10^{-7} \text{ cm}^2$  to  $2.1 \cdot 10^{-6} \text{ cm}^2$ , respectively. The value of  $k$  of the order of  $10^{-7} \text{ cm}^2$  estimated assuming the Poiseuille-like drainage flow overlaps with the data in Table 5.1 found from the drainage rates. Therefore, the two separate estimates of the permeability are in a reasonable

agreement with each other. It is emphasized that drainage through an individual lamella happens in the direction of its generatrix, which may be inclined relative to the z-axis. On the other hand, the cumulative drainage from the foam happens parallel to the z-axis [downward, cf. Eq. (5.19)]. The result obtained shows that the average permeability of the individual lamellae is of the same order as the foam permeability as a whole.

Also presented in Tables 5.1 and 5.2 are the values of the consolidation coefficients and the gas volume fractions. The consolidation coefficient was calculated using the intersection time  $t_i$  between the slopes of the slow and fast drainage processes (cf. Figure 5.5) and the value of the column height using the equation  $c_v = h^2 / (\pi^2 t_i)$ . The consolidation coefficient decreases as shampoo concentration increases. Adding PEO, decreases the consolidation coefficient even further. [The consolidation coefficient shows no general trend corresponding to air flow rate during foam formation.] Adding PEO, decreases the consolidation coefficient [slightly, whereas using only unstable soap raises it significantly.] Lower values of the consolidation coefficient correspond to higher foam stability.

The gas volume fraction,  $\phi$ , is a given parameter; its values are listed in Tables 5.1 and 5.2. Using Eq. (5.7) Poisson's ratio,  $\nu$ , is calculated. The values of  $\nu$  are in the range from 0.02 to 0.05.

The Young's modulus,  $E$ , was calculated using two different ways and the values are compared, as shown in Tables 5.1 and 5.2. First, the Young's modulus was calculated using Eq. (5.7) where it is related to atmospheric (gas) pressure in the bubbles under the assumption that capillary pressure is negligible and the

foam elasticity results only from the gas inside the bubbles. The second way to calculate the Young's modulus is using its relation to the consolidation coefficient, as in Eq. (5.13). Using the values of the consolidation coefficient, average permeability, Poisson's ratio and liquid viscosity from Tables 5.1 and 5.2, Young's modulus was calculated from Eq. (5.13). A fairly good agreement between the values of Young's modulus found by the two methods can be seen in Tables 5.1 and 5.2. It is instructive to see that Young's modulus does not depend on the surfactant concentration. [However, there was some variance for foams formed at the different air flow rates explored,] which corroborates the idea that foam elasticity is associated with the gas entrapped in the bubbles.

To ensure complete mixing for viscosity measurements, solutions were prepared and stirred for an appropriate time. Then, a bottle with a solution was capped and left overnight to allow the foam to settle. The drained fluid was the bulk solution from the foam lamellae. All the aqueous shampoo solutions were found to be Newtonian. On the other hand, the shampoo solution with added PEO was slightly shear-thinning. Its viscosity decreased from 3.8 cP to 3.0 cP when the shear rate increased from  $37.5 \text{ s}^{-1}$  to  $375 \text{ s}^{-1}$ . Since the change in viscosity is small, the average value listed in Table 5.3 was used in all calculations. [Similar action was taken when using USG soaps.]

It is also of interest to compare our data to the empirical formula for the volume fraction of liquid proposed by Ross (1943)

$$\frac{V}{V_0} = \exp(-Kt) \quad (5.34)$$

where  $V$  is the volume of liquid in the foam,  $V_0$  is the initial liquid volume in the foam as in Table 5.5,  $t$  is time and  $K$  is an empirical constant (the inverse characteristic drainage time, which corresponds to diminishing of the liquid volume in the foam to about  $1/3$  of its initial value, and is to be found as a result of curve fitting). [This was only applied to the case of shampoo.] Equation (5.34) is applied to the second half of our data in Figure 5.7, as suggested by Bikerman (1973). The average (per each foam composition) values of  $K$  are  $0.00106 \text{ s}^{-1}$ ,  $0.00080 \text{ s}^{-1}$ ,  $0.00080 \text{ s}^{-1}$  and  $0.00060 \text{ s}^{-1}$  for 2%, 4%, 8%, and 8% shampoo with 0.05% PEO, respectively. It is clearly seen in Figures 5.11a-5.11d that Eq. (5.34) is incapable to describe the initial (slow) drainage stage and the maximum drainage stage, even though it can fit the rest of the dependence with the appropriate choice of the fitting parameter  $K$ .

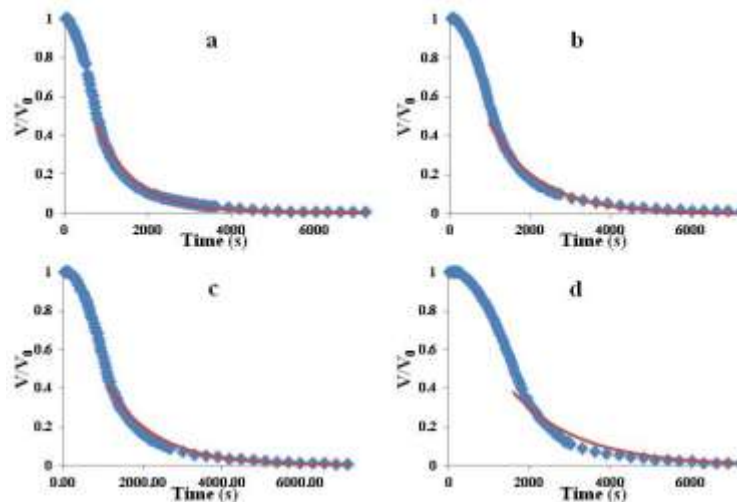


**Figure 5.11.** Drainage data fitted with Eq. (5.34). The diamonds represent the experimental data and the line is the fitted curve according to Eq. (5.34). (a) 2% shampoo, (b) 4% shampoo, (c) 8% shampoo, and (d) 8% shampoo with 0.05% PEO. (p. 5328-5329)

## **5.5 Conclusion**

As stated in Jun et al. (2012):

The present theory treats foam as a consolidating medium possessing elastic properties predominantly due to gas present in the bubbles, as well as a Darcy-like drainage of liquid from their interconnected lamellae. It is predicted that the drainage process begins with a slow stage. This stage lasts on the scale of the characteristic consolidation time. After that it is replaced by a faster drainage stage in which the rate of drainage doubles. This prediction was confirmed by the current experiments with foams with different surfactant concentrations, air volume fraction, and a polymer additive. At the latest stage of foam existence, the drainage could be attributed to a deceleration by the disjoining pressure in liquid lamellae. The experiments also showed that the foam drainage rate in a gravity settler is diminished at higher surfactant concentration to a certain limit of approximately 4% for this surfactant, and beyond the limit with the addition of a small amount of PEO. Furthermore, the foam drainage rate in a gravity settler is diminished due to lower air flow rates at foam formation, and even further with the addition of a small amount of PEO. As predicted, the effective Young's modulus of foam appeared to be determined by the gas present in the bubbles, and is practically independent of surfactant concentration. Overall, the experimental results confirmed the main elements of the theory. The general theory of foam as a consolidating medium can be applied to other situations. (p.5329)

## 6. STRONG SQUEEZE FLOWS OF YIELD-STRESS FLUIDS: THE EFFECT OF NORMAL DEVIATORIC STRESSES

### 6.1 Introduction

This work aims to study squeeze flows when the lubrication approximation does not necessarily hold. Strong squeeze flows are defined as the cases in which a sample is compressed by a disk with the initial speed of 40 cm/s, whereas weak squeeze flows are realized when the disk is softly released manually to avoid any impact of the sample at the beginning of compression. Strong and weak squeeze flows of yield-stress materials are studied experimentally and theoretically. In the experiments, disk-like constant-volume samples of Carbopol solutions and Bentonite dispersions are compressed between two approaching disks being subjected to constant forces. In addition, experiments with shear flows in parallel-plate and vane viscometers are conducted. Using visualization through the transparent wall of the squeezing apparatus, it is demonstrated that the no-slip conditions hold. It is also demonstrated that during the fast stage of strong squeeze flows, the material response can be explained by deviatoric normal stresses, which elucidates the link of strong squeeze flows to elongational flows. The analysis of the data in the framework of the Newtonian and Herschel-Bulkley models shows that in the present case the nonlinearity of the rheological response at the fast stage of strong squeeze flows is not very significant, and a strain-rate-independent viscosity can be used as a reasonable approximation. On the other hand, at the final stage of squeeze flows, when samples spread significantly under the action of a constant squeezing force, the compressive stresses become small enough, and the dominant role is played by the yield stress. It is shown that strong squeeze flow in the squeezing

apparatus represents itself as a convenient tool useful for the measurement of viscosity and the yield stress of complex soft materials.

The theoretical background is introduced in Section 6.2. In Section 6.3 the experimental details are described, including materials, solution and dispersion preparation and shear and squeeze experiments. The experimental results and discussion are contained in Section 6.4, and conclusions are drawn in Section 6.5.

## **6.2 Theoretical Background**

Squeeze flows of viscous Newtonian materials in the Constant Volume flow (iii) were treated in Dienes and Klemm (1946). The resulting expression for the cross-sectional sample area as a function of time,  $A(t)$ , reads

$$\left(\frac{A}{A_0}\right)^4 = 1 + \frac{8\pi}{3} \frac{h_0^2}{A_0^2} \frac{Ft}{\mu} \quad (6.1)$$

where the material viscosity is denoted  $\mu$ , the constant squeezing force- $F$ , the initial sample thickness and cross-sectional area- $h_0$  and  $A_0$ , respectively.

Equation (6.1) implies that the viscous resistance to the radial sample spreading between the disks stems from the shear stresses associated with the no-slip conditions at the disk surfaces and is transmitted into the material bulk by viscous shear stresses [Figure 6.1 (a)]. Moreover, it implies that squeezing with a constant force continues “indefinitely”, as a minimum, until the sample reaches the outer circumference of the squeezing disk. The latter, however, was not the case in the present experiments with Carbopol suspensions and Bentonite dispersions discussed below. In particular, experiments showed that sample spreading proceeds only to a certain radius, which is significantly smaller than that of the disks, after that it stops. It is emphasized that squeeze flow under the action of a constant force (weight, as in the experiments described in



section III) results in a decrease of compressive stress in time, since sample spreading redistributes the same squeezing force over a growing area  $A(t)$ . Therefore, the cessation of sample spreading corresponds to the lowest compressive stress. Such stress can be interpreted as a yield stress in compression  $Y$ , which implies that the materials of interest in the present work can possess not only viscosity but also a yield stress [Nigen (2005); Luu and Forterre (2009); Saidi et al. (2011)]. Such materials do not flow at all, if the stress applied is lower than a certain value, which is the yield stress. On the other hand, they flow when the stresses exceed the yield stress. It is emphasized that Carbopol suspensions and Bentonite dispersions were considered to be Bingham plastics in drop impact experiments [Nigen (2005); Luu and Forterre (2009); Saidi et al. (2011)]. For Bingham plastics, the viscous shear stresses will be concentrated only in the layers near the disks [Figure 6.1 (b)], while the bulk of such materials will experience only deviatoric normal viscous stresses. For example, in the parabolic velocity profile in squeeze flow between solid disks with no-slip conditions, only the near-wall layers of a thickness  $\delta$  will support viscous shear stresses which are higher than the yield stress in shear  $\tau_0$  of a Bingham plastic. Therefore, by definition the central part of the material is assumed to be unyielded and so there are no velocity gradients there as sketched in Figure 6.1 (b).

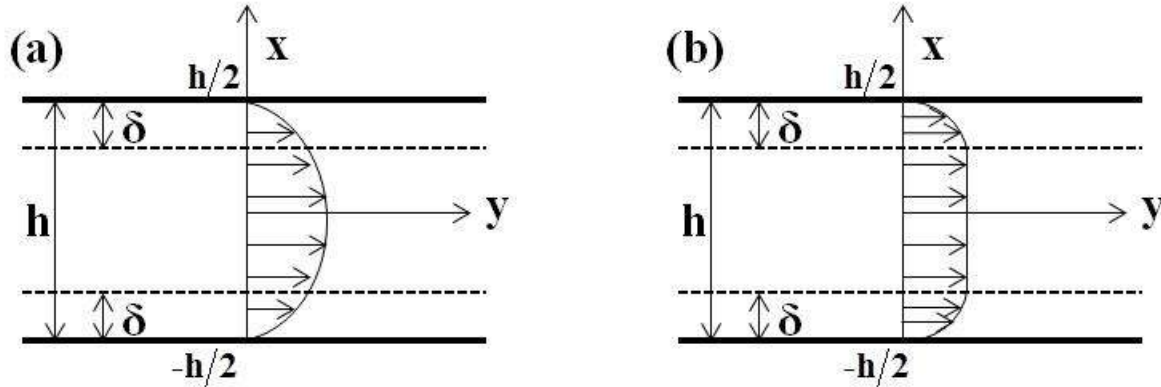


**Figure 6.1.** Schematic of the velocity profiles in squeeze flows of (a) Newtonian material, and (b) Bingham plastic. The current sample thickness is denoted  $h$ .

The thickness of the shear layers  $\delta$  can be estimated from the condition that at  $x = -h/2 + \delta$  the shear stress is equal to the yield stress  $\tau_0$ . For the Poiseuille-like parabolic velocity profile in the shear layer in Figure 6.1 (a) it means that

$$\delta = \frac{h}{2} - \frac{\tau_0 h^2}{8\mu v_0} \quad (6.2)$$

where  $h$  is the sample thickness between the squeezing disks,  $v_0$  is the maximum (in the cross-section) velocity component of flow in the  $y$ -direction of the pure parabolic velocity profile.

In a Bingham fluid, sections of the parabolic velocity profile exist only in the near wall layers, whereas the central part of the velocity profile corresponds to a plug flow since the shear stress there is below the yield stress  $\tau_0$  [cf. Figure 6.1 (b)]. The flow velocity at the boundary between the plug flow domain and the shear layer is given by

$$v_p = v_0 \left[ 1 - \left( \frac{2(h/2 - \delta)}{h} \right)^2 \right] \quad (6.3)$$

and  $v_p$  corresponds to the velocity of the plug flow. Therefore, the average velocity in the cross-section in Figure 6.1 (b) is expressed as

$$\bar{v} = v_0 \left[ \frac{16\delta^3}{3h^3} - \frac{8\delta^2}{h^2} + \frac{4\delta}{h} \right] \quad (6.4)$$

Expressing  $v_0$  from Eq. (6.4), one can rearrange Eq. (6.2) to the following form

$$\delta = \frac{h}{2} - \frac{\tau_0 h^2 \left[ 16\delta^3 / 3h^3 - 8\delta^2 / h^2 + 4\delta / h \right]}{8\mu\bar{v}} \quad (6.5)$$

With the other parameters known from the experiment (see below), this is a cubic equation for  $\delta$ . Of the three possible solutions, two would be complex, and thus unphysical, while only one real and physical. It is emphasized that according to Eq. (6.5), the ratio  $\delta/h$  depends on the Bingham number  $Bn = \tau_0 h / \mu\bar{v}$ .

The velocity  $v=da/dt$ , where  $a$  is the radius of the sample disk in squeezing (the area  $A=\pi a^2$ ). The velocity  $v$  varies during the squeezing process. For the estimates based on Eq. (6.5),

we use the average velocity value:  $\bar{v} = T^{-1} \int_0^T (da/dt) dt = (a_T - a_0) / T$ , where  $a_0$  and  $a_T$  are the

initial and “final” radii (the latter one corresponds to  $t=T$ , the averaging period). The calculations showed that the sensitivity of the dependence of  $2\delta/h$  on time to the  $\pm 10\%$  variation in the value of the velocity is relatively small during the entire squeezing process and especially in the domain corresponding to the maximum slopes of the dependences  $A(t)$  discussed below.

Bingham plastics in squeeze flow should experience significant normal stresses  $\sigma_{xx}$  and  $\sigma_{yy}$  (in the compression and spreading directions, respectively), which affect their resistance to deformation. Covey and Stanmore (1981) and several following works reduced them both to  $-p$  alone (with  $p$  being pressure), i.e. completely neglected the deviatoric normal stresses. For thick enough samples as those of interest in the present work, the effect of these normal deviatoric stresses on the process dynamics can be more significant than that of the shear stress  $\sigma_{xy}$  responsible for Eq. (6.1) for Newtonian fluids (as is shown below). Therefore, dealing with

squeeze flows of the Herschel-Bulkley materials in this section, we neglect the effect of the shear layers of the thickness  $\delta$  adjacent to the disks and consider quasi-one-dimensional compression/spreading of a cylindrical sample. The coordinate system is sketched in Figure 6.2, with the  $x$  axis being parallel to the squeeze direction, and the  $y$  axis being radial (as in Figure 6.1).

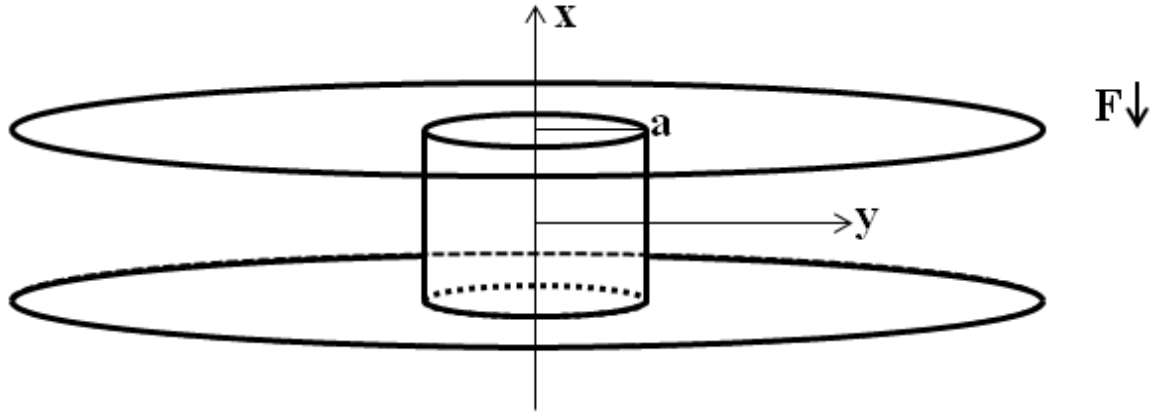


**Figure 6.2.** Sketch of a sample with the coordinate axes.

The origin of the coordinate axes is taken at the sample center of mass. Following [Yarin (1993)], the normal stresses in the  $x$  and  $y$  directions become

$$\sigma_{yy} = -p + \tau_{yy} = 0 \quad (6.6)$$

$$\sigma_{xx} = -p + \tau_{xx} \quad (6.7)$$

where  $\tau_{xx}$  and  $\tau_{yy}$  are the deviatoric normal stresses.

Note that the  $x$  coordinate is used for the compression direction, and the  $y$  coordinate for any radial direction in this axisymmetric case. If one considers the  $z$ - Cartesian coordinate axis normal to the  $x$  and  $y$  coordinate axes, the results for  $\sigma_{zz}$  and  $\tau_{zz}$  will be exactly equal to those for  $\sigma_{yy}$  and  $\tau_{yy}$ , respectively, due to the axial symmetry. If one denotes the unit vectors of the  $x$ ,  $y$  and  $z$  directions as  $\mathbf{i}$ ,  $\mathbf{j}$  and  $\mathbf{k}$ , respectively, and the unit vectors of the radial and azimuthal

directions in the sample cross-section in the  $yz$  plane as  $\mathbf{e}_r$  and  $\mathbf{e}_\theta$ , respectively, it is easy to see that, for example, the deviatoric stress tensor  $\boldsymbol{\tau} = \mathbf{ii}\tau_{xx} + (\mathbf{jj} + \mathbf{kk})\tau_{yy} = \mathbf{ii}\tau_{xx} + (\mathbf{e}_r\mathbf{e}_r + \mathbf{e}_\theta\mathbf{e}_\theta)\tau_{yy}$ . The latter shows that in the present case  $\tau_{rr} = \tau_{\theta\theta} = \tau_{yy} = \tau_{zz}$ .

It is emphasized that the total radial stress in Eq. (6.6) vanishes due to the boundary condition at the sample surface where zero tractions are imposed, since surface tension is typically negligible. Equation (6.6) allows one to find the pressure as  $-p = -\tau_{yy}$  and thus Eq. (6.7) yields

$$\sigma_{xx} = \tau_{xx} - \tau_{yy} \quad (6.8)$$

The compression rate is equal to  $\partial V / \partial x < 0$  where  $V$  is the axial velocity of the sample elements in the compression direction. When the Herschel-Bulkley materials undergo deformation, they flow as power-law fluids. Moreover, if the stresses are much larger than the yield stress  $Y$ , which is the case in squeezing, or the shear stress is sufficiently large compared to  $\tau_0$  to break the internal structure and impose flow in the orthogonal direction as in Ovarlez et al. (2010), one has

$$\tau_{xx} = 2K3^{(n-1)/2} \left| \frac{\partial V}{\partial x} \right|^n \operatorname{sgn} \left( \frac{\partial V}{\partial x} \right) \quad (6.9)$$

$$\tau_{yy} = -K3^{(n-1)/2} \left| \frac{\partial V}{\partial x} \right|^n \operatorname{sgn} \left( \frac{\partial V}{\partial x} \right) \quad (6.10)$$

Combining Eqs. (6.8)-(6.10), we arrive at

$$\sigma_{xx} = K3^{(n+1)/2} \left| \frac{\partial V}{\partial x} \right|^n \operatorname{sgn} \left( \frac{\partial V}{\partial x} \right) \quad (6.11)$$

The force balance at the sample interface with the disk yields

$$\sigma_{xx} \pi a^2 = -mg \quad (6.12)$$

where the squeeze force  $F$  is assumed to be equal to the overall weight of the upper disk with the added masses, as in the present experiments, i.e.  $F=mg$ , with  $m$  being the overall mass and  $g$  gravity acceleration. Also,  $a$  is the sample cross-sectional radius.

Substituting Eq. (6.11) into Eq. (6.12), we arrive at

$$K3^{(n+1)/2} \left| \frac{\partial V}{\partial x} \right|^n \pi a^2 = mg \quad (6.13)$$

where the fact that  $\text{sgn}(\partial V / \partial x) = -1$  in squeeze flow.

In addition, the continuity equation expressing mass conservation and the incompressibility of the sample yields [Yarin (1993)]

$$\frac{\partial a^2}{\partial t} + \frac{\partial Va^2}{\partial x} = 0 \quad (6.14)$$

In the present case the sample stays approximately cylindrical during the entire squeeze test. Therefore, its cross-sectional radius  $a$  does not depend on  $x$ , and Eq. (6.14) reduces to

$$\frac{\partial V}{\partial x} = -\frac{2}{a} \frac{da}{dt} \quad (6.15)$$

Substituting Eq. (6.15) into Eq. (6.13), we obtain

$$3^{(n+1)/2} 2^n \pi K a^{(2-n)} \left( \frac{da}{dt} \right)^n = mg \quad (6.16)$$

The integration of Eq. (6.16) with the initial condition  $A = \pi a_0^2 = A_0$  at  $t = 0$  yields

$$A = A_0 \left[ 1 + \frac{(mg)^{1/n}}{3^{(n+1)/(2n)} n K^{1/n} A_0^{1/n}} t \right]^n \quad (6.17)$$

If  $n=1$  and  $K=\mu$ , Eq. (6.17) reduces to

$$A = A_0 + \frac{mg}{3\mu} t \quad (6.18)$$

The main feature of Eq. (6.18), the linearity of the dependence of the cross-sectional area  $A$  on time  $t$ , is determined exclusively by the normal deviatoric stresses. This result is drastically different from the nonlinear Eq. (6.1) which is determined exclusively by shear stresses.

At the fast stage of sample deformation where the resistance to flow is mostly viscous, the rate of the radial elongation  $\dot{\gamma}_{\text{elong fast}}$  is in the range  $20\text{-}30\text{ s}^{-1}$ , as the results listed in Table 6.6 below reveal. On the other hand, at the second slow stage of sample deformation where the resistance to flow is mostly due to the yield stress, the rate of the radial elongation  $\dot{\gamma}_{\text{elong slow}}$  is in the range  $0.075\text{-}0.33\text{ s}^{-1}$  (cf. Table 6.6). In addition, the shear rate in the shear layers near the disks  $\dot{\gamma}_{\text{shear}}$  is of the order of  $37\text{ s}^{-1}\text{-}64\text{ s}^{-1}$  (Table 6.6). This shows that at the fast deformation stage the elongation and shear rates are of the same order.

## **6.3 Experimental Materials and Apparatus**

### **6.3.1 Materials**

Super-high viscosity Silicone oils of two different viscosities ( $1000\text{ Pa s}$  and  $2500\text{ Pa s}$ ) were obtained from Clearco Products Co., Inc. Bentonite powder (100% pure clay) was obtained from Nutrition for Optimal Wellness (NOW). Carbopol ETD 2050 polymer was generously donated by Lubrizol. Pylakrome Black LX 7828 dye used to color the Silicone oil and Carbopol solutions was generously donated by Pylam Products Company Inc. NaOH was obtained from Sigma Aldrich.

### **6.3.2 Preparations of Solutions and Dispersions**

Carbopol 1 and 3 wt% solutions (denoted as C1 and C3, respectively) were prepared by adding Carbopol ETD 2050 polymer into de-ionized water. The solutions were left under

continuous stirring overnight at 50 °C. 2 or 4% of NaOH was then added to the Carbopol solutions. A negligible amount of black dye was added to the Carbopol solution to change the color from clear to black for the proper visualization. Bentonite 10 wt% dispersions (denoted as B10) were prepared by adding Bentonite powder into de-ionized water under continuous stirring, which prevented clumping and agglomeration. These dispersions were then stirred by magnetic stirrer for several hours and then kept for 72 hours to ensure complete hydration of clay particles.

### **6.3.3 Flow Curves in Simple Shear**

The flow curves of the Carbopol solutions C1 and C3 and Bentonite dispersion B10 were measured using DHR-2 (TA Instruments) shear viscometer. This viscometer allows measurements of viscosity in different configurations. In the present work, a vane tool, as well as parallel-plate geometry was employed. The vane tool had four rectangular blades that protrude from a cylinder to create an outer diameter of 2.80 cm. It was positioned inside a cup that had an inner diameter of 3.02 cm. Each fin of the vane had a height of 4.22 cm, protruded from the inner cylinder by 1.00 cm, and had an outer edge thickness of 0.12 cm which increased to 0.20 cm where it connects to the inner cylinder. The parallel-plate diameter was 4.00 cm. The vane tool was calibrated using standard Silicone oil (Brookfield Eng.) with the viscosity of 0.498 Pa s. To calibrate the vane tool the fluid was tested at several shear rates, and then a calibration factor in the software was adjusted accordingly. The shear strain rate was ramped up from 1 s<sup>-1</sup> to 200 s<sup>-1</sup> and held constant at each speed for 20 s in all the experiments. The shear rate for the vane tool was calculated as  $\dot{\gamma} = \omega(R_0 + R_i)(R_0 - R_i)^{-1} / 2$ , where  $\omega$  is the angular velocity,  $R_0$  is the outer radius, and  $R_i$  is the inner radius.



### **6.3.4 Experimental Setup for Strong and Weak Squeeze Flow**

The experimental setup used to squeeze constant volume samples is shown schematically in Figure 6.3 (a) and as an image in Figure 6.3 (b). Solution and dispersion samples were deposited on the transparent polystyrene disk which is the bottom plate of the squeezing apparatus. A 10 ml cylindrical sample was dispensed using a 60 ml syringe (with the tip removed), and a guide was designed to dispense the sample at the center of the bottom disk. The initial height of the sample  $h_0$  was almost equal to its radius. The sample initial radius  $a_0$  varied from 1.5 to 1.8 cm. The final sample height and radius were  $h_f \approx 0.3$  cm and  $a_f \approx 3$  cm, while both disks radii were 10 cm. During the entire squeezing process the ratio  $h/R$  was approximately of the order of one. Under such conditions the elongational component of resistance to flow can never be neglected compared to the shear one [cf. Meeten (2002)].

The top disk of a known mass was coaxially suspended over the sample at a height of about 0.8 cm using the solenoid-triggered fixtures. Additional masses could be added to the top disk to increase the squeezing force, which was equal to the overall weight of the top disk with the added masses in these experiments. A high speed camera (RedLake Motion Pro) placed beneath the bottom disk recorded sample spreading when they were squeezed by the top disk. Even though some initial imperfections in the samples could be present, with their initial cross-section not being perfectly circular, the experiments showed that during squeezing the samples almost immediately acquired circular cross-sectional shape (see the sequences of the images in Figure 6.8). Therefore, processing of the experimental data was done under the assumption of a perfectly circular cross-section, while the high-speed camera was used to measure variation of its radius in time.

The polystyrene disks had scratches on them due to being wiped with a paper towel during cleaning. Using an optical microscope with  $100\times$  zoom, it was determined that there exist less than 5 scratches on each plate with a depth of approximately of  $5\ \mu\text{m}$  and many ( $>50$ ) scratches with a depth less than  $1\ \mu\text{m}$ .

When the solenoid-triggered fixtures were released by an electric signal, the sample was squeezed by the weight of the top disk with the attached masses. The sample was compressed by the disk falling from about  $0.8\ \text{cm}$  with the speed of  $40\ \text{cm/s}$ , and its radial spreading was recorded by the CCD camera. This process is denoted as strong squeeze flow in the present work, and it consists of two stages: fast spreading, and the following slow spreading. The data acquired at the fast spreading stage was used to determine the effective viscosity. In addition, weak squeeze flows were realized when a mass load was softly released manually to avoid any impact at the beginning of compression. The data acquired during the weak squeeze flow was used to determine the yield stress of the samples.

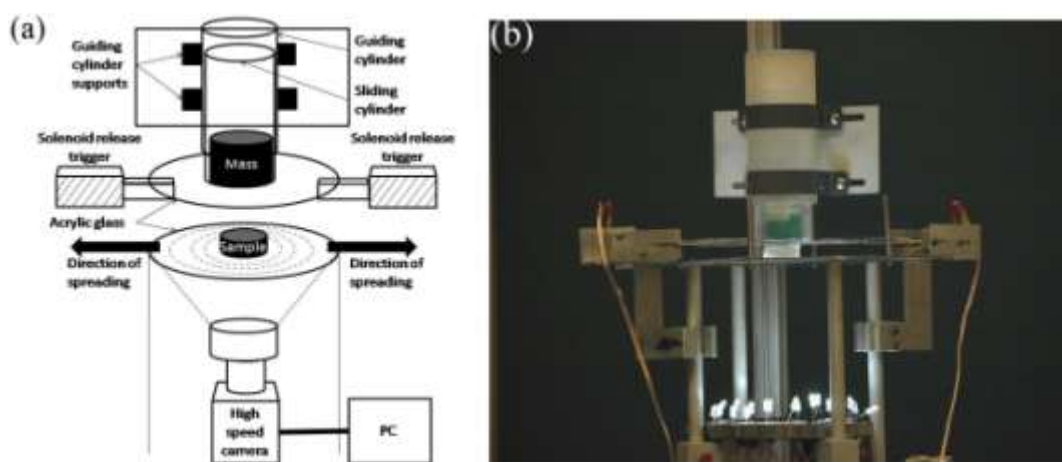


**Figure 6.3.** The experimental setup: (a) schematic, (b) image of the squeezing apparatus.

## **6.4 Experimental Results and Discussion**

### **6.4.1 Flow Curves of Carbopol Solution and Bentonite Clay Dispersion in Simple Shear**

The as-prepared Carbopol solutions C1 and C3 were originally acidic. Then, 2 or 4% NaOH solution was added to the Carbopol solutions. It is known that viscosity of Carbopol solutions increases as pH increases up to 7, whereas beyond this value viscosity decreases as the solutions become excessively basic. Viscosities of two different Carbopol solutions at different pH were measured using both vane and parallel-plate geometries. A 1% Carbopol solution C1 and a 3% Carbopol solution C3 with either 2% or 4% concentration of NaOH were used. The pH values of each solution are shown in Table 6.1. The flow curves of these solutions obtained using vane and parallel-plate geometries are shown in Figures 6.4 (a) and 6.4 (b).

**Table 6.1.** pH of several Carbopol solutions with NaOH added.

	C1	C1 & 2% NaOH	C1 & 4% NaOH	C3	C3 & 2% NaOH	C3 & 4% NaOH
pH	2.4	3.9	4.9	2.4	3.0	3.8

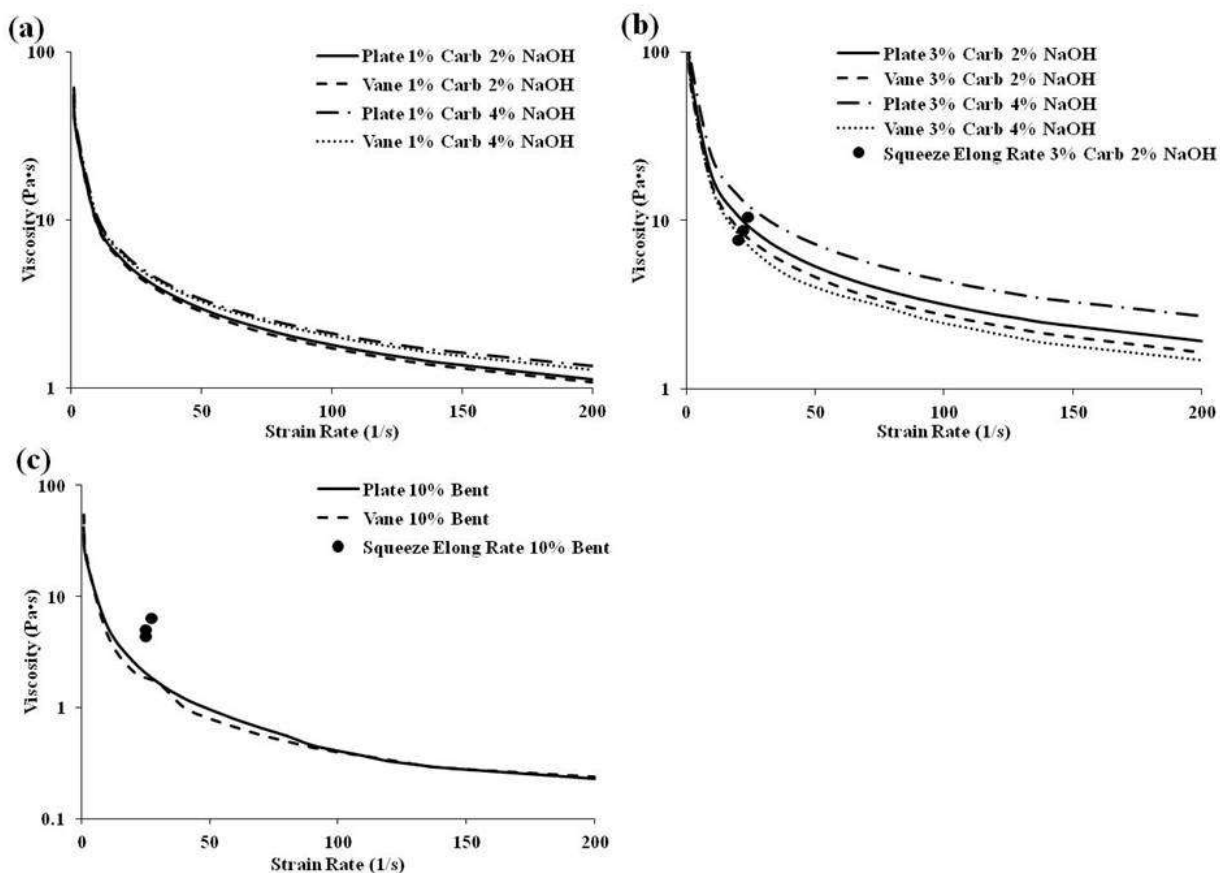


**Figure 6.4.** (a) Flow curves of Carbopol solution C1 at two different concentrations of NaOH. Parallel-plate viscometer: 2% NaOH (solid line) and 4% NaOH (dash-dotted line). Vane viscometer: 2% NaOH (dashed line) and 4% NaOH (dotted line). All lines are practically indistinguishable in this graph. (b) Flow curves of Carbopol solution C3 at two different concentrations of NaOH. Parallel-plate viscometer: 2% NaOH (solid line) and 4% NaOH (dash-dotted line). Vane viscometer: 2% NaOH (dashed line) and 4% NaOH (dotted line). In panel (b) the viscosity values measured in strong squeeze flow of C3 with 2% NaOH (symbols) are superimposed using the same strain rate axis for both shear rate in simple shear and the uniaxial elongation in the radial direction in squeezing. (c) Flow curves of Bentonite dispersion B10. Parallel-plate viscometer: (solid line), vane viscometer (dashed line). In panel (c) the viscosity

values measured in strong squeeze flow of B10 (symbols) are superimposed using the same strain rate axis for the shear rate in simple shear and the uniaxial elongation in the radial direction in squeezing.

The results in Figure 6.4 (a) show that the flow curves for C1 do not depend on pH and do not differ between the results obtained in the vane or parallel-plate geometries. The flow curves for solution C3 in Figure 6.4 (b) show that an increase in pH results in a slight increase in viscosity measured using the parallel-plate viscometer. On the contrary, when the vane viscometer is used, the results demonstrate that an increase in pH results in a decrease in the viscosity. The latter is most probably an experimental artifact attributed to the bubbles present in the solution. It is emphasized that during preparation of Carbopol solutions air is entrapped due to stirring. It is difficult to prevent air entrapment or remove the entrapped air. The increase in Carbopol concentration also increases the viscosity value, especially at lower shear strain rates. The flow curves measured for Bentonite B10 dispersion are shown in Figure 6.4 (c).

It is remarkable to see that in general the flow curves measured using the parallel-plate and vane geometries are in good agreement in Figures 6.4 (a) - 6.4 (c). The flow curves in Figures 6.4 (a) – 6.4 (c) show a significant shear-thinning at relatively low shear rates approximately in the strain rate range  $\dot{\gamma}_{\text{shear}} \leq 10 \text{ s}^{-1}$ . In this range fitting the flow curves using a rheological constitutive equation with a variable effective viscosity is appropriate. On the other hand, in the higher shear rate range  $\dot{\gamma}_{\text{shear}} > 10 \text{ s}^{-1}$  variation of the shear viscosity of Carbopol solutions C1 and C3 and Bentonite dispersion B10 in Figures 6.4 (a) – 6.4 (c) is insignificant and the material behavior in such shear flows can be considered as the one with a constant viscosity. Note, that the fast deformation stage of strong squeezing and the shear layers corresponding to it

demonstrate the strain rates higher than  $10 \text{ s}^{-1}$ ; cf. the end of section II and section IVD. It is also emphasized that during the fast deformation stage of strong squeezing the normal and shear stresses are significantly higher than the yield stress, as the results obtained in the following sections show, therefore the yield stress influence can be completely disregarded.

#### **6.4.2 Squeeze Flow of Pure Newtonian Materials: Silicone Oils**

Two types of super-high viscosity Silicone oil of different viscosities, 1000 Pa s and 2500 Pa s (denoted S1 and S2.5, respectively), which behave as standard Newtonian materials below the critical shear rates of  $1.5 \text{ s}^{-1}$  and  $0.5 \text{ s}^{-1}$ , respectively, were tested using the squeezing apparatus. Squeeze flow experiments were conducted with these materials under three squeezing loads of 165 g, 305 g and 465 g. Figure 6.5 (a) presents the deformation curves for the area  $A$  versus time  $t$  measured for S1 for three different squeezing loads. Though the initial area of S1 samples in each case was the same, the final area of squeezing at the end of recording time was larger for a larger load. To highlight the Newtonian behavior of the Silicone oils, Figure 6.5 (b) depicts the  $A^4(t)$  dependences for S1 corresponding to the data shown in Figure 6.5 (a). The  $A^4(t)$  dependences for S1 appear to be approximately straight lines, in agreement with Eq. (6.1). A similar set of squeeze experiments was conducted with S2.5 oil. Figure 6.6 (a) shows the deformation curves for the dependence of the area  $A$  on  $t$  for S2.5 and the corresponding  $A^4(t)$  dependences are shown in Figure 6.6 (b). The latter are linear, which signifies the Newtonian behavior. Moreover, both S1 and S2.5 continue to spread even after 45 min of recording time, which further substantiates their Newtonian behavior.

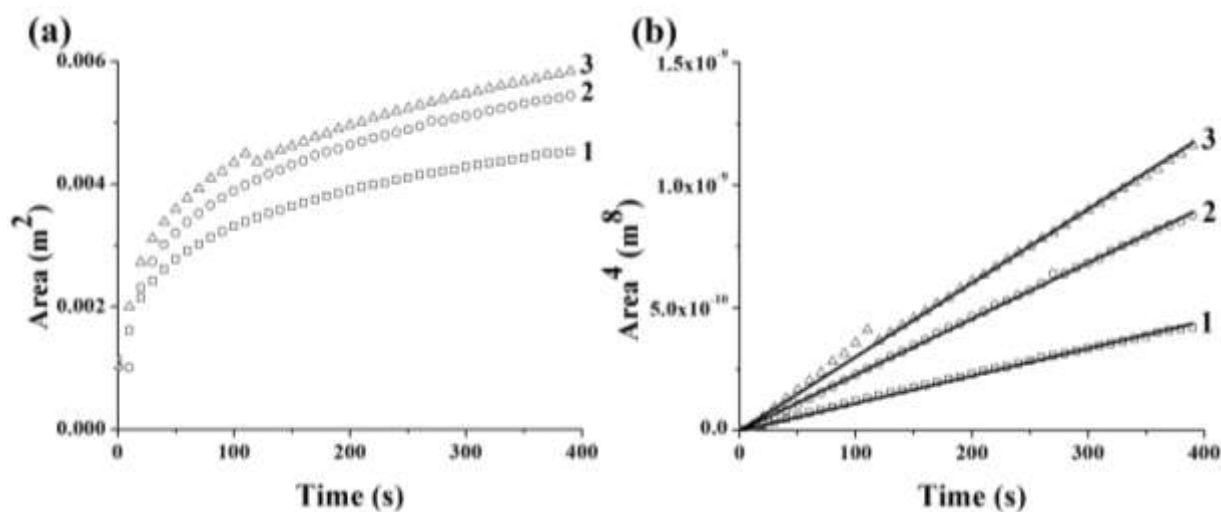


**Figure 6.5.** Typical deformation curves: (a) Area  $A$  versus time  $t$ , and (b) the corresponding  $A^4(t)$  dependences for S1. Curves 1 correspond to 165 g, 2-to 305 g, and 3-to 465 g.

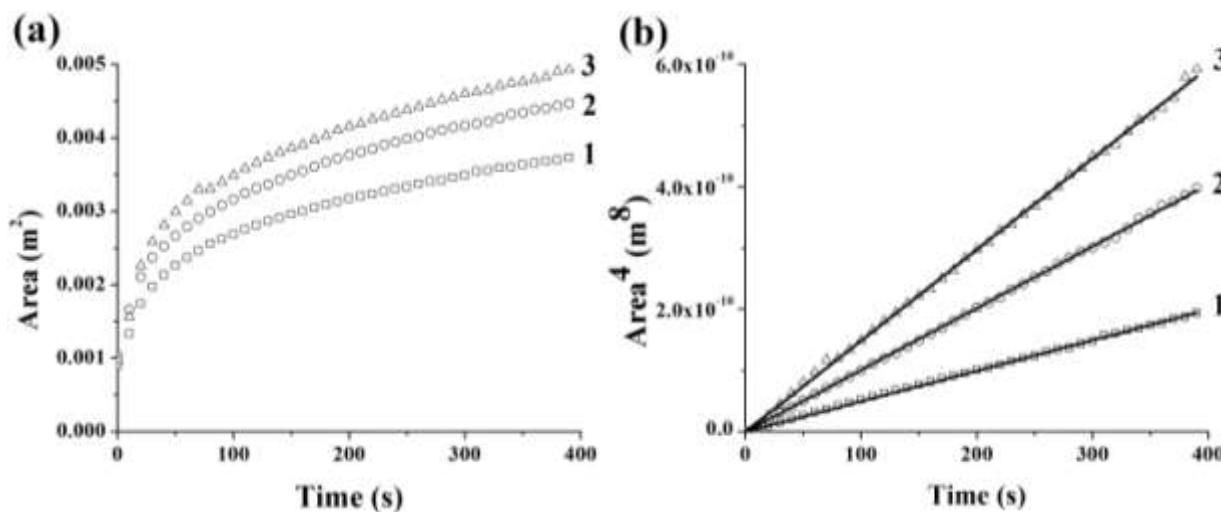


**Figure 6.6.** Typical deformation curves: (a) Area  $A$  versus time  $t$ , and (b) the corresponding  $A^4(t)$  dependences for S2.5. Curves 1 correspond to 165 g, 2-to 305 g, and 3-to 465 g.

The viscosities of the Silicone oils evaluated from the slope of the  $A^4(t)$  dependences in Figures 6.5 (b) and 6.6 (b) are given in Table 6.2. The values correspond to the average of two

separate trials. The viscosity values obtained from squeezing the Silicone oils are in a fairly good agreement with the viscosity values reported by the manufacturer of these oils (cf. Table 6.2 and Figure 6.7).

**Table 6.2.** Viscosity of the Silicone oils measured in the squeeze experiments vs. standard values. The viscosity values listed are the averages of two trials.

Type of oil (standard viscosity)	Squeezing mass (g)	Viscosity (Pa s)
S1 (1000 Pa s)	165	1057
	305	1036
	465	1090
S2.5 (2500 Pa s)	165	2502
	305	2476
	465	2286

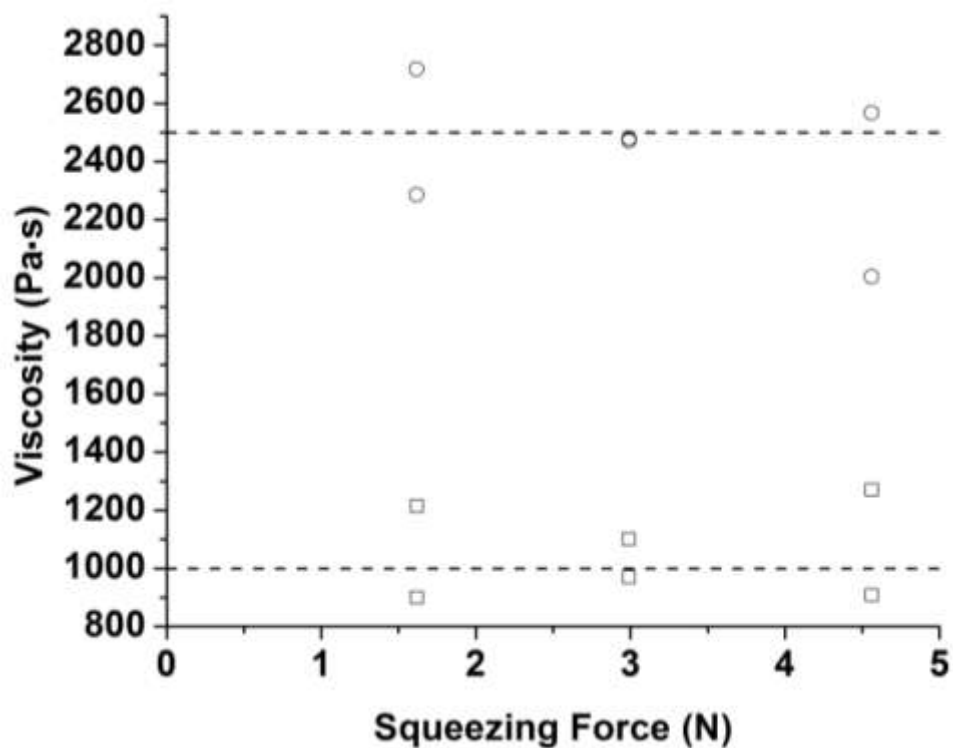


**Figure 6.7.** Viscosity obtained from the squeeze flows of S1 (squares) and S2.5 (circles). Horizontal dashed lines depict the viscosity values provided by the manufacturer of these oils.



### **6.4.3 Squeeze Flow of Carbopol Solution C3 and Bentonite Dispersion B10: No-Slip**

#### **Conditions**

Squeeze flows of different complex solutions and suspensions can produce a significant slip in some cases [Meeten (2004b); Engmann et al. (2005); Divoux et al. (2012)]. To clarify the boundary conditions in strong squeeze flow of C3 and B10, a small pinch of water-insoluble black dye was sprinkled on the bottom surface of the sample before it was dispensed onto the transparent lower disk of the squeezing apparatus. Although the excess dye was removed by blowing onto the sample, there were still some large aggregates present. Then, the sample was dispensed onto the bottom disk and subjected to strong squeezing, where the mass falls freely onto the sample. Both C3 and B10 were squeezed under mass loads of 230 g and 465 g, as represented in Figure 6.8. In each set of images, it is clear that the black dye aggregates embedded in the lower sample layer in contact with the wall stay at the same initial positions and do not move. These direct observations reveal that the no-slip condition holds for both C3 and B10 in the present experiments. It is emphasized that bigger aggregates protruding deeper into the sample can be smeared by the near-wall shear component of the flow which should not be confused with any slip. In addition, the initial circumference of the sample with a dye footprint is marked by the dashed circles in Figure 6.8 to visualize whether the dye particles move relative to the wall, if at all. It was found that the particles hardly cross these circles till the end of the squeezing process, which further confirms the fact that there is no slip at the lower disk.

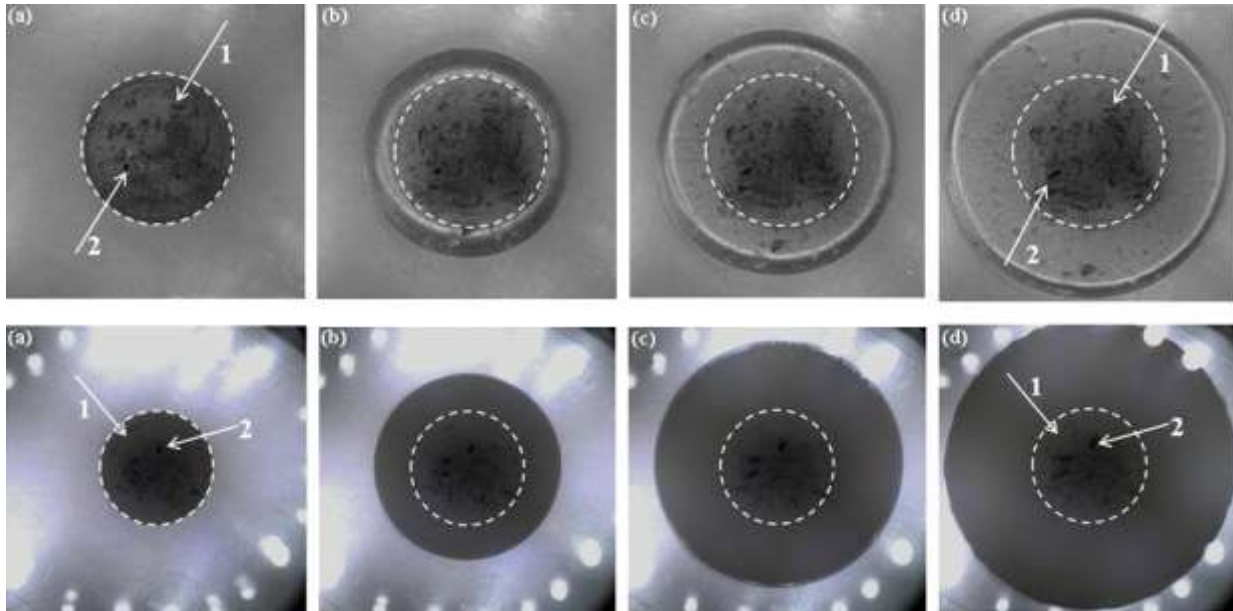


**Figure 6.8.** Upper row: Carbopol solution C3 being strong squeezed under a mass load of 230 g. Lower row: Bentonite dispersion B10 being strong squeezed under a mass load of 465 g. (a)  $t=0$ , (b) 32.5 ms, (c) 39 ms, (d) 45.5 ms. 1- The aggregate of black dye that did not move during the squeezing process. 2- The aggregate of black dye that was smeared because it was deeply embedded into the sample. The dashed circles correspond to the initial circumference of the samples of C3 (in the upper row) and B10 (in the lower row). In the upper row for C3 the bigger dark ring is created by incoming light from the light source being partially refracted due to the sample geometry. Therefore, the inner circumference of the dark ring represents where the material ceases to make contact with the top and bottom disks and the outer circumference represents the leading edge of the sample. In the lower row for B10 the outer circumference of the dark area corresponds to the leading edge of the sample. There is no dark ring in this case because the material is opaque.

#### **6.4.4 Squeeze Flow of Carbopol Solutions and Bentonite Dispersion**

Deformation of samples of Carbopol solutions and Bentonite dispersions, (C3 and B10, respectively) in the squeezing apparatus were studied next. Samples of C3 and B10 were dispensed onto the bottom polystyrene disk and then were squeezed by three squeezing loads of 230 g, 305 g, and 465 g. The sample area during squeezing of these materials was recorded in the same manner as for the Silicone oils. Deformation curves  $A(t)$  for C3 in weak squeezing are shown in Figure 6.9 (a). In particular, being squeezed by a mass of 465 g, C3 demonstrates a decrease in the rate of spreading at approximately  $t=750$  s. At this moment spreading has practically ceased and the sample area has not changed for the rest of the allotted time. It is emphasized that the time range of 400 s in Figure 6.9 (a) is shorter than the above-mentioned cessation of spreading. The latter is seen in Figure 6.11 (b) in the time range of 1500 s. Similarly, being squeezed with a mass of 305 g, spreading of C3 ceases at approximately 600 s [which is not seen in Figure 6.9 (a) with its time range of 400 s], while for 230 g spreading of C3 ceases in less than 15 s after the weight has been applied. The inset in Figure 6.9 (a) shows the deformation curves for the first 30 s of squeezing. This clearly shows that under a low load of 230 g, C3 has already stopped spreading, whereas under the higher loads the spreading continues for a while. The  $A^4(t)$  dependences for C3 dispersion, as shown in Figure 6.9 (b), do not result in straight lines, which clearly distinguish them from the Newtonian behavior corresponding to Eq. (6.1), in particular, from that of the Silicone oils. The results in Figure 6.9 clearly show that C3 possesses a yield stress, below which it does not undergo any further deformation and finally comes to rest completely.

Similarly, B10 was subjected to squeezing in the squeezing apparatus under the same loads as C3. The deformation curves for B10 in weak squeezing are shown in Figure 6.10 (a).

Under all the loads applied, the sample ceased spreading in about 10 s after the beginning of squeezing. To highlight the almost immediate response and flow cessation of the B10 dispersion, the inset in Figure 6.10 (a) shows the deformation curves for the first 30 s of squeezing. The  $A^4(t)$  curves for B10 corresponding to those in Figure 6.10 (a) are shown in Figure 6.10 (b). As in case of C3, the  $A^4(t)$  curves for B10 also differ from straight lines, which again signifies the non-Newtonian behavior of B10.

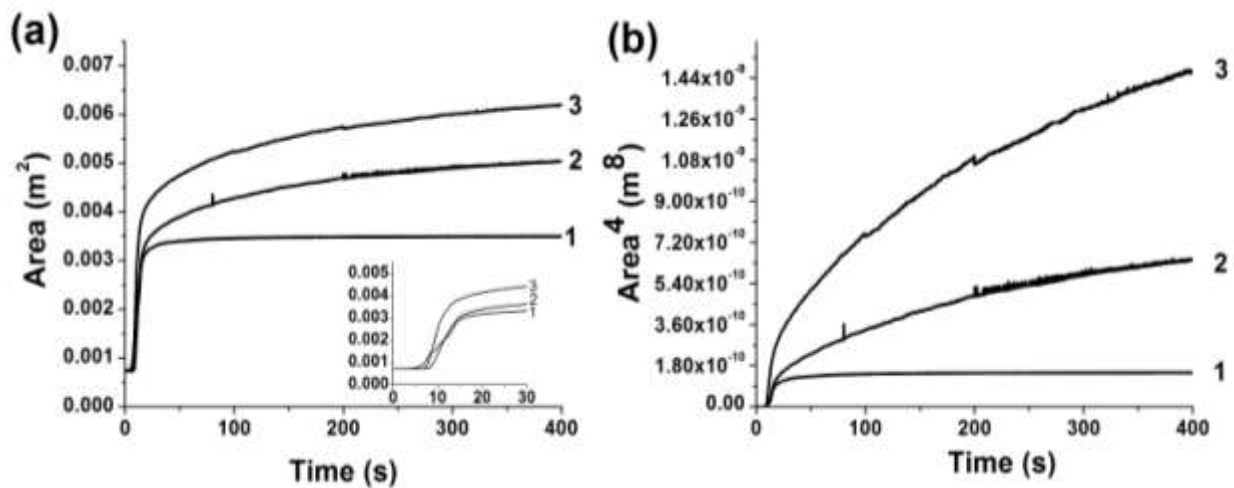


**Figure 6.9.** Typical deformation curves for C3. (a)  $A(t)$ , and (b) the corresponding  $A^4(t)$  dependences. Curves 1 correspond to 230 g, 2-to 305 g, and 3-to 465 g. The inset in panel (a) resolves the initial stage of sample spreading. Weak squeezing: the load was applied softly.

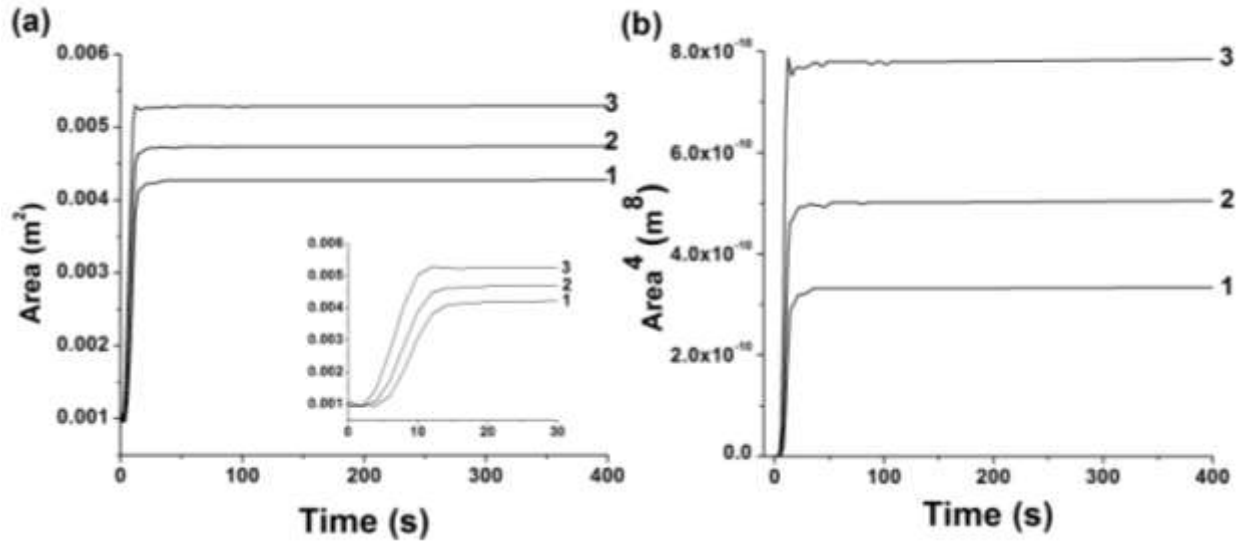


**Figure 6.10.** Typical deformation curves for B10. (a)  $A(t)$ , and (b) the corresponding  $A^4(t)$  dependences. Curves 1 correspond to 230 g, 2-to 305 g, and 3-to 465 g. The inset in panel (a) resolves the initial stage of sample spreading. Weak squeezing: the load was applied softly.

To compare different Bingham materials to Newtonian materials studied in the weak squeeze flows in the present work, Figure 6.11 shows the deformation curves for all materials used when squeezed with 465 g for the initial 1500 s of recording time. The cessation of spreading of C3 and B10 visible in Figure 6.11 (b) results from the yield stress. The long-time dynamics of these materials in squeeze flow is illustrated in Figure 6.11 (b). In Figure 6.11 (a), the abrupt increase in the sample area of C3 and B10 reveals significant differences in viscosity compared to those of the Silicone oils S1 and S2.5. Since C3 and B10 show similar initial slopes, it can be expected from Eq. (6.18) that their viscosities are of the same order and their viscosities are significantly lower than those of the Silicone oils. This conclusion is supported by the viscosity values discussed below. In Figure 6.11 (b) it is seen that the samples of C3 and B10 reached the spreading areas of the same order. Therefore, it is expected that their yield stresses

will be of the same order, which is also supported by the data discussed below. On the contrary, the Newtonian liquids (the Silicone oils), do not show any cessation of spreading, and thus do not possess any yield stress.

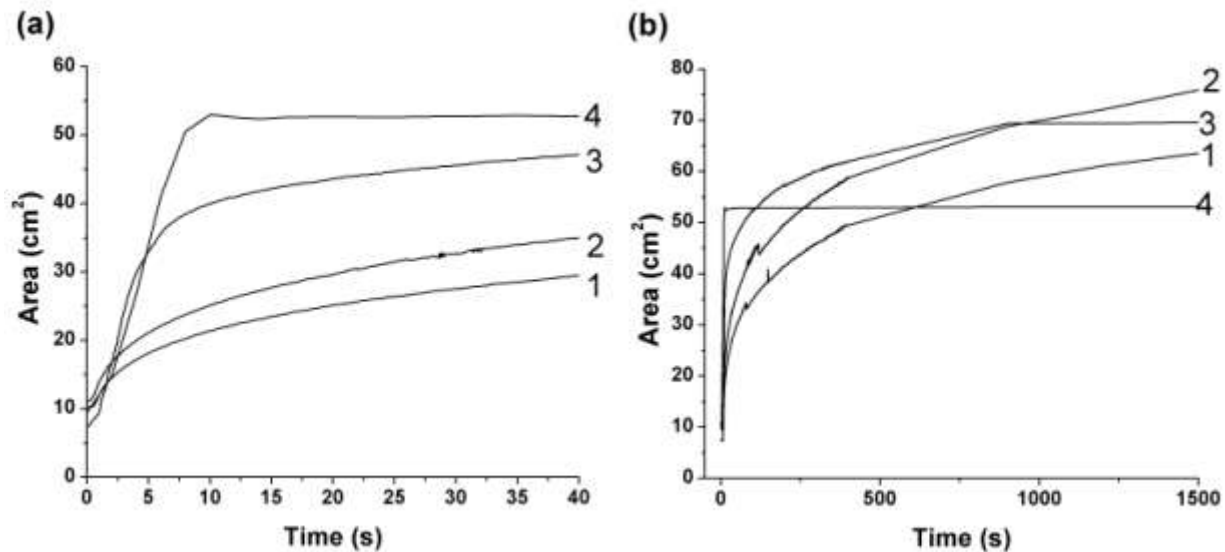


**Figure 6.11.** Comparison of deformation curve for Newtonian (S1, S2.5) and Bingham (C3 and B10) materials under a squeezing load of 465 g. (a) Short time evolution. (b) Longer time behavior. Curve 1-S2.5, 2-S1, 3-C3, and 4-B10. Weak squeezing: the load was applied softly.

The viscosity of the Bingham materials C3 and B10 in strong squeeze flows was then determined using Eq. (6.18) which implies that during the fast stage of such flows the viscous resistance to the elongation in the radial direction in the core is assumed to be dominant compared to the viscous shear resistance in the near-disk layers, which just provide lubrication. Figures 6.12 (a) and 6.12 (b) depict representative deformation curves for C3 and B10, respectively, under mass loads of 230 g, 305 g and 465 g. These dependencies were used to calculate numerically the first derivative of the area with respect to time. Its maximum value was

then used in the derivative of Eq. (6.18) to calculate the corresponding viscosity of the material. Figures 6.12 (a) and 6.12 (b) also show the straight lines tangent to the points of the maximum spreading rate of curves 3, which were used in the derivative of Eq. (6.18) to find the viscosity values. The values of viscosities of C3 and B10 found under different loads are presented in Table 6.3.

**Table 6.3.** Viscosity  $\mu$  and the characteristic time  $\tau_c$  for Carbopol solution C3 and Bentonite dispersion B10 established in strong squeeze experiments. The characteristic time  $\tau_c$ , which is affected not only by the viscous forces but also by the yield stress, is introduced in Eqs. (6.19) and (6.20).

Material	Load (g)	Viscosity (Pa s)	$\tau_c$ (s)
C3	230	7.7	0.00241
	305	8.8	0.00415
	465	10.5	0.00253
B10	230	4.4	0.00362
	305	5.1	0.00502
	465	6.4	0.00545

It is seen that the viscosity values found for the same material under different loads are in fairly good agreement with each other. The mean values and standard deviations of the viscosity in the entire load range according to Table 6.3 are as following:  $\mu = 8.97 \pm 1.22$  Pa s for C3 and  $\mu = 5.30 \pm 0.97$  Pa s for B10. However, the viscosity slightly increases with load, which points at a moderate power-law-like behavior of C3 and B10 in squeeze flow.

If a rheological constitutive equation is absolutely true for a given material, the values of the rheological parameters should be invariant under any conditions and loads [as for example, viscosity of Newtonian liquids (e.g. water, some oils, etc.) is invariant whether it is measured in simple shear or uniaxial elongation flows]. The question is whether it is possible to diminish

rheological parameter variation for the same material found in squeezing under different loads applying the Herschel-Bulkley model. Fitting Eq. (6.17) based on this model to the experimental data for  $A(t)$  in strong squeeze flows, one can achieve practically the same data approximation, as in Figures 6.12 (a) and 6.12 (b) but with  $n=1.1$ ,  $K=5.83 \pm 0.72 \text{ Pa s}^n$  for C3 solution, and  $n=1.1$ ,  $K=3.42 \pm 0.58 \text{ Pa s}^n$  for B10 suspension. However, the power-law approximation does not allow for a better absolutely invariant parameter values than the Newtonian model in the high strain range corresponding to strong squeeze flows. Moreover, the approximation with  $n>1$  deviate from the slightly shear-thinning behavior in shear in the range of shear rates above  $10 \text{ s}^{-1}$  in Figures 6.4 (b) and 6.4 (c). This is similar to the contradiction observed, for example, for polymeric liquids, if a power-law constitutive is applied to them in shear and uniaxial elongation.

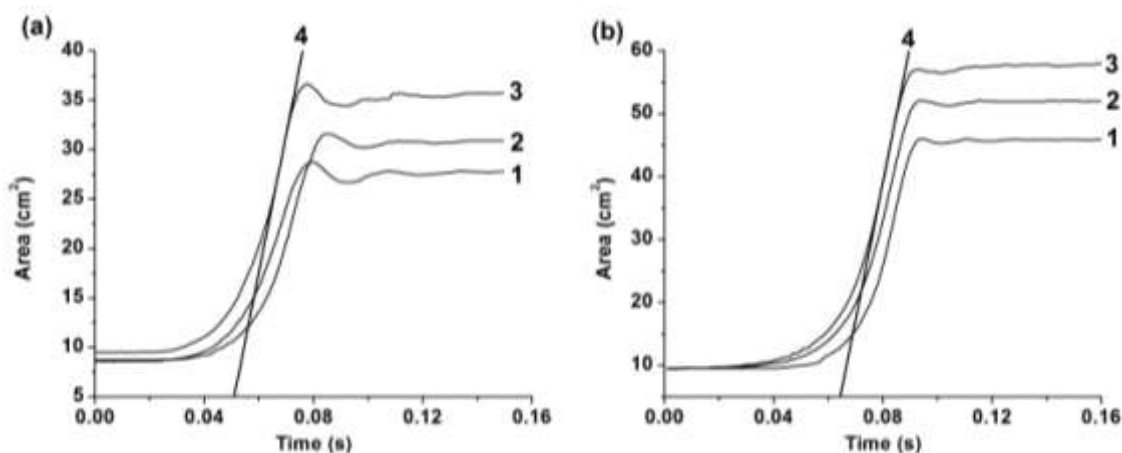


**Figure 6.12.** Typical deformation curves for (a) C3 and (b) B10 in strong squeezing. Curves 1- 230 g, 2-305 g, 3-465 g, and 4-the tangent line corresponding to the instant when the maximum rate of spreading occurs for curves 3.



At the moment when the spreading rate significantly slows down, the stress in the sample approximately has decreased to the level corresponding to the yield stress  $Y$ . The latter can be evaluated from the squeezing force and the area at which the spreading stops. To reveal accurate values of the yield stress from such observations, multiple sample sizes and mass loads were employed. The values of the yield stress found from the experimental data are listed in Table 6.4 for C3 and Table 6.5 for B10.

When squeezed samples become very thin (which means that the yield stress  $Y$  is relatively low), the sample circumferential shape can be significantly curved, so that the vertical cross-section reveals an arch of a relatively small radius of curvature at the sample edge. In such situations, surface tension from the circumference can contribute to the resistance to the sample spreading. This effect might be significant when the sample thickness decreases to the level of millimeter or less and can be evaluated using the Bond number  $Bo = \rho gh^2 / \gamma$  where  $\rho$  is density,  $g$  gravity acceleration,  $\gamma$  is the surface tension, and  $h$  is the sample thickness. As the major constituent of the solutions and dispersions used here was water, the surface tension could be roughly approximated as that of water. In addition, the densities of C3 and B10 are  $1 \text{ g/cm}^3$  and  $1.05 \text{ g/cm}^3$ , respectively. The effect of surface tension would be pronounced in the cases where  $Bo \ll 1$ . Since in the present experiments the Bond number at the final squeezing stage was of the order of 1, as Tables 6.4 and 6.5 show, the effect of surface tension on the values of  $Y$  was neglected. On the other hand, the fading oscillations in the dependence of  $A(t)$  at the beginning of the plateaus in Figures 6.12 (a) and 6.12 (b) can be attributed to the competition of the surface tension and the inertial effects damped by viscosity and the yield stress. Competition of the inertia with a restoring force is typically required for oscillations to set in. In the absence of

visible elastic effects, the restoring force can be associated with surface tension, especially due to the fact that the oscillations set in only when the gap is already small, as Figure 6.12 reveals.

**Table 6.4.** Experimental data for the yield stress of C3.

Mass load (g)	Sample volume (cm <sup>3</sup> )	Final area (cm <sup>2</sup> )	Bond number	Yield stress Y (Pa)
230	10	49.5	0.56	456
	10	52.5	0.49	430
	20	52.2	2.00	433
	25	60.8	2.30	371
305	10	61.2	0.36	489
	10	55.6	0.44	538
465	5	43.9	0.18	1038
	10	60.6	0.37	752
	10	61.5	0.36	742
	15	83.6	0.44	546

**Table 6.5.** Experimental data for the yield stress of B10.

Mass load (g)	Sample volume (cm <sup>3</sup> )	Final area (cm <sup>2</sup> )	Bond number	Yield stress Y (Pa)
165	15	28.3	3.83	572
	20	32.2	5.26	503
230	10	43.2	0.73	522
	10	40.3	0.84	561
	15	52.2	1.12	432
	20	60.2	1.5	375
305	10	47.5	0.60	630
	10	45.7	0.65	654
	15	60.9	0.83	491
465	10	53.1	0.48	860
	10	54.1	0.47	843
	15	69.1	0.64	661

It is seen in Tables 6.4 and 6.5 that the yield stress values found for the same material under different loads or using different sample sizes can differ, albeit on the same order. The mean values and standard deviations of the yield stress are as follows:  $Y = 579 \pm 206$  Pa for C3

and  $Y = 592 \pm 148$  Pa for B10. The corresponding values of  $\tau_0 = Y/3^{1/2}$  are  $\tau_0 = 334 \pm 119$  Pa for C3 and  $\tau_0 = 342 \pm 85$  Pa for B10. These values are close to the values of  $\tau_0$  measured for a number of different materials in squeeze flows in Meeten (2002, 2004a). Note also that for different types of Carbopol in solutions with different concentrations and pH the following values of the yield stress were reported:  $\tau_0 = 150$  Pa at 1 wt% and pH of 6 in Oppong et al. (2006),  $\tau_0 = 150$  Pa at 3 wt% and pH of 7 in Luu and Forterre (2009),  $\tau_0 = 26$  Pa at 1 wt% and pH of 7 in Divoux et al. (2012),  $\tau_0 = 30$  Pa at 2 wt% and pH of 4 in Lee et al. (2011). In addition, for a different Bentonite suspension of 15 wt% Luu and Forterre (2009) reported a yield stress of  $\tau_0 = 124$  Pa.

The shear layer thickness,  $\delta$ , for both C3 and B10 was evaluated for the entire strong squeezing process using Eq. (6.5) with the corresponding average values of the viscosity  $\mu$ , the yield stress  $\tau_0 = Y/3^{1/2}$ , and velocity  $\bar{v}$ , and  $h$  varying in time as in the strong squeezing experiments. It is seen in Figure 6.13 that the shear layer thickness evolves as the sample spreads. Initially, the shear layer thickness comprises 60-70% of the cross-section, therefore providing lubrication for the elongational spreading in the plug-flow zone. At the end of spreading, the shear layer thickness reaches above 90% of the cross-section, and the plug-flow zone dominated by the normal stresses effectively ceases to exist.

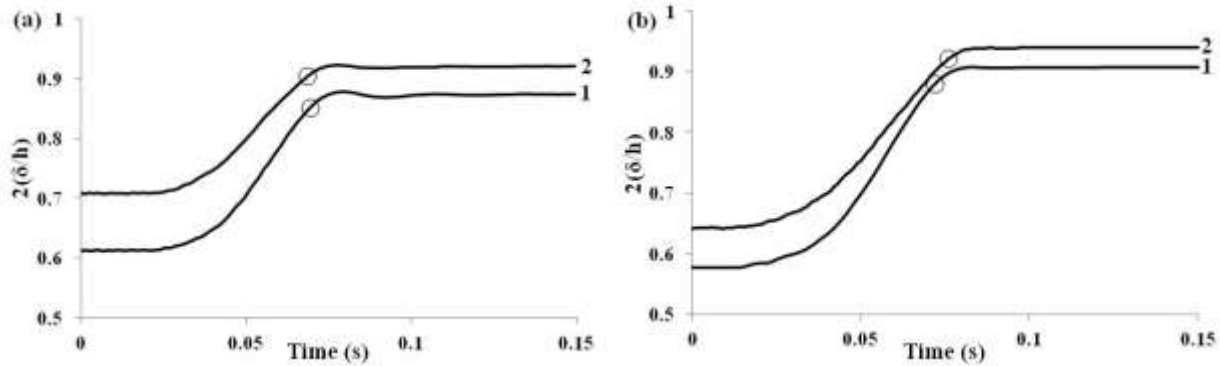


**Figure 6.13.** Shear layer thickness relative to the sample semi-thickness during the entire squeezing process for: (a) C3 solution, and (b) B10 dispersion. The mass load corresponding to curve 1 was 230 g, and to curve 2 - 465 g. The relative shear layer thicknesses corresponding to the maximum slopes of the dependences  $A(t)$  are designated by open circles.

After the fast spreading stage of strong squeeze flow is over, a much slower spreading continues [cf. Figures 6.12 (a) and 6.12 (b)]. The spreading rate at the slow second stage can be approximated as

$$\frac{dA}{dt} = \frac{A_{\max} - A}{\tau_c} \quad (6.19)$$

where  $\tau_c$  is the characteristic time which is now affected not only by the viscous forces but also by the yield stress, and  $A_{\max}$  is the ultimate (maximum) area corresponding to the restrictions imposed by the yield stress.

Integrating Eq. (6.19) from an area  $A_*$  at  $t=t_*$ , we obtain

$$A = A_{\max} + (A_* - A_{\max}) \exp\left(\frac{t_* - t}{\tau_c}\right) \quad (6.20)$$

Equation (6.20) was fitted to the experimental data for each mass load. The resulting values of the characteristic time,  $\tau_c$ , are listed in Table 6.3. Two resulting curves corresponding to Eq. (6.20) are shown in Figures 6.14 (a) and 6.14 (b) for C3 and B10, respectively.

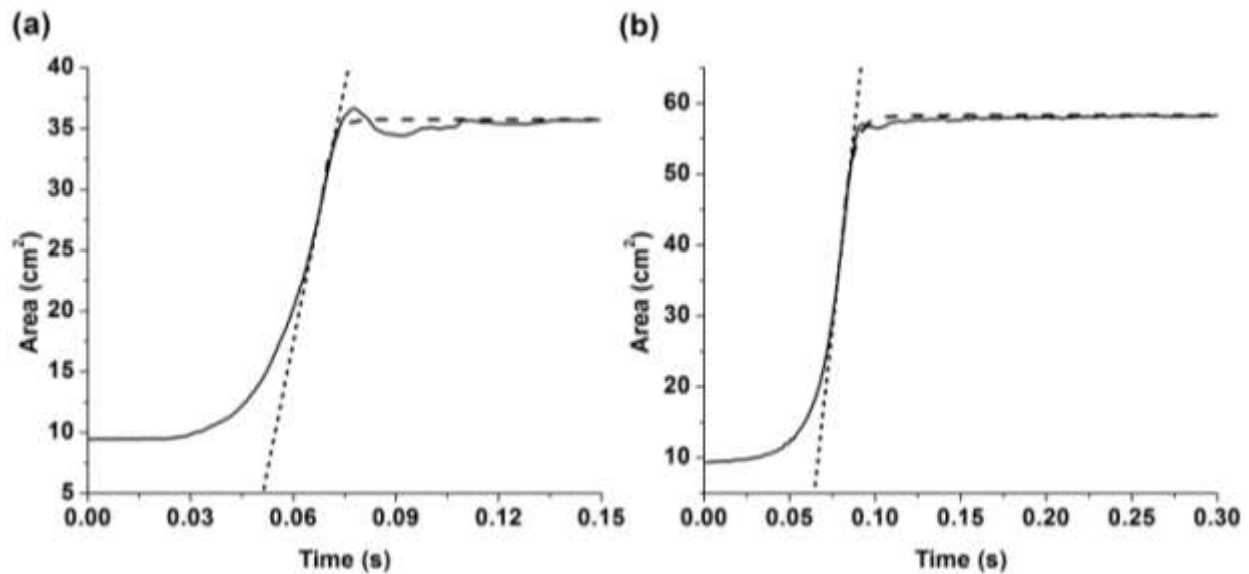


**Figure 6.14.** The experimental deformation curves with the cross-over asymptotics of Eqs. (6.18) and (6.20). (a) C3 and (b) B10 under a mass load of 465 g. The solid line depicts the experimental data, the short-dash line-Eq. (6.18), and the long-dash line-Eq. (6.20). The long-dash lines are plotted according to Eq. (6.20) with  $\tau_c=0.00253$  s for C3 and  $\tau_c=0.00545$  s for B10.

**Table 6.6.** Elongational strain rate during strong squeezing,  $\dot{\gamma}_{\text{elong fast}}$ , elongational strain rate at saturation,  $\dot{\gamma}_{\text{elong sat}}$  calculated using Eq. (6.21) and shear strain rate,  $\dot{\gamma}_{\text{shear}}$  established in squeezing experiments with C3 and B10.

Material	Load (g)	$t_{\text{cess}}$ (s)	$\dot{\gamma}_{\text{elong fast}}$ ( $\text{s}^{-1}$ )	$\dot{\gamma}_{\text{elong slow}}$ ( $\text{s}^{-1}$ )	$\dot{\gamma}_{\text{shear}}$ ( $\text{s}^{-1}$ )
C3	230	0.040	20	0.330	37
	305	0.045	22	0.290	37
	465	0.054	24	0.287	37
B10	230	0.022	25	0.075	64
	305	0.026	25	0.134	64
	465	0.033	27	0.211	64

Note that according to Eq. (6.18), the dependence of the area,  $A$ , on time can be approximated as  $A = mgt / 3\mu$ . The squeezing stress is expressed as  $\sigma_{xx} = mg/A$ . The cessation of the squeezing is expected when  $\sigma_{xx}$  will decrease (as  $A$  increases) to the level of the yield stress  $Y$ , which corresponds to the time moment  $t_{\text{cess}} = 3\mu / Y$ , which is roughly the duration of the strong squeezing process. The values of  $t_{\text{cess}}$  are shown in Table 6.6.

The elongational rate experienced by a material in squeeze flow is defined as

$$\dot{\gamma}_{\text{elong}} = (dA/dt) / 2A \quad (6.21)$$

Its values for the fast and slow (saturation) stages of the strong squeeze flow are listed in Table 6.7. At the fast stage of deformation,  $\dot{\gamma}_{\text{elong fast}}$  is in the range 20-30  $\text{s}^{-1}$  and at the slow stage  $\dot{\gamma}_{\text{elong slow}}$  is in the range 0.075-0.33  $\text{s}^{-1}$  for both C3 and B10 under all mass loads (cf. Table 6.6). On the other hand, the shear rate in the shear layers near the disks is of the order of  $\dot{\gamma}_{\text{shear}} \approx \tau_0 / \mu$ , which is approximately 37  $\text{s}^{-1}$  and 64  $\text{s}^{-1}$  when the overall average values of  $\mu$  and  $Y$  are used for

the estimate, for C3 and B10, respectively. It is seen that at the fast deformation stage the elongation and shear rates are of the same order (Table 6.6).

It is emphasized that in the squeeze flows corresponding to Figures 6.12 (a) and 6.12 (b) the ultimate spreading results from the yield stress being reached on the scale of  $10^{-2}$  s. For comparison, if the data from the experiments of Meeten (2004b) are used, the corresponding dependences  $A(t)$  saturate in about 20 s.

A comparison of the viscosity obtained from both the conventional viscometers and the squeezing apparatus was also investigated. Figure 6.4 (a) shows that the parallel-plate and vane viscometers revealed very close viscosity values at all shear rates for 1% Carbopol solution C1 with added 2 or 4% of NaOH. These viscometers, as well as the squeezing apparatus were also used to measure the viscosity of a 3% Carbopol solution C3 with 2% NaOH [Figure 6.4 (b)]. All three devices reveal a good agreement when the elongational strain rate during the fast stage of strong squeezing (Table 6.6) is superimposed with the shear strain rate axis. Then, the viscosity values are practically the same when found using the data for the fast strong squeezing and shear flows. The comparison for B10 revealed a similar pattern, albeit the squeezing data result in a bit higher viscosity values compared to the corresponding shear flow. On the contrary, the viscosity and shear rate values corresponding to weak squeeze flows of C3 and B10 in Figures 6.9-6.11, all belong to the rapidly rising branches in Figures 6.4 (a) and 6.4 (b). That behavior can be described only in the framework of the Herschel-Bulkley model. That is the reason that in the previous works on weak squeeze flows of non-Newtonian materials the results were attributed to the latter model, whereas the present results on strong squeeze flows can be rationalized in the framework of the Newtonian model (for the fast squeezing stage) and Bingham model for the slow squeezing stage. Moreover, in the strong squeeze flows the normal deviatoric stresses

determine the flow dynamics, whereas in the weak squeeze flows the dynamics is attributed to shear stresses, while the normal stresses are neglected.

#### **6.4.5 The Effects of Thixotropy**

The results obtained with the vane viscometer in shear flow with ramping shear rate up and down in the range 0 to 200 s<sup>-1</sup> revealed good repeatability of the measured values of shear viscosity of C3 and B10 over several ramping cycles, i.e. practically no signs of thixotropic behavior. This conclusion is also corroborated by the fact that at a constant shear rate both materials after a short transient sustained constant shear viscosity values for a long time.

In addition, after using a sandwich spreader to slowly (at approximately 1 rev/s) hand stir the solution for several minutes, samples of C3 and B10 were dispensed on 13 cm by 13 cm polystyrene sheets and covered by a plastic weighing dish. After resting for a time of 30 min, 60 min, 90 min, or 120 min, two samples were tested using the squeezing apparatus under mass loads of 230 g and 465 g. Then, the samples were tested in the squeezing device to measure viscosity. Practically no difference in viscosity was observed for different resting times. Also, no significant difference in the final spreading area was observed which shows that the yield stress is practically insignificantly affected by the resting time. Unfortunately, it was practically impossible to reuse the same sample in the squeezing device to determine whether repeated squeezing and the prior breakdown of the internal structure would have any effect on the rheological parameters.



## **6.5 Conclusion**

Strong squeeze flows of constant-volume samples of two yield-stress materials subjected to constant compressive force revealed that saturation resulting from the yield stress can be achieved on the scale of  $10^{-2}$  s, three orders of magnitude faster than in the previously reported weak squeeze flows. The results showed that the dynamics of the fast stage of the strong squeeze flows can be attributed to the normal deviatoric stresses, rather than to shear stresses. This is associated with the fact that in the present case sample heights in the compression direction are comparable with the cross-sectional radii throughout the entire squeezing process, and the samples were squeezed fast. Processing the data in the frameworks of the Bingham model, or a more general nonlinear Herschel-Bulkley model, revealed that the power-law nonlinearity after the flow sets in is not very significant. Therefore, the Bingham model was found to be a reasonable approximation and the corresponding viscosity and yield stress corresponding to the strong squeeze flows were measured. The comparison of the viscosity values measured in strong squeeze flow with those measured in the high-shear rate shear flows in parallel-plate and vane viscometers revealed a good agreement. On the other hand, viscosities determined in the weak squeeze experiments correspond to the nonlinear behavior previously attributed to the Herschel-Bulkley model. Neither shear, nor squeeze experiments reveal any significant effects of thixotropy.

The rheological responses of such materials as 3 wt% Carbopol solutions and 10 wt% Bentonite dispersions studied in the present work result from a number of complex factors and their reduction in the strong squeeze flows to a simplified Bingham model characterized by viscosity and yield stress should be considered only as a first approximation. For example, Bentonite, a clay material, is well known for its plate-like particles which can arrange in different

ways providing resistance to flow. Carbopol, on the other hand, is a gel-like material that acquires the yield stress due to the entanglement of long flocculated agglomerates. Such complex internal behavior has not been recast so far into a reliable micro-rheological model, which could replace the simplified, albeit very useful, phenomenological models.

## 7. RHEOLOGY OF JOINT MATERIALS

### **7.1 Introduction**

For this investigation, four joint compounds were presented for characterization, namely: a control compound (compound C), a compound with twice the amount of cellulose compared to the control compound (compound F), a compound containing no starch (compound E), and a compound with half the amount of clay compared to the control compound (compound K). Furthermore, the amount of water in each compound has also been adjusted so that each compound gives a similar torque measurement on the Visco-Corder (discussed later). Therefore, the main objectives of this investigation is to understand how different components affect the viscosity and yield stress, and reveal that the squeezing apparatus can distinguish between compounds when the Visco-Corder can not!

The theoretical background in section 7.2 restates the final result of the derivation in Chapter 6. The materials used and experimental details, apparatus and parameters employed, are described in Section 7.3. In Section 7.4 the results and discussion contain qualitative observations and measured quantitative parameters. The conclusion is in Section 7.5.

### **7.2 Theoretical Background**

In this study, the cylindrical sample placed between two disks was subjected to a constant force, while the approach velocity varies. The volume of the sample was constant between the disks. It was assumed that the viscous forces are dominating while the effect of inertia, surface tension and gravity is negligible.

The process was modeled as quasi one-dimensional squeezing as shown in Figure 7.1 and the dependence of area of the cylindrical sample during squeezing was found to be varying linearly with time as shown in Eq. (7.1). The derivation is in section 6.2.

$$A = A_0 + \frac{mg}{3\mu} t \quad (7.1)$$

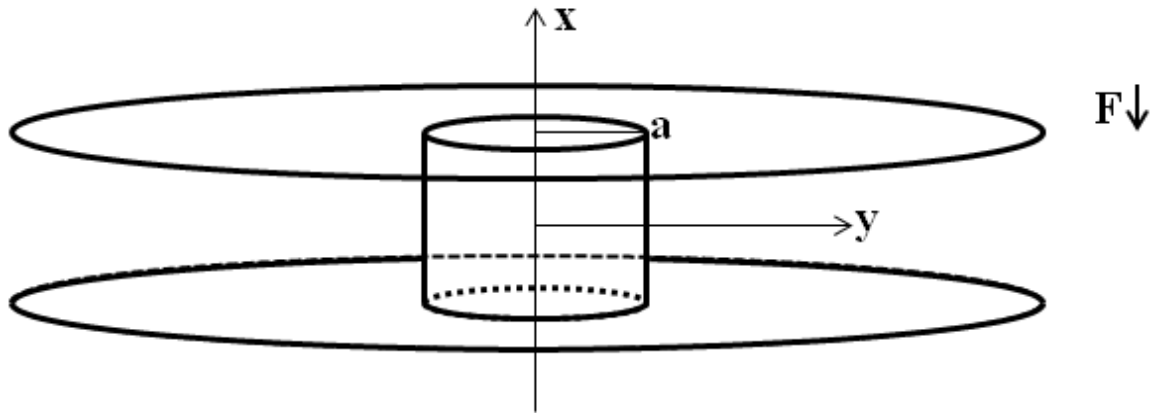


**Figure 7.1.** Sketch of a sample with the coordinate axes.

### **7.3 Experimental Setup**

#### **7.3.1 Experimental Apparatuses**

The experimental setup used to create squeeze flows of constant volume samples is shown schematically in Figures 7.2 (a) and 7.2 (b). A detailed description of the experimental set-up has been given in the previous report. USG's Visco-Corder and spindle, shown in Figures 7.2 (c) and 7.2 (d), uses a spring's resistance to measure the torque produced from fluid flow. During an experiment, a cup filled with fluid is fixed upon the steel platform and is rotated by a motor in the bottom of the machine while the spindle stays fixed.

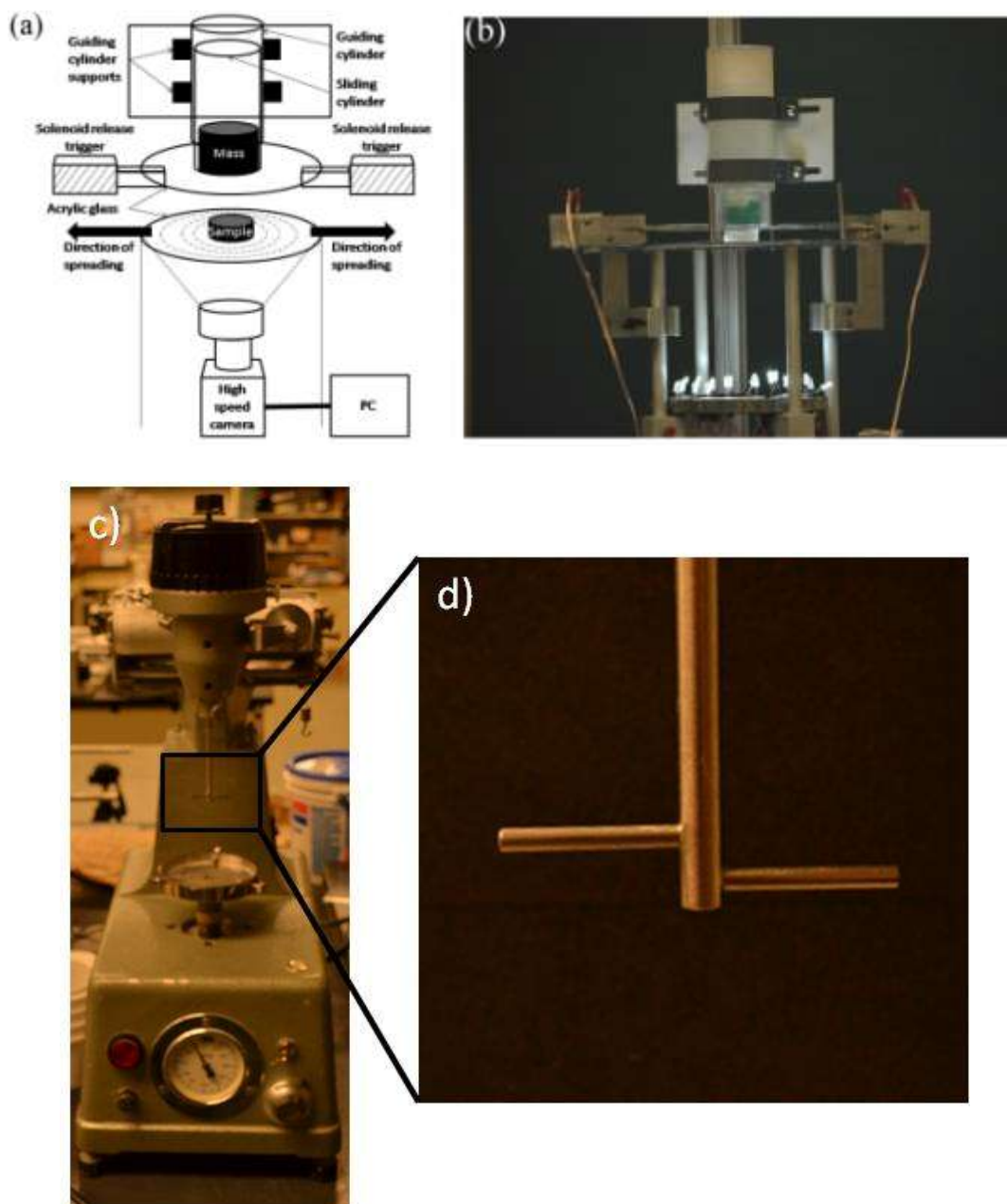


**Figure 7.2.** (a) Schematic of the squeezing device experimental setup. (b) Image of squeezing device. (c) Image of Visco-Corder. (d) Image of spindle used in Visco-Corder.

### 7.3.2 Experimental Methods

To measure viscosity using the Visco-Corder, calibration fluids were used to translate the torque measured into viscosity. The calibration fluids used were silicone oils (Brookfield

Engineering) having viscosities of 0.49 Pa·s, 0.99 Pa·s, and 4.9 Pa·s. As described in Banfill (1994), a best fit linear relationship for each fluid was established between the torque and rpm (Figure 7.3). The slope of the line created from this relationship divided by the silicone oils respective viscosity created a proportionality factor,  $G = 0.04272 \text{ m}\cdot\text{mm}/\text{rpm}\cdot\text{s}$ , (shown in Table 7.1). During the testing of the silicone oils, the rpm was ramped from 20 rpm to 200 rpm and back to 20 rpm (1 cycle) in 20 rpm increments with a holding time of 25 seconds at each rpm. The torque measurement was read before each speed change. During the testing of joint compounds, the testing procedure was the same, although two cycles were conducted.

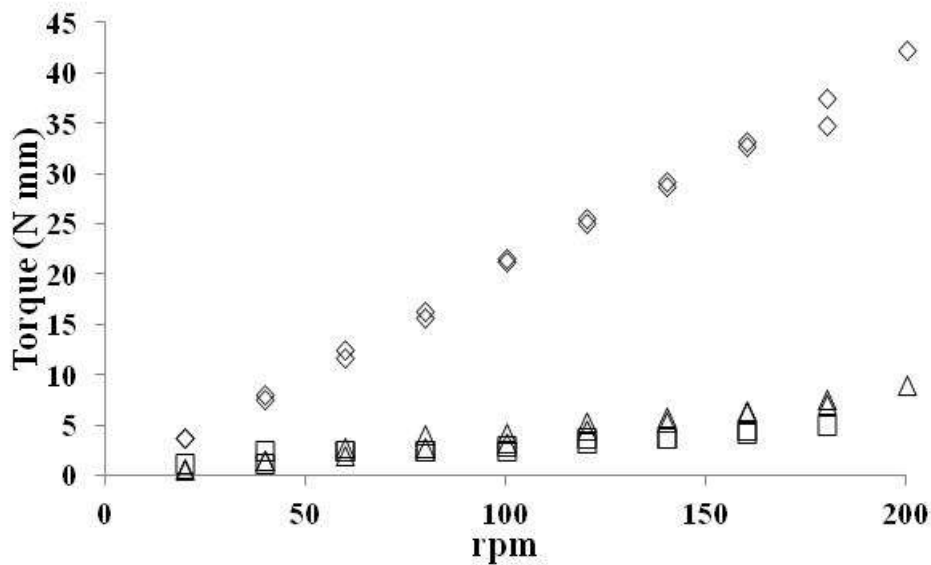


**Figure 7.3.** Experimental data from the Visco-Corder using three silicone oils of viscosity 0.49 Pa·s (squares), 0.99 Pa·s (triangles), and 4.90 Pa·s (diamonds).

**Table 7.1.** Calculation of the proportionality factor relating data from the Visco-Corder to the viscosity of the fluid.

Silicone oil type	Viscosity, $\mu$ (Pa·s)	Slope of torque and rpm relationship, $m$ (N mm/rpm)	Proportionality factor, $G = m/\mu$ , (m mm/rpm s)
490	0.49	0.0210	0.0429
990	0.99	0.0423	0.0427
4900	4.90	0.2086	0.0426

When measuring the viscosity using the squeezing apparatus, the following procedure was employed. When the compound container was initially opened, it was stirred using a household mixer with a beater type attachment on medium speed for two minutes. Then, using a 60 mL syringe with a removed tip, the compound was extracted into the syringe. The syringe was placed above the bottom plate of the apparatus using a centering guide and 10 mL of material was plunged onto the plate. The compound was separated from the syringe with a small putty knife using a sawing motion. Lastly, the sample was squeezed using a mass load of the top plate, and additional mass when necessary. There were four trials completed for each mass load, however, the second, third and fourth trials used the material still existing in the syringe. The consistency of the results revealed that four trials are sufficient to gain accurate data of viscosity.

The time to complete one trial is approximately 4 minutes, therefore the material in the beginning of the fourth trial has not been stirred for roughly 12 minutes. This is not of concern since it will be found in the thixotropy section of this report that the viscosity does not significantly change during this period. However, before refilling the syringe, the material in the container was again stirred for at least one minute. This process was completed for mass loads of 165g, 315g, and 465g.

When measuring the yield stress the following process was followed. When the compound container was initially opened, it was stirred using a household mixer with a beater

type attachment on medium speed for two minutes. Then, using a 60 mL syringe with a removed tip, the compound was extracted into the syringe. Then the syringe was placed above the bottom plate of the apparatus using a centering guide and 10 mL of material was plunged onto the plate.

The top plate was loaded with a mass of 230g, 330g, and 430g, and lowered slowly on to the material (to inhibit any inertial effects). Then, the material was allowed to flow for at least 45 minutes. It has been determined from a previous report that 45 minutes is sufficient for the material to cease flowing. At the end of the trial, all remaining material inside the syringe was discarded and again the material in the container was stirred for two minutes before the next trial. Due to very consistent results, each material was only tested twice under each mass load.

Some components in joint compound, such as clay, are thixotropic. A basic method to determine thixotropic effects is by measuring the difference in viscosity immediately after stirring and after a significant resting period. To prepare the compound, a “T” shaped stirrer (invented after the viscosity and yield stress experiments were conducted) was attached to a drill and the compound was mixed for at least two minutes between medium and full speed. The compound was dispensed using a 60 mL syringe, as stated earlier, but on very thin polystyrene sheets and allowed to rest until the time of the test. At the time of the test, the polystyrene sheet and sample were both placed on the bottom disc and the viscosity test resumed as previously stated using a mass load of 465 g. It was determined that the polystyrene sheet has no influence on the viscosity since it is very similar to acrylic in its affinity towards water based products. To deter drying of the waiting sample, a plastic weighing dish was placed upside down over the dispensed sample. In one trial set, the weighing dish was not used to see the effects of drying on the sample. During normal use of joint compound, letting the material rest for over an hour is not



recommended due to drying of the surface layer and should be stirred. Therefore, the viscosities of the compounds were measured using the squeezing device for up to 80 minutes.

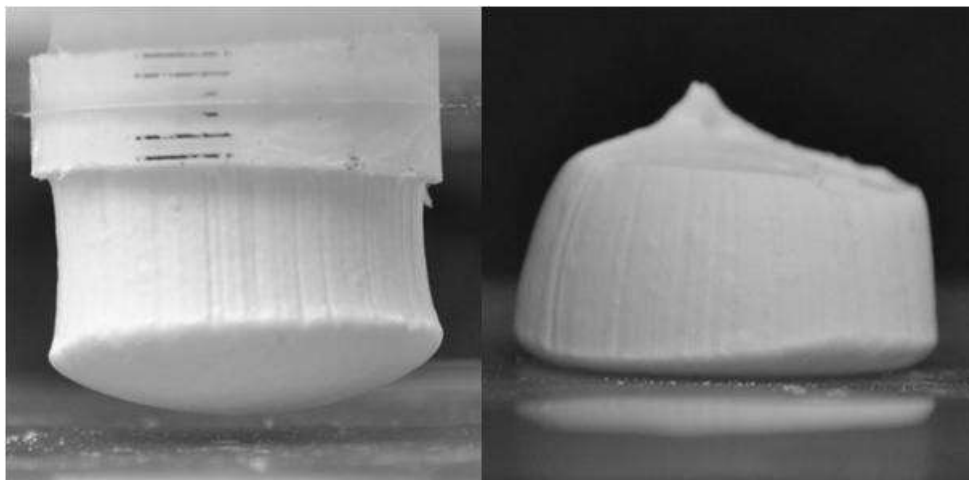
## **7.4 Results and Discussion**

### **7.4.1 Qualitative Observations**

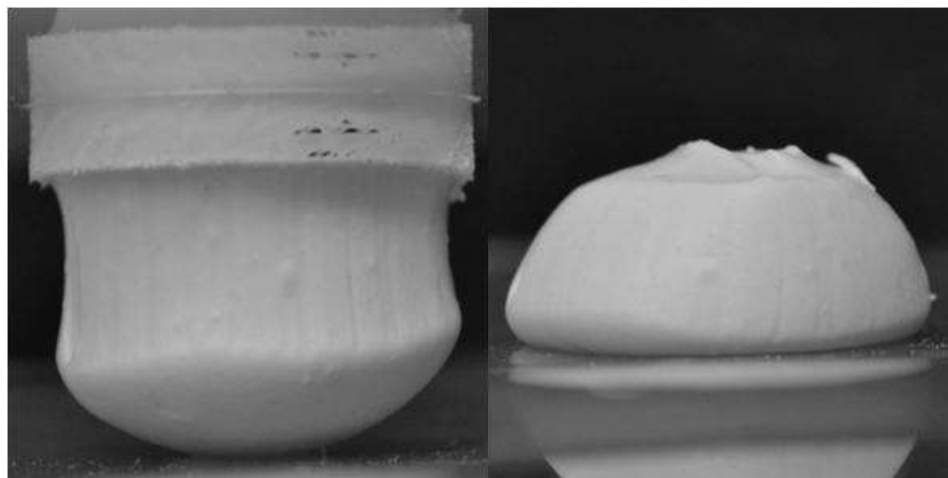
Four different types of joint compounds were provided by USG, a control compound (compound C), a compound with twice the amount of cellulose as the control compound (compound F), a compound with no starch (compound E), and a compound with half the amount of clay as the control compound (compound K). To qualitatively differentiate between the different joint compounds, images of the 10 ml sample were taken as the compound was being dispensed and one minute after separation from the 60 mL syringe using a sandwich spreader. The discussion is centered at the images in Figures 7.7 – 7.7.

Figure 7.4 shows the dispensed sample of compound C forming a convex bulge at the bottom of the partially dispensed sample. Also, the widest section of the partially dispensed compound was slightly wider than the syringe opening, which manifested a certain amount of the elastic-like response, i.e. the phenomenon similar to the so-called die swell. Note also that the compound samples were falling onto the bottom disk slightly under their own weight causing stretching in the vertical direction and shrinkage in the radial direction, also known as necking. After dispensing, compound C restored its cylindrical-like shape. In compound F, as shown in Figure 7.5, similar effects such as bottom bulging, elastic swell and stretching also occur but are more pronounced than in compound C (Figure 7.4). Compound C holds its shape well after being dispensed and the streaking lines from dispensing stay distinct, whereas in compound F the streaking lines seem to fade. Compound F has twice as much cellulose than compound C, which

may lower the yield stress of the compound, justifying this observation. The elimination of starch in compound E gives rise to an almost perfect plug-like flow, shown in Figure 7.6. As the sample is dispensed, there is a slight convex bulge but the sample exhibits no die swell or necking. After the sample is dispensed, it keeps its cylindrical shape and the streak lines are still pronounced. These characteristics are the result of a high yield stress. Lastly, compound K acts similarly to compound E by exhibiting a large convex bulge, necking due to sample falling under its own weight and a small amount of die swell (Figure 7.7). Furthermore, after the sample was dispensed it showed some slumping and the removal of the streaking lines revealing a possible decrease in yield stress.



**Figure 7.4.** Dispensing a sample of compound C (left). The sample after it had been cut from the dispenser (right).



**Figure 7.5.** Dispensing a sample of compound F (left). The sample after it had been cut from the dispenser (right).

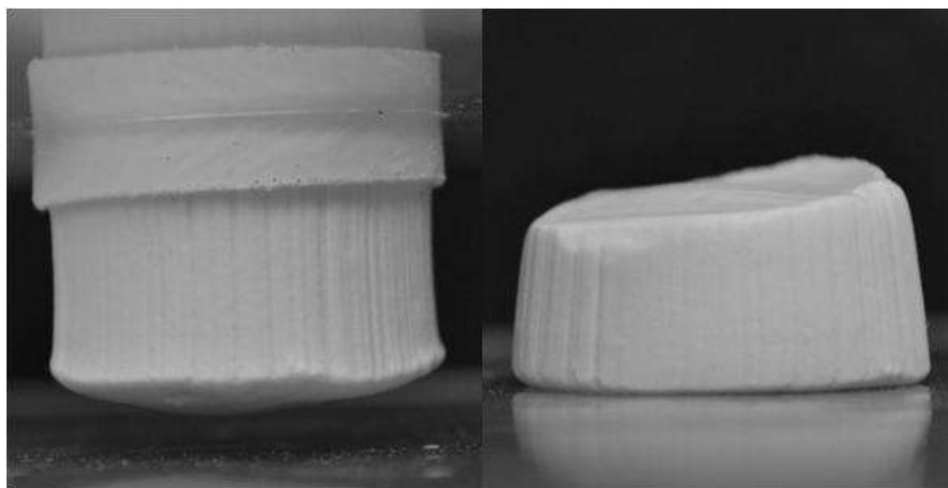


**Figure 7.6.** Dispensing a sample of compound E (left). The sample after it had been cut from the dispenser (right).

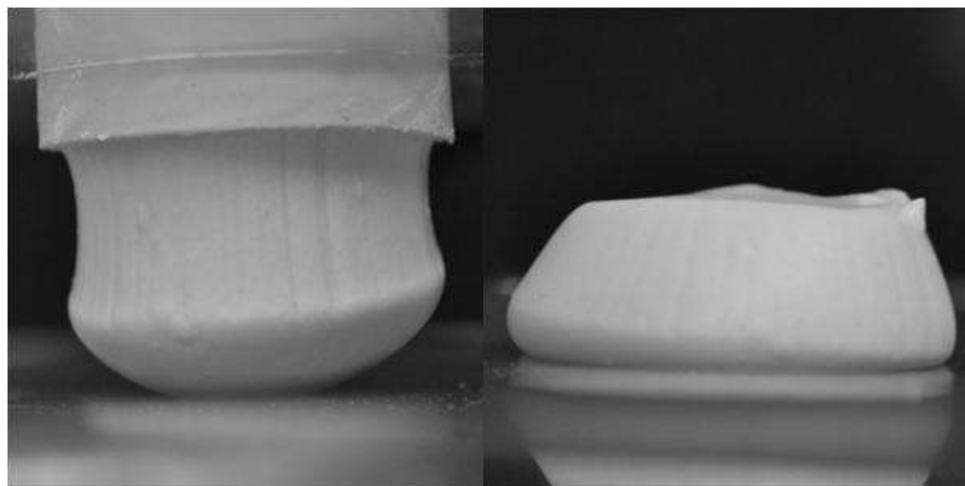


**Figure 7.7.** Dispensing a sample of compound K (left). The sample after it had been cut from the dispenser (right).

#### **7.4.2 Measuring Effective Viscosity**

The Visco-Corder measured the torque produced at each rpm for the four joint compounds using the procedure described above. Looking at the torque vs. rpm curves shown in Figure 7.8, it is very difficult to distinguish between the compounds. To find the viscosity of each compound, each two cycle curve was fitted using a parabolic equation. The instantaneous slope of the fitting line at each rpm was determined using the derivative of the fitting equation and the respective rpm value. Dividing the instantaneous slope by the proportionality constant,  $G = 0.04272 \text{ m}\cdot\text{mm}/\text{rpm}\cdot\text{s}$ , calculates the viscosity at each 20 rpm increment for each compound. The results are shown in Figure 7.9. The difference in viscosity between joint compounds at low rpm is very small and indistinguishable at higher rpm. Assuming that the rpm is proportional to the shear rate, the joint compounds show a shear thinning behavior, which is counter to previous findings.

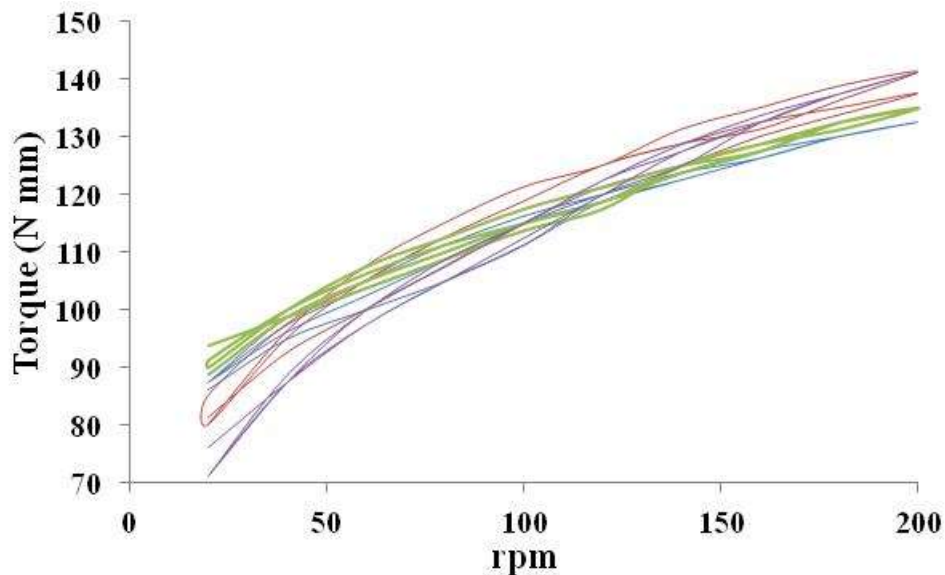


**Figure 7.8.** Experimental data of joint compounds using the Visco-Corder. Data points were taken every 20 rpm, however, the utilization of lines helps discern different compound curves. Compound C (blue), compound F (red), compound E (green), and compound K (purple).

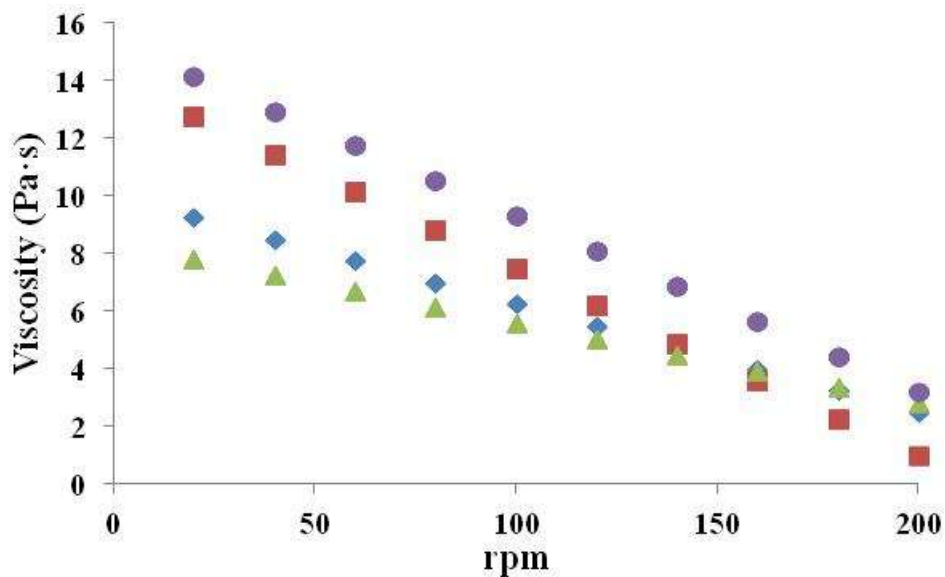


**Figure 7.9.** Calculated viscosity found using the Visco-Corder for each joint compound. Compound C (blue diamond), compound F (red square), compound E (green triangle), and compound K (purple circle).

Two different procedures were used for squeezing the dispensed sample over the acrylic disk. In the first process the top plate with added mass was supported on the solenoid fixtures at a fixed height. As the solenoid is triggered, the top plate falls on the dispensed sample and squeezes it. This process is referred to as fast squeezing. In the second process, the top plate is slowly lowered until it makes contact with the top surface of the dispensed sample and then is left to squeeze the sample gradually. This process is referred to as slow squeezing. The effective viscosities of the joint compounds were found from fast squeezing, with shear stresses being negligible. The series of images recorded during the process of fast squeezing was analyzed with Matlab using the Image Processing Toolbox. Squeezing of the joint compounds was recorded at 2000 fps. The area of the sample at each time instant was then measured in terms of pixels and converted to  $\text{cm}^2$  using a reference sample size. Finally, the effective viscosity was found using Eq. (7.1).

**Table 7.2.** Average effective viscosities of various joint compounds with variances for all mass loads employed. Values with an (\*) had a single outlier and removed from calculation.

Load	Compound C (Pa·s)	Compound F (Pa·s)	Compound E (Pa·s)	Compound K (Pa·s)
165 g	$18.5 \pm 2.8$	$15.1 \pm 0.7$	$25.2 \pm 1.1^*$	$24.5 \pm 3.7$
315 g	$24.0 \pm 2.1$	$18.4 \pm 1.5$	$28.8 \pm 3.3$	$23.0 \pm 2.1$
465 g	$28.4 \pm 3.7^*$	$21.4 \pm 1.0^*$	$32.6 \pm 3.0^*$	$25.5 \pm 2.0^*$

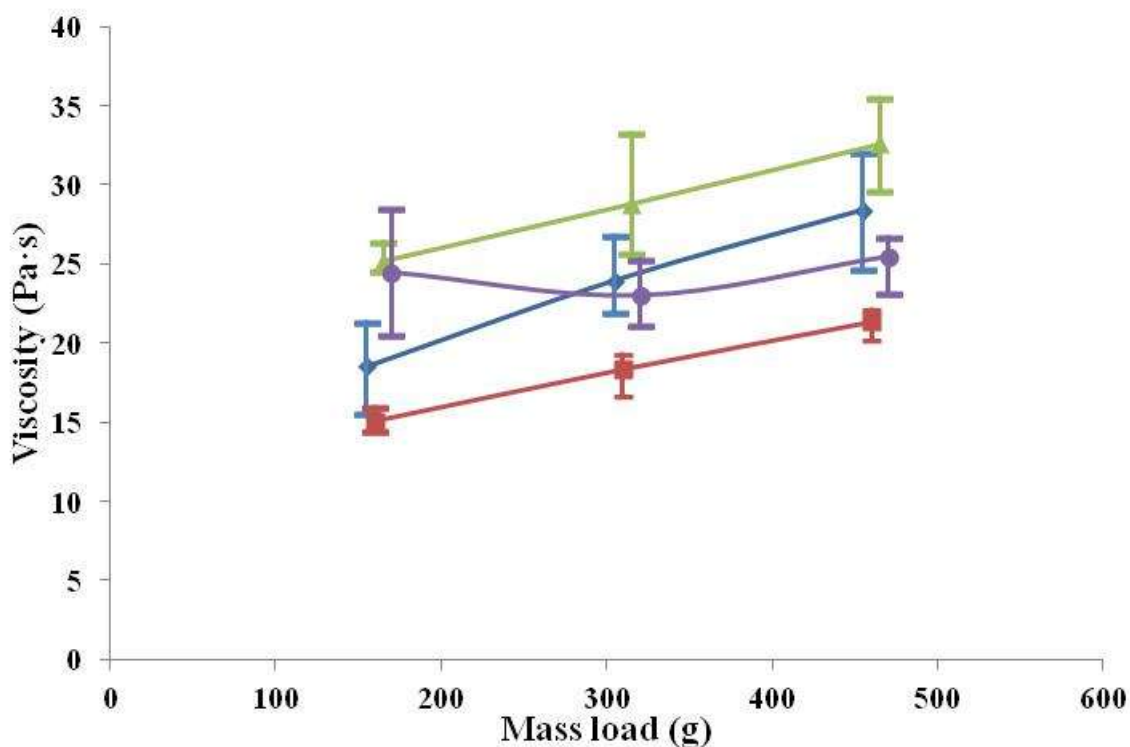


**Figure 7.10.** Average effective viscosities for different joint compounds under mass loads of 165g, 315g, and 415g. The error bar represents the maximum and minimum values of viscosity measured. Compound C (blue diamond), compound F (red square), compound E (green triangle), and compound K (purple X). To clearly see the error bars, the values of the mass loads were shifted either positively or negatively around the mass loads used; compound E represents the correct mass load. Lines were added for guidance.

Four fast squeezing experimental trials were conducted under three different mass loads (165 g, 315 g and 415 g) for each joint compound. The average effective viscosities with the variances are given in Table 7.2 and average effective viscosities with maximum and minimum values are shown as error bars in Figure 7.10. The control compound, compound C, exhibits expected behavior compared to previous studies on All Purpose joint compound, albeit with presumably slightly more water explaining a difference of 5 Pa·s lower in viscosity at each mass

load for compound C. Compound F, containing twice the amount of cellulose than the control compound, exhibits an approximate 22% drop in viscosity at each mass load compared to compound C. Although the specific rheological behavior of the cellulose is unknown, it is speculated that the viscosity of the cellulose is lower than the viscosity of compound C, therefore the addition of cellulose decreases the overall viscosity of the compound. On the other hand, the deletion of starch in compound E raises the viscosity at each mass load, however at higher mass loads the increase in viscosity is less pronounced. The change in viscosity is likely due to the elimination of a low viscosity component or an absence in water since starch is known for its water absorbing ability and water was added respectively to make the viscosities the same according to the Visco-Corder. Unlike compounds F and E, the reduction of clay found in compound K changed the behavior of the fluid from slightly dilatant to more Newtonian like. That is, the viscosity remains approximately constant, equal to that of compound C under mass load of 315g, under the three different mass loads. This indicates that the clay has a direct connection to the thickening behavior of the compound.

#### **7.4.3 Yield Stress Measurements**

It has been demonstrated that the deformation curves of joint compounds do not follow the Newtonian behavior (Figure 7.13). Moreover it was found that the joint compounds possess a yield stress. Thus, the joint compounds possess both an effective viscosity and yield stress and represent themselves Bingham fluids. These fluids flow as Newtonian viscous fluids only when the stresses exceed the yield stress. To estimate the yield stress of these joint compounds the slow squeezing procedure was employed. It was shown that Eq. (7.1) which describes the behavior of the joint compounds in the squeezing tests, completely disregards the shear stresses



at the disk surfaces which dominate flows of Newtonian fluids. For Bingham fluids, the viscous shear stresses can be concentrated in narrow layers near the disks, while the bulk of material experience only normal viscous stresses as Eq. (7.1) implies. Indeed, in the parabolic velocity profile characteristic of Newtonian fluids in squeezing flow between solid disks with no-slip conditions, only the near-wall layers of the thickness  $\delta$  support high viscous shear stresses higher than a possible yield stress of a Bingham fluid. Therefore, in the case of Bingham fluids the central part of the material cannot sustain any shear flow and can reveal only a uniform velocity profile shown in Figure 7.11 (b).

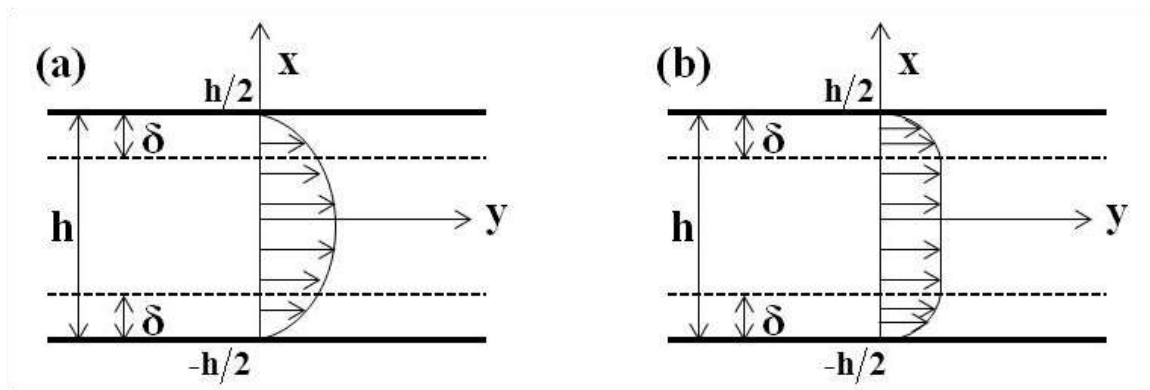


**Figure 7.11.** Schematic of the velocity profiles in squeezing flows of (a) Newtonian and (b) Bingham fluids.

In the slow squeezing process, the top plate was gradually lowered on the sample which then slowly spreads. As the joint compound spreads under a constant force, the area  $A(t)$  increases and the stress associated with it decreases. When the joint compounds do not spread further, i.e. the stress approaches the yield stress. The yield stress in shear  $\tau_0$  is related to the yield stress in compression  $Y$  by the von Mises yield criterion. The former can be evaluated from the relation  $\tau_0 = Y/\sqrt{3}$  and  $Y = \sigma_{xx} = F/A_{fin}$ , where  $F$  is the constant force acting on the compound and  $A_{fin}$  is the final spreading area. The yield stress was calculated experimentally for each joint

compound under three weights, 230 g, 330 g, and 430 g. The average values of the yield stress for each weight are given in Table 7.3.

**Table 7.3.** Experimental values of the yield stress of different joint compounds averaged over two experiments.

Load	Compound C (Pa)	Compound F (Pa)	Compound E (Pa)	Compound K (Pa)
230 g	647	385	622	424
330 g	803	482	803	499
430 g	970	550	931	592

Each compound was only measured twice for the yield stress since very consistent values were obtained. All joint compounds revealed a shear-thickening behavior as the yield stress increases with load (Table 7.3). Overall, compounds C and E show similar yield stress values, as do compounds F and K. Compounds F and K have a yield stress that is 40% less than compounds C and E for all mass loads. Figure 7.12 shows the yield stress for each joint compound with load. It is clear that starch has no effect on the internal structure of joint compound which manifests a yield stress. However, the effect of doubling the cellulose content or halving the clay content have the same effect on lowering the yield stress. The lowering of the yield stress as a result of lowering the concentration of a self-organizing, rod-like, thixotropic material, such as clay, is straight forward. The doubling the amount of cellulose to reduce the yield stress is, however, non trivial. It is speculated that the yield stress was lowered because the extra cellulose deterred the clay from being able to construct a microstructure, therefore lowering the yield stress.

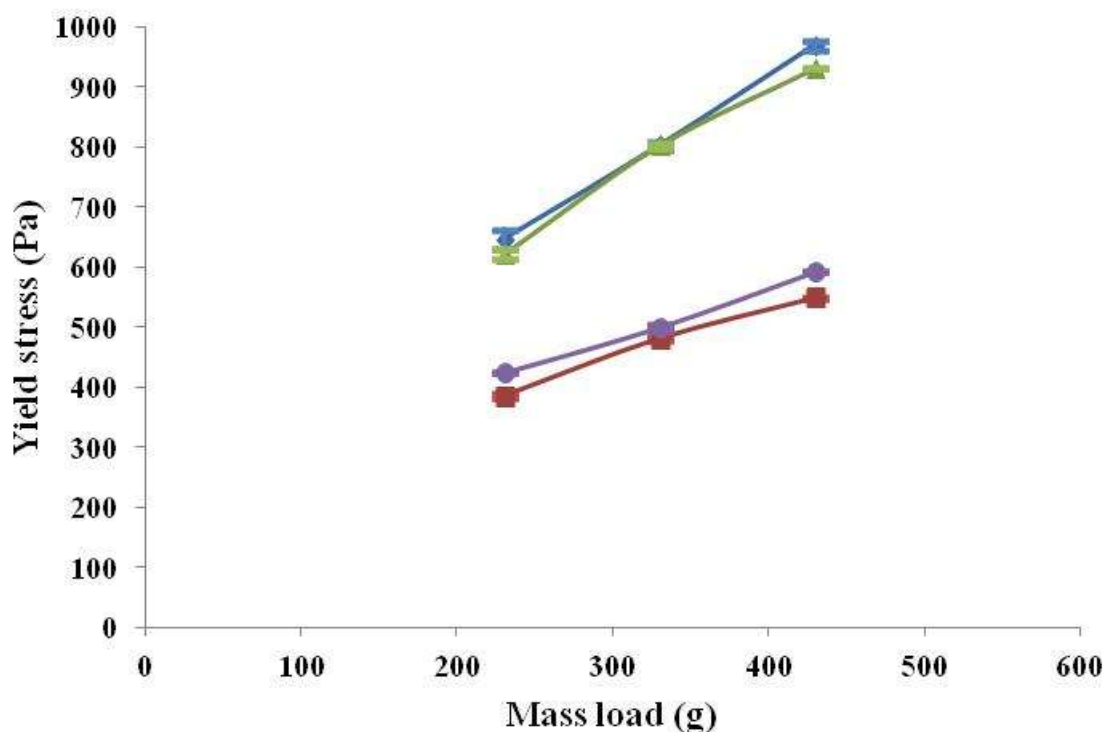


**Figure 7.12.** Average yield stress for different joint compounds under various mass loads. The error bar represents the experimental values of yield stress measured and the symbol represents the average from Table 7.3. Compound C (blue diamond), compound F (red square), compound E (green triangle), and compound K (purple circle). Lines were added for guidance.

After the fast spreading stage is over, a much slower spreading continues (cf. Figure 7.13). The spreading rate at the slower second stage can be approximated as

$$\frac{dA}{dt} = \frac{A_{\max} - A}{\tau_c} \quad (7.2)$$

where  $\tau_c$  is the characteristic time which is now affected not only by the viscous forces but also by the yield stress, and  $A_{\max}$  is the ultimate (maximum) area corresponding to the restrictions imposed by the yield stress.

Integrating Eq. (7.2) from an initial area  $A^*$  at  $t=t^*$ , we obtain

$$A = A_{\max} + (A_* - A_{\max}) \exp\left(\frac{t_* - t}{\tau_c}\right) \quad (7.3)$$

Equation (7.3) was fitted to the experimental data for each mass load. The resulting values of the characteristic time,  $\tau_c$ , are listed in Table 7.4. It can be seen from Table 7.4 that the two compounds with the lower yield stress, compounds F and K, also have the most dramatic change in  $\tau_c$  between mass loads of 165 g and 315 g. This is counterintuitive because when the yield stress is large, it should have a more dramatic impact on the cessation of spreading causing  $\tau_c$  to be small.

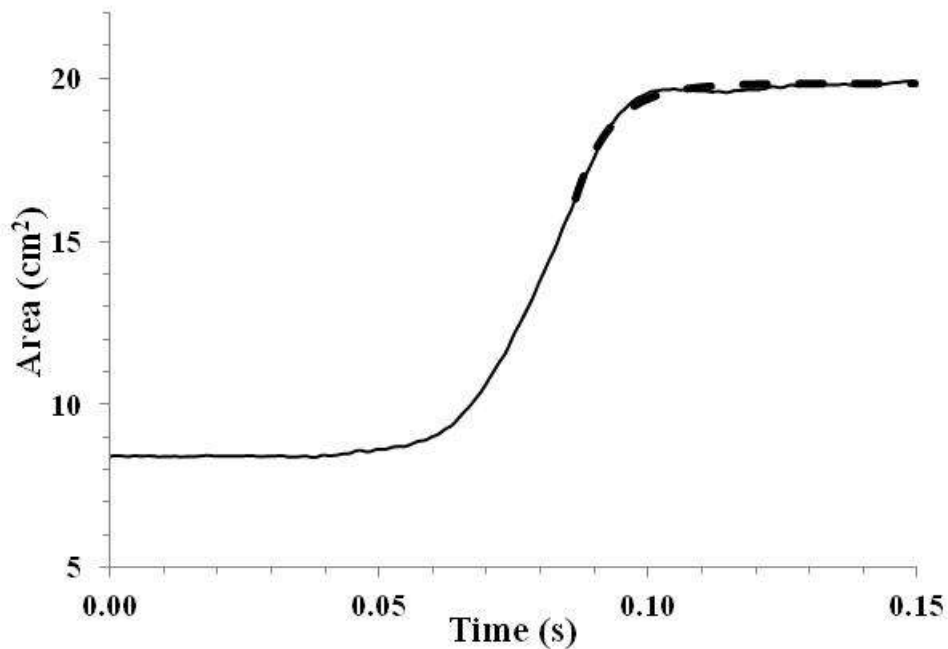


**Figure 7.13.** The experimental deformation curves with Eq. (7.3) fitted for compound C under mass load of 415 g. The solid line depicts the experimental data and the dash line is Eq. (7.3) with  $\tau_c=0.00667$  s.

According to Eq. (7.1), the dependence of the area,  $A$ , on time can be approximated as  $A = mgt / 3\mu$ . The squeezing stress is expressed as  $\sigma_{xx} = mg/A$ . The cessation of the squeezing is expected when  $\sigma_{xx}$  will decrease (as  $A$  increases) to the level of the yield stress  $Y$ , which corresponds to the time moment  $t_{cess} = 3\mu/Y$ , which is roughly the duration of the fast squeezing process. The values of  $t_{cess}$  are shown in Table 7.5.

**Table 7.4.** Characteristic time,  $\tau_c$ , for different joint compounds under different loads.

Load	Compound C (s)	Compound F (s)	Compound E (s)	Compound K (s)
165 g	0.0071	0.0113	0.0114	0.0150
315 g	0.0084	0.0057	0.0092	0.0083
465 g	0.0074	0.0066	0.0075	0.0085

**Table 7.5.** Cessation of fast squeezing time moment  $t_{cess}$  for different joint compounds under different loads.

Load	Compound C (s)	Compound F (s)	Compound E (s)	Compound K (s)
165 g	0.06	0.08	0.08	0.12
315 g	0.05	0.07	0.07	0.08
465 g	0.05	0.06	0.06	0.07

The radial elongational strain rate experienced by the material in the fast squeezing test is defined as  $\dot{\gamma}_{elong} = (dA/dt)/2A$ . The shear rate in the shear layers near the disks is equal to

$$\dot{\gamma}_{\text{shear}} = \left. \frac{\partial v}{\partial x} \right|_{x=\delta} = \left. \frac{4Vx}{H^2} \right|_{x=\delta} = \frac{\tau_0}{\mu} \quad (7.4)$$

The values of  $\dot{\gamma}_{\text{elong}}$  and  $\dot{\gamma}_{\text{shear}}$  are presented in Tables 7.6 and 7.7, respectively. The values for the elongational strain rate for fast and saturation stages of the squeezing process are listed in Table 7.6. The saturation squeezing stage begins where the fast squeezing stage ends, or when the yield stress begins to slow the radial spreading of the sample, causing a much slower spreading to continue. The elongational strain rate during fast squeezing increases with load. The elongational strain rate for the fast squeezing process is within a range of 10-20 s<sup>-1</sup> and for the saturation squeezing process is within a range of 0.7-2.0 s<sup>-1</sup> (Table 7.6). It is seen that at the fast deformation stage, the shear strain rate is two times that of the fast elongational strain rate for the joint compounds.

Overall, the predominantly quasi-one-dimensional elongational character of deformation of joint compounds in fast squeezing experiments is a reliable approximation. The shear layers near the disk surfaces play the role of lubrication layers where the no-slip boundary condition is reconciled.

**Table 7.6.** Elongational strain rate (s<sup>-1</sup>) for fast and slow stages for different joint compounds under different loads.

Load	Compound C		Compound F		Compound E		Compound K	
	fast	sat	fast	sat	fast	sat	fast	sat
165 g	13.6	1.2	13.4	0.7	11.1	0.9	9.0	0.9
315 g	15.4	1.2	16.9	1.2	13.6	1.5	14.4	1.3
415 g	16.9	1.5	18.6	1.6	13.5	1.2	18.1	1.8

**Table 7.7.** Shear strain rate ( $s^{-1}$ ) for different joint compounds under different loads.

Load	Compound C	Compound F	Compound E	Compound K
165 g	29.6	22.4	23.9	15.3
305 g	32.8	25.1	26.7	21.5
405 g	36.4	27.1	30.6	24.4

#### **7.4.4 Thixotropy**

Components in joint compound, such as attapulgite clay, are considered thixotropic. Thixotropy is a change in viscosity by the breakage of structure inside the material due to continuous agitation and a rebuilding of structure in the absence of agitation. Therefore, to measure the effect on viscosity due to thixotropic effects, the viscosities of the compounds under a mass load of 465 g were measured up to 80 minutes after the cessation of stirring of the material. The results are shown in Figure 7.14. Throughout the elapsed time, all compounds increase in viscosity, although compound F only increases slightly. Furthermore, all compound's viscosities remain relative to the others, such as compound E continually having the highest viscosity and compound F having the lowest. If the data is fitted to a linear relationship, as in Table 7.8, it can be seen that compounds C and E have similar increases in viscosity. Interestingly compound K, having half the amount of clay as compound C, has approximately half the viscosity growth rate which may indicate that the amount of clay influences thixotropic behavior. However, compound F having the lowest viscosity growth rate has the same amount of clay as compound C, but does have twice the amount of cellulose. This may be an indication that an abundance of cellulose, a gelling agent, may deter the reorganization rate of the clay structure.

The intercept of the best fit line at 0 minutes agrees fairly well with the viscosities shown in Table 7.2, albeit slightly higher. Lastly, drying of the material increases the viscosity, although not as much as expected. Overall, there was no dramatic change in viscosity during the tested time frame, therefore thixotropic effects are not of concern since they are easily removed by a quick stirring of the compound.

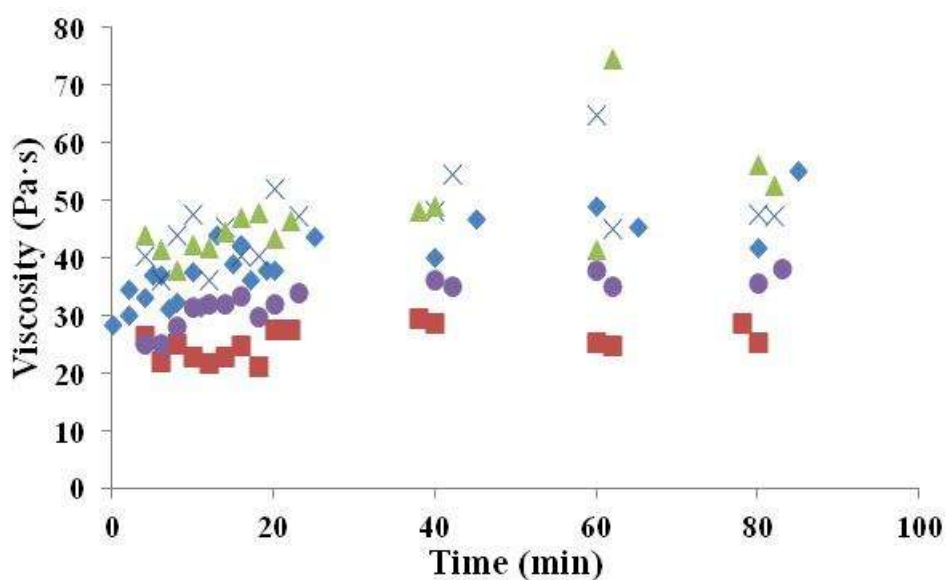


**Figure 7.14.** Viscosities of compounds under a mass load of 465 g after up to 80 minutes of resting time. Compound C (blue diamond), compound C uncapped (blue X), compound F (red square), compound E (green triangle), and compound K (purple circle).

**Table 7.8.** Parameters for a best fit line for viscosity data in Figure 7.14.

Compound	Slope of best fit line	Intercept of best fit line at 0 min
C	0.21	34
C uncapped	0.14	42
F	0.04	24
E	0.21	41
K	0.12	29



## **7.5 Conclusion**

Four compounds were received for investigation. One was a control compound and the other three had an altered concentration of a single major component. Then, an amount of water was added to each compound so that the torque measured by the Visco-Corder over several rpm was the same, thereby making them indistinguishable. This investigation had two main objectives: first, to show that the squeezing apparatus could distinguish between compounds either by measuring viscosity and/or yield stress, and second, to reveal the effect of the addition or subtraction of a single component. Both of these objectives were completed successfully. The squeezing apparatus was able to distinguish between the different compounds by their own characteristic combination of viscosity and yield stress. Furthermore, the change in viscosity or yield stress due to component concentration provided information about how to tailor the compound to produce specific characteristics. It was found that: doubling the amount of cellulose decreased the viscosity and yield stress, removing the starch increased the viscosity but left the yield stress unchanged, and removing half of the clay removed the thickening behavior and decreased the yield stress.

## 8. BENTONITE DISPERSIONS: TRANSITION FROM LIQUID-LIKE TO SOLID-LIKE BEHAVIOR AND CRACKING

### 8.1 Introduction

Cylindrical samples of 11-13 wt% aqueous bentonite dispersions with a range of resting times after preparation (0 to 72 h) were subject to axial squeezing and revealed a transition from a Bingham liquid-like behavior to solid-like behavior. The liquid-like behavior is characterized by viscous spreading arrested by the yield stress, whereas the solid-like behavior is characterized by stasis at lower loads followed by cracking above some critical level of load. A mechanical response, dependent on resting time, implied irreversible aging as a result of slow swelling of the clay crystallites, i.e. the internal structure being built over time in the material at rest. Dispersions of 11 wt% and 12 wt% transitioned from liquid-like to solid-like behavior in a single experiment at a resting time of 24 h and 3 h, respectively. At higher concentrations (13-22 wt%) the material always behaves as a solid. The solid-like behavior is distinguished from the liquid-like behavior by the appearance of cracks. The additional bending and buckling experiments conducted with dispersions of 18-22 wt% revealed Young's moduli of 330-500 kPa, yield stresses of 9-15 kPa, cracking stresses of 15-25 kPa, and cracking strains of 8-10%. For all concentrations explored, a linear dependence of the yield stress on concentration was found. It is demonstrated for the first time that liquid bentonite dispersions at a concentration of 11-12 wt% reveal transition to a solid in a single experiment where they become capable of developing different families of cracks (radial and inclined) during uniaxial compression.

Section 8.2 describes the materials, methods of preparation, and apparatuses used in the experiments. The results of each experiment are given in section 8.3. A discussion of the results is in Section 8.4. Conclusions are in Section 8.5.

## **8.2 Experimental Materials and Apparatus**

### **8.2.1 Material**

Bentonite powder (100 wt% pure clay) was obtained from NOW FOODS Inc. and mixed with DI water to prepare 11 wt%, 12 wt%, 13 wt%, 18 wt%, 20 wt%, and 22 wt% bentonite dispersions. The bentonite powder is a sodium type bentonite according to the manufacturer and has a particle size of 5-10  $\mu\text{m}$ . Bentonite dispersions were prepared by mechanical mixing using a handheld kitchen mixer (Hamilton Beach) with the standard mixer attachment initially for 10 min, left for at least 3 days to ensure hydration, and again mixed before each test, except those which required a resting time.

Air bubbles were not entrained during the creation of the bentonite dispersions by taking great care not to fold the material while stirring (several stirrers were tried) as well as forcefully banging of the plastic container on the table which caused the bubbles to rise to the surface during and immediately after stirring. The prepared dispersions were discarded if any significant air pockets were observed when they were dispensed.

The 11 wt%, 12 wt%, and 13 wt% bentonite dispersions were chosen based on their ability to crack under stress due to compression. If the concentration was decreased further, to 10 wt% or less, then no cracking of the sample would occur given the allotted resting time. This is corroborated by our earlier study in Pelot et al. (2013). However, Gotoh and Shimizu (1965) showed that cracking of lower concentrations of bentonite could be observed if the samples were left to rest (and solidify by evaporation) for seven days. If the concentration of bentonite is 13

wt%, then cracking occurs without any resting time and represents itself as the initial concentration that results in an immediate solid-like response after stirring. In some cases 12 wt% dispersions without any resting time did crack but only near the plates which squeeze the sample (see subsection 8.2.2 below), not through the bulk of the sample.

The higher concentrations of bentonite were chosen due to their ability to retain the sample shape for bending experiments (see subsection II.B below). The bending experiments were chosen to find the mechanical behavior because Thusyanthan et al. (2007) demonstrated that when materials are too weak to be clamped their mechanical properties can be found by a bending test. The higher-concentration samples were also tested in buckling experiments (see subsection II.C below) to independently measure the necessary strain to cause cracking. Concentrations higher than those tested here (i.e.  $> 22$  wt%), were extremely difficult to prepare and test using the methods described below. It was found empirically in this work, but is not reported here in detail, that mechanical properties of bentonite dispersions at 18 wt%, 20 wt%, and 22 wt% did not change with resting time.

### **8.2.2 Squeezing Experiment**

Dispersions of 11 wt%, 12 wt% and 13 wt% bentonite were stored in 60 mL syringes (with the tip-end removed) and covered with paraffin wax until the designated test moment. This represents the resting time in this article. Each syringe full of clay was weighed immediately after being filled and before the test moment to ensure the absence of evaporation during the resting period. All dispersions weighed the same to an accuracy of a 0.1 g regardless of the resting time. Moreover, since each squeeze experiment lasted less than 3 min, no evaporation drying was observed in the present work, in distinction from Gotoh and Shimizu (1965) who left their samples resting for seven days.

When the dispersion is plunged out of the syringe there is slip at the syringe wall allowing the internal structure inside the clay bulk to remain intact. This is evident from two phenomena: first, there exists no leftover residue on the inside of the syringe implying that all material is moved as one body, and second, the leading edge of the material as it is pushed out of the syringe is blunt corresponding to pure plug flow, in distinction from highly-viscous Newtonian liquids which reveal a parabolic shaped leading edge (Figure 8.1). Therefore, Figures 8.1(a) and 8.1(b) illustrate that an 11 wt% bentonite dispersion with no rest time slips at the syringe wall. Of the samples used in this investigation this concentration and rest time exhibits the most liquid-like behavior when squeezed. In our previous paper Pelot et al. (2013), we proved by directly observing seeded particles that 10 wt% bentonite dispersion, which reveals a liquid-like behavior, satisfies the no-slip condition at the squeezing disk surfaces.

A sample is pushed out of the syringe and sliced from the tube using a spreading knife. Each cylindrical sample used for squeezing (sketched in Figure 8.2) is 10 ml in volume with approximate dimensions of 3 cm in diameter and 1.5 cm in height. The sample is placed on a transparent polystyrene sheet which is secured to the bottom plate. The upper plate in the squeezing apparatus is also lined with a transparent polystyrene sheet to ensure similar boundary conditions. A detailed description of the squeezing apparatus, and the complete stress and flow field of the squeeze flow can be found in Pelot et al. (2013); the modified version used in the present work is sketched in Figure 8.3 and briefly discussed below. Note also, that Pelot et al. (2013) gave a detailed discussion of the rheological constitutive equations used to describe squeeze flows of different concentrated suspensions and emulsions, including those of clay dispersions.

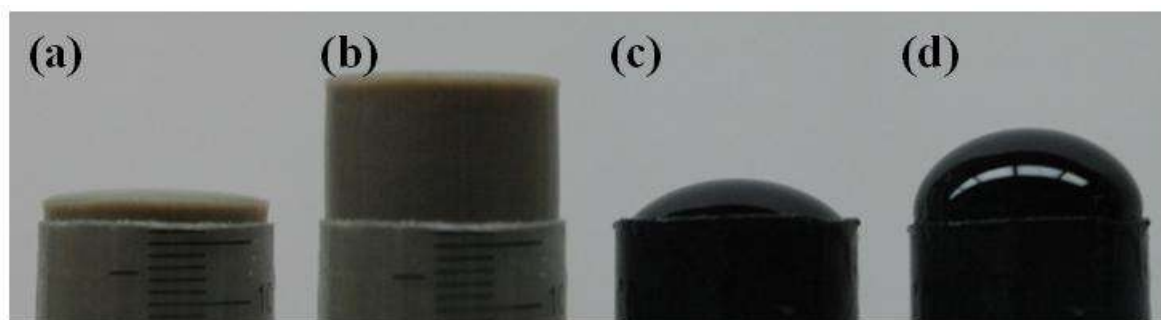


**Figure 8.1.** (a) and (b) The leading edge of 11 wt% bentonite dispersion. (c) and (d) The leading edge of a  $10^4$  Pa·s silicone oil. The samples were pushed from syringe by a plunger.

The squeezing apparatus employs the weight of the upper plate as the driving force for squeezing. In this investigation, the weight was gradually increased. This was achieved by the following modification of the Pelot et al. (2013) device (Figure 8.3). A reservoir was attached to the upper plate of the squeezing apparatus, which could be gradually filled with water to increase the mass load. The upper plate of the squeezing apparatus had an initial (without water added) mass of 67 g. This initial load caused the relatively fresh samples of 11 wt% and 12 wt% to bulge and led to some minor spreading of the samples. Then water was manually added to the reservoir at a rate of 1-2 g/s using a syringe and tubing until the upper plate showed significant vertical displacement. Given the previous results of Pelot et al. (2013) who used a 10 wt% clay dispersion, it was expected that the sample would bulge or spread as the mass increased and it would stop spreading at some moment if no more water was added, typical of a Bingham-like yield stress material. However, in the present case of more concentrated clay dispersions it was discovered that there exists a critical mass of about 80 g at a resting time of 24 h for an 11 wt% dispersion, and about 128 g at a resting time of 3 h for a 12 wt% dispersion that caused the sample to spread continually until suddenly cracking occurred. Hence, a significant displacement of the upper plate mentioned above was observed. Furthermore, the rate of increasing mass at 1-

2 g/s was found to be appropriate for these samples because the sample had ample time to respond to the additional mass load by spreading. In some cases, the mass required to cause cracking exceeded the maximum mass that could be added to the top plate (by the addition of water only). Therefore, a 100 g mass was initially added to the top plate and then water was added.

It should be emphasized that care was taken to ensure that the mass needed to crack the sample is not ramp-rate dependent. After the first sample was tested and the mass needed to cause cracking was found, samples following the first were brought to a loading mass (of water) under the critical mass of the first sample, then ample time was allowed to pass before more loading commenced. Furthermore, the rate at which mass (water) was added was intentionally chosen in order for the material to fully respond to the load before more water was added as a load. Therefore, the ramp-rate was not important.

Two high speed CCD (charge coupled device) cameras were used to capture images of the sample spreading and the appearance of cracking (shear banding) visible at the free surface of the sample as straight lines inclined by angle  $\alpha$  as sketched in Figure 8.2(b). One camera viewed the sample from below (RedLake Motion Pro) and another viewed the sample from the side (Phantom Miro EX4), as shown in Figure 8.3. The cameras were synchronized using an event at the beginning of each trial.

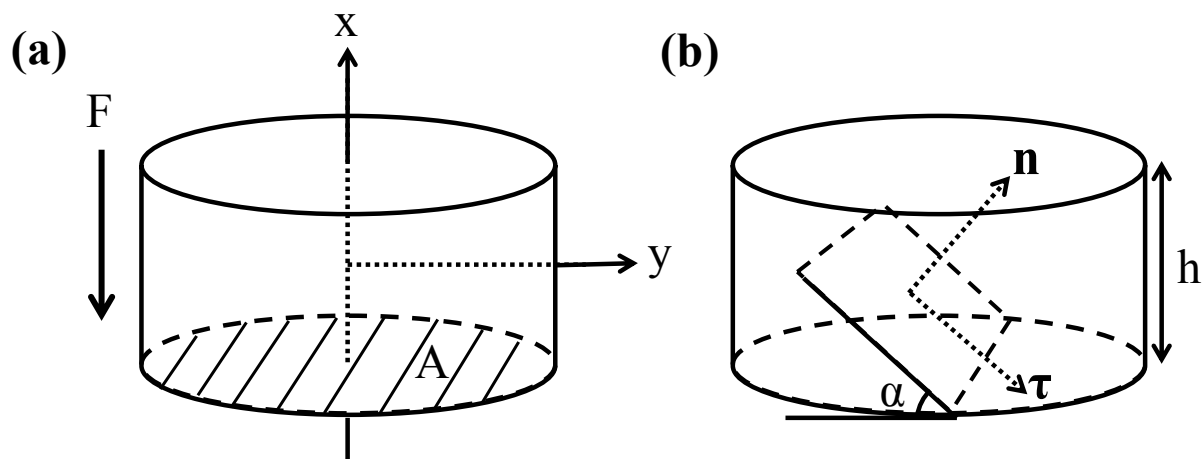


**Figure 8.2.** A sketch of a sample with: (a) Vertical and radial coordinates,  $x$  and  $y$ , respectively, the force,  $F$ , and the cross-sectional area,  $A$ . (b) The height of the sample,  $h$ , the shear plane defined by the unit normal,  $\mathbf{n}$ , its unit tangent,  $\boldsymbol{\tau}$ , and the angle of inclination of the plane,  $\alpha$ .



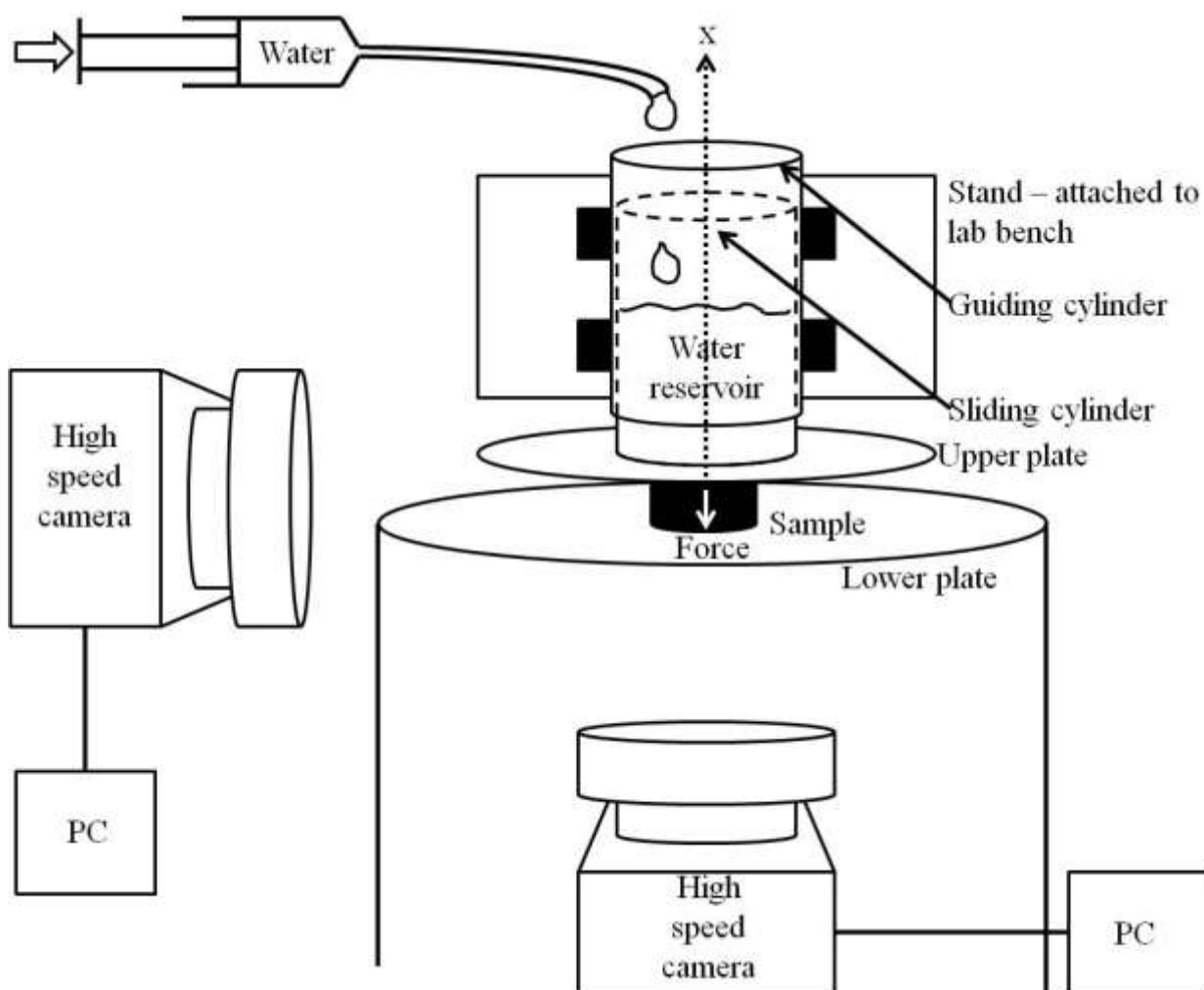


**Figure 8.3.** Sketch of the apparatus used in squeezing experiments. By adding water to the reservoir, the magnitude of the magnitude of the applied force  $F$  can be increased in time.

### **8.2.3 Bending Experiment**

Bending experiment accredited to the PhD student Seongchul Jun.

A layer of bentonite dispersion was installed in the three-point bending setup as shown in Figure 8.4(a). On top of the bentonite layer, a slender bar distributed the applied force uniformly over the center line between the two cylindrical supports spaced 10 cm apart [Figure 8.4(a)]. The slender bar was attached to a linear actuator which moved downward at a speed of 3 mm/s. The bar bent the bentonite dispersion layer and the corresponding bending force was measured by the

transducer (Imada DS2-11). The force magnitude was displayed by the force transducer in real time at a rate of 1000 Hz. The entire bending process and the corresponding force magnitude were simultaneously recorded by a CCD camera (Phantom Miro 4) from the side until the sample started cracking. All bending experiments were done with zero resting time after dispersion preparation.

#### **8.2.4 Buckling Experiment**

Buckling experiment accredited to the PhD student Seongchul Jun.

Buckling of the sample was developed to independently measure the cracking strain and view the initial instances of cracking, as depicted in Figure 8.4(b). In this case, the bentonite layer was buckled by two opposite compressive forces applied at the edge. Under the bentonite layer, between the two sides, there was a very flexible copper mesh which supported the layer. The top view images were recorded by the CCD camera (Phantom Miro 4). Simultaneously, the side view was recorded by another CCD camera (COHO 2222-2340). All buckling experiments were done with zero resting time after dispersion preparation.

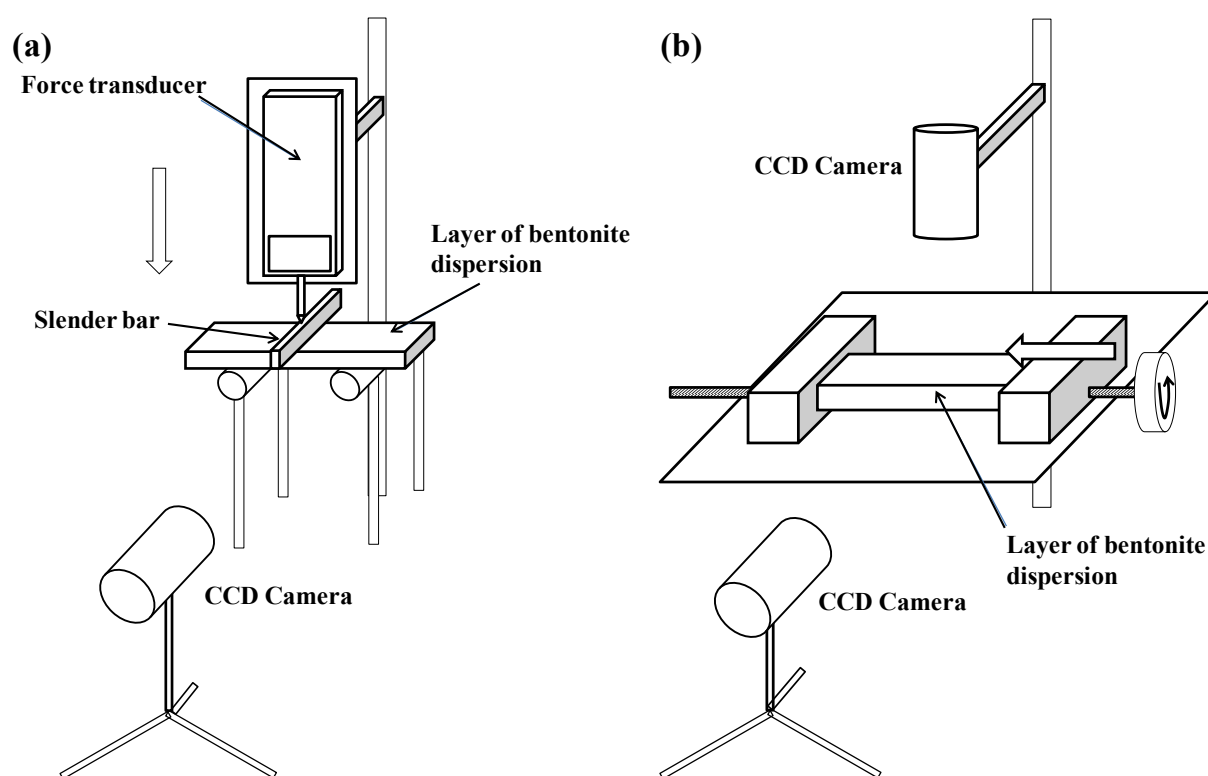


**Figure 8.4.** (a) Sketch of the three-point bending setup for layers of bentonite dispersions. (b) Sketch of the buckling setup used to evaluate cracking stress of bentonite dispersion layers.

## **8.3 Results**

### **8.3.1 Squeezing Experiment**

Dispersions of 11 wt%, 12 wt%, and 13 wt% bentonite were compressed using the squeezing apparatus, and several representative images are shown in Figures 8.5 and 8.7. The mass load used for squeezing was increased until a crack appeared at the free surface of the sample. Images of the sample while being loaded were taken to record the load necessary to induce cracking. If no crack appeared in the sample, then the sample was continually loaded until it became very thin, in which case it was assumed that the sample would not crack if additional mass was applied.

Figure 8.5 shows images of bentonite dispersions of 11 wt%, 12 wt%, and 13 wt%, respectively, being compressed after a 48 h resting period. These images show the sample spreading radially until the critical strain is reached to cause cracking. This is a drastic distinction from the behavior of the less concentrated 10 wt% bentonite dispersions studied by Pelot et al. (2013) which spread without any cracking occurring, and stop spreading in a disk-like shape when the yield stress is reached. However, in the present case at 11 wt% of clay and a resting time of 48 h the sample initially bulges and spreads; then, as it continues to spread, faint angled cracks appear but never become distinct [Figure 8.5(a) and 8.5(b)]. Figure 8.5(c) shows a 12 wt% sample with a resting time of 48 h initially loaded with 67 g but there is no bulging of the sides. However, with further loading the middle of the sample slightly protrudes. Upon even further loading the sample distinctly cracks which is easily seen by the discontinuity of the vertical line in Figure 8.5(d) caused by the syringe as the sample was expelled. Although no more loading was added once the crack appeared, the sample continued to spread and developed a regularly spaced cracking pattern around the entire sample [Figure 8.5(d)]. Figure 8.5(e) shows a 13 wt% sample with a resting time of 48 h initially loaded with 67 g and again there is no bulging of the sides. This sample had a defect because the top of the sample was not in complete contact with the top plate, as is seen in Figure 8.5(e). The initial crack in this sample starts at the point where the sample and the top plate separate, meaning that this defect likely acted as a stress concentrator. Despite the defect, this sample still required the largest load to crack compared to the aforementioned 11 wt% and 12 wt% samples. Also cracking was further accompanied by a catastrophic failure, meaning that sample cracked several more times under a constant load [Figure 8.5(f)]. The difference in behavior of the samples as they are being loaded reveals that small changes in concentration can have a dramatic influence on how the sample spreads and how it reacts to loading. Comparing the results for a 10 wt% bentonite dispersion from Pelot et al.

(2013) with those of the present work, namely 11-13 wt%, one can conclude that in the narrow 10-13 wt% range the dispersions undergo a transition from the Bingham liquid-like behavior characterized by a viscosity and yield stress to a solid-like behavior characterized by cracking.

To further visualize the reaction of bentonite samples of different concentrations to a continuously increasing load, Figure 8.6 shows the cross-sectional area of the samples versus time or load. The area of the 11 wt% sample approximately increased in a linear manner once the load was applied a fully developed deformation process established. After a faint crack has appeared, at the moment marked in Figure 8.6 by the circle on the line, the sample continued spreading at approximately the same pace, even though the load was kept constant from that time on. On the other hand, the 12 wt% and 13 wt% dispersions show a small change in area while the load is being increased. However, once the crack appears and the loading ceases at the moments marked with the circles on the corresponding curves, a large change in slope is observed, as shown the dashed and dashed-dotted lines in Figure 8.6. That means that once the sample cracks a different type of spreading, other than flow, occurs. This type of spreading is due to failure caused by cracking of the material. Furthermore, the 13 wt% sample has a higher slope during failure than the 12 wt% sample meaning that the former case was more catastrophic.

Compressed samples of bentonite dispersions of 11-13 wt% after different resting times were studied next. At every resting time samples of 11 wt% dispersion bulges around the circumference, however, only after resting for 24 h do these samples crack, albeit faintly. The faint cracking pattern could be caused by water flowing to the free surface of the material due to pressure within the material or a realignment of the clay platelets within the material giving a lighter color, albeit it is unclear at this time why the color change occurs. The results for the 12 wt% dispersion are shown in Figure 8.7. At 12 wt%, a sample that has just been created (resting time of 0 h) shows liquid-like behavior by exhibiting a flow profile around the circumference

and reveals no cracks [Figure 8.7(a)]. At a resting time of 3 h, corresponding to Figure 8.7(b), the sample bulges slightly and then cracks. As the resting time is increased, the samples show less bulging at the free surface and more distinct, regular cracking patterns. For the samples of 13 wt% dispersions it was clear that bentonite behavior was solid-like, since cracking occurred without any allotted resting time. Furthermore, the cracks become more distinct as the resting time increases suggesting there may be different types of solid-like behavior. In Figure 8.7 it can be observed that the distance between cracks seems to decrease as resting time increases providing evidence that the material becomes more brittle with increasing resting time. Moreover, in Figure 8.7 for a 12 wt% dispersion we see that the longer resting time requires a higher load to reach cracking of the sample, whereas for 13 wt% dispersion this dependence becomes non-monotonous, and after a longer resting time the cracking load could decrease in some cases.

For the uniaxial compression, the stress tensor  $\boldsymbol{\sigma} = \sigma_{xx} \mathbf{ii}$  (with  $\mathbf{i}$  being the unit vector of the x-axis in Figure 8.2). Then, calculating the shear stress as  $\sigma_{nr} = \boldsymbol{\tau} \cdot \boldsymbol{\sigma} \cdot \mathbf{n}$ , and accounting for the fact that  $\mathbf{i} \cdot \mathbf{n} = \cos \alpha$ ,  $\boldsymbol{\tau} \cdot \mathbf{i} = -\sin \alpha$  (cf. Figure 8.2b), and  $\sigma_{xx} = -F/A$ , we arrive at

$$|\sigma_{nr}| = \frac{F}{2A} \sin 2\alpha \quad (8.1)$$

where the compressive force magnitude is denoted  $F$ , the cross-sectional area is  $A$ , and the magnitude of the shear stress  $\sigma_{nr}$  is found at the plane inclined by an angle  $\alpha$  to the sample bottom (see Figure 8.2).

This shear stress reaches its maximum at  $\alpha = 45^\circ$ , and it is instructive to check whether the 11-13 wt% bentonite samples crack at the planes tilted to the compression axis by  $45^\circ$ . Figure 8.8 shows the data for the magnitude of the compressive stress  $|\sigma_{xx}| = F/A$  based on the force value and the cross-sectional area at the moment of cracking, the cross-sectional diameter  $D$  ( $A = \pi D^2 / 4$ ), the measured value of the angle  $\alpha$ , and the corresponding shear stress found using

Eq. (8.1). It is instructive to see that, indeed, the cracking planes are tilted rather close to  $\alpha=45^\circ$ , as measured from the images similar to those in Figures 5 and 7. Figure 8.8 shows that the values of the shear stress causing catastrophic slip lines and crack formation are rather insensitive to the resting time, but strongly depend on the concentration, being about 300 MPa for 11 wt%, 600 MPa for 12 wt% and 1000-1200 MPa for 13 wt%.

Note that an 11 wt% sample could also reveal simultaneously a liquid-like or a viscoelastic (see below) bulging and a solid-like cracking as is seen in Figure 8.9. In some cases cracks might be vertical rather than inclined.

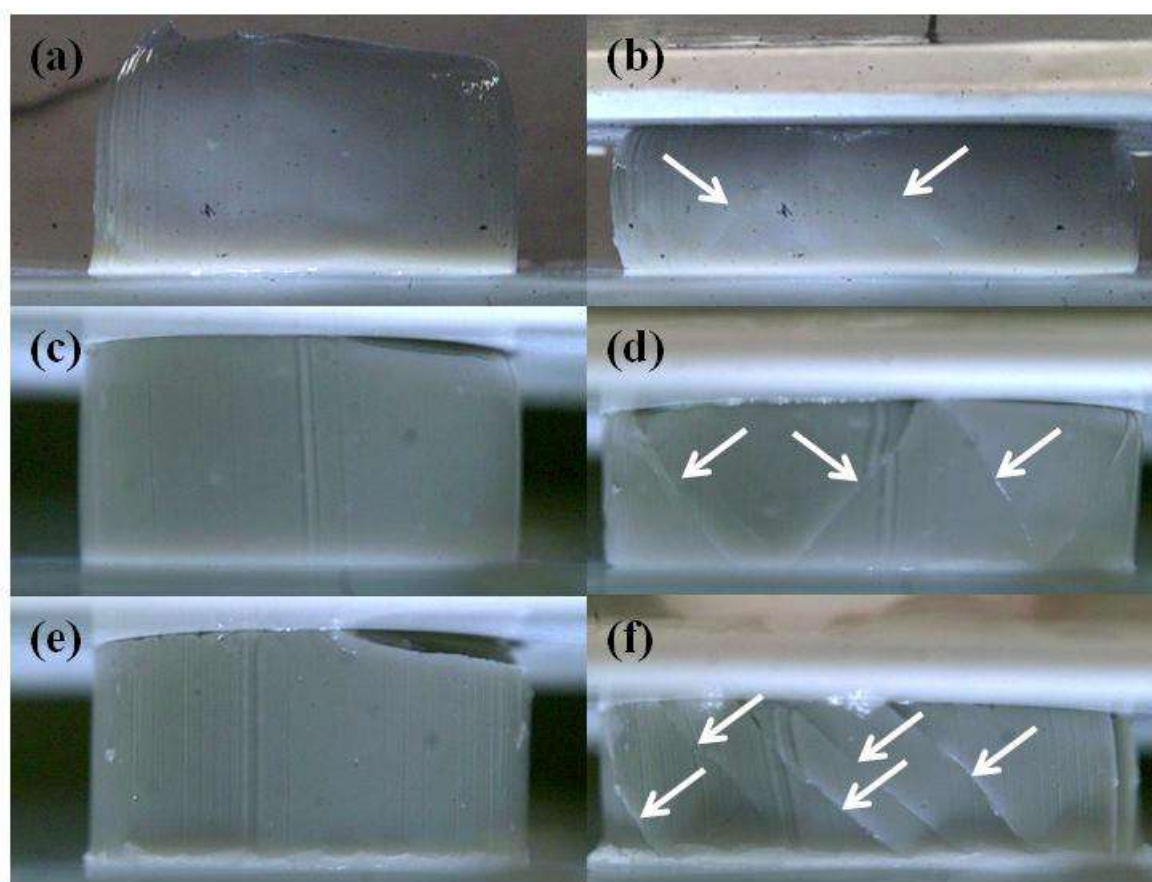


**Figure 8.5.** Samples of several bentonite dispersions after a 48 h resting period which revealed cracking during compression under different loads. Cracks are highlighted by arrows. A sample of 11 wt% bentonite: (a) Initial sample image, (b) final spreading of the sample under 84 g load. A sample of 12 wt% bentonite: (c) Initial sample image, (d) final spreading of the sample under 153 g load. The vertical line at the center of the sample was caused by an irregularity in the syringe. A sample of 13 wt% bentonite (this trial is an example of a sample that spread very quickly once cracking initiated): (e) Initial sample image, (f) final spreading of the sample under 275 g load. The vertical line at the center of the sample was caused by an irregularity in the syringe.



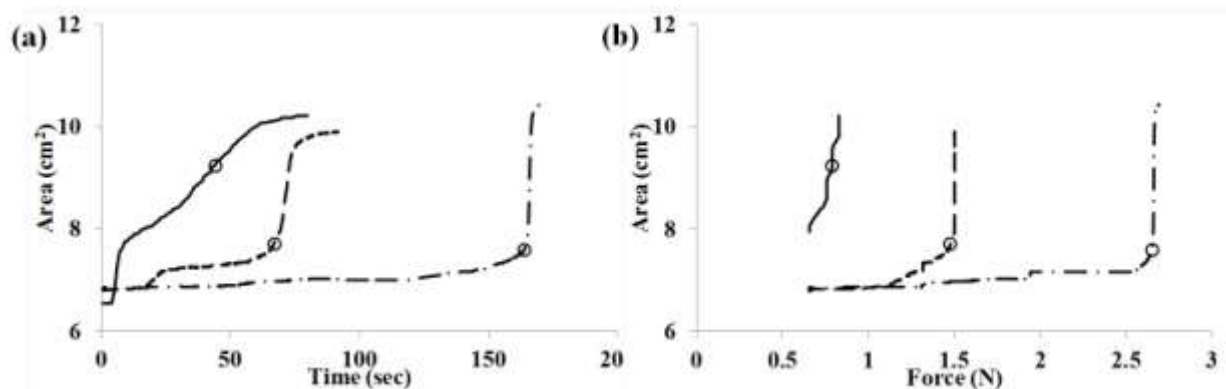


**Figure 8.6.** Cross-sectional area  $A$  [cf. Figure 8.2(a)] of bentonite dispersion samples as they spread due to an increasing load in time. (a) Area versus time, (b) Area versus force. 11 wt% with a resting time of 48 h with corresponding images labeled as in Figures 5(a) and 5(b) (solid line). 12 wt% with a resting time of 48 h with corresponding images labeled as in Figures 5(c) and 5(d) (dashed line). 13 wt% with a resting time of 48 h with corresponding images labeled as in Figures 5(e) and 5(f) (dashed-dotted line).

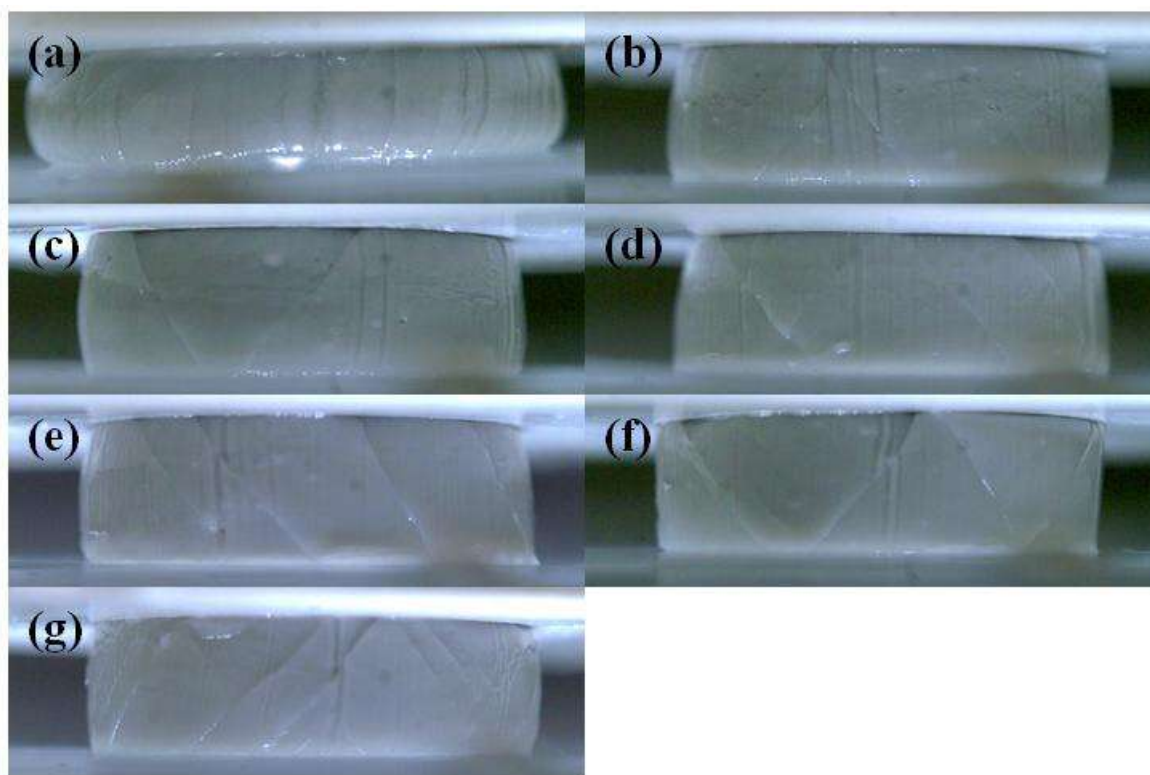


**Figure 8.7.** Final images from the video of a 12 wt% bentonite sample being squeezed under load causing cracking after different resting times: (a) 0 h resting, cracking load 131 g, (b) 3 h resting, cracking load 142 g, (c) 6 h resting, cracking load 107 g, (d) 12 h resting, cracking load 120 g, (e) 24 h resting, cracking load 123 g, (f) 48 h resting, cracking load 153 g, and (g) 72 h resting, cracking load 172 g.

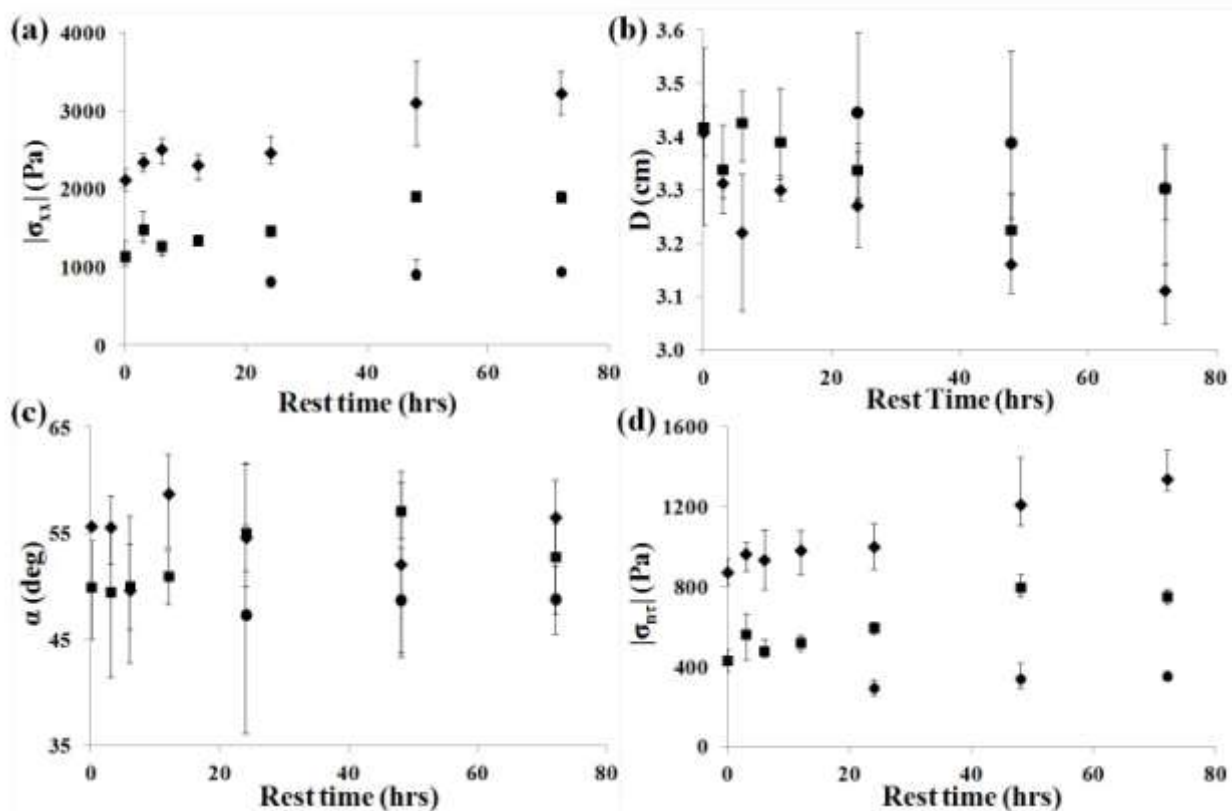


**Figure 8.8.** The data corresponding to the appearance of the first crack. (a) The magnitude of the compressive stress  $\sigma_{xx}$ , (b) the cross-sectional diameter  $D$ , (c), the cracking plane angle  $\alpha$  measured from the images, (d) the shear stress magnitude  $\sigma_{nr}$ . The data for the 11 wt% bentonite samples (circles), 12 wt% bentonite (squares), and 13 wt% bentonite (diamonds). Error bars represent maximum and minimum values for each set of experiments.

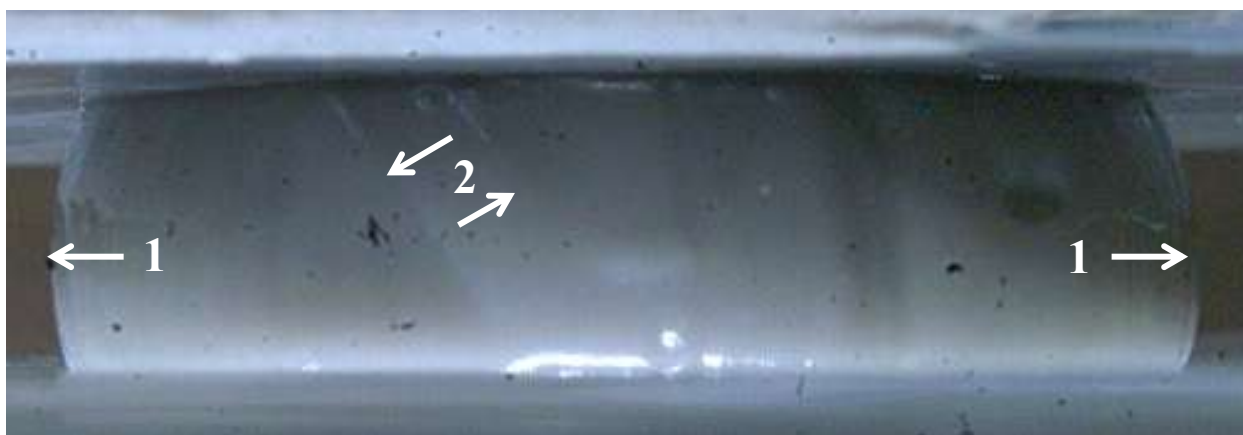


**Figure 8.9.** Sample that reveals both liquid-like and solid-like behavior. The 11 wt% bentonite after a resting time of 24 h and under a mass load of 83 g (40 s after loading started; achieved at the rate 1-2 g/s). Bulging around the circumference (1) and cracking (2).

To further resolve the phenomenology of liquid-to-solid transition in bentonite dispersions, the resting time for 11 wt% bentonite was reduced from 24 h to 12 h. Such samples were loaded at a slow rate of 0.46 g/s and bulging around their circumference was observed from a side view. In Figure 8.10 it is seen that the sample undergoes a slight bulging during initial loading, since the magnitude of the compressive stress acting on it is below the yield stress, and therefore the sample deforms only slightly. Once the stress applied to the sample is greater than the yield stress, the sample starts spreading radially under an approximately constant stress. As the load is increased, the circumferential (tip) diameter of the sample increases to accommodate the added load. It should be emphasized that no visible cracks, either inclined or vertical are seen in Figure 8.10. Note also, that the increase in the sample size visible in Figure 8.10 is significantly smaller than the one revealed in squeezing of 10 wt% liquid-like bentonite dispersions by Pelot et al. (2013).

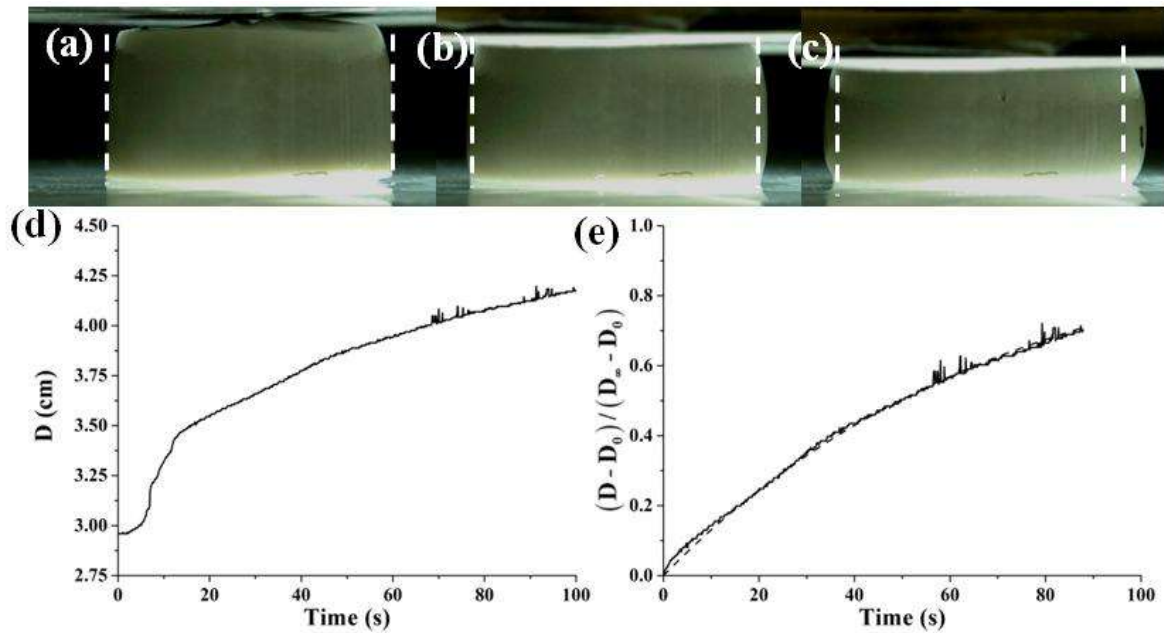


**Figure 8.10.** (a)-(c) Images of 11% bentonite after a resting time of 12 h being slowly compressed by the top plate. In particular, panel (a) corresponds to the initial time, (b)-to 7 s after loading has been started, and (c)-to 10 s. The initial sample configuration is traced by the dashed straight lines in panels (a)-(c). The corresponding creeping evolution of the circumference tip diameter of the sample in (a)-(c) is depicted in panel (d). The latter are reminiscent of those in Figure 8.9. (e) Strain versus time, and fitting according to the Kelvin-Voigt rheological constitutive equation with  $t=0$  corresponding to 12 s of panel (d) when a pronounced bulging has started to develop under an approximately constant compression stress;  $D_0 = 3.33$  cm and  $D_\infty = 4.5$  cm; solid line-the experimental data, dashed line-the Kelvin-Voigt model.

The solid-state deformation with a finite shape memory, as that corresponding to the fully developed bulging visible in Figure 8.10(c) can be interpreted as the Kelvin-Voigt viscoelastic response to load. Then, the current strain  $\varepsilon$  being normalized by the ultimately achievable strain  $\varepsilon_\infty$  can be expressed in terms of the tip diameter  $D$  as  $(D - D_0) / (D_\infty - D_0)$ , where  $D_0$  is the

initial diameter value at  $t=0$  in Figure 8.10(e) when fully developed bulging has started. According to the Kelvin-Voigt rheological constitutive equation (te Nijenhuis 2007),

$$\frac{D - D_0}{D_\infty - D_0} = 1 - \exp(-t / \theta) \quad (8.2)$$

where  $\theta$  is the relaxation time.

Equation (8.2) can be fitted to the data in Figure 8.10(e), which yields the relaxation time  $\theta=71.4$  s. It should be emphasized that this pseudo-Kelvin-Voigt viscoelastic creep of samples transitional from liquid-like (at 10 wt% bentonite) to solid-like can be accompanied by invisible micro-cracking, i.e. possess solid-like features.

### **8.3.2 Bending Experiment**

Specific characteristics of a material are required to test it in the squeezing apparatus. First, the material must be able to be inserted into a dispensing device without air entrapment; this typically means that the material must exhibit some liquid-like behavior. Second, the material must have a sufficiently high yield stress or an extremely high viscosity, such as in Pelot et al (2013), otherwise the material will spread before the compressive force can be applied. Unfortunately, attempts to collect samples with bentonite concentrations greater than 13 wt% in a tip-less syringe caused large air gaps to be present within the bulk material that could not be removed. As the concentration of bentonite dispersions increased, the more solid-like they became, however, they were still too soft to be clamped and therefore were ineligible for a tensile test. As a result, the next available mechanical test is the three-point bending test. For the bending test, the bentonite dispersion must be unyielding under its own weight. It was found by trial and error that 15 wt% dispersions satisfied this condition, but still exhibited some liquid-like behavior when force was applied by the slender bar. Consequently, to ensure solid-like behavior

the lowest concentration used in the bending and buckling experiments described below was 18 wt%.

Layers of 18 wt%, 20 wt%, and 22 wt% bentonite dispersions were subject to bending tests [Figure 8.4(a)] to characterize their mechanical properties. To that aim, a force  $f$  was applied normally at the sample center by the force transducer and the corresponding deflection  $u|_{x=L/2}$  at the center was measured as shown in Figures 11 and 12. The cross-sectional sizes, the thickness  $h$ , width  $b$ , and length between the two supports  $L$  were 1.5 cm, 5 cm and 10 cm, respectively.

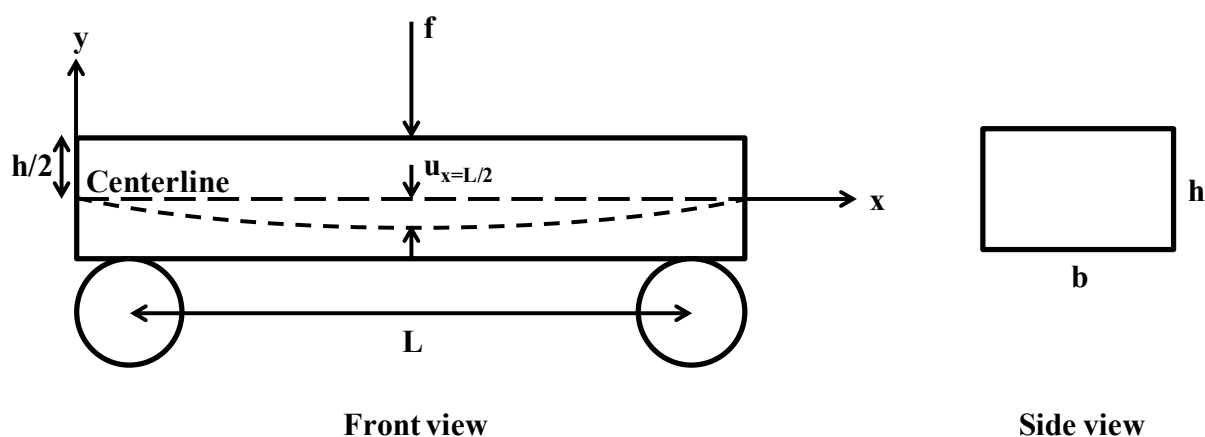


**Figure 8.11.** Sketch of the bending test and the sample cross-section.

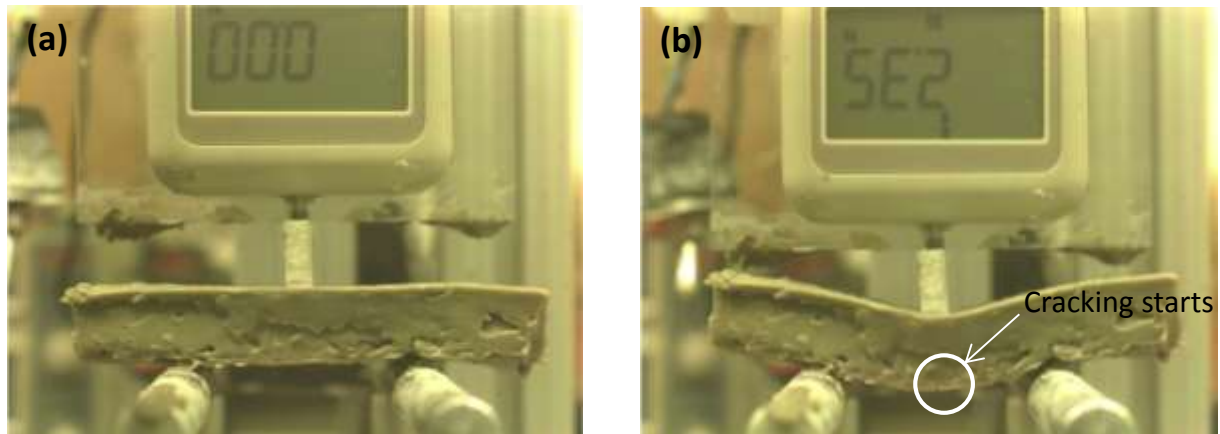


**Figure 8.12.** The images of the 18 wt% bentonite layer subjected to pure bending. (a) The initial intact sample. (b) The bent state at the moment when cracking starts at the bottom surface.

The force-deflection dependences for bentonite samples of different concentrations were measured. The strain at the top and bottom surfaces  $y=\pm h/2$  achieves a maximum value approximately equal to

$$\varepsilon = \frac{h}{2R} \quad (8.3)$$

where  $h$  is the thickness of the sample, and  $R$  is the radius of curvature of the neutral surface related to the small deflection as

$$u|_{x=L/2} = R \left\{ 1 - \cos \left[ \arcsin \left( \frac{L}{2R} \right) \right] \right\} \quad (8.4)$$

Assuming that the sample is subject to pure bending and using Eq. (8.3), the normal stress in the  $x$ -direction is expressed as

$$\sigma_{xx} = \frac{M_b h}{2I_{zz}} \quad (8.5)$$

where  $M_b = fL/4$  is the bending moment and  $I_{zz} = bh^3/12$  is the cross-sectional moment of inertia.



The expressions (3)-(5) allow one to recast the force-deflection  $f = f(u|_{x=L/2})$  into the stress-strain dependence  $\sigma_{xx} = \sigma_{xx}(\varepsilon)$ . The corresponding stress-strain dependences are shown in Figure 8.13. The elastic limit, which is defined as the maximum reversible deformation after unloading, was measured in the bending experiment. In the range of the elastic response, Young's modulus was established. When the plastic regime set in, the yield stress and strain of the bentonite dispersion samples were measured. Lastly, the stress and strain at cracking were also determined. All of the mechanical properties characterizing bentonite dispersions found during the bending experiments are listed in Table 8.1. Overall, a higher bentonite content results in a higher stress at the same strain as is seen in Figure 8.13. The corresponding mechanical properties are shown in Figure 8.14 for different bentonite contents. In particular, note that the cracking stress increases while the cracking strain decreases as the bentonite content increases. It should be emphasized that the stress-strain dependence of the concentrated bentonite dispersions was measured for the first time, as to our knowledge.

**Table 8.1.** Rheological parameters of bentonite dispersions based on three trials in each case.

Item	Unit	18 wt% bentonite	20 wt% bentonite	22 wt% bentonite
Thickness, h	cm	1.5	1.5	1.5
Young's modulus, E	kPa	337±16	386±21	499±48
Yield stress, Y	kPa	9.1±0.4	10.4±1.1	14.8±1.4
Strain at yield, $\varepsilon_Y$	%	2.7±0.1	2.7±0.19	3.0±0.25
Stress at cracking, $\sigma_{crack}$	kPa	15.9±0.8	19.5±0.6	25.6±2.3
Strain at cracking, $\varepsilon_{crack}$	%	9.8±0.3	9.1±0.3	8.2±0.7

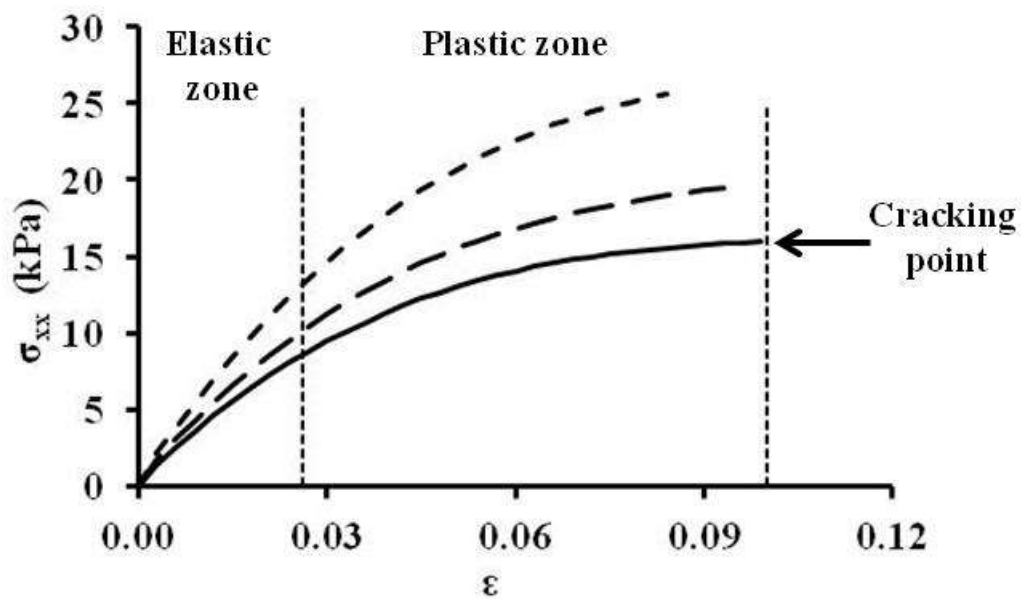


**Figure 8.13.** Stress-strain dependences of bentonite dispersions of different contents. Solid line corresponds to 18 wt% bentonite, long dash - 20 wt% bentonite, and short dash - 22 wt% bentonite.

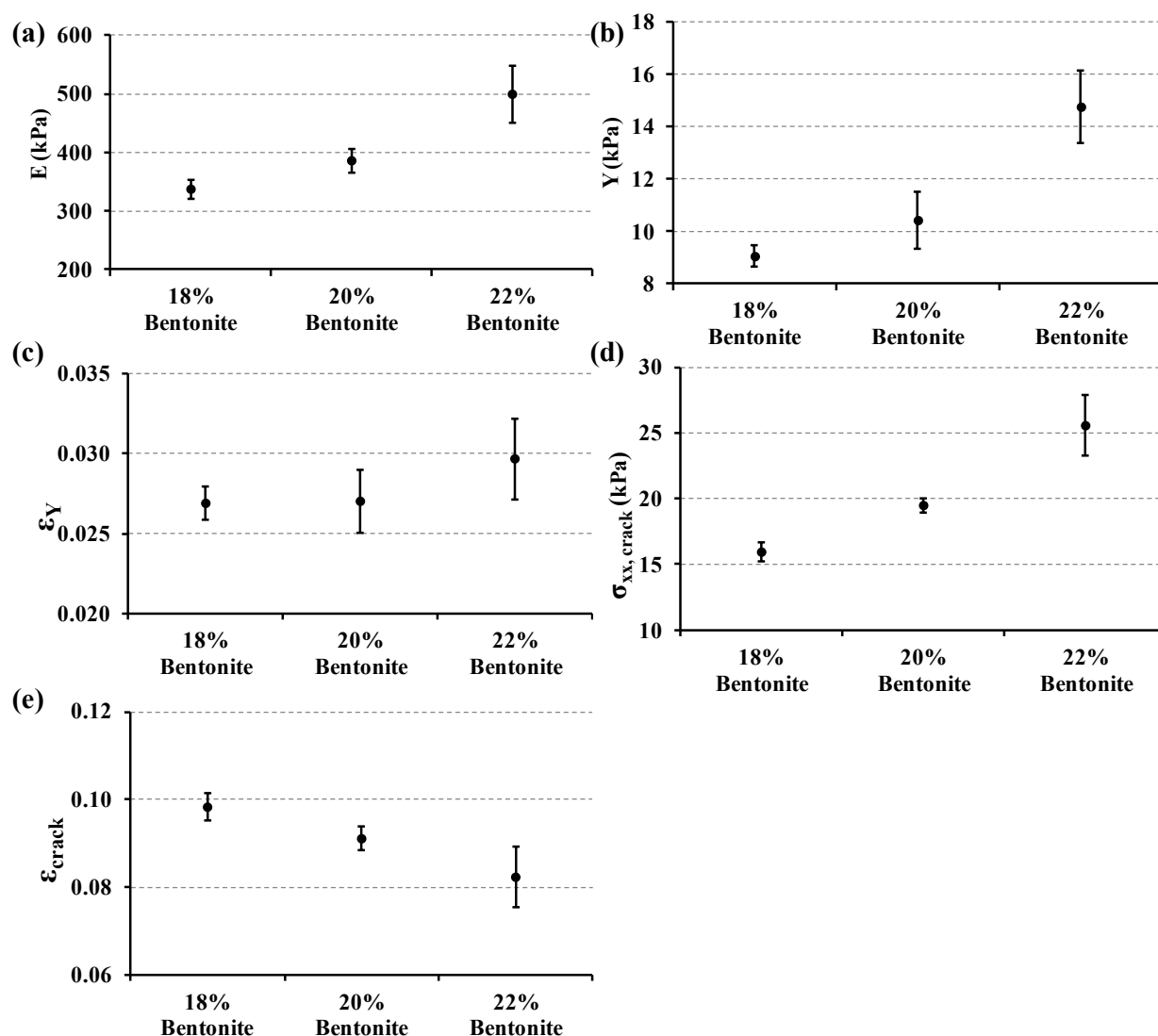


**Figure 8.14.** The measured rheological parameters of bentonite dispersions corresponding to Table 8.1. (a) Young's modulus  $E$ . (b) Yield stress  $Y$ . (c) Strain at yield  $\epsilon_Y$ . (d) Stress at cracking  $\sigma_{xx, crack}$ . (e) Strain at cracking  $\epsilon_{crack}$ .

The stress-strain dependences discussed above show that the 18-22 wt% bentonite samples possess an elastic zone (below  $\epsilon = 2.7\%$ ) followed by a subsequent plastic zone where the stress keeps increasing until cracking starts at the bottom surface, as shown in Figure 8.13.

### **8.3.3 Buckling Experiment**

Buckling experiments were conducted to visualize and measure cracking characteristics, especially exactly at the moment when cracking occurs [Figure 8.4(b)]. This provides an independent measurement of the cracking stress and strain and helps to visualize the onset of the cracking (the latter was difficult in the bending experiments). The results revealed that cracking occurred at the radius of curvature  $R$  approximately equal to 9 cm, and the corresponding strain at cracking was approximately 8% as shown in Table 8.2. This strain value is in good agreement with the result of the bending experiments in subsection III.B, which is  $9.1 \pm 0.3\%$  for 20 wt% of bentonite (cf. Table 8.1). As expected, the onset of cracking in buckling revealed a slightly lower strain than in bending, where only fully developed cracks were visible when they propagated to the edge of the sample.

**Table 8.2.** Strain at cracking in the buckling experiment for 20 wt% bentonite.

No. of trial	1	2	3	Average
Radius of curvature (cm)	11	8.4	8.6	9.3
Strain at cracking	6.8 %	8.9 %	8.7 %	8.0 %

### **8.4 Discussion**

Clay platelets self-organize within the liquid due to forces caused by cation repulsion within the swelling layer and the surface charge of platelets. This was compared to a house of cards by van Olphen (1964). According to van Olphen (1964), if the concentration is sufficiently high and bentonite platelets are able to fill the available volume, edge-to-edge and edge-to-face

associations will result in gelation of bentonite. Clearly, at low concentrations the cards feel each other's presence and organize accordingly to create a yield stress but will flow when a sufficiently large external stress is applied. As the concentration increases, the number of "cards" increases. Then, there exists a concentration where enough "cards" are present to create a stable structure. Stress can be applied to this structure while still holding its shape. This represents a high enough concentration for bentonite dispersion to act like a solid-like material. Then, as a solid, when the stress exceeds the critical shear stress, such bentonite dispersion would crack, which is observed in the present work.

Moreover, bentonite possesses two mechanisms that result in solid-like behavior of its dispersions. First, increasing concentration allows an optimum distance between platelets to be reached so that structural skeleton within the material is easily attainable, as described above. Second, bentonite is a non-thixotropic material (Pelot et al. 2013) which shows an irreversible aging as a result of slow swelling of the clay crystallites. The formation of the fully developed structural skeleton results in the observed solid-like behavior of concentrated bentonite dispersions.

When a sample was being loaded in our squeezing apparatus, a range of mechanical reactions arose. If there existed a loose internal structure, either by a lack of concentration or resting time, the sample began to bulge around the circumference, created a rounded profile and spread as a liquid until the yield stress was achieved. If the load continued to increase, then the sample would again spread until the yield stress was achieved, as in Pelot et al. (2013). On the other hand, when there existed a well-defined internal structure, either by an excess in concentration or a long resting time, the outer surface of the sample remains undisturbed and spreads radially. As the load was increased by adding more water to the reservoir, the sample continued to spread and was stretched radially and azimuthally, which resulted in radial cracks

described by Eq. (8.1). Interestingly, there exists an intermediate state of the material between solid-like and liquid-like behavior, such as in the images of 11 wt% bentonite samples with a resting time of 24 h where both types of behavior are visible (cf. Figure 8.9). That is, at first the sample bulges around the circumference, then under a sufficiently high load the sample shows weak signs of cracking. By weak it is meant that faint angled lines can be seen in the sample, as in Figure 8.9. After increasing the load by adding water, the sample continues to spread as a liquid. This type of behavior has also been discussed by Logan (1978) for rocks that can experience transition from macroscopic brittle to ductile behavior. Note also, that during transition from liquid-like to solid-like behavior, cracks can be invisible/absent, or vertical or inclined, and the material behavior formally corresponds to that of viscoelastic solid of the Kelvin-Voigt rheological constitutive equation, with strain response to stress possessing a measurable finite relaxation time and slowly approaching saturation.

The concentrations used in this study were chosen specifically so that at small resting times, less than a few hours, bentonite dispersions will act as a liquid. That is it will flow when stressed and not crack. This is evident from the results for the 11 wt% bentonite samples up to and including 12 h resting time, and 12 wt% bentonite samples at 0 h resting time. It has been shown before that even at lower concentrations of bentonite after extremely long resting times samples can also become solid and reveal cracking at very low stress levels [Gotoh and Shimizu (1965)]. Besides resting time, an increase in concentration also causes more solid-like behavior even if the concentration change is only 1 wt%. As mentioned above, the 12 wt% bentonite concentration represents the highest concentration that will exhibit liquid-like behavior immediately after stirring after hydration has taken place. For the 13 wt% bentonite samples our results showed that the samples crack under compression immediately after being formed.

A bentonite dispersion will possess a more developed structure with an increase in concentration and resting time since the stress level which causes cracking is an indicator of the structure strength [Figure 8.8(a) and 8.8(d)]. Indeed, the load needed to cause cracking increases with bentonite concentration and resting time. Also, from Figure 8.8(b) it is seen that an increase in concentration causes the diameter at sample failure to decrease with an increase in concentration. Similarly, an increase in resting time required a lower strain to induce cracking. Therefore, both an increase in load and decrease in strain (at cracking) occur at higher concentrations of bentonite. In both cases concentration increase and resting time increase, the diameter at cracking did decrease, albeit slightly.

After the solid-like behavior was attained in bentonite dispersion, either by an increase of concentration or resting time, it was of interest to explore whether further increases in concentration would result in commensurate stress levels needed to cause failure of bentonite dispersion samples. Therefore, two additional types of experiments (bending and buckling) were conducted to find the stress at cracking and the yield stress for higher (18-22 wt%) concentrations of bentonite dispersions. Then, comparing the results of the three types of experiments (squeezing, bending and buckling) for the entire range of bentonite concentrations explored (11-22 wt%) it was found that the yield stress belongs to the same linear dependence on the concentration as shown in Figure 8.15(a). The normal cracking stress seemingly reveals two different linear dependences on the concentration for those samples which were studied in the squeeze and bending experiments, respectively as shown in Figure 8.15(b). The results in Figure 8.15(b) for the 11-13 wt% concentrations correspond to the magnitude of the compressive normal stress, while those for the 18-22 wt% range – to the tensile normal stress. Therefore, the linear dependences for them differ. It should be emphasized that it is very difficult to collect an intermediate set of data between these two regimes because it is practically impossible to prepare

bentonite dispersions above 13 wt% to be compressed in the squeeze apparatus and dispersions below 18 wt% to be subjected to three-point bending.

An additional information on the rheological conditions corresponding to the transition from liquid to solid and purely solid behavior of bentonite dispersions was provided by measurements of the storage and loss moduli  $G'$  and  $G''$ , respectively, conducted using a TA Instruments rheometer (model HR-2) with a 40 mm diameter crosshatched Peltier plate attachment. The data acquired for 11 wt% and 22 wt% bentonite dispersions are shown in Figures 16(a) and 16(b), respectively. The loss angle  $\delta = \arctan(G'' / G')$  for 11 wt% bentonite was in the range from  $5^\circ$  to  $30^\circ$  at frequencies of the order of 1 Hz, and practically  $90^\circ$  at frequencies from 70 to 100 Hz depending on the strain. On the other hand, for the 22 wt% bentonite  $\delta$  was in the range from  $3^\circ$  to  $5^\circ$  at frequencies of the order of 100 Hz, and  $18^\circ$  to  $29^\circ$  at a frequency of 0.2 Hz depending on the strain. The values of  $\delta$  for 11 wt% bentonite approaching  $90^\circ$  reveals that this transitional sample tends is not very far from the Bingham fluid (10 wt% bentonite; Pelot et al. 2013). On the other hand, the loss angle  $\delta$  for 22 wt% bentonite approaching  $0^\circ$  reveals that this sample is practically solid. For 22 wt% bentonite dispersion at 2% strain Figure 8.16(b) yields the shear modulus  $G = \sqrt{G'^2 + G''^2}$  as  $G = 122$  kPa, which yields Young's modulus  $E=3G$  as  $E=366$  kPa. This value is in a reasonable agreement with  $E=499$  kPa in Figure 8.14(a). At 5% strain  $G = 76$  kPa and  $E = 228$  kPa.

Cracking of bentonite dispersions using compression was reported in Gotoh and Shimizu (1965). Their bentonite dispersions differ from the present study for two reasons. Their samples had a resting time of seven days, and the preparation method allowed them to remove coarse particles from their samples. Such samples always revealed a solid-like behavior and never a liquid-to-solid transition found in the present work. A longer resting time has been shown in the present work to increase the cracking stress and it is inferred that finer and a more uniform



particle size will create a more stable structure which correlates with an increase in cracking stress. Figure 8.17 shows the shear stress found in Gotoh and Shimizu (1965) for compression and viscometer tests as well as the results from the present work. The shearing box results of Gotoh and Shimizu (1965) were not included in Figure 8.17 because they are in agreement with their other two tests. In both studies, the shear stress displays a linear dependence on bentonite concentration and, as expected, the results of Gotoh and Shimizu (1965) are slightly higher than the results found in the present study. It is emphasized that in distinction from the present work, Gotoh and Shimizu (1965) did not observe the transition from the liquid-like to solid-like behavior in bentonite dispersions.

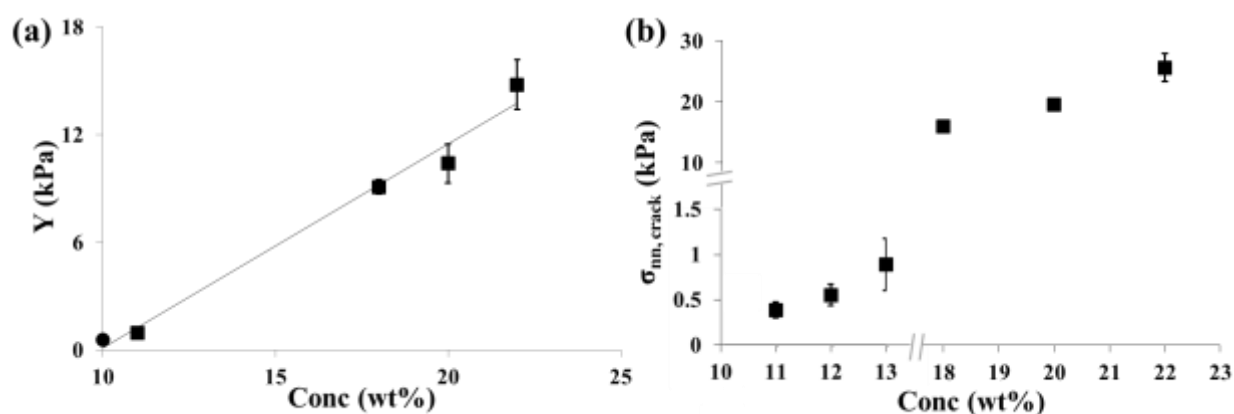


**Figure 8.15.** (a) Yield stress versus bentonite concentration found in the present study (squares) and in Pelot et al. (2013) (circle). It is emphasized that this linear dependence spans the yield stress  $Y$  found for the liquid-like bentonite dispersions with  $Y$  found for the solid-like bentonite dispersions. The yield stress  $Y=F/A$ . (b) Average (over all resting times) stress magnitude at cracking versus bentonite concentration. Error bars represent the standard deviation. Some error bars are too small to be seen. Note that in panel (b) the magnitude of the normal stress at

cracking of the 11-13 wt% bentonite dispersions in the squeezing experiments is found as  $\sigma_{nn} = (F/A)\cos^2\alpha$ , which is to be compared to  $\sigma_{xx}$  in the bending and buckling experiments.

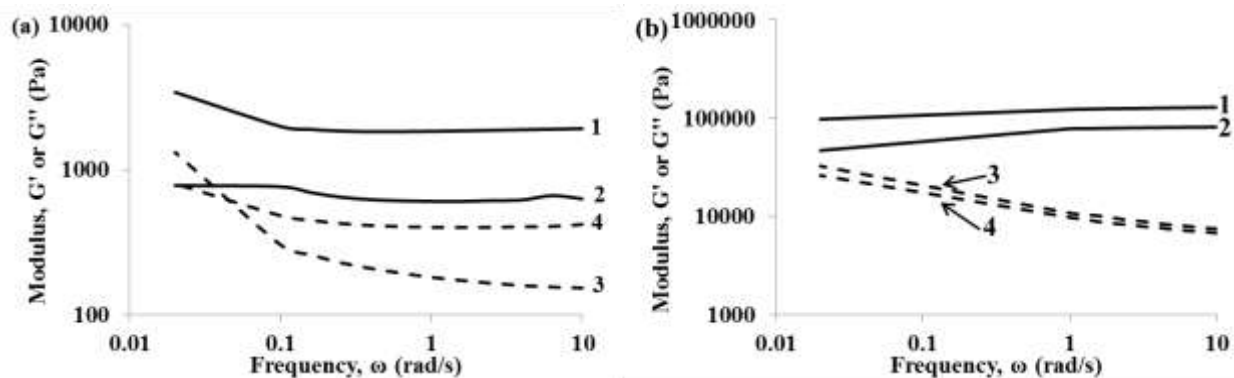


**Figure 8.16.** Storage (solid lines) and loss (dashed lines) moduli. (a) 11 wt% bentonite: 1-storage modulus at 10% strain, 2-storage modulus at 30% strain, 3-loss modulus at 10% strain, 4-loss modulus at 30% strain. (b) 22 wt% bentonite: 1-storage modulus at 2% strain, 2-storage modulus at 5% strain, 3-loss modulus at 2% strain, 4-storage modulus at 5% strain.

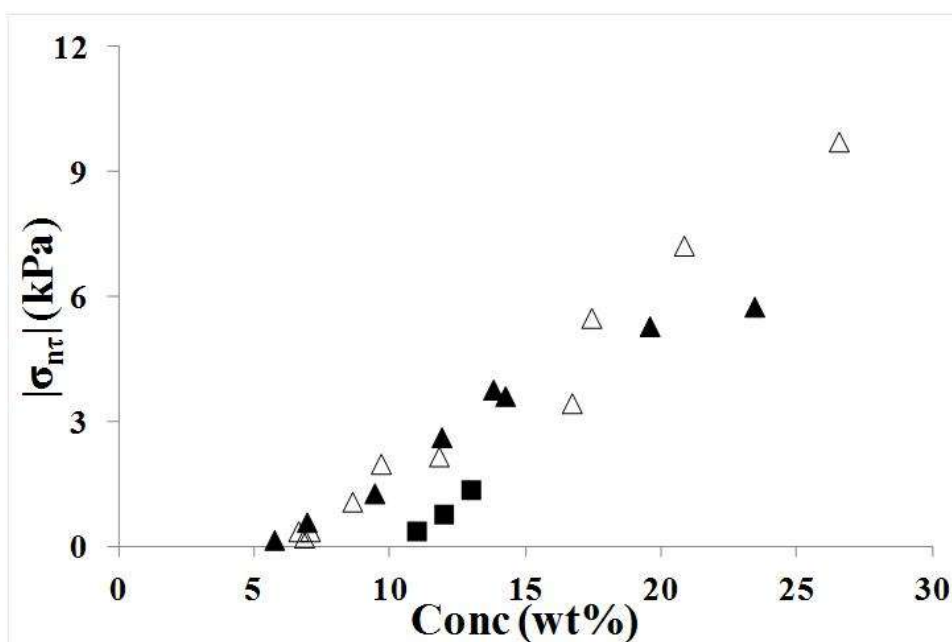


**Figure 8.17.** Shear stress required to initiate cracking at different concentrations after 3 days resting time (squares) found in the present work, and in Gotoh and Shimizu (1965) for 7 days of resting time (compression – open triangles and in shear – solid triangles).

### **8.5 Conclusion**

Bentonite dispersions were studied over a range of concentrations and resting times. The mechanical properties of the 11 wt%, 12 wt%, and 13 wt% dispersions were investigated using a squeezing apparatus, and those of the 18 wt%, 20 wt%, and 22 wt% dispersions were studied using a three-point bending test and a buckling experiment. At lower bentonite concentrations (11-13 wt%) a transition between a liquid-like and solid-like behavior was revealed in the experiments with the squeezing apparatus. In particular, at concentrations of 11 wt% and 12 wt%, after short enough resting times, cylindrical samples of the bentonite dispersion spread radially until the flow was arrested by the yield stress, as Bingham liquids. On the other hand, at these concentrations for longer resting times, or at 13 wt% at any resting time the samples behaved as solid bodies, and either held the compressive load or cracked when it exceeded a critical value. Transition from a liquid-like to a solid-like behavior in a single experiment was also observed for the 11-12 wt% bentonite dispersions. The dependence of the mechanical response on the resting time implies that bentonite dispersions are irreversibly aging materials. At higher concentrations (18-22 wt%) the material behavior was solid-like. The bending experiments revealed a linear elastic response followed by plasticity and cracking. The bending and buckling tests revealed crack formation at approximately the same value of strain at cracking. The results of the bending experiment were used to measure Young's modulus, the yield stress, stress and strain at cracking, and the stress-strain dependence as a function of bentonite concentration. The higher bentonite concentrations in the samples corresponded to larger Young's modulus, yield stress and cracking

stress, as well as smaller strain at cracking. The dependence of the yield stress on the bentonite concentration was found to be linear in the entire 11-22 wt% range of bentonite concentration. Overall, the liquid-to-solid transition of dispersions of bentonite particles at the concentration close to 11-12 wt%, followed by the solid-like behavior characterized by cracking discovered in the present work is an amazing phenomenon, shedding new light on mechanical behavior of clay suspensions, as well as probably many other suspensions and dispersions.

## 9. SPREADING OF CARBOPOL GELS: NEWTONIAN VERSUS NON-NEWTONIAN EFFECTS

### 1. Introduction

This Chapter aims to study flow within a wedge of a Non-Newtonian material at the angles larger than those typically used in the lubrication approximation. Flow within a wedge occurs when a soft material is pulled by a moving plate through a decreasing cross-section determined by the wedge until it exits at a designated minimum height. The flow can be viewed as a combination of Couette and Poiseuille flows. In the experiment, a Carbopol solution is pulled through the wedge at various angles and exit heights using a conveyer belt at different speeds. The wedge is fixed at the exit by a pivot joint but at the entrance is free to rotate. Furthermore, a force gauge is placed at the entrance, halting the rotating of the wedge, which measures the resulting force caused by the pressure under the wedge. Using visualization through the transparent wall of the wedge, seeding particles inside the solution were tracked and a velocity profile was constructed for several flow cases. The experimental velocity profile based on the Herschel-Bulkley rheological constitutive equation is compared to the analytical result of the lubrication approximation for a Newtonian fluid, as well as a Bingham fluid. The experimental and analytical velocity profiles for a Newtonian fluid are similar near the moving plate and near the exit where the shear rate overcomes the yield stress. By using the balance of moments of force acting onto the plate from the material and the gauge resisting the movement of the upper plate of the wedge, an effective viscosity is determined. This viscosity is found to be in agreement with the values measured using a vane viscometer. However, near the wedge surface the yield stress dominates and creates a domain with a plug flow typical of the yield

stress materials as predicted by the Bingham model. Two types of core formation, attached and floating, are visualized in the present experiments. The reduction of the reverse flow velocity and core formation near the wedge by the yield stress is in good agreement is found in the experiment and discussed in the light of the theoretical predictions. The viscosity value found for the Bingham model is an order of magnitude larger than that for the Newtonian model but may be associated with the shear-thinning behavior of the Herschel-Bulkley fluid.

The theoretical background based on the Newtonian fluid model and a summary of Bingham fluid model by Tichy (1991) are discussed in Section 9.2. The experimental setup and method are described in detail in Section 9.3. The experimental results are presented versus the theory from both models in Section 9.4. A discussion of the results is in Section 9.5. Conclusions are drawn in Section 9.6.

## **9.2 Theoretical Background**

### **9.2.1 Pressure and Flow Pattern for a Newtonian Fluid**

Spreading flow, when the inclined plate is tilted relative to the surface by a sufficiently small angle  $\alpha$  (cf. Figure 9.1), which is similar to that in screws extruders and journal bearings, can be effectively tackled in the framework of the so-called lubrication approximation [Schlichting (1987), Tadmor and Gogos (2006); Loitsyanskii (1966)]. It is emphasized that for soft materials the viscosity is always sufficiently high to neglect the inertial effects and consider the flow as being completely dominated by viscous forces. To have a steady-state flow pattern, we assume that the inclined plate does not move, whereas the horizontal plate (wall) with a soft material adhering to it due to the no-slip condition is moving in the positive direction along the  $x$  axis with velocity  $V_0$  (Figure 9.1). The effect of the inclined plate is initially felt as an adverse

pressure gradient (see Figure 9.2). As a result, pressure first increases in the  $x$ -direction from its initial value on the left from the wedge-like gap between the plates, where it is equal to the atmospheric pressure  $p_0$ . However, since at the exit from the wedge-like gap between the plates at  $x=L$  the free surface appears again and is again exposed to the atmospheric pressure, pressure there should be equal once more to  $p_0$ . Therefore, after reaching the maximum at a certain  $x=x_*$ , pressure starts to decrease, as shown schematically in Figure 9.2.

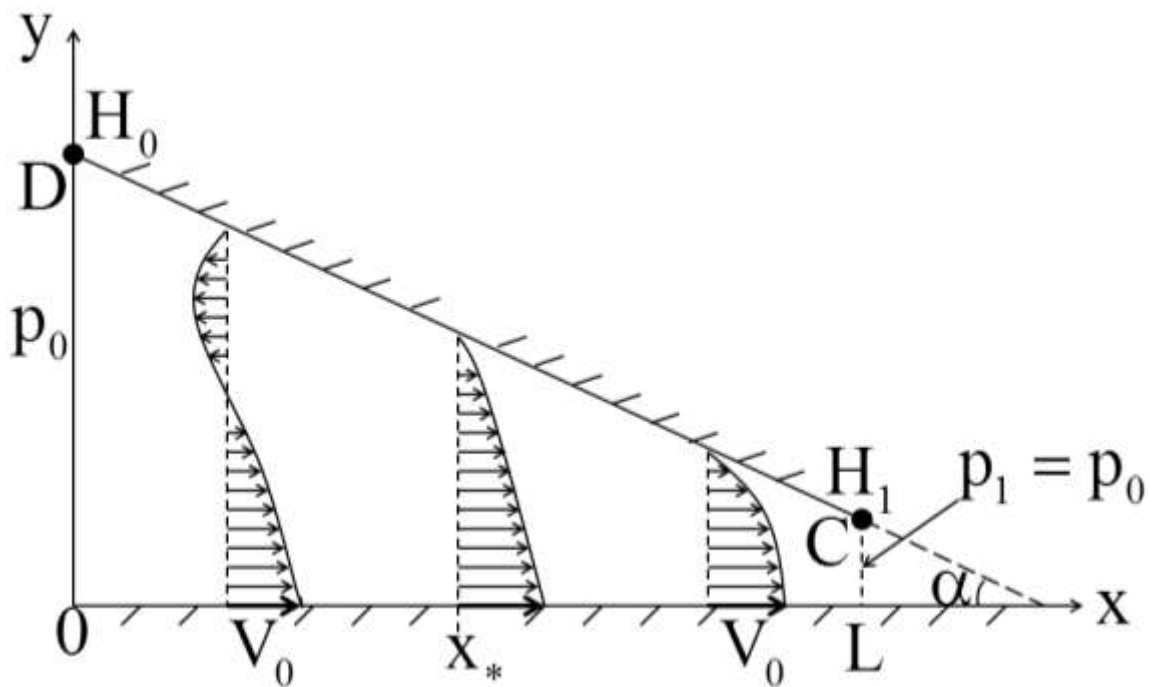


**Figure 9.1.** Spreading flow and the corresponding flow field.

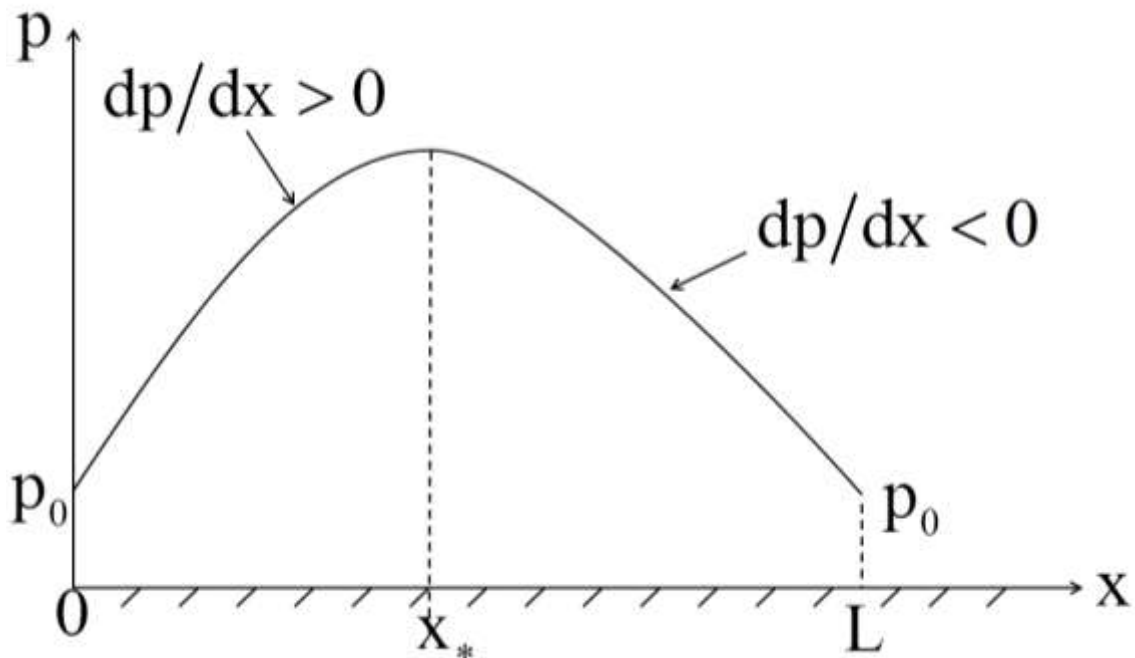


**Figure 9.2.** Sketch of pressure distribution corresponding to Figure 9.1.

It is intuitively clear that the adverse pressure gradient at  $0 \leq x \leq x_*$  will result in a reverse flow ( $u < 0$ ) in part of the velocity profile corresponding to this range (see Figure 9.1). Only at  $x = x_*$  where  $dp/dx = 0$ , the effect of the pressure gradient on the velocity profile should disappear and the latter should become linear, as expected in the simple shear flow. On the other hand, in the interval  $x_* \leq x \leq L$  the pressure gradient  $dp/dx < 0$ , i.e. facilitates the flow along the  $x$  axis. Therefore, the velocity profile becomes parabolic there (see Figure 9.1). It should be emphasized that in the simple shear flows at high Reynolds numbers, vortex formation would be possible. However, in the present case, the Reynolds numbers are expected to be low, and the shear at the boundary between the forward and reverse velocity will not create vortices. This allows one to assume that the pressure gradient in the vertical direction can be neglected.



### 9.2.2 Lubrication Approximation for a Newtonian Fluid

In the lubrication approximation the longitudinal velocity component  $u$  is much larger than the lateral one,  $v$ . On the other hand,  $\partial \bullet / \partial y \gg \partial \bullet / \partial x$ . Under these assumptions, the Stokes equations for the creeping flow under consideration are reduced to the following Reynolds equation for pressure [Tadmor and Gogos (2006)]

$$\frac{d}{dx} \left( H^3 \frac{dp}{dx} \right) = 6\mu V_0 \frac{dH}{dx} \quad (9.1)$$

where  $\mu$  is viscosity, and the gap thickness  $H$  can be taken as if the inclined plate is straight as in Figure 9.1

$$H(x) = H_0 - \frac{H_0 - H_1}{L} x \quad (9.2)$$

Solutions of Eq. (9.1) are subject to the following boundary conditions, as discussed above,

$$x = 0, \quad p = p_0 \quad (9.3)$$

$$x = L, \quad p = p_0 \quad (9.4)$$

Solving Eq. (9.1) with the boundary conditions (9.3) and (9.4), we obtain in the dimensionless form

$$\bar{p} = \bar{p}_0 + \frac{6}{(\bar{H}_0 - 1)} \left[ \frac{1}{\bar{H}_0 - (\bar{H}_0 - 1)\bar{x}} - \frac{1}{\bar{H}_0} \right] - \frac{6\bar{H}_0}{(\bar{H}_0^2 - 1)} \left\{ \frac{1}{[\bar{H}_0 - (\bar{H}_0 - 1)\bar{x}]^2} - \frac{1}{\bar{H}_0^2} \right\} \quad (9.5)$$

In Eq. (9.5)  $x$  is rendered dimensionless by  $L$ ,  $p$  and  $p_0$  by  $\mu V_0 L / H_1^2$ , and the geometric parameter  $\bar{H}_0 = H_0 / H_1$ . The pressure distribution (9.5) reaches maximum at

$$\bar{x}_* = \frac{\bar{H}_0}{\bar{H}_0 + 1} \quad (9.6)$$

The dimensionless velocity distribution corresponding to the pressure distribution (9.5) is found as [Schlichting (1987)]

$$\bar{u}(\bar{x}, \bar{y}) = 1 - \frac{\bar{y}}{\bar{H}} + \frac{\bar{y}\bar{H}}{2} \frac{d\bar{p}}{d\bar{x}} \left( \frac{\bar{y}}{\bar{H}} - 1 \right) \quad (9.7)$$

where according to Eq. (9.2)

$$\bar{H} = \bar{H}_0 - (\bar{H}_0 - 1)\bar{x} \quad (9.8)$$

In Eqs. (9.7) and (9.8)  $u$  is rendered dimensionless by  $V_0$ , and  $y$  and  $H$  by  $H_1$ . Equations (9.7) and (9.5) determine the velocity and pressure fields corresponding to the sketches in Figures 9.1 and 9.2, respectively.

Given the velocity field of Eq. (9.7) and accounting for the fact that due to the continuity equation  $\partial v / \partial y = -\partial u / \partial x$ , we find the dimensionless stress components in the following form

$$\bar{\sigma}_{xx} = -\bar{p} + 2 \frac{H_1^2}{L^2} \frac{\partial \bar{u}}{\partial \bar{x}} \quad (9.9)$$

$$\bar{\sigma}_{xy} = \frac{H_1}{L} \frac{\partial \bar{u}}{\partial \bar{y}} \quad (9.10)$$

$$\bar{\sigma}_{yy} = -\bar{p} - 2 \frac{H_1^2}{L^2} \frac{\partial \bar{u}}{\partial \bar{x}} \quad (9.11)$$

The stress components in Eqs. (9.9)-(9.11) are rendered dimensionless by  $\mu V_0 L / H_1^2$ .

In the spreading process the ratio  $H_1/L \ll 1$ , if the angle of inclination is small,  $\alpha \ll 1$ , therefore,  $\cos \alpha$  is close to 1. As a result, the dimensionless normal force  $\bar{F}_n$  acting at the inclined plate rendered dimensionless by  $\mu V_0 L^2 W / H_1^2$  (where  $W$  is the plate width) reduces to

$$\overline{F}_n = \int_0^1 \overline{\sigma_{xx}} \Big|_{y=\overline{H}} d\overline{x} = - \int_0^1 \overline{p} \Big|_{y=\overline{H}} d\overline{x} \quad (9.12)$$

The last integral in Eq. (9.12) is evaluated using Eq. (9.5). Note, that the term  $\overline{p}_0$  in the latter is immaterial since it will be inevitably compensated by the atmospheric pressure of air acting at the “free” surface of the inclined plate. Therefore, the total normal force is equal to

$$\overline{F}_{n,\text{total}} = - \frac{6}{(\overline{H}_0 - 1)} \left[ \frac{\ln \overline{H}_0}{(\overline{H}_0 - 1)} - \frac{1}{\overline{H}_0} \right] + \frac{6}{\overline{H}_0 (\overline{H}_0 + 1)} \quad (9.13)$$

In the approximation of small inclination we are dealing with,  $\overline{H}_0 = 1 + \gamma$ , where  $\gamma \ll 1$ . Then, Eq. (9.13) reduces to  $\overline{F}_{n,\text{total}} = -\gamma/2$ , and the dimensional normal stress becomes

$$F_{n,\text{total}} = - \frac{(\overline{H}_0 - 1)}{2} \frac{\mu V_0 L^2}{H_1^2} W \quad (9.14)$$

To find the point of application of this force, one needs also to calculate the moment of normal stresses acting on the inclined plate relative to point C in Figure 9.1. In the approximation we are dealing with, the dimensionless moment  $\overline{M}_{C,\text{total}}$  rendered dimensionless by  $\mu V_0 L^3 W / H_1^2$  is equal to

$$\overline{M}_{C,\text{total}} = - \int_0^1 (1 - \overline{x}) \overline{p} d\overline{x} \quad (9.15)$$

To evaluate this integral in the limit of small inclination when  $\overline{H}_0 = 1 + \gamma$  and  $\gamma \ll 1$ , we can expand the dimensionless pressure of Eq. (9.5) as

$$\overline{p} = 3\gamma\overline{x} - 3\gamma\overline{x}^2 \quad (9.16)$$

where, as before, the term  $\overline{p_0}$  is omitted, since its effect is compensated by the air pressure outside the inclined plate. Note, that using Eqs. (9.16) and (9.12), we recover once again the previously obtained result

$$\overline{F_{n,\text{total}}} = -\frac{\gamma}{2} \quad (9.17)$$

Substituting Eq. (9.16) into Eq. (9.15) and evaluating the integral, we obtain in the same limit of small  $\gamma$

$$\overline{M_{C,\text{total}}} = -\frac{\gamma}{4} \quad (9.18)$$

The location of the center of pressure  $\overline{x_f}$  is determined by the equality of the moment  $\overline{M_{C,\text{total}}}$  to the moment of force  $\overline{F_{n,\text{total}}}$ , which yields

$$\overline{M_{C,\text{total}}} = \overline{F_{n,\text{total}}} (1 - \overline{x_f}) \quad (9.19)$$

and thus

$$\overline{x_f} = 1 - \frac{\overline{M_{C,\text{total}}}}{\overline{F_{n,\text{total}}}} \quad (9.20)$$

Equations (9.17), (9.18) and (9.20) yield

$$\overline{x_f} = \frac{1}{2} \quad (9.21)$$

i.e. in the limit of the small slope of the inclined plate ( $\gamma \ll 1$ ), the center of pressure is located at the center of that plate or, in the other words, the force  $\overline{F_{n,\text{total}}}$  is applied at that point.

In the experiment the dimensionless force  $\overline{F_{\text{exp}}}$  which keeps the inclined plate at its position against the pressure from the soft material underneath is determined by the following

moment-of-force balance (cf. Figure 9.3) when  $\overline{F}_{\text{exp}}$  is measured at the upper end of the inclined plate

$$|\overline{F}_{\text{exp}}| = |\overline{F}_{n,\text{total}}| (1 - \overline{x}_f) \quad (9.22)$$

which yields with the help of Eqs. (9.17) and (9.21)

$$|\overline{F}_{\text{exp}}| = \frac{\gamma}{4} \quad (9.23)$$

The latter yields the magnitude of the dimensional force

$$|F_{\text{exp}}| = \frac{(\overline{H}_0 - 1) \mu V_0 L^2}{4 H_1^2} W \quad (9.24)$$

which can be re-written as

$$\mu = |F_{\text{exp}}| / \left[ \frac{(\overline{H}_0 - 1) V_0 L^2}{4 H_1^2} W \right] \quad (9.25)$$

Therefore, by measuring the magnitude of force  $|F_{\text{exp}}|$ , we can find the viscosity of a soft material from Eq. (9.25) where all the other parameters are the governing parameters of the experiment, i.e. are known from scratch.

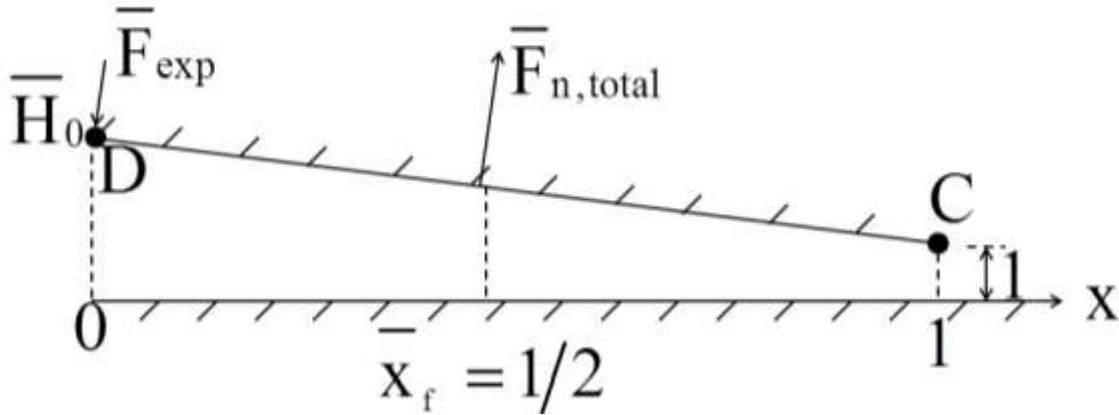


**Figure 9.3.** The balance of forces.

An improved approximation for the normal force acting onto the inclined plate can be obtained by relaxing the assumption of a small angle  $\alpha$ . Then, the normal stress and force are given by the following expressions

$$\overline{\sigma}_{nn} = \overline{\sigma}_{xx} \sin^2 \alpha + 2\overline{\sigma}_{xy} \sin \alpha \cos \alpha + \overline{\sigma}_{yy} \cos^2 \alpha \quad (9.26)$$

$$\overline{F}_n = \int_0^1 \overline{\sigma}_{xx} \frac{dx}{\cos \alpha} \quad (9.27)$$

where the force is rendered dimensionless by  $\mu V_0 L^2 W / H_1^2$ . The shear stresses have still been neglected, since it was found that at relatively small angles ( $\alpha < 5^\circ$ ) the shear stress contributes less than 1% of the force, and at  $\alpha = 20^\circ$  when  $\overline{H}_0 = 80$  it contribute only 20% of the force.

To find the point of application of this force, one needs also to calculate the moment of normal stresses acting on the inclined plate relative to point C in Figure 9.3. The dimensionless moment  $\overline{M}_{C,\text{total}}$  rendered dimensionless by  $\mu V_0 L^2 W / H_1^2$  is equal to

$$\overline{M}_{C,\text{total}} = \int_0^1 (1 - \bar{x}) \overline{\sigma}_{xx} \frac{d\bar{x}}{\cos\alpha} \Big|_{\bar{y}=\bar{H}} \quad (9.28)$$

Note that  $\overline{M}_{C,\text{total}}$  is a function of  $\overline{H}_0$  and the angle of inclination. The location of the center of pressure  $\bar{x}_f$  is determined by the equality of the moment  $\overline{M}_{C,\text{total}}$  to the moment of force  $\overline{F}_{n,\text{total}}$ , which is Eq. (9.19). In the experiment the force is measured at  $\bar{x} = 0$ , therefore

$$|\overline{F}_{\text{exp}}| = |\overline{F}_{n,\text{total}}| (1 - \bar{x}_f) = \overline{M}_{c,\text{total}} \quad (9.29)$$

Then, the dimensional force to be measured is

$$|\overline{F}_{\text{exp}}| = \overline{M}_{c,\text{total}} \frac{\mu V_0 L^2}{H_1^2} W \quad (9.30)$$

and the viscosity found using these measurements is given by

$$\mu = \frac{|\overline{F}_{\text{exp}}| H_1^2}{\overline{M}_{c,\text{total}} V_0 L^2 W} \quad (9.31)$$

Therefore, to measure the effective viscosity of soft materials, the restraining force  $|\overline{F}_{\text{exp}}|$  applied to the inclined plate to keep it in the position will be measured. Then, viscosity will be found from Eq. (9.31), since all the other parameters involved are the governing parameters of the experiment which are given.

### **9.2.3. Pressure Distributions for a Newtonian Fluid**

Using Eq. (9.5), the pressure distribution along the wedge-like gap between the plates can be found for different  $\overline{H}_0$  values as shown in Figure 9.4. When the value of  $\overline{H}_0$  is close to one (i.e. the angle of inclination is small), the pressure maximum in the wedge-like gap is reached at

$\bar{x}_* \approx 1/2$  (see Figure 9.4). Equations (9.5) and (9.7) yield the following expression for the maximum pressure in the gap (the atmospheric pressure is disregarded, as explained before)

$$\bar{p}_{\max} = \frac{3}{2} \left[ \frac{\bar{H}_0 - 1}{\bar{H}_0^2 + \bar{H}_0} \right] \quad (9.32)$$

This expression reaches its maximum at  $\bar{H}_0 = 2.414$ , which is the global pressure maximum possible in the wedge-like gap (see Figure 9.4). At  $\bar{H}_0 > 2.414$  the maximum pressure in the gap decreases with increasing value of  $\bar{H}_0$  and the center of pressure,  $\bar{x}_f$ , continues to shift towards the pivot point of the wedge-like domain, as shown in Figure 9.4. This means, for example, that during the application of soft materials, which is typically practiced at  $\bar{H}_0 > 2.414$ , an increase in angle of inclination will result in a reduction in force acting on the inclined plate.

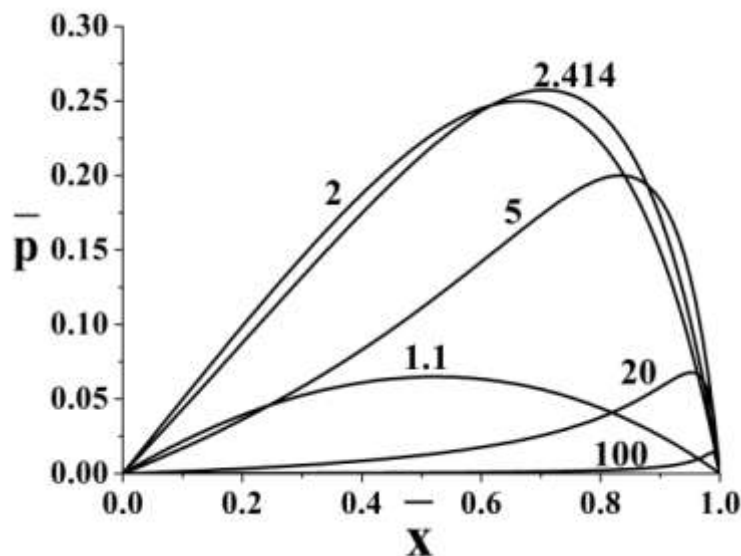


**Figure 9.4.** Pressure distribution along the wedge-like domain between the two plates. The values of  $\bar{H}_0$  are labeled by the numerals near the curves.



### 9.2.4. Velocity Field for a Newtonian Fluid

The velocity fields are fully determined by Eqs. (9.5) and (9.7). They are illustrated in Figure 9.5. At low angles of inclination, when  $\bar{H}_0 < 2$ , there is no reverse flow. At  $\bar{H}_0 > 2$ , the reverse flow appears and becomes fully visible, as seen in Figure 9.5. The reverse flow enhances as  $\bar{H}_0$  increases.

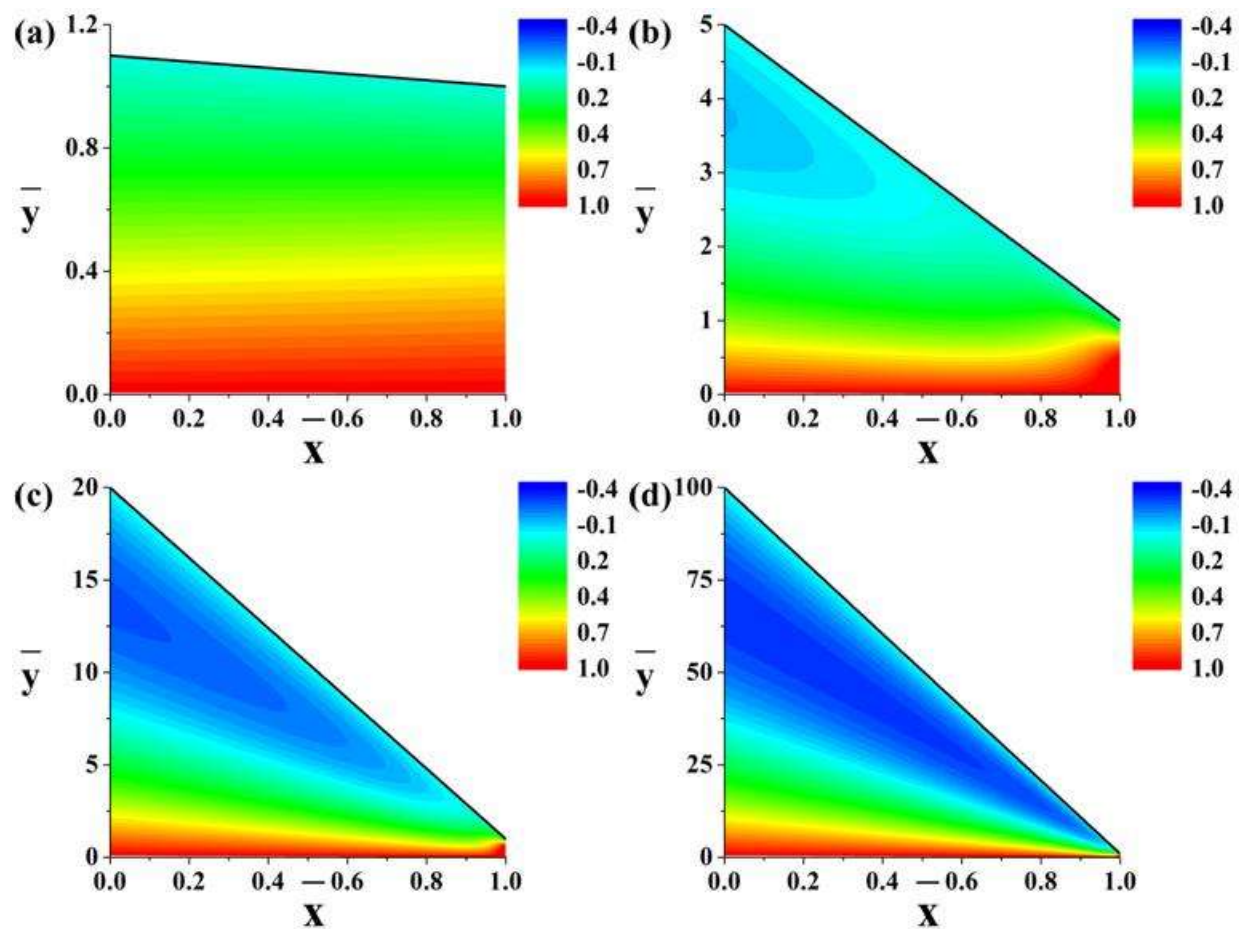


**Figure 9.5.** Dimensionless velocity field shown as a contour plot. Panel (a)-  $\bar{H}_0 = 1.1$ , (b)  $\bar{H}_0 = 5$ , (c)  $\bar{H}_0 = 20$  and (d)  $\bar{H}_0 = 100$ .

### **9.2.5. Pressure Distribution Under an Upper Surface Shaped as a Quadratic Profile for a Newtonian Fluid**

It is also of interest to investigate how the pressure distribution will under a quadratically-shaped upper surface compared to the linearly-shaped one. A nonlinear upper surface can be encountered with during the application of soft materials with the use of some tools. The Reynolds equation (9.1) can be integrated as

$$\bar{p} = 6 \int_0^{\bar{x}} \frac{d\bar{x}}{\bar{H}^2} + \bar{C}_1 \int_0^{\bar{x}} \frac{d\bar{x}}{\bar{H}^3} + \bar{C}_2 \quad (9.33)$$

where  $\bar{x}$  is rendered dimensionless by  $L$ ,  $H$  by  $H_1$ ,  $p$  and  $C_2$  by  $\mu V_0 L / H_1^2$ , and  $C_1$  by  $\mu V_0 H_1$ . Solutions of Eq. (9.33) are subject to the following boundary conditions related to Eqs. (9.3) and (9.4)

$$\bar{x} = 0, \quad \bar{p} = 0 \quad (9.34)$$

$$\bar{x} = 1, \quad \bar{p} = 0 \quad (9.35)$$

Then, Eqs. (9.33)-(9.35) yield

$$\bar{p} = 6 \left[ \int_0^{\bar{x}} \frac{d\bar{x}}{\bar{H}^2} - \int_0^{\bar{x}} \frac{d\bar{x}}{\bar{H}^3} \left( \int_0^1 \bar{H}^2 d\bar{x} \right) \left( \int_0^1 \bar{H}^3 d\bar{x} \right)^{-1} \right] \quad (9.36)$$

A quadratic function

$$\bar{H} = \bar{a}\bar{x}^2 + \bar{b}\bar{x} + \bar{c} \quad (9.37)$$

was used to evaluate the integrals in Eq. (9.36), where  $\bar{a}$ ,  $\bar{b}$ , and  $\bar{c}$  are rendered dimensionless by  $H_1$ , and the following equalities hold

$$\bar{b} = 1 - \bar{H}_0 - \bar{a}, \quad \bar{c} = \bar{H}_0 \quad (9.38)$$

The corresponding pressure distributions for different curvatures of the typical upper surfaces are depicted in Figure 9.6. The figure shows that as the upper surface becomes more curved, the maximum pressure shifts toward the entrance. . Also note that not all the upper surface shapes with a minimum before the exit can result in a negative pressure near the exit. In addition such curved shapes significantly increase the maximum pressure.

It should be emphasized that thin spreading tools can acquire curved shapes due to a significant force applied. A typical 6” spreading knife was fixed at the end and was bent by gripping the handle and pushing down using sufficient physical force. Images of the bent knife were taken and mapped onto a dimensionless coordinate plane (Figure 9.7). The corresponding shapes were approximated by the quadratic function and pressure distributions calculated (see Figure 9.8). Figure 9.8(b) shows a 20% increase and Figure 9.8(d) shows a 32% increase in maximum pressure due to the curved shape but there is a decrease in pressure as the value of  $\bar{H}_0$  increases between the figures.

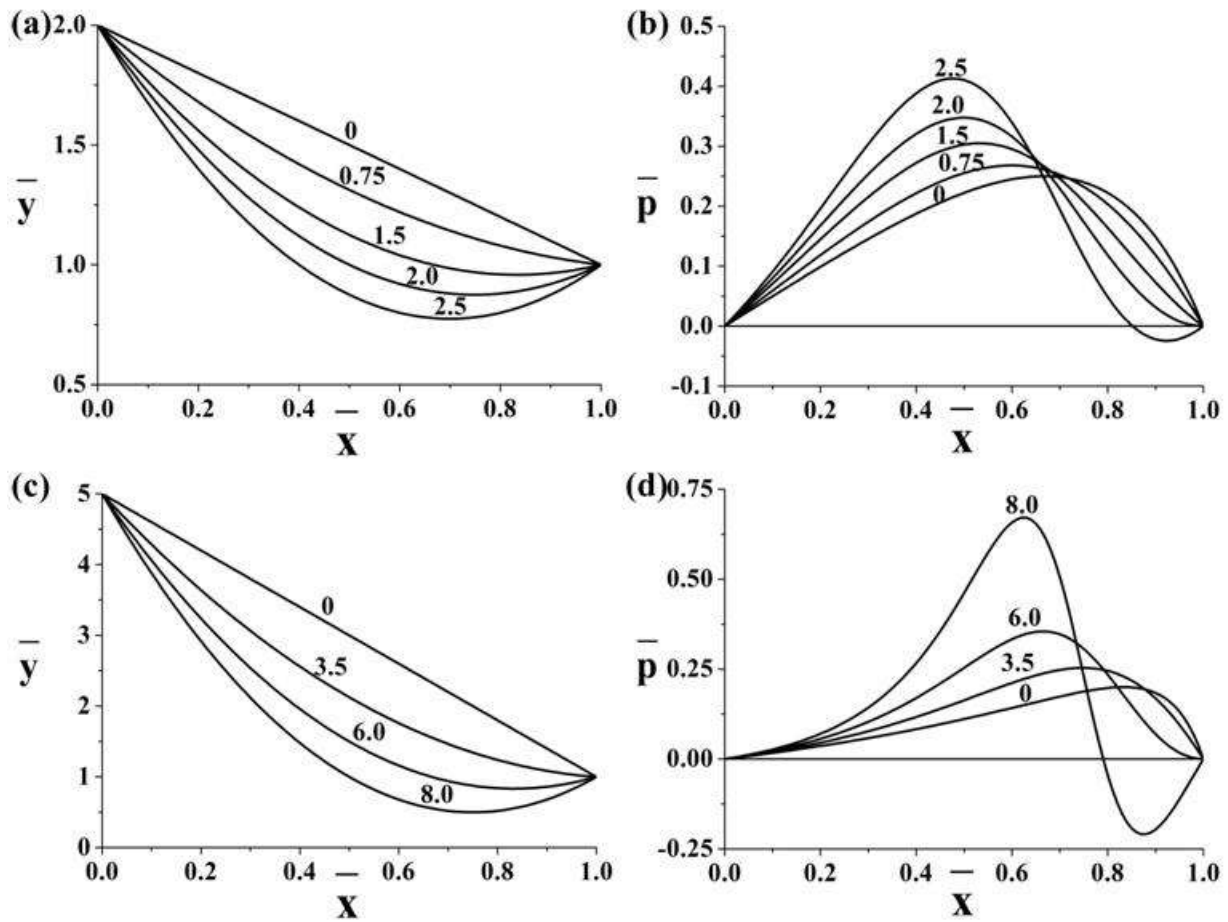


**Figure 9.6.** Dimensionless height and pressure distributions versus dimensionless longitudinal coordinate for  $\bar{H}_0 = 2$  (a) and (b), as well as for  $\bar{H}_0 = 5$  (c) and (d). Here  $\bar{H}$  is given by Eq. (9.37) and the lines are labeled by the corresponding values of  $\bar{a}$ , associated with the curvature.

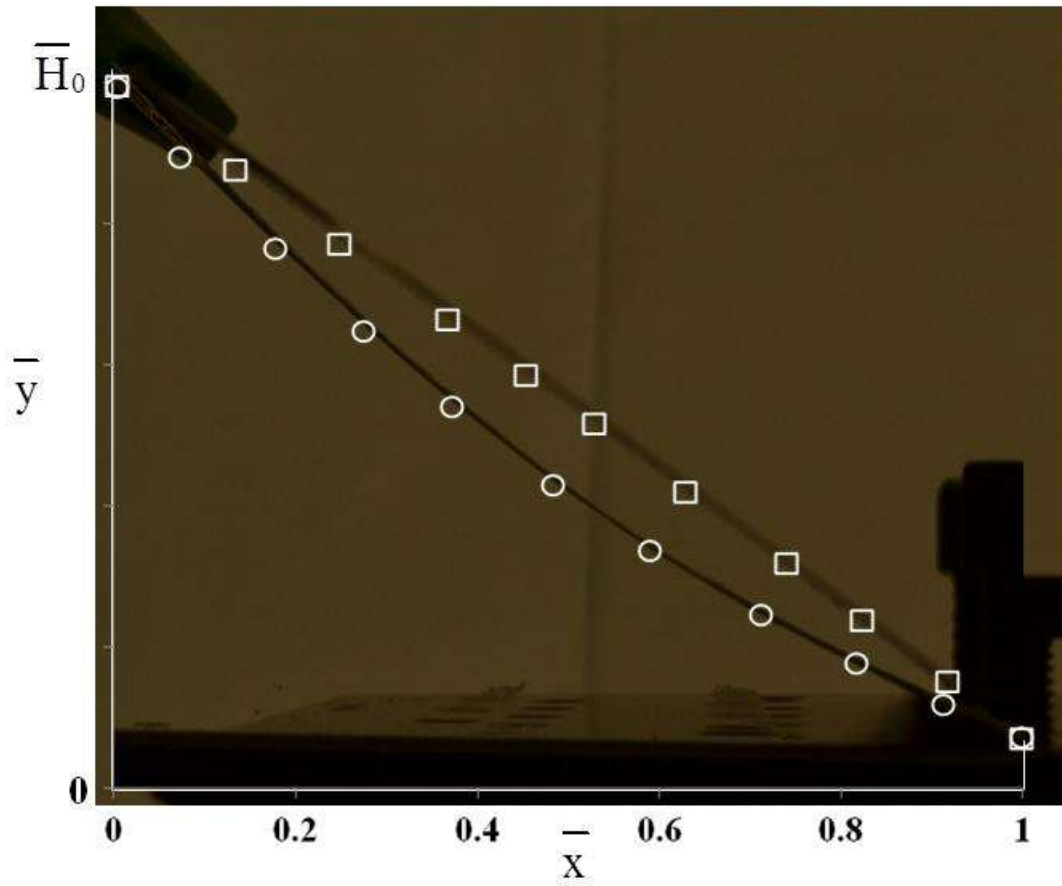


**Figure 9.7.** Bending the knife. Squares correspond to the linear shape and circles to the curved quadratic shape.

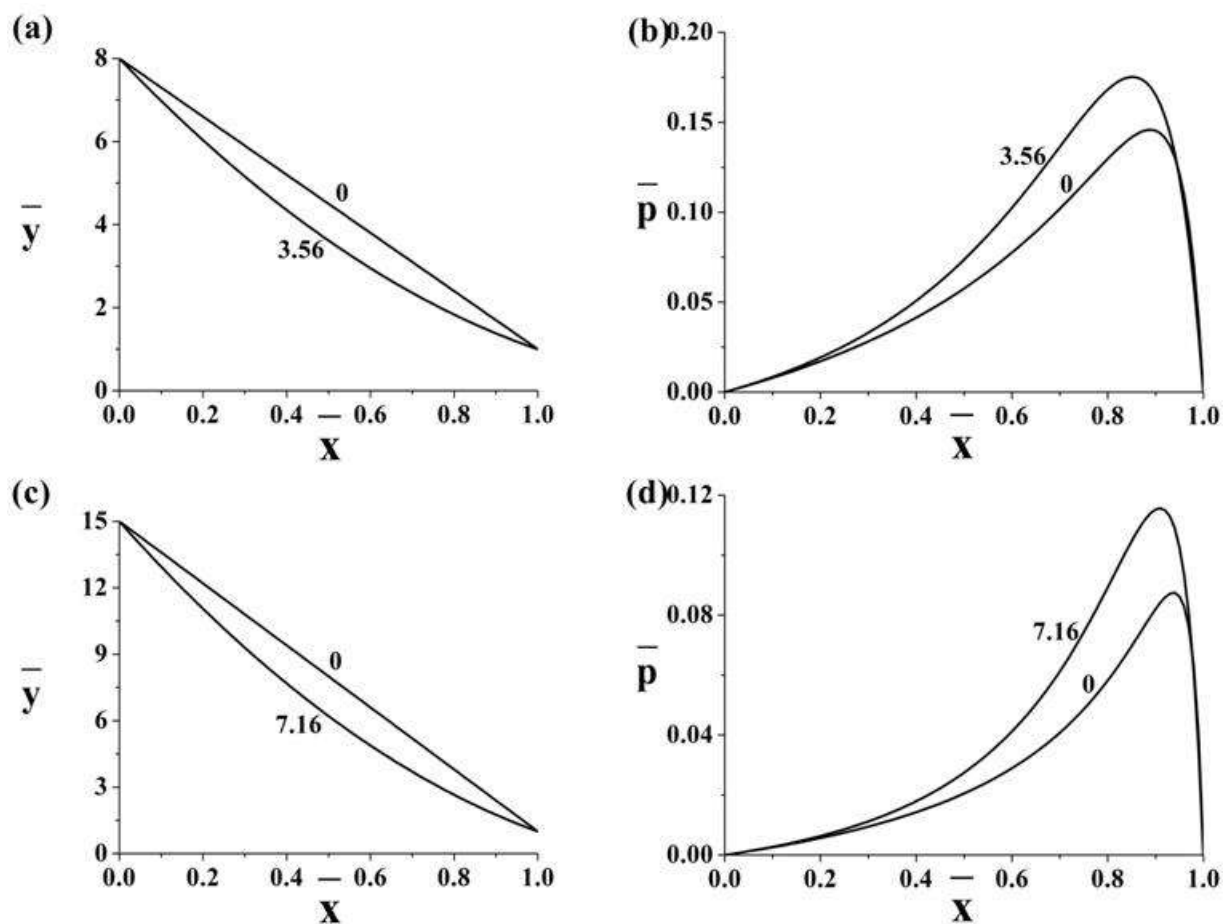


**Figure 9.8.** Dimensionless height and pressure versus dimensionless longitudinal coordinate corresponding to the knife in Figure 9.7 for  $\bar{H}_0 = 8$  (a) and (b), as well as for  $\bar{H}_0 = 15$  (c) and (d). The lines are labeled by the corresponding values of  $\bar{a}$  related to the curvature.

## **9.2.6. Velocity profile for a Bingham fluid from Tichy (1991)**

### **9.2.6.a. Floating Core**

A floating core is defined as a region of flow with zero shear rate. The core has boundaries of  $y = H_a$  at the lower interface between the flow domain and the rigid core, and

$y = H_b$  at the upper interface between the rigid core and the flow domain. Define the shear stress using the Bingham model as

$$\tau_{xy} = \mu \frac{\partial u}{\partial y} \pm \tau_0 \quad (9.39)$$

where  $\tau_0$  is the yield stress. Then, the x-component of the inertialess momentum balance equation becomes

$$0 = -\frac{dp}{dx} + \frac{\partial}{\partial y} \left[ \mu \frac{\partial u}{\partial y} \pm \tau_0 \right] \quad (9.40)$$

The boundary conditions are imposed as

$$y = 0, u = V_0 \quad (9.41a)$$

$$y = 0, \left. \frac{\partial u}{\partial y} \right|_{\text{Bingham}} = \left. \frac{\partial u}{\partial y} \right|_{\text{Newtonian}} \quad (9.41b)$$

$$y = H, \left. \frac{\partial u}{\partial y} \right|_{\text{Bingham}} = \left. \frac{\partial u}{\partial y} \right|_{\text{Newtonian}} \quad (9.41c)$$

The boundary conditions, Eqs. (9.41b) and (9.41c), assume that since at either wall the shear stress is the dominant stress, the shear rate will be equal whether the fluid is Bingham or Newtonian. This results in the following set of equations for the velocity profile for the flow domains and the floating core:

$$0 \leq y \leq H_a: u = V_0 - \left[ \frac{\pm \tau_0 - \tau_1}{\mu} \right] y + \frac{1}{2\mu} \frac{dp}{dx} y^2 \quad (9.42a)$$

$$H_a \leq y \leq H_b: u = V_0 - \left[ \frac{\pm \tau_0 - \tau_1}{\mu} \right] H_a + \frac{1}{2\mu} \frac{dp}{dx} H_a^2 \quad (9.42b)$$

$$H_b \leq y \leq H: u = V_0 - \left[ \frac{\pm \tau_0 - \tau_2}{\mu} \right] (y - H) + \frac{1}{2\mu} \frac{dp}{dx} (y - H)^2 \quad (9.42c)$$

where

$$\tau_1 = \frac{-dp/dx}{2H(dp/dx) \pm 4\tau_0} \left[ H^2 \frac{dp}{dx} \pm 2H\tau_0 + 2\mu(V_0 - V_1) \right] \quad (9.43a)$$

$$\tau_2 = \tau_1 + H \frac{dp}{dx} \quad (9.43b)$$

$$H_a = \left( \frac{\pm\tau_0 - \tau_1}{dp/dx} \right) \quad (9.43c)$$

$$H_b = H_a - 2 \left( \frac{\pm\tau_0}{dp/dx} \right) \quad (9.43d)$$

and  $V_1$  is the velocity of the top plate [a non-zero  $V_1$  is included for completeness following Tichy (1991)], whereas in this Chapter only the case  $V_1=0$  will be considered. The  $+\tau_0$  in the above equations corresponds to the case when  $dp/dx$  is negative and vice versa, otherwise it should be  $-\tau_0$ . Note that if  $\tau_0=0$  the velocity profile for a Newtonian fluid is recovered. As stated in Tichy (1991), “The integration of velocity in the wedge leads to a complicated expression for the volume flow rate,  $q$ , from which the pressure gradient  $dp/dx$  cannot be determined in closed form.”

$$\begin{aligned} q \left[ 12\mu \left( \frac{dp}{dx} \right)^2 \left( H \frac{dp}{dx} \pm 2\tau_0 \right)^2 \right] &= - \left( H \frac{dp}{dx} \right)^5 + \left( \frac{dp}{dx} \right)^4 \left[ -(\pm 7H^4\tau_0) + 6\mu H^3(V_0 + V_1) \right] \\ &+ \left( \frac{dp}{dx} \right)^3 \left[ -16H^3\tau_0^2 \pm 24\mu H^2\tau_0(V_0 + V_1) \right] \left( \frac{dp}{dx} \right)^2 \\ &\times [ -(\pm 8H^2\tau_0^3) + 24\mu H\tau_0^2(V_0 + V_1) \pm 12\mu^2\tau_0(V_0 + V_1)^2 ] \\ &+ 16 \left( \frac{dp}{dx} \right) H\tau_0^4 \pm 16\tau_0^5 \end{aligned} \quad (9.44)$$



Therefore, it is suggested by Tichy (1991) to “implicitly solve the fifth degree polynomial equation for  $dp/dx$  at each  $x$ , based on a guess of  $q$ .” Due to the complexity of Eq. (9.44), a constant pressure gradient is assumed until the maximum pressure is reached, as in Figure 9.10.

### **9.2.6.b. Core Attached to Upper Surface**

An attached upper core is defined as a fluid domain that has the same velocity as the top plate to which it is attached. The  $x$ -projection of the momentum balance for flow domain below it reads

$$0 = -\frac{dp}{dx} + \frac{\partial}{\partial y} \left[ \mu \frac{\partial u}{\partial y} + \tau_0 \right] \quad (9.45)$$

with the boundary conditions

$$y = 0, \quad u = V_0 \quad (9.46a)$$

$$y = H_a, \quad \frac{\partial u}{\partial y} = 0 \quad (9.46b)$$

This results in the following velocity profile in the flow domain and in the undeformed upper core, respectively,

$$0 \leq y \leq H_a: \quad u = V_0 - \left[ \frac{-\tau_0 - \tau_1}{\mu} \right] y + \frac{1}{2\mu} \frac{dp}{dx} y^2 \quad (9.47a)$$

$$H_a \leq y \leq H: \quad u = V_1 \quad (9.47b)$$

where

$$\tau_1 = -\tau_0 - \sqrt{2\mu \frac{dp}{dx} (V_0 - V_1)} \quad (9.48a)$$

$$H_a = \left( \frac{-\tau_0 - \tau_1}{dp/dx} \right) = \sqrt{\frac{2\mu(V_0 - V_1)}{dp/dx}} \quad (9.48b)$$

The volumetric flow rate is found as

$$q = \int_0^{H_a} u \, dy \quad (9.49)$$

With  $V_1=0$ , Eq. (9.49) results in a constant pressure gradient of

$$\frac{dp}{dx} = \frac{2\mu V_0^3}{9q^2} \quad (9.50)$$

Regarding Eq. (9.48b), it is important to note, as stated in Tichy (1991), that “the extent of the (attached upper) core does not depend on  $\tau_0$ . This can be appreciated by noting that the flow profile is quadratic with specified values at two points and specified curvature due to  $dp/dx$ . Only the shear stress varies directly with  $\tau_0$ .” When the yield stress is sufficiently high, the pressure gradient and  $H_a$  are constant until  $H(x) = H_a$ . Beyond this point there may be no core. At sufficiently low eccentricities (in journal bearings), the shear rate is non-zero at any point and cores do not form. In this case the pressure is always that of the Newtonian fluid.

According to Tichy (1991), the proper case is determined by calculating the positions of the core and identifying whether the said positions occur within the wedge geometry. If

$$H_a \leq H_b \leq 0 \text{ or } H \leq H_a \leq H_b \text{ or } 0 \leq H_a = H_b \leq H : \text{No core, Newtonian profile} \quad (9.51a)$$

$$0 < H_a < H_b < H : \text{Floating core} \quad (9.51b)$$

$$0 < H_a < H \leq H_b : \text{Attached upper core} \quad (9.51c)$$

The lower attached core is not considered in this work because it is relevant when the top plate is moving or near the exit when the pressure gradient is positive. In this experimental work, the top

plate is fixed and the pressure gradient is only positive extremely close to the exit and experimentally differentiating between a plug flow and Newtonian flow in this region is extremely difficult.

The parameters are rendered dimensionless, according to Tichy (1991), as follows

$$\bar{u} = \frac{u}{V_0}, \bar{y} = \frac{y}{H}, \bar{H}_a = \frac{H_a}{H}, \bar{H}_b = \frac{H_b}{H}, \bar{\tau}_0 = \frac{\tau_0 H}{\mu V_0}, \frac{d\bar{p}}{d\bar{x}} = \frac{dp}{dx} \frac{H^2}{\mu V_0} \quad (9.52)$$

which using Eqs. (9.7), (9.42), and (9.47) give the velocity profiles shown in Figure 9.9.

The pressure gradient in the theory of this Chapter for Newtonian fluids was rendered dimensionless using the scale of  $\mu V_0 / H_1^2$ . To convert it to the scaling used in Tichy (1991), a factor of  $H_1^2 / H^2$  was employed. In this work the pressure gradient used for determining the velocity profile of a Bingham fluid will be assumed to be the same for as a Newtonian fluid but written using the scaling in Tichy (1991). Although  $dp/dx$  increases until a maximum pressure is achieved for a Newtonian fluid, when it is rendered dimensionless using Eq. (9.52),  $d\bar{p}/d\bar{x}$  is approximately constant because  $H(x)$  is decreasing. This led to a pressure gradient approximately equal to the value used in Tichy (1991) for all  $\bar{H}_0$  corresponding to the experiments. Figure 9.10 shows the two extreme experimental cases and the value used by Tichy (1991). When  $\bar{H}_0 = 9.6$  (Figure 9.10; solid line) and  $\bar{H}_0 = 86.5$  (Figure 9.11; dashed line) the flow becomes that of a Newtonian fluid when  $\bar{x} > 0.80$  and  $\bar{x} > 0.98$ , respectively. This is discussed in detail in Section V. After the velocity profiles were determined, the dimensionless coordinates  $\bar{y}$ ,  $\bar{H}_a$ , and  $\bar{H}_b$  were then recast to match the non-dimensionalization used in the experimental and Newtonian velocity profiles shown in Figures 9.17 – 9.24.

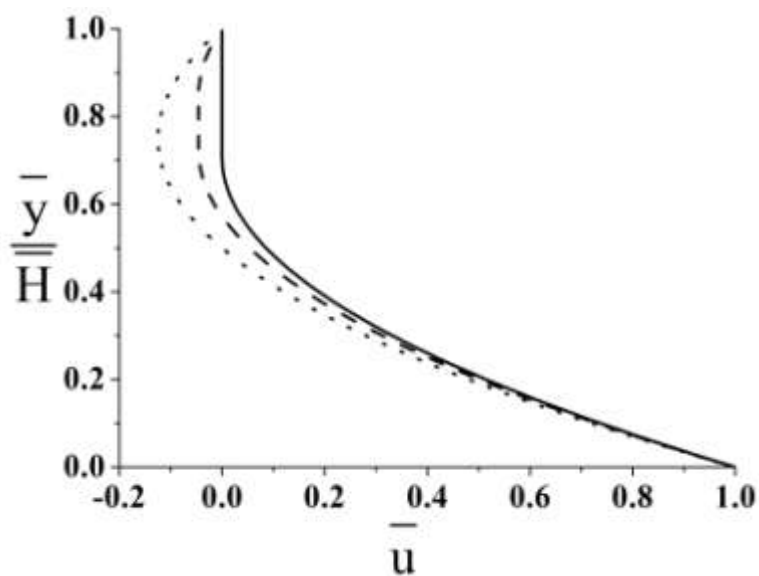


**Figure 9.9.** Typical velocity profile for attached upper core (solid line) with  $\bar{\tau}_0 = 1.0$ , floating core (dashed line) with  $\bar{\tau}_0 = 0.25$ , and no core (dotted line). For all profiles  $dp/d\bar{x} = 4$ .

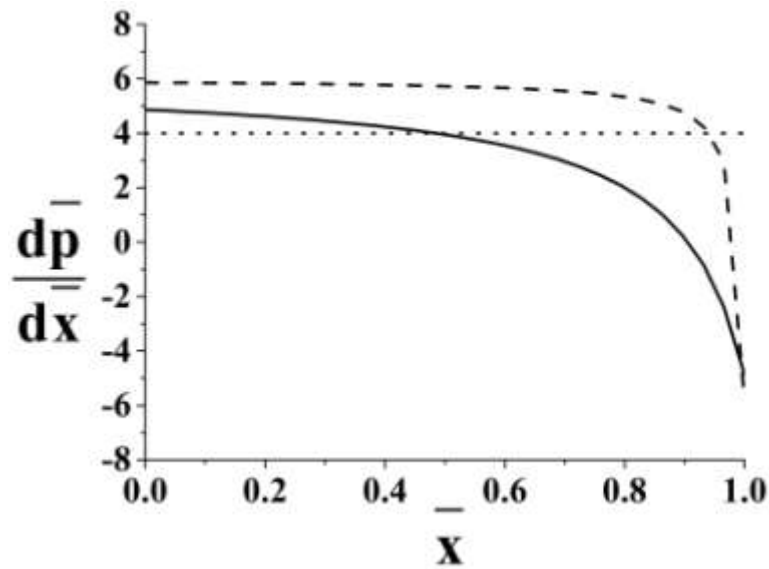


**Figure 9.10.** Dimensionless pressure gradient  $\overline{dp}/\overline{dx}$  for the two extreme experimental cases  $\overline{H}_0 = 9.6$  (solid line) and  $\overline{H}_0 = 86.5$  (dashed line) compared to the pressure gradient used in Figure 9.9 (dotted line).

In Figure 9.9, representative velocity profiles for a Newtonian fluid (Eq. 9.7) and a Bingham fluid with either an attached upper core or floating core (Eq. 9.47 and Eq. 9.42 rendered dimensionless) are presented. At the moving wall all three profiles have the same shear rate because the shear stress created at the wall is much larger than the pressure gradient. As the velocity profile moves further from the moving wall, the same pressure gradient will create three unique profiles.

Note that the magnitude of the yield stress does not dictate the size of the attached upper core but only plays a role in deciding whether the core will detach to become a floating core. According to Tichy (1991), if the pressure gradient,  $dp/dx > 2V_0\mu/H^2$  a core will form and the size of the core will increase with an increase in the yield stress for the floating core case. In the

reverse flow region, caused by the adverse pressure gradient, the shear stress will be sufficiently low compared to the yield stress to create a plug. In the floating-core case the size of the plug is dependent on the yield stress and pressure gradient. At a location  $x$  along the film when the stress magnitude  $|\tau_{xy}|$  is greater than the yield stress  $\tau_0$ , the Bingham model reduces to the conventional lubrication Newtonian result.

### **9.3 Experimental Materials and Apparatus**

#### **9.3.1 Material Preparation**

A 1.5% Carbopol-940 (Lubrizol) aqueous solution was prepared by following Novean's specifications. First, 30 g of Carbopol powder was dissolved in 1970 mL of water. The Carbopol was slowly added to water, while stirring on a hotplate at 50°C, with a magnetic stirrer set to the highest sustainable setting. The solution was allowed stirring overnight. The acidic Carbopol solution was neutralized by slowly adding 1 M NaOH to the required amount specified by the manufacturer. This process created a gel with a viscosity of 8 Pa·s and yield stress of 570 Pa, found using the squeezing apparatus described in Pelot et al. (2013). Using a TA Instruments rheometer described in Pelot et al. (2013), with a vane propeller, additional information on the rheological behavior of the gel was acquired, as shown in Figure 9.11. The results show the power-law behavior in shear with the exponent  $n$  and the consistency index  $K$  being  $n = 0.12$  and  $K = 88 \text{ Pa}\cdot\text{s}^n$ , as well as the yield stress  $\tau_0 = 570 \text{ Pa}$ . Due to the extremely low value of the behavior index found using a vane propeller, a parallel plate geometry with smooth plates and with rough plates (80 grit rough sand paper attached to the top and bottom plates) was employed at shear rates of  $1 \text{ s}^{-1}$  to  $100 \text{ s}^{-1}$  and  $10 \text{ s}^{-1}$  to  $200 \text{ s}^{-1}$  (Figure 9.11). The behavior index and

consistency index found using smooth plates are  $n = 0.17$  and  $K = 196 \text{ Pa}\cdot\text{s}^n$ , while those obtained using rough plates are  $n = 0.23$  and  $K = 176 \text{ Pa}\cdot\text{s}^n$ , respectively. Rheological behavior of Carbopol gels of the same concentration have been investigated by Eshtiaghi et al. (2012) using the Couette geometry, and Curran et al. (2006) using concentric cylinders. Their results revealed  $n = 0.5$  as well as  $K = 54 \text{ Pa}\cdot\text{s}^n$  and  $K = 30 \text{ Pa}\cdot\text{s}^n$  and the yield stress values of  $\tau_0 = 169 \text{ Pa}$  and  $\tau_0 = 200 \text{ Pa}$ , respectively.

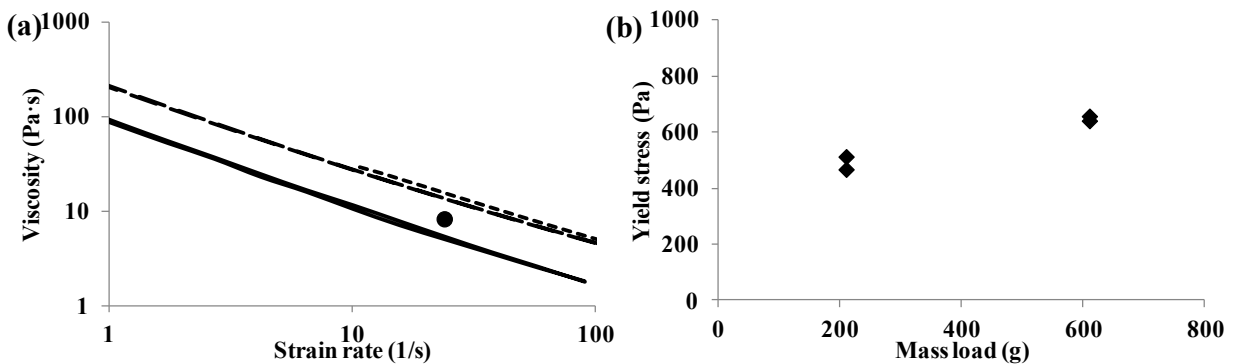


**Figure 9.11.** (a) Viscosity of Carbopol 940 found using vane propeller (solid line), parallel plate with smooth plates (long dash) and rough plates (short dash), and the squeezing apparatus (circle). The fitting line for the vane data reveals the rheological parameter values as  $n = 0.12$  and  $K = 88 \text{ Pa}\cdot\text{s}^n$ , parallel plate with smooth plates-as:  $n = 0.17$  and  $K = 196 \text{ Pa}\cdot\text{s}^n$  and using rough plates-as:  $n = 0.23$  and  $K = 176 \text{ Pa}\cdot\text{s}^n$ . (b) Yield stress,  $\tau_0$ , for different mass loads measured using the squeezing apparatus.

### 9.3.2 Experimental Procedure

In the experimental setup shown in Figure 9.12 a layer of Carbopol gel was transported on the lower surface moving to the right, while the inclined spreading plate was stationary. The

spreading plate was made of acrylic which was 15 cm long, 10 cm wide, and 0.95 cm thick. The moving lower surface was an “infinitely” long polystyrene sheet. It was pulled at different velocities by an AC motor (Leeson M1145033). The force gauge, Imada DS2-11, was connected to a fixed stand and was always strictly perpendicular to the inclined plate at any inclination. Due to the Carbopol gel pressure, it could partially escape from the wedge-like gap sidewise. To prevent such deviations from the two-dimensional flow, vertical walls were fixed on both sides of the wedge.

The preliminary experiments on Carbopol spreading revealed that bubbles inevitably entrapped inside the gel may serve as seeding particles. However, it was found that washed coffee blended in the Carbopol gel are better seeding particles because of their size commensurate with the image resolution. They are also preferable given their availability, contrast, and non-hazardous nature. The images with these seeding particles being visible are shown in Figures 9.12(b) and 9.13.



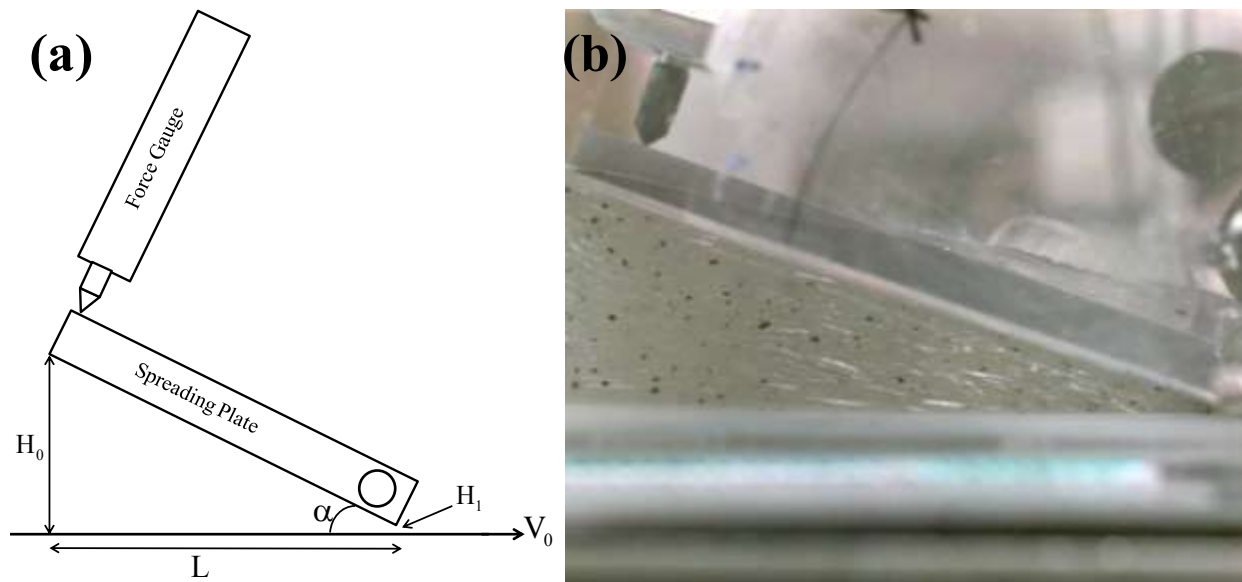


**Figure 9.12.** Sketch (a) and image (b) of the experimental setup with the  $20^\circ$  angle of inclination of the spreading plate.

The wedge-like gap of the spreading setup shown in Figure 9.12 was adjusted for varying the exit height and the angle of inclination of the spreading plate. A wet film thickness gauge was used to measure the thickness of the layer gel after it exited from the wedge-like gap. It appeared to be equal to the exit height  $H_1$  since practically no swelling was found (which means that the gel was inelastic). In this study the exit height  $H_1$  ranged between 0.6 mm and 1.5 mm at the three inclination angles,  $5^\circ$ ,  $10^\circ$ , and  $20^\circ$ . The velocity of the moving surface was either 0.167 m/s or 0.240 m/s. The range of the parameters chosen is characteristic of the applications. The length of the material ribbon applied onto the moving surface varied between 1 m and 1.25 m creating a steady-state flow in the wedge-like gap for approximately 5 to 6 s.

## **9.4 Results**

Since Carbopol gels reveal pseudoplastic power-law rheology in shear flow, it is expected that there should be practically no flow inside such domains where the shear rate is relatively low. Indeed, its effective viscosity corresponding to these domains should be very high, or alternatively the shear stress there should be lower than the yield stress. Therefore, it might be found that inside the boundaries of these domains one would expect to see a stagnation zone with Carbopol being the working fluid, rather than a reverse flow for Newtonian fluids, which is, indeed, corroborated by the experimental data on the left in Figures 9.17 – 9.24. The theoretically predicted shear rate fields for Newtonian fluid found using the derivative of Eq. (9.7) are shown in Figure 9.14. The domains with the low shear rate would be prone to stagnation in the case of Carbopol due to either high effective viscosity or the shear stress lower than the yield stress, as is seen in Figures 9.17 – 9.24 on the left.

Experimentally found velocity profiles were observed for a number of geometries (not typically identified as qualified for the lubrication approximation to hold) and are contrasted to the theoretical velocity profiles of a Bingham fluid and a Newtonian fluid at the inclination angle and exit height of  $5^\circ$  and 0.6 mm, respectively, in Figure 9.17,  $5^\circ$  and 1.5 mm in Figure 9.18,  $10^\circ$  and 0.8 mm in Figure 9.19,  $10^\circ$  and 1.5 mm in Figure 9.20,  $20^\circ$  and 0.6 mm in Figure 9.21,  $20^\circ$  and 1.3 mm in Figure 9.22, and at a higher velocity of the moving surface at  $20^\circ$  and 0.65 mm in Figure 9.23,  $20^\circ$  and 1.5 mm in Figure 9.24, respectively. The experimental velocity is rendered dimensionless by the speed of the conveyer, or moving plate, pulling the fluid. In each of the experimental plots, arrows pointing to two positions in the reverse flow region identify a representative velocity in the respective area. Furthermore, the same positions are identified in

the theoretical Bingham and Newtonian fluid velocity profiles labeled with the respective theoretical velocity.

Figures 15 and 16 illustrate the presence of an attached upper core and a floating core in the Carbopol flows. In the two consecutive images in Figure 9.15 particles 1 and 2 are at rest relative to the motionless spreading plate. On the other hand, in Figure 9.16 at a higher inclination angle it is seen that all three highlighted particles move in the reverse flow region, with particles 2 and 3 being faster than particle 1.

The experimental parameters are listed in Table 9.1. The Newtonian viscosity in Table 9.1 was found using Eq. (9.31). The theoretical Bingham fluid velocity profiles, which employ the case of a floating core (Eq. 9.42), are sensitive to the dimensionless yield stress,  $\bar{\tau}_0 = \tau_0 H / \mu V_0$ . The dimensional yield stress,  $\tau_0$ , is a fixed parameter, the wedge geometry,  $H$ , and wall velocity,  $V$ , are known per experiment; therefore, the viscosity,  $\mu$ , was adjusted accordingly so that the theoretical velocity at the points indicated by the arrows corresponded to the velocities found experimentally. These viscosity values are also presented in Table 9.1.

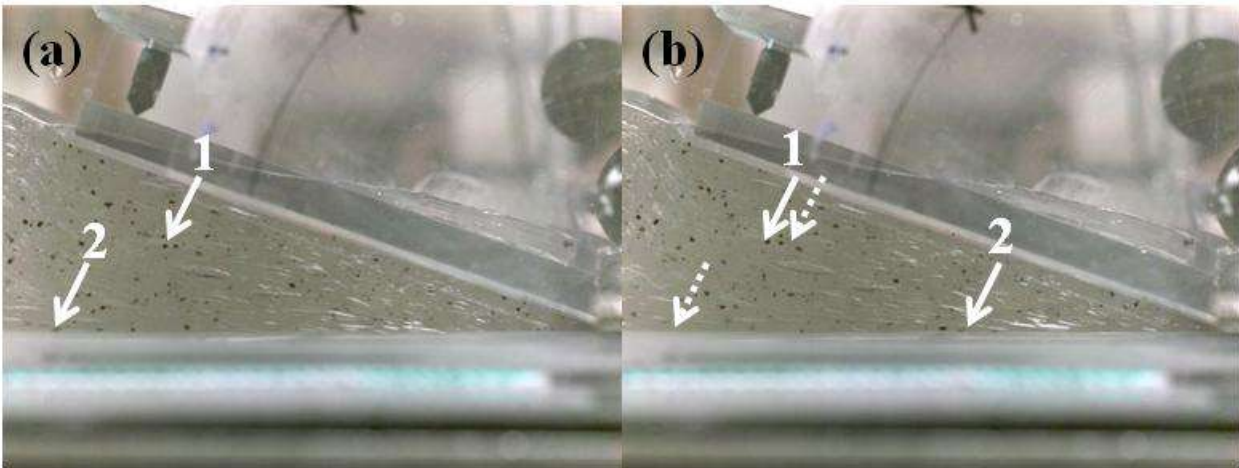


**Figure 9.13.** Two consecutive images of seeding particles 0.5 s apart. The inclination angle is  $20^\circ$ , the exit height is 0.65 mm, and the velocity of the moving surface is 0.24 m/s. Solid arrows in panel (a) point to two specific particles, and dashed arrows in panel (b) point to the same particles in 0.5 s.

**Table 9.1.** Experimental parameters and calculated viscosity using the Newtonian model (Eq. 9.31) and the Bingham model (Eq. 9.52).

Angle (deg)	Exit height, $H_1$ (mm)	$\bar{H}_0$	Velocity (m/s)	Force (N)	Newtonian viscosity (Pa·s)	Yield stress (Pa)	Bingham viscosity (Pa·s)
5	0.6	22.8	0.167	19.1	4.8	570	43
5	1.5	9.6	0.167	15.0	6.0	570	$\leq 50^{**}$
10	0.8	33.6	0.167	13.5	11.8	570	83
10	1.5	18.4	0.167	7.9	8.6	570	89
20	0.6	86.5	0.167	8.1	22.5	570	155
20	1.3	40.5	0.167	6.8	21.8	570	155
20	0.65	79.9	0.240	9.8	19.2	570	130
20	1.5	35.2	0.240	9.7	22.5	570	130

\*\* The dimensionless theoretical Bingham velocity profile for an attached upper core is independent of the yield stress; therefore the viscosity value was obtained by identifying the dimensionless yield stress which set  $\bar{H}_b > \bar{H}(\bar{x}=0)$ .

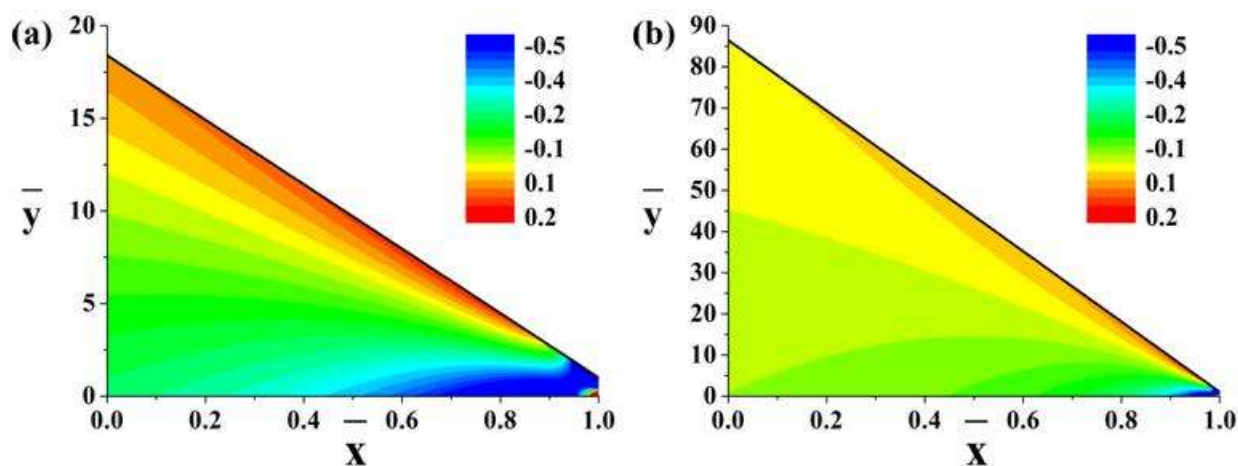


**Figure 9.14.** Shear rate fields  $\frac{d\bar{u}}{d\bar{y}}$  for Newtonian fluid found using Eq. (9.7) for: (a)  $\bar{H}_0 = 18.4$ , and (b)  $\bar{H}_0 = 86.5$ .

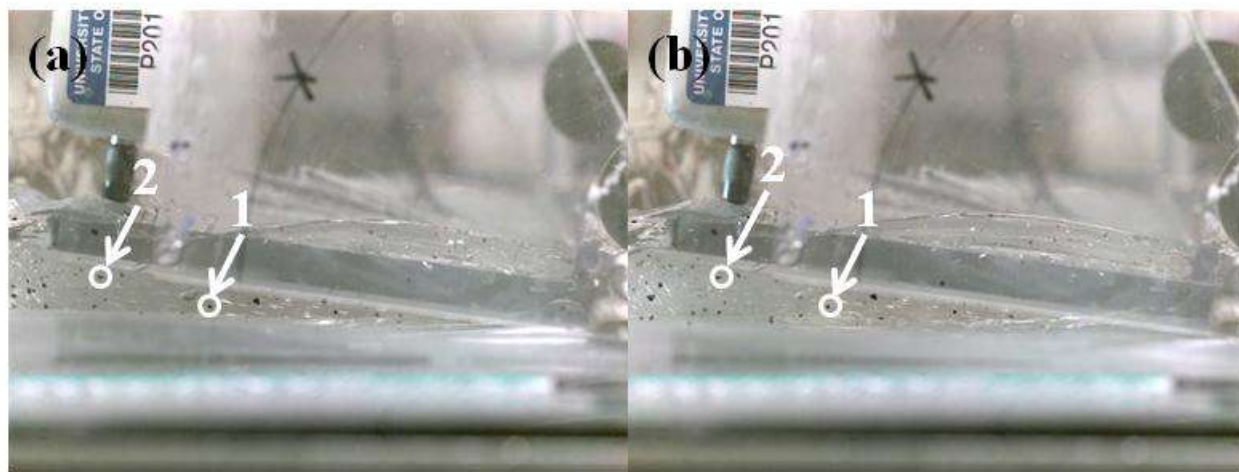


**Figure 9.15.** Stagnation zone close to the inclined spreading plate. The inclination angle of the plate is  $5^\circ$  with the exit height of 1.5 mm;  $\bar{H}_0 = 9.6$ . The two consecutive images are taken 3 s apart (the right-hand side image first). Arrows point to two seeding particles (encircled) that reveal no motion.

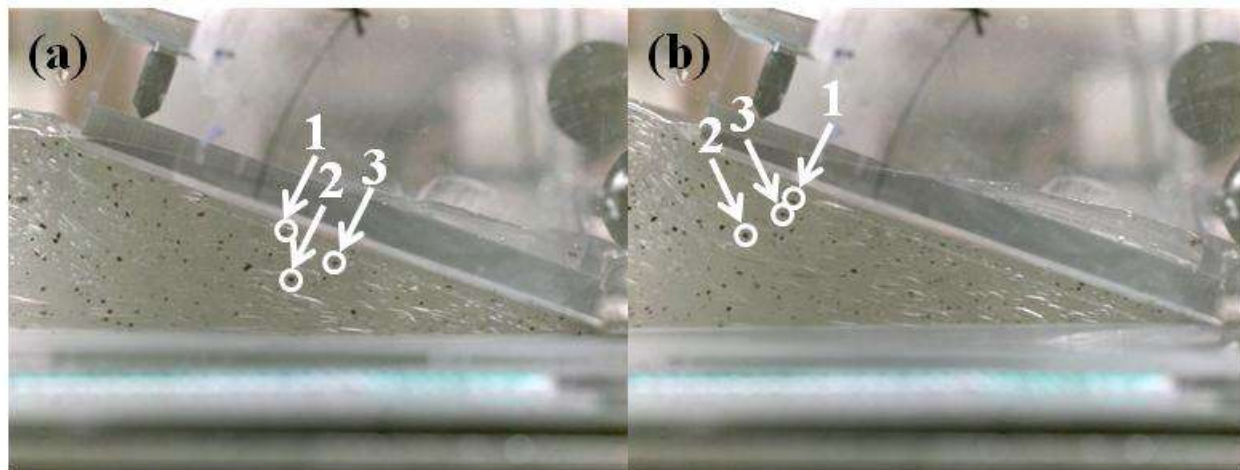


**Figure 9.16.** Reverse flow zone. The angle of the spreading plate inclination is  $20^\circ$  with the exit height of 0.650 mm;  $\overline{H}_0 = 79.9$ . The two consecutive images are taken 4 s apart (the right-hand side image first). All three particles (encircled) move in the reverse direction, with particle 1 being slower than particles 2 and 3.



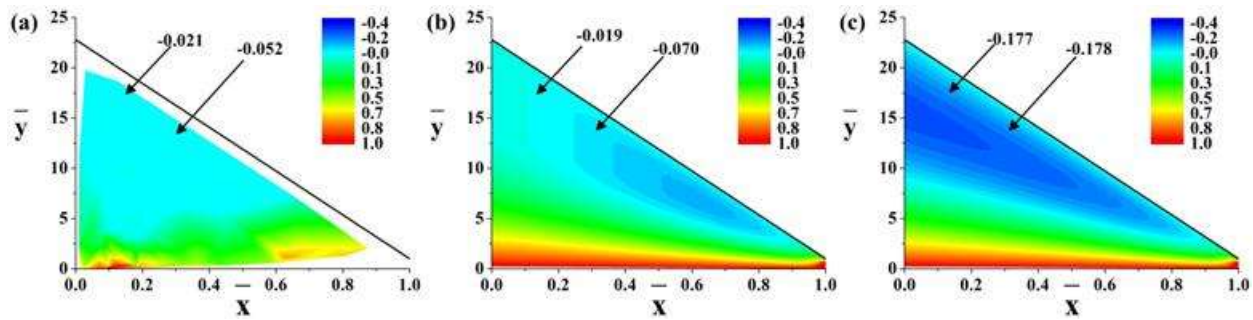


**Figure 9.17.** Experimental velocity fields measured for Carbopol gel (a) under a wedge at  $\alpha = 5^\circ$  and  $H_1 = 0.6$  mm versus the corresponding theoretical velocity fields for a (b) Bingham fluid with a floating core from  $\bar{x} = 0$  to  $\bar{x} = 0.92$ , and no core, or Newtonian profile, from  $\bar{x} = 0.92$  to  $\bar{x} = 1$  and (c) Newtonian fluid. Legend shows the dimensionless velocity values where the wall velocity is 0.167 m/s. Arrows in (a) point to representative velocities in the respective region of flow and in (b) and (c) the theoretical velocities are given at the same respective location as in (a).

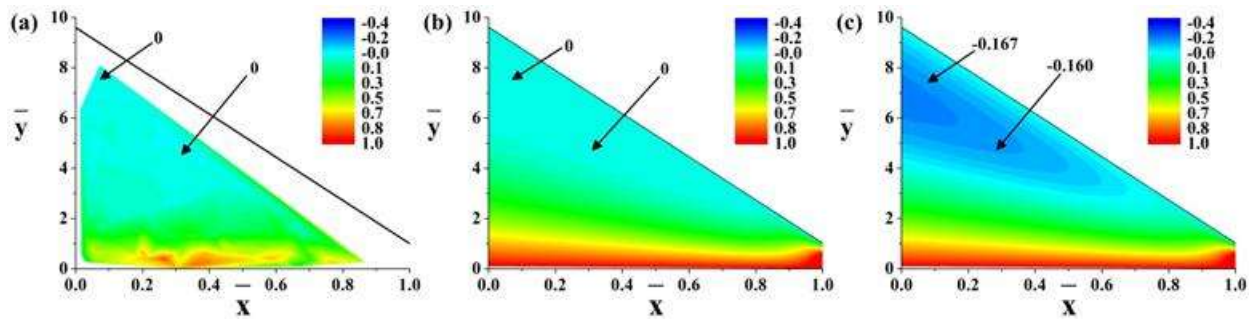


**Figure 9.18.** Experimental velocity fields measured for Carbopol gel (a) under a wedge at  $\alpha = 5^\circ$  and  $H_1 = 1.5$  mm versus the corresponding theoretical velocity fields for a (b) Bingham fluid with an attached upper core from  $\bar{x} = 0$  to  $\bar{x} = 0.80$ , and no core, or Newtonian profile, from  $\bar{x} = 0.80$  to  $\bar{x} = 1$  and (c) Newtonian fluid. Legend shows the dimensionless velocity values where the wall velocity is 0.167 m/s. Arrows in (a) point to representative velocities in the respective region of flow and in (b) and (c) the theoretical velocities are given at the same respective location as in (a).



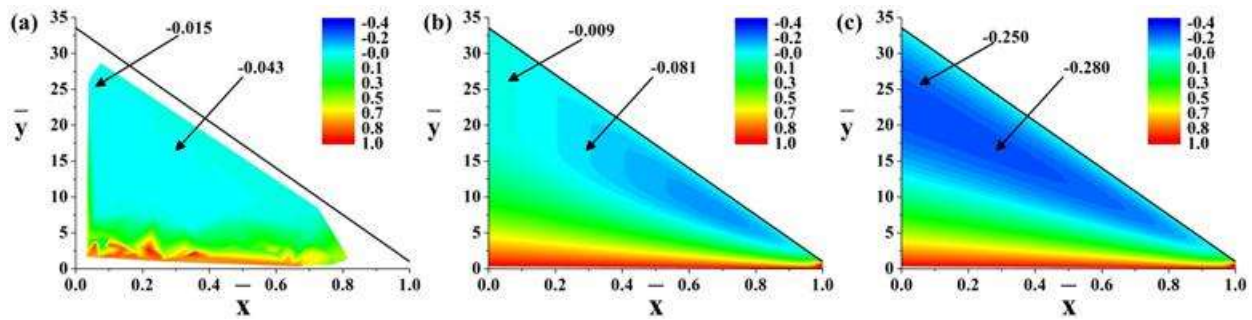


**Figure 9.19.** Experimental velocity fields measured for Carbopol gel (a) under a wedge at  $\alpha = 10^\circ$  and  $H_1 = 0.8$  mm versus the corresponding theoretical velocity fields for a (b) Bingham fluid with a floating core from  $\bar{x} = 0$  to  $\bar{x} = 0.95$ , and no core, or Newtonian profile, from  $\bar{x} = 0.95$  to  $\bar{x} = 1$  and (c) Newtonian fluid. Legend shows the dimensionless velocity values where the wall velocity is 0.167 m/s. Arrows in (a) point to representative velocities in the respective region of flow and in (b) and (c) the theoretical velocities are given at the same respective location as in (a).

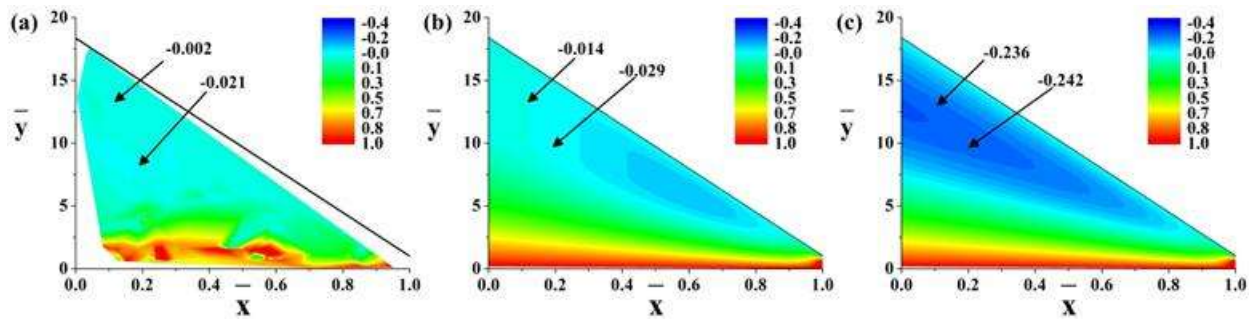


**Figure 9.20.** Experimental velocity fields measured for Carbopol gel (a) under a wedge at  $\alpha = 10^\circ$  and  $H_1 = 1.5$  mm versus the corresponding theoretical velocity fields for a (b) Bingham fluid with a floating core from  $\bar{x} = 0$  to  $\bar{x} = 0.90$ , and no core, or Newtonian profile, from  $\bar{x} = 0.90$  to  $\bar{x} = 1$  and (c) Newtonian fluid. Legend shows the dimensionless velocity values where the wall velocity is 0.167 m/s. Arrows in (a) point to representative velocities in the respective region of flow and in (b) and (c) the theoretical velocities are given at the same respective location as in (a).

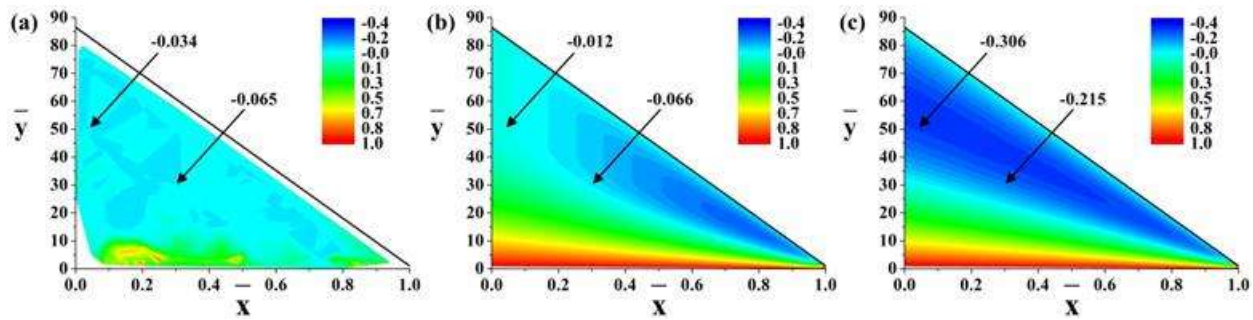


**Figure 9.21.** Experimental velocity fields measured for Carbopol gel (a) under a wedge at  $\alpha = 20^\circ$  and  $H_1 = 0.6$  mm versus the corresponding theoretical velocity fields for a (b) Bingham fluid with a floating core from  $\bar{x} = 0$  to  $\bar{x} = 0.98$ , and no core, or Newtonian profile, from  $\bar{x} = 0.98$  to  $\bar{x} = 1$  and (c) Newtonian fluid. Legend shows the dimensionless velocity values where the wall velocity is 0.167 m/s. Arrows in (a) point to representative velocities in the respective region of flow and in (b) and (c) the theoretical velocities are given at the same respective location as in (a).

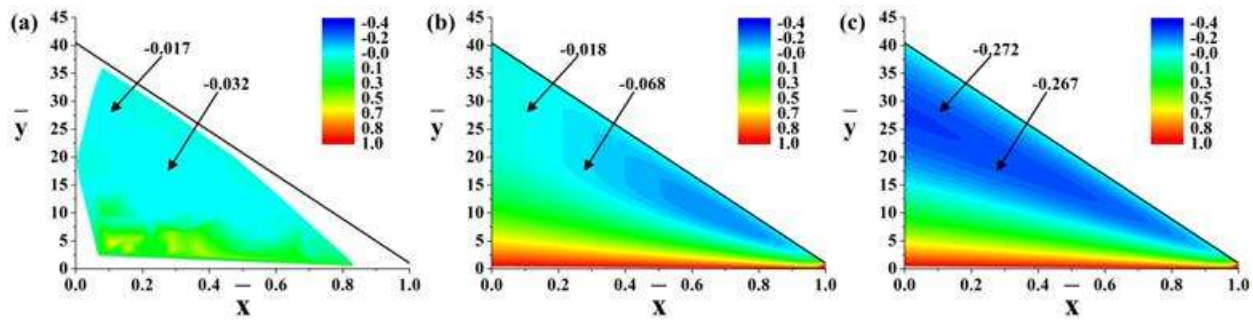


**Figure 9.22.** Experimental velocity fields measured for Carbopol gel (a) under a wedge at  $\alpha = 20^\circ$  and  $H_1 = 1.3$  mm versus the corresponding theoretical velocity fields for a (b) Bingham fluid with a floating core from  $\bar{x} = 0$  to  $\bar{x} = 0.96$ , and no core, or Newtonian profile, from  $\bar{x} = 0.96$  to  $\bar{x} = 1$  and (c) Newtonian fluid. Legend shows the dimensionless velocity values where the wall velocity is 0.167 m/s. Arrows in (a) point to representative velocities in the respective region of flow and in (b) and (c) the theoretical velocities are given at the same respective location as in (a).

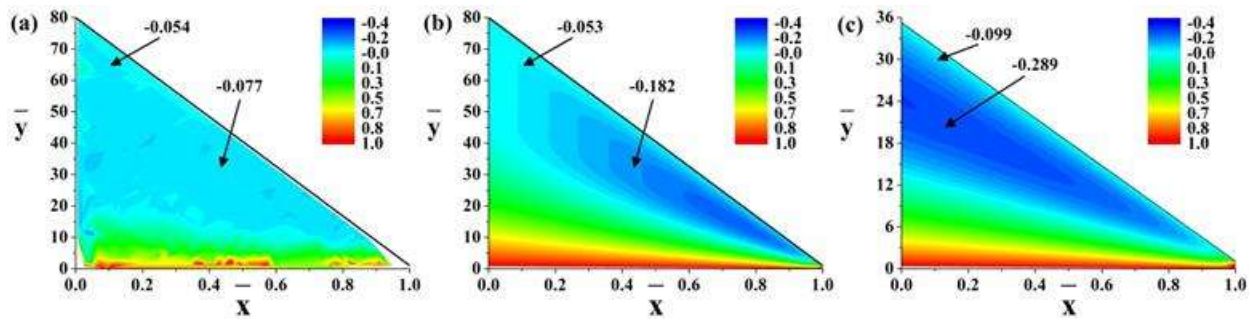


**Figure 9.23.** Experimental velocity fields measured for Carbopol gel (a) under a wedge at  $\alpha = 20^\circ$  and  $H_1 = 0.65$  mm versus the corresponding theoretical velocity fields for a (b) Bingham fluid with a floating core from  $\bar{x} = 0$  to  $\bar{x} = 0.98$ , and no core, or Newtonian profile, from  $\bar{x} = 0.98$  to  $\bar{x} = 1$  and (c) Newtonian fluid. Legend shows the dimensionless velocity values where the wall velocity is 0.240 m/s. Arrows in (a) point to representative velocities in the respective region of flow and in (b) and (c) the theoretical velocities are given at the same respective location as in (a).

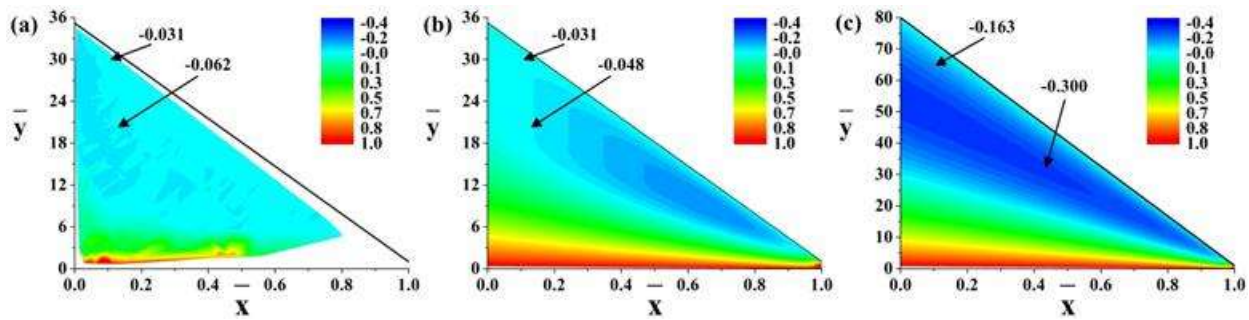


**Figure 9.24.** Experimental velocity fields measured for Carbopol gel (a) under a wedge at  $\alpha = 20^\circ$  and  $H_1 = 1.5$  mm versus the corresponding theoretical velocity fields for a (b) Bingham fluid with a floating core from  $\bar{x} = 0$  to  $\bar{x} = 0.95$ , and no core, or Newtonian profile, from  $\bar{x} = 0.95$  to  $\bar{x} = 1$  and (c) Newtonian fluid. Legend shows the dimensionless velocity values where the wall velocity is 0.240 m/s. Arrows in (a) point to representative velocities in the respective region of flow and in (b) and (c) the theoretical velocities are given at the same respective location as in (a).

## 9.5 Discussion

Near the moving wall, the shear rate is high and from Figure 9.9 it can be seen that a Bingham fluid and Newtonian fluid result in approximately the same theoretical velocity profiles. This is also the case for every experiment. The forward flow region, designated from green to red in Figures 9.17 – 9.24, found from experiment is in good agreement, in magnitude and position, with both the Bingham and Newtonian theoretical results. The agreement is better when  $\bar{H}_0$  is small and as  $\bar{H}_0$  increases the experimentally found forward velocity region decreases in height although it still shows similar magnitudes. This discrepancy is likely due to comparing a shear-thinning fluid in experiment to theoretical Bingham and Newtonian models.

Away from the moving wall, the shear rate decreases and pressure gradient is able to push the fluid backwards causing a reverse flow region. It is in this region where the greatest distinction between a Newtonian and Bingham fluids occurs. In the theoretical Newtonian case the velocity profile shows strong reverse flow that increases as  $\bar{H}_0$  increases. However, the theoretical velocity profile for a Bingham fluid illustrates how the yield stress of the fluid can arrest or slow the flow in the reverse flow region.

An example of the fluid in the reverse flow region being arrested can be seen in Figure 9.18 where  $\bar{H}_0 = 9.6$ . In Figure 9.18(a) the experimental velocity profile shows that fluid above  $\bar{y} \approx 4$  is not moving and the corresponding images in Figure 9.15 confirm this. This is corroborated by the velocity profile for a Bingham fluid shown in Figure 9.18(b) which has an attached upper core (Eq. 9.47). The viscosity value, shown in Table 9.1, for this case was determined by identifying the lowest viscosity value at which the criteria for a floating core case is not met, when  $H_b > H(x)$ , at the entrance of the wedge. In other words, a viscosity value less than or equal to 50 Pa·s satisfies the condition for an attached upper core and a viscosity value greater than 50 Pa·s would make the criteria for a floating core to be true. Comparing the experimental profile to the theoretical Newtonian profile emphasizes the role that the yield stress has on the reverse flow profile. Two points are identified in the experimental profile where the velocity is  $\bar{u} = 0$ . However, in the velocity profile for the Newtonian fluid the velocity values are  $\bar{u} = -0.167$  and  $\bar{u} = -0.160$ .

At a higher angle of inclination of the spreading plate, the adverse pressure gradient is sufficient to generate reverse flow illustrated by the motion of particles 2 and 3 in Figure 9.16 relative to the spreading plate which is at rest. The respective position of these two particles does

not change, which shows that there is a plug flow core in the reverse flow zone. Examples of fluid being slowed due to the yield stress in the reverse flow region as well as the Newtonian velocity profiles for the same geometry are shown in Figures 9.17, and 9.19 – 9.24. The images highlighting a floating core in Figure 9.16 correspond to the experimental data in Figure 9.23. The experimental velocity profiles [Figures 9.17(a), 9.19(a) – 9.24(a)] show that the reverse flow velocity at the point indicated by the arrows ranges from  $\bar{u} = -0.015$  to  $\bar{u} = -0.077$ , albeit when  $\bar{H}_0 = 18.4$  there is  $\bar{u} = -0.002$ . The theoretical velocities for a Bingham fluid [Figures 9.17(b), 9.19(b) – 9.24(b)] at the indicated points show velocity values ranging from  $\bar{u} = -0.009$  to  $\bar{u} = -0.081$ , albeit when  $\bar{H}_0 = 79.9$  the theoretical reverse velocity at one point is  $\bar{u} = -0.182$ . In general, the theoretical velocity values found for a Bingham fluid are in very good agreement with the experimental velocity values. On the other hand, the theoretical velocity values predicted for a Newtonian fluid at the points indicated range from  $\bar{u} = -0.099$  to  $\bar{u} = -0.300$  which is an order of magnitude higher than the values found experimentally.

The conditions for a specific type of core to exist are presented in Eqs. (9.51). In all the theoretical Bingham velocity profiles that were mapped using a floating core, the boundary between flow and rigid zone,  $H_b$ , became greater than the wedge opening,  $H$ , at  $\bar{x} \geq 0.9$ . Each figure has the specified value; in general, as  $\bar{H}_0$  increased the coordinate at which  $H_b$  became larger than  $H$  also increased. Furthermore, at the same coordinate when  $H_b > H$ ,  $H_a$  became greater than 1 for the attached upper core. At  $\bar{H}_0 = 9.6$ , an attached core was mapped for the theoretical Bingham velocity profile until  $\bar{x} \geq 0.8$ ,  $H_a$  became greater than the wedge opening,



H. Therefore, the exiting part of the flow for all  $\overline{H}_0$  is mapped using a Newtonian fluid since no core exists as shown in Figures 9.17 – 9.24, as instructed by Eq. (9.51).

Despite the discrepancy in the theoretical velocity flow field of a Newtonian fluid compared to the experimental data, relevant information from the measured force can be obtained. This is especially important since the pressure profile cannot be explicitly obtained in the case of a Bingham fluid. The ability to obtain the pressure profile in the theoretical Newtonian case allows the torque balance to be acquired and gives relevance to the measured force.

The measured force gauge data in Table 9.1 reveals three trends found in the experiments with Carbopol gels that agree with the predictions of the Newtonian fluid theory. They are of interest to applications involving sensory feedback during the spreading process. The first trend is observed when keeping the exit height,  $H_1$ , constant; then, the force decreases as  $\overline{H}_0$  increases. For example, in the experiments with  $H_1$  equal to 0.6 mm to 0.8 mm and  $\overline{H}_0 = 22.8$ ,  $\overline{H}_0 = 33.6$ , and  $\overline{H}_0 = 86.5$ , the force respectively decreases from 19.1 N, to 13.5 N, and to 8.1 N. Similarly in the case of  $H_1$  equal to 1.3 mm to 1.5 mm, experiments with  $\overline{H}_0 = 9.7$ ,  $\overline{H}_0 = 18.4$ , and  $\overline{H}_0 = 40.5$ , revealed respectively the force decreasing from 15.0 N to 7.9 N, and to 6.8 N.

The second trend found with Carbopol gels which is similar to the Newtonian behavior is seen when keeping  $\overline{H}_0$  constant, while increasing  $H_1$ ; then the force is increasing. In the experiments with  $\overline{H}_0$  set at 22.8 and 18.4, the two relatively close values, and  $H_1$  set to 0.6 mm and 1.5 mm, respectively, the measured force decreased from 19.1 N to 7.9 N. The same trend

was present in experiments with  $\overline{H}_0$  set to 33.6 and 40.5, where the measured force decreased from 13.5 N to 6.8 N as  $H_1$  increased from 0.8 mm to 1.3 mm.

The third trend which was similar in the experiments with Carbopol gels as compared to the predictions of the Newtonian flow theory was observed when the velocity of the moving surface was increasing, while both  $H_1$  and  $\overline{H}_0$  were kept constant; then the force was increasing. According to Eq. (9.31) for a Newtonian fluid, the force  $F$  is proportional to the velocity of the moving surface  $V_0$ , since the viscosity  $\mu$  and the other experimental parameters are constant. Therefore, the force should increase in the same proportion as the velocity. Indeed, the ratio of the two velocities is  $0.167/0.240 = 0.7$  and the ratio of the forces from experiments with  $\overline{H}_0 = 40.5$  ( $V_0=0.167$  m/s) and with  $\overline{H}_0 = 35.2$  ( $V_0=0.240$  m/s) it is  $6.8$  N/ $9.7$  N =  $0.7$ . The experiments with  $\overline{H}_0 = 86.5$  ( $V_0=0.167$  m/s) and with  $\overline{H}_0 = 79.9$  ( $V_0=0.240$  m/s) at the same velocity ratio had a force ratio of  $8.1$  N/ $9.8$  N =  $0.83$ , which is also not far from  $0.7$ . Considering the experimental error, it was shown that the force is directly proportional to velocity, which is correctly captured by the theory for Newtonian fluid.

The viscosity values in Table 9.1 present the results for a theoretical Newtonian fluid by direct calculation employing Eq. (31) and using the measured force. Alternatively, the viscosity values for the theoretical Bingham fluid were found by adjusting the viscosity so that the velocity profile matched the experimental data. The evaluated Newtonian viscosities were in the range from  $4.8$  Pa·s to  $22.5$  Pa·s in agreement with the experiment. Using the fitting parameters  $n = 0.17$  and  $K = 196$  Pa·s <sup>$n$</sup>  found from the parallel plate geometry with smooth plates, shown in Figure 9.11, these viscosity values correspond to shear rates of  $88$  s<sup>-1</sup> and  $13.6$  s<sup>-1</sup>, respectively. Alternatively, the viscosity values found using the Bingham model range from  $43$  Pa·s to  $155$

Pa·s, which corresponds to shear rates of  $6.2 \text{ s}^{-1}$  and  $1.3 \text{ s}^{-1}$ , respectively. Near the exit where the core vanishes, i.e.  $H_a > H$  and  $H_b > H$ , the flow transforms to that of a Newtonian fluid. Therefore the shear rate at the wedge exit can be approximated using the plate speed and exit height resulting in the value of the order of  $100 \text{ s}^{-1}$ , which is in agreement with the rheological data presented in Figure 9.11. Furthermore, the shear rate near the moving plate is also of the same order of  $100 \text{ s}^{-1}$ . This is calculated employing a rough estimate based on Figure 9.9 where it can be seen that the shear rate below  $\bar{y} = 0.2$  is roughly the same for any case. Therefore, taking  $\partial\bar{u}/\partial\bar{y} = (1-0.5)/(0.2-0) = 2.5$  and using  $V_0 = 0.167 \text{ m/s}$  and approximating  $y = 0.01 \text{ m}$ , the dimensional  $\partial u/\partial y = 42 \text{ s}^{-1}$  and increases nearer to the wall. The region near the exit and the moving plate represents the highest shear rates within the wedge where, correspondingly, the fluid behaves as a Newtonian one. As one moves towards the reverse flow region, the shear rate will only decrease meaning that the viscosity will only increase for a shear-thinning fluid. Since the velocity of the theoretical reverse flow region in the framework of the Bingham model was found by adjusting the viscosity so that the theory matched the experimental velocities, the viscosities found using the Bingham model are likely to represent the viscosity of Carbopol in the region of low shear. In the velocity profile corresponding to the Bingham fluid, the viscosity of the fluid had a direct impact on the configuration of the yield surface in the reverse flow, since the yield stress is a fixed parameter. In this reverse flow region, if a shear rate exists, it is relatively small compared to that near the moving wall and near the exit where the flow is practically Newtonian. Then, it is expected that the viscosity values for a pseudoplastic power-law fluid in a region of low shear reveal higher values of viscosity. Therefore, it seems that the combination of the two models (the Newtonian and the Bingham ones) allows for a

comprehensive understanding of how the viscosity of a power-law fluid changes due to the changing shear rate inside of a wedge.

The comparison of the predictions of the Newtonian and the Bingham models to experimental data has elucidated the advantages and disadvantages of both models. It is seen that near the moving wall, where the shear rate is high and no core is formed, both predicted velocity profiles agree with the experimental data. Only in the reverse flow region does the difference between the two models become evident. Experimentally, two rigid core types were identified, namely the attached upper core and the floating core. These cores had a dramatic influence on the reverse flow domain and were correctly predicted by the Bingham model. Although the theoretical Newtonian model was unable to reveal core formation, its closed form of the Reynolds' equation makes finding the pressure profile simple. With the pressure profile available, trends in the force acting on the wedge from the fluid under different wedge opening angles and the moving wall velocity were correctly predicted in the framework of the Newtonian model.

During the experiments, it was observed that trapped air bubbles would recirculate within the fluid and would periodically exit the front of the wedge-like gap. Furthermore, air bubbles were formed at the contact line between the rolling edge at the back of the wedge and the moving surface. These bubbles would typically stay near the moving surface and exit the wedge. This will be explored in the future.

## **9.6 Conclusion**

Carbopol gels exhibit pseudoplastic power-law fluid behavior in simple shear flows, as well as possess a yield stress. The general flow structure in the wedge-like flow can be

characterized using an analytical Newtonian fluid model in domains of high shear, albeit the Bingham fluid model must be used in lower shear domains. The latter reveals the characteristic reverse flow zone containing a rigid core, which is also observed in the experiments with Carbopol.

The agreement of the viscosity values measured in the wedge-like flow experiments based on the Newtonian fluid model with the one measured in the simple shear flow at the shear rate corresponding to the shear rate near the entrance of the wedge-like gap is quite remarkable. Furthermore, in the domains of low shear it was found in the framework of the Bingham fluid model that the viscosity increases, as expected for a shear-thinning fluid. Overall, it appears that using both Newtonian and Bingham models in conjunction elucidates more information than only for a single model.

## 10. CONCLUSION

In the framework of this work several novel methods of characterization of the mechanical properties of different materials used in the construction industry were developed. In some cases, such as characterization of foam properties, drainage in gravity settler was used to reveal a new perspective of foam as a consolidating medium. By using the gravity settler, properties of foam can be elucidated by measuring the drainage rate. It was shown how different surfactant concentrations, air flow rate, and polymer additives affect the mechanical properties of foam, which can be used to create a stronger and lighter wallboard.

In other cases, a new squeeze apparatus was developed and built with an accompanying theoretical model which provided a new framework for measuring the mechanical properties of soft solids, and revealed their rheological nature as that of Bingham-like materials. The squeeze apparatus is a constant volume device which employs normal stresses to cause soft solid to flow. The squeezing device allows for the viscosity and yield stress of soft solids to be measured. This device stresses the material in the normal direction causing a different type of flow to occur than in typical shear rheometry. The difference in flow type allows the mechanical properties of construction materials, such as joint compound, to be measured and clearly distinguished. Namely, materials with a similar shear viscosity do not necessarily have a similar elongational viscosity therefore they can be distinguished from one another. Moreover, the yield stress can be measured directly using the squeezing device, whereas it is only indirectly interpreted in a shear-based devices. The squeezing device can be altered to find unique properties of concentrated dispersions, such as the transition from liquid-like behavior to solid-like behavior. That is, at one concentration the material will flow as a liquid when stressed, however, at a slightly higher concentration the material will act as a solid and crack when being stressed.

In addition, a second apparatus for the mechanical characterization of soft solids was developed. It employed a moving conveyer belt that forces material through a wedge-shaped geometry, causing the material to be spread similarly to the practical applications. This spreading device measures the upward resistance force of the material as it is being drawn into the wedge-shape geometry. This can be translated into the force felt by practitioners as they are spreading construction materials, such as joint compounds. Also, the quality of the deposited compound, or its absence, i.e. formation of defects (craters), as it exits the wedge could be observed and interpreted using this device.

An additional element of the present work was development of core-shell nanofibers mats with self-healing properties, which are of interest for reinforcing laminated materials.

The novel devices, techniques and materials developed and explored in this thesis will enable construction materials to be characterized and improved through a number of methods. This characterization can then be used to optimize the material properties and closely fit them to particular application needs.

## 11. CITED LITERATURE

- Aksel, N., & Heymann, L. (2007). Rheology of suspensions and emulsions. In Tropea, C., Yarin, A. L., & J. Foss (Eds.), *The Springer Handbook of Experimental Fluid Mechanics* (680-720). Berlin: Springer.
- Akthar, F. K., & Evans, J. R. G. (2010). High porosity (> 90%) cementitious foams. *Cement and Concrete Research*, 40(2), 352-358.
- Astarita, G., & Marrucci, G. (1974). Principles of Non-Newtonian Fluid Mechanics. New York: McGraw-Hill.
- Banfill, P. F. G. (1994). Rheological methods for assessing the flow properties of mortar and related materials. *Construction and Building materials*, 8(1), 43-50.
- Barenblatt, G.I., Entov, V.M., & Ryzhik, V.M. (Academy of S. of the U.S.S.R. (SU)). (1989). Theory of fluid flows through natural rocks.
- Barnes, H.A. (2007). Thixotropy, rheopexy, yield stress. In Tropea, C., Yarin, A. L., & J. Foss (Eds.), *The Springer Handbook of Experimental Fluid Mechanics* (661-679). Berlin: Springer.
- Batra, R. L. (1966). Rheodynamic lubrication of a journal bearing. *Applied Scientific Research, Section A*, 15(1), 331-344.
- Bazilevsky, A. V., Sun, K., Yarin, A. L., & Megaridis, C. M. (2007b). Selective intercalation of polymers in carbon nanotubes. *Langmuir*, 23(14), 7451-7455.
- Bazilevsky, A. V., Sun, K., Yarin, A. L., & Megaridis, C. M. (2008). Room-temperature, open-air, wet intercalation of liquids, surfactants, polymers and nanoparticles within nanotubes and microchannels. *Journal of Materials Chemistry*, 18(6), 696-702.
- Bazilevsky, A. V., Yarin, A. L., & Megaridis, C. M. (2007a). Co-electrospinning of core-shell fibers using a single-nozzle technique. *Langmuir*, 23(5), 2311-2314.
- Bhakta, A., & Ruckenstein, E. (1995). Drainage of a standing foam. *Langmuir*, 11(5), 1486-1492.
- Bielawski, C. W., & Grubbs, R. H. (2007). Living ring-opening metathesis polymerization. *Progress in Polymer Science*, 32(1), 1-29.
- Bikerman, J. J., (1973). Foams. New York: Springer.
- Blaiszik, B. J., Kramer, S. L. B., Olugebefola, S. C., Moore, J. S., Sottos, N. R., & White, S. R. (2010). Self-healing polymers and composites. *Annual Review of Materials Research*, 40, 179-211.



- Blaiszik, B. J., Sottos, N. R., & White, S. R. (2008). Nanocapsules for self-healing materials. *Composites Science and Technology*, 68(3), 978-986.
- Bleay, S. M., Loader, C. B., Hawyees, V. J., Humberstone, L., & Curtis, P. T. (2001). A smart repair system for polymer matrix composites. *Composites Part A: Applied Science and Manufacturing*, 32(12), 1767-1776.
- Bohnhoff, G., Shackelford, C., Malusis, M., Scalia, J., Benson, C., Edil, T., Di Emidio, G., Katsumi, T., and F. Mazzieri, (2013). Novel bentonites for containment barrier applications. In *Proc., 18th Int. Conf. on Soil Mechanics and Geotechnical Engineering—Challenges and Innovations in Geotechnics* (pp. 2997-3000). Presses des Ponts, Paris.
- Brown, E. N., White, S. R., & Sottos, N. R. (2005). Retardation and repair of fatigue cracks in a microcapsule toughened epoxy composite—Part I: Manual infiltration. *Composites Science and Technology*, 65(15), 2466-2473.
- Brown, E. N., White, S. R., & Sottos, N. R. (2005). Retardation and repair of fatigue cracks in a microcapsule toughened epoxy composite—Part II: In situ self-healing. *Composites Science and Technology*, 65(15), 2474-2480.
- Bucknall, C. B., Drinkwater, I. C., & Smith, G. R. (1980). Hot plate welding of plastics: factors affecting weld strength. *Polymer Engineering & Science*, 20(6), 432-440.
- Butt, H. J. (2011). Controlling the flow of suspensions. *Science*, 331(6019), 868-869.
- Campanella, O. H., & Peleg, M. (2002). Squeezing flow viscometry for nonelastic semiliquid foods—theory and applications. *Critical reviews in food science and nutrition*, 42(3), 241-264.
- Cardoso, F. A., John, V. M., & Pileggi, R. G. (2009). Rheological behavior of mortars under different squeezing rates. *Cement and Concrete Research*, 39(9), 748-753.
- Carlsson, L. A., & Aksoy, A. (1991). Analysis of interleaved end-notched flexure specimen for measuring mode II fracture toughness. *International journal of fracture*, 52(1), 67-77.
- Chen, Q., Zhang, L. F., Yoon, M. K., Wu, X. F., Arefin, R. H., & Fong, H., (2012a). Epoxy composites reinforced and/or toughened with electrospun SiO<sub>2</sub> nanofibers. *Journal of Applied Polymer Science*, 124, 444-451.
- Chen, Q., Zhang, L., Rahman, A., Zhou, Z., Wu, X. F., & Fong, H. (2011). Hybrid multi-scale epoxy composite made of conventional carbon fiber fabrics with interlaminar regions containing electrospun carbon nanofiber mats. *Composites Part A: Applied Science and Manufacturing*, 42(12), 2036-2042.
- Chen, Q., Zhang, L., Zhao, Y., Wu, X. F., & Fong, H. (2012b). Hybrid multi-scale composites developed from glass microfiber fabrics and nano-epoxy resins containing electrospun glass nanofibers. *Composites Part B: Engineering*, 43(2), 309-316.

- Cheng, D. C. (1986). Yield stress: a time-dependent property and how to measure it. *Rheologica Acta*, 25(5), 542-554.
- Cho, S. H., White, S. R., & Braun, P. V. (2009). Self-Healing Polymer Coatings. *Advanced Materials*, 21(6), 645-649.
- Chou, T. W. (1992). Microstructural design of fiber composites. Cambridge University Press.
- Clem, A. G. (1961). Industrial applications of bentonite. *Clays and Clay Minerals*, 10, 272-283.
- Colak, A. (2000). Density and strength characteristics of foamed gypsum. *Cement and Concrete Composites*, 22(3), 193-200.
- Coussot, P., Tocquer, L., Lanos, C., & Ovarlez, G. (2009). Macroscopic vs. local rheology of yield stress fluids. *Journal of Non-Newtonian Fluid Mechanics*, 158(1), 85-90.
- Covey, G. H., & Stanmore, B. R. (1981). Use of the parallel-plate plastometer for the characterisation of viscous fluids with a yield stress. *Journal of Non-Newtonian Fluid Mechanics*, 8(3), 249-260.
- Curran, S. J., Hayes, R. E., Afacan, A., Williams, M. C., & Tanguy, P. A. (2002). Properties of Carbopol Solutions as Models for Yield-Stress Fluids. *Journal of food science*, 67(1), 176-180.
- Dienes, G. J., & Klemm, H. F. (1946). Theory and application of the parallel plate plastometer. *Journal of Applied Physics*, 17(6), 458-471.
- Divoux, T., Tamarii, D., Barentin, C., Teitel, S., & Manneville, S. (2012). Yielding dynamics of a Herschel–Bulkley fluid: a critical-like fluidization behaviour. *Soft Matter*, 8(15), 4151-4164.
- Dorier, C., & Tichy, J. (1992). Behavior of a Bingham-like viscous fluid in lubrication flows. *Journal of non-newtonian fluid mechanics*, 45(3), 291-310.
- Doshi, J., & Reneker, D. H. (1995). Electrospinning process and applications of electrospun fibers. *Journal of electrostatics*, 35(2), 151-160.
- Dransfield, K., Baillie, C., & Mai, Y. W. (1994). Improving the delamination resistance of CFRP by stitching—a review. *Composites Science and Technology*, 50(3), 305-317.
- Dror, Y., Salalha, W., Avrahami, R., Zussman, E., Yarin, A. L., Dersch, R., Greiner, A., & Wendorff, J. H. (2007). One-Step Production of Polymeric Microtubes by Co-electrospinning. *Small*, 3(6), 1064-1073.
- Dzenis, Y. A. (2004). Spinning continuous fibers for nanotechnology. *Science*, 304, 1917-1919.
- Dzenis, Y. A. (2008). Structural nanocomposites. *Science*, 319, 419-420.

Dzenis, Y. A., & Reneker, D. H. (2001). U.S. Patent No. 6,265,333. Washington, DC: U.S. Patent and Trademark Office.

Engmann, J., Servais, C., & Burbidge, A. S. (2005). Squeeze flow theory and applications to rheometry: a review. *Journal of non-newtonian fluid mechanics*, 132(1), 1-27.

Eshtiaghi, N., Yap, S. D., Markis, F., Baudez, J. C., & Slatter, P. (2012). Clear model fluids to emulate the rheological properties of thickened digested sludge. *Water research*, 46(9), 3014-3022.

Estellé, P., & Lanos, C. (2007). Squeeze flow of Bingham fluids under slip with friction boundary condition. *Rheologica acta*, 46(3), 397-404.

Fowler, A. C. (1997). *Mathematical models in the applied sciences* (Vol. 17). Cambridge University Press.

Foster, M. D. (1955). The relation between composition and swelling in clays. *Clays and clay minerals*, 3, 205-220.

Garg, A. C., & Mai, Y. W. (1988). Failure mechanisms in toughened epoxy resins—A review. *Composites science and technology*, 31(3), 179-223.

Germick, R. J., Rehill, A. S., & Narsimhan, G. (1994). Experimental investigation of static drainage of protein stabilized foams—comparison with model. *Journal of food engineering*, 23(4), 555-578.

Gilford III, J., Hassan, M. M., Rupnow, T., Barbato, M., Okeil, A., & Asadi, S. (2013). Dicyclopentadiene (DCPD) and Sodium Silicate Microencapsulation for Self-Healing of Concrete. *Journal of Materials in Civil Engineering*.

Gotoh, R., & Shunizu, K. (2012). Slip Fracture and Shear Strength of Bentonite Gels. In *ICFI, Japan 1965*.

Greiner, A., & Wendorff, J. H. (2007). Electrospinning: a fascinating method for the preparation of ultrathin fibers. *Angewandte Chemie International Edition*, 46(30), 5670-5703.

Gupta, S. G., Rathi, C., & Kapur, S. (2013). Biologically Induced Self Healing Concrete: A Futuristic Solution for Crack Repair. *International Journal of Applied Sciences and Biotechnology*, 1(3), 85-89.

Hager, M. D., Greil, P., Leyens, C., van der Zwaag, S., & Schubert, U. S. (2010). Self-Healing Materials. *Advanced Materials*, 22(47), 5424-5430.

Hansen, C. J., Wu, W., Toohey, K. S., Sottos, N. R., White, S. R., & Lewis, J. A. (2009). Self-Healing Materials with Interpenetrating Microvascular Networks. *Advanced Materials*, 21(41), 4143-4147.

- Hassanien, M. M., Abou-El-Sherbini, K. S., & Al-Muaikel, N. S. (2010). Immobilization of methylene blue onto bentonite and its application in the extraction of mercury (II). *Journal of hazardous materials*, 178(1), 94-100.
- Hayes, S. A., Jones, F. R., Marshiya, K., & Zhang, W. (2007). A self-healing thermosetting composite material. *Composites Part A: Applied Science and Manufacturing*, 38(4), 1116-1120.
- Hoffman, U., Endel, K., & Wiln, K. (1933). Crystal structure and swelling of montmorillonite. *Zeit. Krist*, 86, 340-348.
- Hoffner, B., Gerhards, C., & Peleg, M. (1997). Imperfect lubricated squeezing flow viscometry for foods. *Rheologica acta*, 36(6), 686-693.
- Huang, M., & Yang, J. (2011). Facile microencapsulation of HDI for self-healing anticorrosion coatings. *Journal of Materials Chemistry*, 21(30), 11123-11130.
- Jones, A. S., Rule, J. D., Moore, J. S., Sottos, N. R., & White, S. R. (2007). Life extension of self-healing polymers with rapidly growing fatigue cracks. *Journal of the Royal Society Interface*, 4(13), 395-403.
- Jones, R. M. (1999). *Mechanics of Composite Materials* (2nd Ed.). Philadelphia: Taylor and Francis.
- Jun, S., Pelot, D. D., & Yarin, A. L. (2012). Foam consolidation and drainage. *Langmuir*, 28(12), 5323-5330.
- Kan, L. L., & Shi, H. S. (2012). Investigation of self-healing behavior of Engineered Cementitious Composites (ECC) materials. *Construction and Building Materials*, 29, 348-356.
- Karakaya, M. Ç., Karakaya, N., & Bakır, S. (2011). Some properties and potential applications of the Na-and Ca-bentonites of ordu (NE Turkey). *Applied Clay Science*, 54(2), 159-165.
- Kessler, M. R., Sottos, N. R., & White, S. R. (2003). Self-healing structural composite materials. *Composites Part A: applied science and manufacturing*, 34(8), 743-753.
- Kim, J. K., & Mai, Y. W. (1991). High strength, high fracture toughness fibre composites with interface control—a review. *Composites Science and Technology*, 41(4), 333-378.
- Koch, D. (2002). Bentonites as a basic material for technical base liners and site encapsulation cut-off walls. *Applied Clay Science*, 21(1), 1-11.
- Koehler, S. A., Hilgenfeldt, S., & Stone, H. A. (2000). A generalized view of foam drainage: experiment and theory. *Langmuir*, 16(15), 6327-6341.
- Kokkoli, E., & Zukoski, C. F. (2000). Interaction forces between hydrophobic and hydrophilic self-assembled monolayers. *Journal of Colloid and Interface Science*, 230(1), 176-180.

- Komine, H., & Ogata, N. (1996). Prediction for swelling characteristics of compacted bentonite. *Canadian Geotechnical Journal*, 33(1), 11-22.
- Koos, E., & Willenbacher, N. (2011). Capillary forces in suspension rheology. *Science*, 331(6019), 897-900.
- Kornev, K. G., Neimark, A. V., & Rozhkov, A. N. (1999). Foam in porous media: thermodynamic and hydrodynamic peculiarities. *Advances in Colloid and Interface Science*, 82(1), 127-187.
- Kruglyakov, P. M., Karakashev, S. I., Nguyen, A. V., & Vilкова, N. G. (2008). Foam drainage. *Current Opinion in Colloid & Interface Science*, 13(3), 163-170.
- Landau, L. D., & Lifshitz, E. M. (1987). *Fluid Mechanics*. New York: Pergamon Press.
- Landau, L. D., & Lifshitz, E. M. (1970). *Theory of Elasticity* (2nd ed). Oxford. Pergamon.
- Lane, R. A. (2005). High performance fibers for personnel and vehicle armor systems. *AMPTIAC Quarterly*, 9(2), 3-9.
- Lee, D., Gutowski, I. A., Bailey, A. E., Rubatat, L., de Bruyn, J. R., & Frisken, B. J. (2011). Investigating the microstructure of a yield-stress fluid by light scattering. *Physical Review E*, 83(3), 031401.
- Lin, S., Cai, Q., Ji, J., Sui, G., Yu, Y., Yang, X., Ma, Y., & Deng, X. (2008). Electrospun nanofiber reinforced and toughened composites through in situ nano-interface formation. *Composites Science and Technology*, 68(15), 3322-3329.
- Lipscomb, G. G., & Denn, M. M. (1984). Flow of Bingham fluids in complex geometries. *Journal of Non-newtonian Fluid Mechanics*, 14, 337-346.
- Logan, J. M. (1978). Creep, stable sliding, and premonitory slip. *Pure and Applied Geophysics*, 116(4-5), 773-789.
- Loitsyanskii, L. G. (1966). *Mechanics of Liquids and Gases*. Oxford: Pergamon.
- Low, I. M., & Mai, Y. M., (1990). Fracture properties and failure mechanism of pure and toughened epoxy resins. In H. P. Cheremisinoff (Ed) *Handbook of Ceramics and Composites* (105-150). New York: Marcel Dekker.
- Luckham, P. F., & Rossi, S. (1999). The colloidal and rheological properties of bentonite suspensions. *Advances in Colloid and Interface Science*, 82(1), 43-92.
- Luu, L. H., & Forterre, Y. (2009). Drop impact of yield-stress fluids. *Journal of Fluid Mechanics*, 632(1), 301-327.

- Magrabi, S. A., Dlugogorski, B. Z., & Jameson, G. J. (2001). Free drainage in aqueous foams: model and experimental study. *AIChE journal*, 47(2), 314-327.
- Mahto, V., & Sharma, V. P. (2004). Rheological study of a water based oil well drilling fluid. *Journal of Petroleum Science and Engineering*, 45(1), 123-128.
- Marshall, C. E. (1937). The colloidal properties of the clays as related to their crystal structure. *Journal of Physical Chemistry*, 41(7), 935-942.
- Marshall, C. E., & Krinbill, C. A. (1942). The Clays as Colloidal Electrolytes. *The Journal of Physical Chemistry*, 46(9), 1077-1090.
- Matos, G. R., Buckingham, D. A., DiFrancesco, C. A., Porter, K. E., Berry, C., Crane, M., Goonan, T., & Sznoppek, J. (2005). *Historical statistics for mineral and material commodities in the United States*. Reston, VA: US Geological Survey. Available online at <http://pubs.usgs.gov/ds/2005/140/>. (Accessed 08/27/2013)
- McKinley, G. H. (2007). Elongational flows. In Tropea, C., Yarin, A. L., & J. Foss (Eds.), *The Springer Handbook of Experimental Fluid Mechanics* (646-661). Berlin: Springer.
- Meeten, G. (2002). Constant-force squeeze flow of soft solids. *Rheologica Acta*, 41(6), 557-566.
- Meeten, G. H. (2000). Yield stress of structured fluids measured by squeeze flow. *Rheologica Acta*, 39(4), 399-408.
- Meeten, G. H. (2001). Squeeze flow between plane and spherical surfaces. *Rheologica Acta*, 40(3), 279-288.
- Meeten, G. H. (2004a). Squeeze flow of soft solids between rough surfaces. *Rheologica Acta*, 43(1), 6-16.
- Meeten, G. H. (2004b). Effects of plate roughness in squeeze-flow rheometry. *Journal of Non-Newtonian Fluid Mechanics*, 124(1), 51-60.
- Meeten, G. H. (2010). Comparison of squeeze flow and vane rheometry for yield stress and viscous fluids. *Rheologica Acta*, 49(1), 45-52.
- Mering, J. (1946). On the hydration of montmorillonite. *Transactions of the Faraday Society*, 42, B205-B219.
- Milne, A. A. (1954). A theory of rheodynamic lubrication lubrication and wear division. *Colloid & Polymer Science*, 139(1), 96-101.
- Murphy, E. B., & Wudl, F. (2010). The world of smart healable materials. *Progress in Polymer Science*, 35(1), 223-251.



Murray, H. H. (2000). Traditional and new applications for kaolin, smectite, and palygorskite: a general overview. *Applied Clay Science*, 17(5), 207-221.

Norrish, K. (1954). The swelling of montmorillonite. *Discussions of the Faraday Society*, 18, 120-134.

Nasseri, S., Bilston, L., Fasheun, B., & Tanner, R. (2004). Modelling the biaxial elongational deformation of soft solids. *Rheologica Acta*, 43(1), 68-79.

Nigen, S. (2005). Experimental investigation of the impact of an (apparent) yield-stress material. *Atomization and Sprays*, 15(1), 103-118.

Olugebefola, S. C., Aragón, A. M., Hansen, C. J., Hamilton, A. R., Kozola, B. D., Wu, W., Geubelle, P. H., Lewis, J. A., Sottos, N. R., & White, S. R. (2010). Polymer microvascular network composites. *Journal of Composite Materials*, 44(22), 2587-2603.

Oppong, F. K., Rubatat, L., Frisken, B. J., Bailey, A. E., & de Bruyn, J. R. (2006). Microrheology and structure of a yield-stress polymer gel. *Physical Review E*, 73(4), 041405.

Ovarlez, G., Barral, Q., & Coussot, P. (2010). Three-dimensional jamming and flows of soft glassy materials. *Nature Materials*, 9(2), 115-119.

Özden, E., Menciloglu, Y. Z., & Papila, M. (2010). Engineering chemistry of electrospun nanofibers and interfaces in nanocomposites for superior mechanical properties. *ACS Applied Materials & Interfaces*, 2(7), 1788-1793.

Pagano, N. J. (1974). On the calculation of interlaminar normal stress in composite laminate. *Journal of Composite Materials*, 8(1), 65-81.

Pang, J. W. C., & Bond, I. P. (2005). 'Bleeding composites'—damage detection and self-repair using a biomimetic approach. *Composites Part A: Applied Science and Manufacturing*, 36(2), 183-188.

Pang, J. W., & Bond, I. P. (2005). A hollow fibre reinforced polymer composite encompassing self-healing and enhanced damage visibility. *Composites Science and Technology*, 65(11), 1791-1799.

Park, J. H., & Braun, P. V. (2010). Coaxial Electrospinning of Self-Healing Coatings. *Advanced materials*, 22(4), 496-499.

Patel, A. J., Sottos, N. R., Wetzel, E. D., & White, S. R. (2010). Autonomic healing of low-velocity impact damage in fiber-reinforced composites. *Composites Part A: Applied Science and Manufacturing*, 41(3), 360-368.

Pelletier, M., Brown, R., Shukla, A., & Bose, A. (2011). Self-healing concrete with a microencapsulated healing agent. *University of Rhode Island, Kingston, RI, USA*.

Pelot, D. D., Sahu, R. P., Sinha-Ray, S., & Yarin, A. L. (2013). Strong squeeze flows of yield-stress fluids: The effect of normal deviatoric stresses. *Journal of Rheology*, 57, 719.

Pelot, D. D., Jun, S., & Yarin, A. L. (2014). Bentonite dispersions: Transition from liquid-like to solid-like behavior and cracking. *Journal of Rheology*. (under review).

Pelot, D. D., Klep, N., & Yarin, A. L. (in preparation). Spreading of Carbopol gels: Newtonian vs. non-Newtonian effects.

Phillips, J. N., & Mysels, K. J. (1955). Light scattering by aqueous solutions of sodium lauryl sulfate. *The Journal of Physical Chemistry*, 59(4), 325-330.

Pipes, R. B., & Pagano, N. J. (1970). Interlaminar stresses in composite laminates under uniform axial extension. *Journal of Composite Materials*, 4(4), 538-548.

Pusch, R. (1992). Use of bentonite for isolation of radioactive waste products. *Clay Miner*, 27, 353-361.

Qian, S., Zhou, J., De Rooij, M. R., Schlangen, E., Ye, G., & Van Breugel, K. (2009). Self-healing behavior of strain hardening cementitious composites incorporating local waste materials. *Cement and Concrete Composites*, 31(9), 613-621.

Qian, S. Z., Zhou, J., & Schlangen, E. (2010). Influence of curing condition and precracking time on the self-healing behavior of Engineered Cementitious Composites. *Cement and Concrete Composites*, 32(9), 686-693.

Rabideau, B. D., Lanos, C., & Coussot, P. (2009). An investigation of squeeze flow as a viable technique for determining the yield stress. *Rheologica Acta*, 48(5), 517-526.

Rahman, A., (2011). Fabrication and Mechanical Characterization of Novel Hybrid Carbon-Fiber/Epoxy Composites Reinforced with Toughening/Self-Repairing Nanofibers at Interfaces (M.S. Thesis), North Dakota State University, ND, USA.

Ramani, M. V., Kumar, R., & Gandhi, K. S. (1993). A model for static foam drainage. *Chemical Engineering Science*, 48(3), 455-465.

Reneker, D. H., & Chun, I. (1996). Nanometre diameter fibres of polymer, produced by electrospinning. *Nanotechnology*, 7(3), 216.

Reneker, D. H., & Yarin, A. L. (2008). Electrospinning jets and polymer nanofibers. *Polymer*, 49(10), 2387-2425.

Reneker, D. H., Yarin, A. L., Fong, H., & Koombhongse, S. (2000). Bending instability of electrically charged liquid jets of polymer solutions in electrospinning. *Journal of Applied Physics*, 87, 4531.



Reneker, D. H., Yarin, A. L., Zussman, E., & Xu, H. (2007). Electrospinning of nanofibers from polymer solutions and melts. *Advances in Applied Mechanics*, 41, 43-346.

Reynolds, O. (1886). On the theory of lubrication and its application, *Phil. Trans. Royal Soc. London* 177, 157-234.

Reznik, S. N., & Yarin, A. L. (2002). Strong squeezing flow between parallel plates leads to rolling motion at the contact line. *International Journal of Multiphase Flow*, 28(6), 911-925.

Ross, S. (1943). Foam and Emulsion Stabilities. *The Journal of Physical Chemistry*, 47(3), 266-277.

Rule, J. D., Sottos, N. R., & White, S. R. (2007). Effect of microcapsule size on the performance of self-healing polymers. *Polymer*, 48(12), 3520-3529.

Saïdi, A., Martin, C., & Magnin, A. (2011). Effects of surface properties on the impact process of a yield stress fluid drop. *Experiments in Fluids*, 51(1), 211-224.

Saint-Jalmes, A., & Langevin, D. (2002). Time evolution of aqueous foams: drainage and coarsening. *Journal of Physics: Condensed Matter*, 14(40), 9397.

Saint-Jalmes, A., Vera, M. U., & Durian, D. J. (1999). Uniform foam production by turbulent mixing: new results on free drainage vs. liquid content. *The European Physical Journal B-Condensed Matter and Complex Systems*, 12(1), 67-73.

Schlichting, H., (1987). *Boundary-Layer Theory* (7th Ed.). McGraw Hill.

Schmets, A. J., & van der Zaken, G. (2007). *Self healing materials: an alternative approach to 20 centuries of materials science* (Vol. 100). S. van der Zwaag (Ed.). Springer.

Shaukat, A., Sharma, A., & Joshi, Y. M. (2012). Squeeze flow behavior of (soft glassy) thixotropic material. *Journal of Non-Newtonian Fluid Mechanics*, 167, 9-17.

Shchukin, D. G., & Möhwald, H. (2007). Self-Repairing Coatings Containing Active Nanoreservoirs. *Small*, 3(6), 926-943.

Sherwood, J. D., & Durban, D. (1998). Squeeze-flow of a Herschel–Bulkley fluid. *Journal of Non-Newtonian Fluid Mechanics*, 77(1), 115-121.

Siguín, D., Ferreira, S., Froufe, L., & Garcia, F. (1993). The relationship between isomorphous substitutions and swelling in montmorillonites. *Journal of Materials Science*, 28(22), 6163-6166.

Sinha-Ray, S., Pelot, D. D., Zhou, Z. P., Rahman, A., Wu, X. F., & Yarin, A. L. (2012). Encapsulation of self-healing materials by coelectrospinning, emulsion electrospinning, solution blowing and intercalation. *Journal of Materials Chemistry*, 22(18), 9138-9146.

Sinha-Ray, S., Sahu, R. P., & Yarin, A. L. (2011). Nano-encapsulated smart tunable phase change materials. *Soft Matter*, 7(19), 8823-8827.

Sinha-Ray, S., Yarin, A. L., & Pourdeyhimi, B. (2010). The production of 100/400nm inner/outer diameter carbon tubes by solution blowing and carbonization of core-shell nanofibers. *Carbon*, 48(12), 3575-3578.

Sinha-Ray, S., Zhang, Y., Yarin, A. L., Davis, S. C., & Pourdeyhimi, B. (2011). Solution blowing of soy protein fibers. *Biomacromolecules*, 12(6), 2357-2363.

Skujans, J., Vulans, A., Iljins, U., & Aboltins, A. (2007). Measurements of heat transfer of multi-layered wall construction with foam gypsum. *Applied Thermal Engineering*, 27(7), 1219-1224.

Sottos, N., White, S., & Bond, I. (2007). Introduction: self-healing polymers and composites. *Journal of The Royal Society Interface*, 4(13), 347-348.

Stephan, J. (1874). Versuche uber die scheinbare adhasion. *Akad. Wiss. Math. Naturwiss*, 69, 713-735.

Stevenson, P., Mantle, M. D., Sederman, A. J., & Gladden, L. F. (2007). Quantitative measurements of liquid holdup and drainage in foam using NMRI. *AIChE journal*, 53(2), 290-296.

Sun, Z., Zussman, E., Yarin, A. L., Wendorff, J. H., & Greiner, A. (2003). Compound Core-Shell Polymer Nanofibers by Co-Electrospinning. *Advanced Materials*, 15(22), 1929-1932.

Tadmor, Z., and C. G. Gogos, (2006). Principles of Polymer Science. Wiley.

Tay, Y. Y., Stewart, D. I., & Cousens, T. W. (2001). Shrinkage and desiccation cracking in bentonite-sand landfill liners. *Engineering Geology*, 60(1), 263-274.

te Nijenhuis, K., (2007). Measurements in shear flow; Rheogoniometers and rheometers. In Tropea, C., Yarin, A. L., & J. Foss (Eds.), *The Springer Handbook of Experimental Fluid Mechanics* (627-646). Berlin: Springer.

Tenney, D., and Pipes, R. B. (2001). "Advanced composites development for aerospace applications," The 7th Japan Int. SAMPE Sym. Exhibition, Tokyo, Japan.

Terzaghi, K., (1947). Theoretical Soil Mechanics (4th ed.). New York: Wiley.

Theron, A., Zussman, E., & Yarin, A. L. (2001). Electrostatic field-assisted alignment of electrospun nanofibres. *Nanotechnology*, 12(3), 384.

Thusyanthan, N. I., Take, W. A., Madabhushi, S. P. G., & Bolton, M. D. (2007). Crack initiation in clay observed in beam bending. *Geotechnique*, 57(7), 581-594.

- Tonyan, T. D., & Gibson, L. J. (1992a). Strengthening of cement foams. *Journal of Materials Science*, 27(23), 6379-6386.
- Tonyan, T. D., & Gibson, L. J. (1992b). Structure and mechanics of cement foams. *Journal of Materials Science*, 27(23), 6371-6378.
- Toohey, K. S., Sottos, N. R., Lewis, J. A., Moore, J. S., & White, S. R. (2007). Self-healing materials with microvascular networks. *Nature Materials*, 6(8), 581-585.
- Trask, R. S., Williams, G. J., & Bond, I. P. (2007). Bioinspired self-healing of advanced composite structures using hollow glass fibres. *Journal of the Royal Society Interface*, 4(13), 363-371.
- Trask, R. S., Williams, H. R., & Bond, I. P. (2007). Self-healing polymer composites: mimicking nature to enhance performance. *Bioinspiration & Biomimetics*, 2(1), P1.
- Tsai, S. W. (2005). Three decades of composites activities at US Air Force Materials Laboratory. *Composites Science and Technology*, 65(15), 2295-2299.
- van der Zwaag, S. (2007). Self healing materials: an alternative approach to 20 centuries of materials science (Vol. 100). Springer.
- Van Olphen, H. (1964). Internal mutual flocculation in clay suspensions. *Journal of Colloid Science*, 19(4), 313-322.
- Vimmrová, A., Keppert, M., Svoboda, L., & Černý, R. (2011). Lightweight gypsum composites: Design strategies for multi-functionality. *Cement and Concrete Composites*, 33(1), 84-89.
- Wada, S., Hayashi, H., & Haga, K. (1973). Behavior of a Bingham Solid in Hydrodynamic Lubrication: Part 1, General Theory. *Bulletin of JSME*, 16(92), 422-431.
- Wada, S., Hayashi, H., & Haga, K. (1974). Behavior of a Bingham Solid in Hydrodynamic Lubrication: Part 3, Application to Journal Bearing. *Bulletin of JSME*, 17(111), 1182-1191.
- Weaire, D., Findlay, S., & Verbist, G. (1995). Measurement of foam drainage using AC conductivity. *Journal of Physics: Condensed Matter*, 7(16), L217.
- Weinstein, S. J., & Ruschak, K. J. (2004). Coating flows. *Annu. Rev. Fluid Mech.*, 36, 29-53.
- White, S. R., Sottos, N. R., Geubelle, P. H., Moore, J. S., Kessler, M., Sriram, S. R., Brown, E. N., & Viswanathan, S. (2001). Autonomic healing of polymer composites. *Nature*, 409(6822), 794-797.
- Wilson, A., Epstein, M. B., & Ross, J. (1957). The adsorption of sodium lauryl sulfate and lauryl alcohol at the air-liquid interface. *Journal of Colloid Science*, 12(4), 345-355.
- Wool, R. P. (2001). Polymer science: a material fix. *Nature*, 409(6822), 773-774.

- Wu, D. Y., Meure, S., & Solomon, D. (2008). Self-healing polymeric materials: A review of recent developments. *Progress in Polymer Science*, 33(5), 479-522.
- Wu, X. (2009). Fracture of advanced composites with nanostructured interfaces: Fabrication, characterization and modeling. VDM Verlag, Germany.
- Wu, X. F., & Dzenis, Y. A. (2005). Experimental determination of probabilistic edge-delamination strength of a graphite–fiber/epoxy composite. *Composite Structures*, 70(1), 100-108.
- Wu, X. F., Rahman, A., Zhou, Z., Pelot, D. D., Sinha-Ray, S., Chen, B., Payne, S., & Yarin, A. L. (2013). Electrospinning core-shell nanofibers for interfacial toughening and self-healing of carbon-fiber/epoxy composites. *Journal of Applied Polymer Science*, 129(3), 1383-1393.
- Wu, M., Johannesson, B., & Geiker, M. (2012). A review: Self-healing in cementitious materials and engineered cementitious composite as a self-healing material. *Construction and Building Materials*, 28(1), 571-583.
- Yang, F. (1998). Exact solution for compressive flow of viscoplastic fluids under perfect slip wall boundary conditions. *Rheologica Acta*, 37(1), 68-72.
- Yang, Y., Lepech, M. D., Yang, E. H., & Li, V. C. (2009). Autogenous healing of engineered cementitious composites under wet–dry cycles. *Cement and Concrete Research*, 39(5), 382-390.
- Yang, Y., Yang, E. H., & Li, V. C. (2011). Autogenous healing of engineered cementitious composites at early age. *Cement and Concrete Research*, 41(2), 176-183.
- Yarin, A. L. (1993). Free Liquid Jets and Films: Hydrodynamics and Rheology. New York: Longman Scientific & Technical and Wiley & Sons.
- Yarin, A. L. (2011). Coaxial electrospinning and emulsion electrospinning of core–shell fibers. *Polymers for Advanced Technologies*, 22(3), 310-317.
- Yarin, A. L., Koombhongse, S., & Reneker, D. H. (2001). Taylor cone and jetting from liquid droplets in electrospinning of nanofibers. *Journal of Applied Physics*, 90(9), 4836-4846.
- Yarin, A. L., Szczech, J. B., Megaridis, C. M., Zhang, J., & Gamota, D. R. (2006). Lines of dense nanoparticle colloidal suspensions evaporating on a flat surface: formation of non-uniform dried deposits. *Journal of Colloid and Interface Science*, 294(2), 343-354.
- Yin, T., Rong, M. Z., Zhang, M. Q., & Yang, G. C. (2007). Self-healing epoxy composites–Preparation and effect of the healant consisting of microencapsulated epoxy and latent curing agent. *Composites Science and Technology*, 67(2), 201-212.
- Youngblood, J. P., and Sottos, N. R., (2008). "Bioinspired Materials." *Mrs Bulletin* 33.

Yu, Q. L., & Brouwers, H. J. H. (2011). Microstructure and mechanical properties of  $\beta$ -hemihydrate produced gypsum: an insight from its hydration process. *Construction and Building Materials*, 25(7), 3149-3157.

Zussman, E., Yarin, A. L., Bazilevsky, A. V., Avrahami, R., & Feldman, M. (2006). Electrospun Polyaniline/Poly (methyl methacrylate)-Derived Turbostratic Carbon Micro-/Nanotubes. *Advanced Materials*, 18(3), 348-353.

## 12. APPENDIX

The following are statements from the publisher granting permission to use previously published articles in this thesis. Permission granted by the Royal Society of Chemistry addresses the work on self-healing core shell fibers from Sections 2.1.2 and 3.1 as well as Chapter 4. Permission granted by the American Chemical Society addresses the work on foam consolidation and drainage from Sections 2.2 and 3.2 as well as Chapter 5. Permission granted by AIP Publishing addresses the work on squeeze flows from Sections 2.3 and 3.3 as well as Chapter 6.

### Acknowledgements to be used by RSC authors

Authors of RSC books and journal articles can reproduce material (for example a figure) from the RSC publication in a non-RSC publication, including theses, without formally requesting permission providing that the correct acknowledgement is given to the RSC publication. This permission extends to reproduction of large portions of text or the whole article or book chapter when being reproduced in a thesis.

The acknowledgement to be used depends on the RSC publication in which the material was published and the form of the acknowledgements is as follows:

- For material being reproduced from an article in *New Journal of Chemistry* the acknowledgement should be in the form:
  - [Original citation] - Reproduced by permission of The Royal Society of Chemistry (RSC) on behalf of the Centre National de la Recherche Scientifique (CNRS) and the RSC
- For material being reproduced from an article *Photochemical & Photobiological Sciences* the acknowledgement should be in the form:
  - [Original citation] - Reproduced by permission of The Royal Society of Chemistry (RSC) on behalf of the European Society for Photobiology, the European Photochemistry Association, and RSC
- For material being reproduced from an article in *Physical Chemistry Chemical Physics* the acknowledgement should be in the form:
  - [Original citation] - Reproduced by permission of the PCCP Owner Societies
- For material reproduced from books and any other journal the acknowledgement should be in the form:
  - [Original citation] - Reproduced by permission of The Royal Society of Chemistry

The acknowledgement should also include a hyperlink to the article on the RSC website.

The form of the acknowledgement is also specified in the RSC agreement/licence signed by the corresponding author.

Except in cases of republication in a thesis, this express permission does not cover the reproduction of large portions of text from the RSC publication or reproduction of the whole article or book chapter.

A publisher of a non-RSC publication can use this document as proof that permission is granted to use the material in the non-RSC publication.



Rightslink® by Copyright Clearance Center

		<a href="#">Home</a> <a href="#">Create Account</a> <a href="#">Help</a>
	<p><b>ACS Publications Title:</b> Foam Consolidation and Drainage</p> <p><b>Author:</b> S. Jun, D. D. Pelot, and A. L. Yarin</p> <p><b>Publication:</b> Langmuir</p> <p><b>Publisher:</b> American Chemical Society</p> <p><b>Date:</b> Mar 1, 2012</p> <p>Copyright © 2012, American Chemical Society</p>	<p>User ID</p> <p>Password</p> <p><input type="checkbox"/> Enable Auto Login</p> <p><input type="button" value="Log In"/></p> <p><a href="#">Forgot Password/User ID?</a></p> <p>If you're a copyright.com user, you can login to RightsLink using your copyright.com credentials. Already a RightsLink user or want to learn more?</p>

**PERMISSION/LICENSE IS GRANTED FOR YOUR ORDER AT NO CHARGE**

This type of permission/license, instead of the standard Terms & Conditions, is sent to you because no fee is being charged for your order. Please note the following:

- Permission is granted for your request in both print and electronic formats, and translations.
- If figures and/or tables were requested, they may be adapted or used in part.
- Please print this page for your records and send a copy of it to your publisher/graduate school.
- Appropriate credit for the requested material should be given as follows: "Reprinted (adapted) with permission from (COMPLETE REFERENCE CITATION). Copyright (YEAR) American Chemical Society." Insert appropriate information in place of the capitalized words.
- One-time permission is granted only for the use specified in your request. No additional uses are granted (such as derivative works or other editions). For any other uses, please submit a new request.

[BACK](#) [CLOSE WINDOW](#)

Copyright © 2013 Copyright Clearance Center, Inc. All Rights Reserved. [Privacy statement](#).  
Comments? We would like to hear from you. E-mail us at [customer@copyright.com](mailto:customer@copyright.com)



**THE SOCIETY OF RHEOLOGY LICENSE  
TERMS AND CONDITIONS**

Dec 16, 2013

This is a License Agreement between David D Pelot ("You") and The Society of Rheology ("SoR") provided by Copyright Clearance Center ("CCC"). The license consists of your order details, the terms and conditions provided by The Society of Rheology, and the payment terms and conditions.

All payments must be made in full to CCC. For payment instructions, please see information listed at the bottom of this form.

License Number	3290910484319
Order Date	Dec 16, 2013
Publisher	AIP Publishing LLC
Publication	Journal of Rheology
Article Title	Strong squeeze flows of yield-stress fluids: The effect of normal deviatoric stresses
Author	D. D. Pelot, R. P. Sahu, S. Sinha-Ray, et al.
Online Publication Date	Mar 13, 2013
Volume number	57
Issue number	3
Type of Use	Thesis/Dissertation
Requestor type	Author (original article)
Format	Print and electronic
Portion	Excerpt (> 800 words)
Will you be translating?	No
Title of your thesis / dissertation	Mechanics of Construction Materials
Expected completion date	Mar 2014
Estimated size (number of pages)	200
Total	0.00 USD

**Terms and Conditions**

The Society of Rheology -- Terms and Conditions: Permissions Uses

The Society of Rheology ("SOR") hereby grants to you the non-exclusive right and license to use and/or distribute the Material according to the use specified in your order, on a one-time basis, for the specified term, with a maximum distribution equal to the number that you have ordered. Any links or other content accompanying the Material are not the subject of this license.

1. You agree to include the following copyright and permission notice with the reproduction of the Material: "Reprinted with permission from [FULL CITATION]. Copyright [PUBLICATION YEAR], The Society of Rheology." For an article, the copyright and permission notice must be printed on the first page of the article or book chapter. For photographs, covers, or tables, the copyright and permission notice may appear with the Material, in a footnote, or in the reference list.
2. If you have licensed reuse of a figure, photograph, cover, or table, it is your responsibility to ensure that the material is original to SOR and does not contain the copyright of another entity, and that the copyright notice of the figure, photograph, cover, or table does not indicate that it was reprinted by SOR, with permission, from another source. Under no circumstances does SOR, purport or intend to grant permission to reuse material to which it does not hold copyright.
3. You may not alter or modify the Material in any manner. You may translate the Material into another language only if you have licensed translation rights. You may not use the Material for promotional purposes. SOR reserves all rights not specifically granted herein.
4. The foregoing license shall not take effect unless and until SOR or its agent, Copyright Clearance Center, receives the Payment in accordance with Copyright Clearance Center Billing and Payment Terms and Conditions, which are incorporated herein by reference.
5. SOR or the Copyright Clearance Center may, within two business days of granting this license, revoke the license for any reason whatsoever, with a full refund payable to you. Should you violate the terms of this license at any time, SOR, The Society of Rheology, or Copyright Clearance Center may revoke the license with no refund to you. Notice of such revocation will be made using the contact information provided by you. Failure to receive

- such notice will not nullify the revocation.
6. SDR makes no representations or warranties with respect to the Material. You agree to indemnify and hold harmless SDR, The Society of Rheology, and their officers, directors, employees or agents from and against any and all claims arising out of your use of the Material other than as specifically authorized herein.
  7. The permission granted herein is personal to you and is not transferable or assignable without the prior written permission of SDR. This license may not be amended except in a writing signed by the party to be charged.
  8. If purchase orders, acknowledgments or check endorsements are issued on any forms containing terms and conditions which are inconsistent with these provisions, such inconsistent terms and conditions shall be of no force and effect. This document, including the CCC Billing and Payment Terms and Conditions, shall be the entire agreement between the parties relating to the subject matter hereof.

**This Agreement shall be governed by and construed in accordance with the laws of the State of New York. Both parties hereby submit to the jurisdiction of the courts of New York County for purposes of resolving any disputes that may arise hereunder.**

**If you would like to pay for this license now, please remit this license along with your payment made payable to "COPYRIGHT CLEARANCE CENTER" otherwise you will be invoiced within 48 hours of the license date. Payment should be in the form of a check or money order referencing your account number and this invoice number RLNK501183263.**

**Once you receive your invoice for this order, you may pay your invoice by credit card. Please follow instructions provided at that time.**

**Make Payment To:**  
 Copyright Clearance Center  
 Dept 001  
 P.O. Box 843006  
 Boston, MA 02284-3006

**For suggestions or comments regarding this order, contact RightsLink Customer Support: [customer-care@copyright.com](mailto:customer-care@copyright.com) or +1-877-622-5543 (toll free in the US) or +1-978-646-2777.**

**Gratis licenses (referencing \$0 in the Total field) are free. Please retain this printable license for your reference. No payment is required.**

## 13. CURRICULUM VITAE

### DAVID D. PELOT

---

#### CAREER OBJECTIVES

Identify components within fluid materials which influence flow behavior and provide cost effective alternatives without altering final product performance. Provide a variety of fluid measurement techniques to characterize fluids. Experimentally simulate fluid flow during manufacturing or application to understand flow behavior.

#### EDUCATION

UNIVERSITY OF ILLINOIS AT CHICAGO, CHICAGO, IL Aug. 2009 – May 2014  
Ph.D. Candidate, Mechanical Engineering  
Advisor: Professor Alexander Yarin

WESTERN MICHIGAN UNIVERSITY, KALAMAZOO, MI Aug. 2001 – May 2006  
Bachelor of Science in Education  
Major: Secondary Education – Physics  
Minor: Mathematics

#### RESEARCH EXPERIENCE

MULTISCALE MECHANICS AND NANOTECHNOLOGY LABORATORY Sept. 2010 – Present

- Designed, prototyped, and built an apparatus for spreading of soft solids and compared results with two mathematical models.
- Derived mathematical model, designed, prototyped, and built the apparatus for constant volume squeeze flow of soft solids.
- Actively assisted other graduate students in projects involving pool boiling, filtration, surfactant films, and foams.
- Conducted product development research for Fortune 500 company.
- Presented corporate research projects to upper level management on a regular basis via oral presentations and written reports.

#### PUBLICATIONS

1. **Pelot, D. D.**, Klep, N., and A. L. Yarin (in preparation). Spreading of Carbopol gels: Newtonian vs. non-Newtonian effects.
2. **Pelot, D. D.**, Jun, S., and A. L. Yarin, (2014). Bentonite dispersions: Transition from liquid-like to solid-like behavior and cracking. *Journal of Rheology*. (under review).
3. **Pelot, D. D.**, Sahu, R. P., Sinha-Ray, S., and A. L. Yarin, (2013). Strong squeeze flows of yield-stress fluids: The effect of normal deviatoric stresses. *Journal of Rheology*, **57**, 719-742.
4. Wu, X. F., Rahman, A., Zhou, Z., **Pelot, D. D.**, Sinha-Ray, S., Chen, B., Payne, S., and A. L. Yarin, (2013). Electrospinning core-shell nanofibers for interfacial toughening and self-healing of carbon-fiber/epoxy composites. *Journal of Applied Polymer Science*, **129**(3), 1383-1393.
5. Sinha-Ray, S., **Pelot, D.D.**, Zhou, Z.P., Rahman, A., Wu, X. -F., and A. L. Yarin, (2012). Encapsulation of self-healing materials by coelectrospinning, emulsion electrospinning, solution blowing and intercalation. *Journal of Materials Chemistry*, **22**, 9138-9146.
6. Jun, S., **Pelot, D. D.**, and A. L. Yarin, (2012). Foam consolidation and drainage, *Langmuir*, **28**(12), 5323-5330.

#### MENTORING AND TEACHING EXPERIENCE

MENTOR, MULTISCALE MECHANICS AND NANOTECHNOLOGY LABORATORY June 2013 – Aug. 2013  
*National Science Foundation Research Experiences for Undergraduates*

- Taught undergraduate student the basic concepts of fluid dynamics and polymer behavior and Mentored student to a level of competency to accomplish lab tasks independently.

*TEACHING ASSISTANTSHIP, UNIVERSITY OF ILLINOIS AT CHICAGO**Course: ME211 Fluid Mechanics Laboratory**Jan. 2014 – May 2014**Course: ME321 Heat Transfer Laboratory**Jan. 2013 – May 2013**Course: ME341 Experimental Methods in Mechanical Engineering**Sept. 2011- Dec. 2011*

- Laboratory courses that demonstrate rigid body rotation, jet impact, Bernoulli's equation, drag, and pipe flow using experiments; Fourier rate equation, thermal conductivity constant, forced convection, and local heat transfer coefficient using experiments; Fundamentals of pressure calibrations, flow velocity measurements, refrigeration cycle, air conditioning, and centrifugal pumps. (respectively)
- Assessed student laboratory reports using self made rubric and managed all administrative duties involved.

*KENWOOD ACADEMY HIGH SCHOOL, CHICAGO PUBLIC SCHOOLS, IL**Aug. 2007 – July 2009*

- Subjects taught include Remedial Algebra 1, Honors Algebra 1, and Algebra 2. Leader of the Algebra 1 course team.

*BENTON HARBOR HIGH SCHOOL, BENTON HARBOR PUBLIC SCHOOLS, MI**Aug. 2006 – July 2007*

- Subjects taught include Algebra 2, Fundamentals of Geometry, and Geometry.

**PROFESSIONAL DEVELOPMENT***INSTITUTE OF INDUSTRIAL ENGINEERS SIX SIGMA GREEN BELT CERTIFIED**Apr. 2013*

- Understand concepts of problem solving, data collection and interpretation, variation, process capability, and cost analysis.

**PROFESSIONAL SOCIETIES***ASME, UIC CHAPTER**Jan. 2012 – Present*

- Mentored UIC ASME officers in organization, leadership, teamwork, and budgeting, Jan. 2013– Dec. 2014. Also, performed duties as Treasurer and Secretary, Aug. 2012– Aug 2013.

**COMPUTER AND TECHNICAL SKILLS**

- MatLab, OriginPro, Microsoft Office, Instron machine, Imada force gauge, Phantom Miro high-speed camera, RedLake Motion Pro high-speed camera, Brookfield viscometer, TA Instruments Discovery Hybrid Rheometer, Visco-Corder.

**AWARDS AND GRANTS***AMERICAN PHYSICAL SOCIETY CONFERENCE, DENVER, CO**MAR. 2014*

- Presented squeeze flow measuring device in the topic "Instrumentation and Measurement."

*LITVIN GRADUATE HONOR AWARD**APR. 2013*

- In recognition of academic achievement as well as service to the mechanical engineering department and undergraduate/graduate student community.

*NSF CIVIL, MECHANICAL, AND MATERIAL INNOVATION CONFERENCE**July 2012*

- Awarded the honor of presenting student poster titled "Creating Self Healing Materials through Core-Shell Electrospinning" based on the publication in the Journal of Materials Chemistry.

*NSF PIRE GRANT "INTELLIGENT STRUCTURAL HEALTH MANAGEMENT OF SAFETY-CRITICAL AEROSPACE, CIVIL AND MECHANICAL STRUCTURES" DALIAN UNIV. OF TECH., DALIAN, CHINA**June 2012*

- Conducted research using Brillouin optical time domain analysis of model cable-stayed bridge and visited laboratories of Dalian University of Technology in China.